

# UC San Diego

## Research Theses and Dissertations

### Title

Investigations into the Effects of Long-Term Seawater Exposure on Graphite/Epoxy Composite Materials

### Permalink

<https://escholarship.org/uc/item/2wm9s2cf>

### Author

Sloan, Forrest E.

### Publication Date

1991

Peer reviewed

## INFORMATION TO USERS

This manuscript has been reproduced from the microfilm master. UMI films the text directly from the original or copy submitted. Thus, some thesis and dissertation copies are in typewriter face, while others may be from any type of computer printer.

**The quality of this reproduction is dependent upon the quality of the copy submitted.** Broken or indistinct print, colored or poor quality illustrations and photographs, print bleedthrough, substandard margins, and improper alignment can adversely affect reproduction.

In the unlikely event that the author did not send UMI a complete manuscript and there are missing pages, these will be noted. Also, if unauthorized copyright material had to be removed, a note will indicate the deletion.

Oversize materials (e.g., maps, drawings, charts) are reproduced by sectioning the original, beginning at the upper left-hand corner and continuing from left to right in equal sections with small overlaps. Each original is also photographed in one exposure and is included in reduced form at the back of the book.

Photographs included in the original manuscript have been reproduced xerographically in this copy. Higher quality 6" x 9" black and white photographic prints are available for any photographs or illustrations appearing in this copy for an additional charge. Contact UMI directly to order.

# U·M·I

University Microfilms International  
A Bell & Howell Information Company  
300 North Zeeb Road, Ann Arbor, MI 48106-1346 USA  
313/761-4700 800/521-0600



**Order Number 9130764**

**Investigations into the effects of long-term seawater exposure on  
graphite/epoxy composite materials**

**Sloan, Forrest Eugene, Ph.D.**

**University of California, San Diego, 1991**

**Copyright ©1991 by Sloan, Forrest Eugene. All rights reserved.**

**U·M·I**  
300 N. Zeeb Rd.  
Ann Arbor, MI 48106



UNIVERSITY OF CALIFORNIA, SAN DIEGO

**Investigations into the Effects of Long-Term Seawater Exposure  
on Graphite/Epoxy Composite Materials**

A dissertation submitted in partial satisfaction of the  
requirements for the degree of Doctor of Philosophy  
in Oceanography

by

**Forrest Eugene Sloan**

Committee in charge:

Professor R. J. Seymour, Chair  
Professor D. J. Faulkner  
Professor E. D. Goldberg  
Professor J. B. Kosmatka  
Professor J. B. Talbot  
Professor B. H. Zimm

1991

**Copyright 1991**  
**by**  
**Forrest Eugene Sloan**

The dissertation of Forrest Eugene Sloan is approved, and it  
is acceptable in quality and form for publication on microfilm:

Bruno H. Zimm  
Edward D. Galley  
Gay B. Talbot  
John B. Jurek  
Paul J. Flory  
R. K. Sorenson

University of California, San Diego

1991



**This dissertation is dedicated to Jennifer.**

## Table of Contents

	Signature Page .....	iii
	Dedication Page .....	iv
	Table of Contents .....	v
	List of Figures and Tables .....	viii
	Acknowledgements .....	xi
	Vita, Publications and Fields of Study .....	xiii
	Abstract .....	xiv
<b>I</b>	<b>Composite Materials and the Marine Environment .....</b>	<b>1</b>
	1.1. Introduction .....	1
	1.2. Background .....	3
	1.2.1. Mechanical Properties of Composites .....	3
	1.2.2. Constituent Materials in Composites .....	3
	1.2.2.1. Reinforcing Fibers .....	3
	1.2.2.2. Polymer Matrix Materials .....	6
	1.2.3. Fiber-Reinforced Composites in the Marine Industry .....	7
	1.2.4. Selection of Materials for Seawater Testing .....	10
	1.2.5. Damage Mechanisms in the Marine Environment .....	10
	1.2.5.1. Moisture Absorption .....	11
	1.2.5.2. Salinity .....	14
	1.2.5.3. Galvanic Corrosion .....	15
	1.2.5.4. Wave Loading (Fatigue) .....	18
	1.2.5.5. Ultraviolet Radiation (Sunlight) .....	19
	1.2.5.6. Biological Activity .....	20
	1.3. Experimental Methods .....	21
	1.4. Summary .....	22
	Tables .....	23
	Figures .....	29
<b>II</b>	<b>Effect of Environmental Conditions on Moisture Uptake .....</b>	<b>33</b>
	2.1. Introduction .....	33
	2.2. Background .....	34
	2.2.1. Moisture Uptake by Diffusion .....	34
	2.2.2. Formation of Calcareous Deposits .....	37
	2.3. Experimental Procedure .....	40
	2.4. Results and Discussion .....	42
	2.4.1. Weight Gain Results .....	42
	2.4.2. Qualitative Chemical Analysis of Surface Films .....	45
	2.5. Conclusions .....	47
	Tables .....	49
	Figures .....	53
<b>III</b>	<b>The Effect of Seawater Exposure on Shear Strength .....</b>	<b>69</b>
	3.1. Introduction .....	69
	3.2. Background .....	69
	3.2.1. Shear Testing Using Composite Beam Specimens .....	69
	3.2.2. Compliance of a Symmetric Composite Beam .....	70

3.3.	Experimental Procedure .....	72
3.4.	Results and Discussion .....	73
3.4.1.	Moisture Content of the Conditioned Specimens .....	73
3.4.2.	Non-Dimensional Data Analysis .....	74
3.4.3.	Changes in Shear Strength .....	74
3.4.4.	Changes in Shear Modulus .....	75
3.5.	Conclusions .....	77
	Tables .....	78
	Figures .....	80
<b>IV</b>	<b>The Effect of Seawater Exposure on Mode I</b>	
	<b>Interlaminar Crack Growth .....</b>	<b>82</b>
4.1.	Introduction .....	82
4.2.	Experimental Procedure .....	83
4.2.1.	Specimen Preparation .....	83
4.2.2.	Compliance Determination .....	84
4.2.3.	Experimental Matrix .....	85
4.2.4.	Environmental Conditioning .....	85
4.2.5.	Test Environment .....	86
4.2.6.	Fracture Testing .....	86
4.3.	Results and Conclusions .....	87
4.3.1.	Compliance Results .....	87
4.3.2.	Results of Fracture Testing .....	88
4.3.3.	Crack Growth Results .....	89
4.3.4.	SEM Analysis .....	89
4.3.5.	Discussion .....	90
4.4.	Conclusions .....	93
	Tables .....	95
	Figures .....	97
<b>V</b>	<b>Anodic Polarization (Stray-Current) Damage .....</b>	<b>110</b>
5.1.	Introduction .....	110
5.2.	Background .....	110
5.2.1.	Anodic Polarization (Stray-Current Corrosion) .....	110
5.2.2.	Oxygen Evolution on Carbon and Graphite .....	111
5.2.3.	Oxidation of Carbon/Graphite .....	112
5.3.	Experimental Procedure .....	114
5.4.	Results and Discussion .....	115
5.5.	Conclusions .....	118
	Figures .....	119
<b>VI</b>	<b>Cathodic Polarization (Galvanic Coupling) Damage .....</b>	<b>129</b>
6.1.	Introduction .....	129
6.2.	Background .....	129
6.2.1.	Galvanic Coupling Damage .....	129
6.2.2.	Cathodic Reactions on Carbon and Graphite .....	130
6.2.3.	Graphite Degradation by Excess Peroxide .....	132
6.2.4.	Formation of Calcareous Films .....	132

6.3. Experimental Procedure .....	133
6.4. Results and Discussion .....	134
6.4.1. Experimental Results .....	134
6.4.2. Chemical Attack of the Epoxy Resin .....	135
6.5. Conclusions .....	136
Figures .....	138
<b>VII Cathodic Polarization Damage Mechanisms .....</b>	<b>145</b>
7.1. Introduction .....	145
7.2. Background .....	146
7.2.1. pH Levels Under a Calcareous Film .....	146
7.2.2. Investigation of Oxygen Reduction .....	151
7.2.2.1. Rotating Disk and Ring-Disk Electrodes .....	152
7.2.2.2. Oxygen Reduction .....	154
7.2.3. Properties of Hydrogen Peroxide .....	156
7.2.4. FTIR Analysis of Graphite/Epoxy Composites .....	157
7.3. Experimental Procedure .....	158
7.3.1. pH of Galvanically Coupled Samples .....	158
7.3.2. High pH Exposure Study .....	159
7.3.3. Rotating Ring-Disk Study .....	160
7.3.4. H <sub>2</sub> O <sub>2</sub> Exposure Study .....	161
7.3.5. FTIR Analysis .....	161
7.4. Experimental Results .....	163
7.4.1. pH Under a Calcareous Film .....	163
7.4.2. Rotating Ring-Disk Study .....	164
7.4.3. Long-term Exposure Experiments .....	164
7.4.4. FTIR Analysis .....	165
7.5. Discussion .....	166
7.6. Conclusions .....	173
Tables .....	175
Figures .....	177
<b>VIII Summary and Recommendations .....</b>	<b>193</b>
8.1. Introduction .....	193
8.2. Summary .....	194
8.2.1. The Effect of Moisture on Static Properties .....	194
8.2.2. The Inadequacy of Static Testing .....	195
8.2.3. Monitoring Damage in Composites .....	196
8.2.4. Delamination Growth in a Moist Environment .....	197
8.2.5. Electrochemical Damage Mechanisms .....	198
8.3. Conclusions .....	200
List of References .....	201
Appendix A: General Laminate Theory .....	212
Appendix B: Environmental Testing using a Compliant Load-Frame ..	219

## List of Figures and Tables:

### Chapter I

Table 1.1. Axial properties of composite laminates .....	23
Table 1.2. Transverse properties of composite laminates .....	24
Table 1.3. Shear properties of composite laminates .....	24
Table 1.4. Mechanical properties of common fiber families .....	25
Table 1.5. Characteristics of fiber families .....	26
Table 1.6. Mechanical properties of thermosetting plastics .....	27
Table 1.7. Mechanical properties of engineering thermoplastics .....	28
Figure 1.1. Fiber-dominated tensile and compressive strength of composites .....	29
Figure 1.2. Specific stiffness of composites .....	30
Figure 1.3. Matrix-dominated shear and transverse strength of composites .....	31
Figure 1.4. Matrix-dominated stiffness of composites .....	32

### Chapter II

Table 2.1. Principle constituents of seawater .....	49
Table 2.2. Fickian diffusivity coefficients in T300/934 graphite/epoxy .....	49
Table 2.3. Summary of moisture absorption results .....	50
Table 2.4. Results of weight removal operations .....	51
Table 2.5. Distribution of absorbed moisture .....	52
Figure 2.1. A laminate made up of distinct unidirectional composite plies .....	53
Figure 2.2. Schematic diagram of the cathodic polarization experiment .....	53
Figure 2.3. Moisture uptake in T300/934 graphite/epoxy samples .....	54
Figure 2.4. SEM micrograph of the surface of an unsoaked specimen .....	55
Figure 2.5. SEM micrograph of a specimen soaked in tapwater .....	56
Figure 2.6. SEM micrograph of a specimen soaked in seawater .....	57
Figure 2.7. Photograph of the underside of a calcareous edge deposit .....	58
Figure 2.8. SEM micrograph of the underside of a calcareous edge deposit .....	59
Figure 2.9. Broken fiber detail of Fig. 2.8 .....	60
Figure 2.10. SEM micrograph of the underside of a calcareous edge deposit .....	61
Figure 2.11. Close-up view of Fig. 2.10 .....	62
Figure 2.12. Photograph of the underside of a calcareous face deposit .....	63
Figure 2.13. Photograph of a blister formed underneath a face deposit .....	64
Figure 2.14. SEM micrograph of the underside of a face deposit .....	65
Figure 2.15. SEM micrograph of the outside surface of a face deposit .....	66
Figure 2.16a. X-ray diffraction spectra of powdered calcareous deposit .....	67
Figure 2.16b. X-ray diffraction spectra of a calcareous face deposit .....	68

### Chapter III

Table 3.1. Moisture content of tested samples .....	78
Table 3.2. Shear-modified bending stiffness, $E_s$ .....	78
Table 3.3. Effect of conditioning on shear strength .....	79
Table 3.4. Calculated tensile and shear modulus .....	79
Figure 3.1. Schematic of the four-point bending test .....	80
Figure 3.2. A beam deflecting under four-point loading .....	80
Figure 3.3. Apparent strain versus shear stress in four-point bending .....	81

### Chapter IV

Table 4.1. Environmental conditioning test matrix .....	95
Table 4.2. Effect of environment on Mode I fracture resistance .....	95
Table 4.3. Effect of moisture on Mode I fracture resistance .....	96
Figure 4.1. Constant-extension-rate tensile tester .....	97
Figure 4.2. Compliant load-frame for static loading of DCB specimens .....	97
Figure 4.3. Compliance data of 30-ply AS4/3501-5a DCB specimens .....	98
Figure 4.4. Compliance data of DCB specimens after seawater fatigue .....	99
Figure 4.5. Fracture resistance as a function of crack length .....	100
Figure 4.6. Fiber bridging in a DCB specimen fatigued in seawater .....	101
Figure 4.7. Total crack growth during fatigue loading .....	102
Figure 4.8. Crack growth rates in air and in seawater .....	103
Figure 4.9. Energy applied during crack growth experiments .....	104
Figure 4.10. SEM micrograph of a Mode I fracture surface .....	105
Figure 4.11. Transition from static fracture to fatigue cracking .....	106
Figure 4.12. Transition from fatigue cracking to static fracture .....	107
Figure 4.13. Debonded and broken fibers behind the crack tip .....	108
Figure 4.14. Hackle markings at the crack tip .....	109

### Chapter V

Figure 5.1. Anodic polarization experiment .....	119
Figure 5.2. Anodic polarization scans on AS4/3501 graphite/epoxy .....	120
Figure 5.3. Steady-state current as a function of applied potential .....	121
Figure 5.4. Time elapsed before matrix cracking and discoloration .....	122
Figure 5.5. SEM micrograph of an unpolarized (control) specimen .....	123
Figure 5.6. Detail view of the control specimen .....	124
Figure 5.7. Specimen anodically polarized to 750 mV (SCE) for 14 days .....	125
Figure 5.8. Detail view of the specimen polarized to 750 mV .....	126
Figure 5.9. Specimen anodically polarized to 1900 mV (SCE) for 3 days .....	127
Figure 5.10. Detail view of the specimen polarized to 1900 mV .....	128

## Chapter VI

Figure 6.1. Cathodic polarization experiment .....	138
Figure 6.2. Schematic diagram of the four-point bending test .....	138
Figure 6.3. Shear strength data for conditioned T300/934 graphite/epoxy .....	139
Figure 6.4. SEM micrograph of Mode II fracture in a control specimen .....	140
Figure 6.5. Degraded area on the edge of a cathodically polarized sample .....	141
Figure 6.6. Detail view of the degraded area shown in Fig. 6.5 .....	142
Figure 6.7. Micrograph of the corroded sample inside the degraded area .....	143
Figure 6.8. Micrograph of the corroded sample outside the degraded area .....	144

## Chapter VII

Table 7.1. Environmental parameters used in the pH model .....	175
Table 7.2. Results of RRDE experiments .....	175
Table 7.3. FTIR band assignments in cured TGDDM/DDS epoxy .....	176
Table 7.4. Assignment of extraneous bands in FTIR spectra .....	176
Figure 7.1. Ion fluxes at a surface film .....	177
Figure 7.2. The rotating disk electrode .....	177
Figure 7.3. The rotating ring-disk electrode .....	178
Figure 7.4. The graphite/epoxy disk electrode .....	178
Figure 7.5. Pourbaix diagram for hydrogen peroxide .....	179
Figure 7.6. Theoretical pH under a surface film .....	180
Figure 7.7. Theoretical pH under a film with experimental data .....	181
Figure 7.8. Histogram of experimental under-film pH data .....	182
Figure 7.9. Disk-to-ring current ratio for the RRDE experiments .....	183
Figure 7.10. Disk-to-ring current ratio for the RRDE experiments .....	184
Figure 7.11. FTIR spectrum of powdered graphite/epoxy .....	185
Figure 7.12. FTIR spectrum of powdered graphite cloth .....	186
Figure 7.13. FTIR spectrum of cured 3501-5a epoxy .....	187
Figure 7.14. FTIR spectrum of 3501-5a after 8 months at pH=12 .....	188
Figure 7.15. FTIR spectrum of 3501-5a after 1 year in 5% H <sub>2</sub> O <sub>2</sub> .....	189
Figure 7.16. FTIR spectrum of cured 934 epoxy .....	190
Figure 7.17. FTIR spectrum of cathodically polarized 934 epoxy .....	191
Figure 7.18. FTIR spectrum of 934 epoxy after baking at 200 °C .....	192

### Acknowledgements:

I would like to thank the members of my doctoral committee for all of their advice and discussion over the last few years. Special thanks goes to my dissertation advisor Dr. Richard Seymour for allowing me the freedom to study the things that I thought were important (but occasionally pointing out why they were not). I would also like to thank Dr. Jan Talbot for valuable advice on electrochemical techniques, and for the use of her laboratory facilities. My thanks to Dr. Bruno Zimm and Dr. Charles Perrin of the Chemistry Department for their help in identifying polymer degradation mechanisms. Thanks also to Dr. Anne Hoger for her encouragement and for advice on solid mechanics and viscoelasticity.

I would also like to thank the staff at SIO for all of their help during my time here, in particular Dave Aglietti and John Lyons of the Hydraulics Laboratory for assisting my experimental work and Martha Rognon of the Ocean Engineering Research Group for helping me get through the UC paperwork jungle. Special thanks goes to Meredith Sessions for all of his technical advice on everything from 3-phase motors to hard disk drives. I also want to thank the staff of the SIO graduate office for making the interface with UCSD and OGSR so painless. A special thank-you/congratulations goes to Betty Stover on her retirement after 25 years of taking care of wayward SIO graduate students like me.

The materials used in the present experiments were donated by several local corporations, and I would like to thank those people involved. The T300/934 graphite/epoxy laminate used in the studies of Chapters 2, 6, and 7 was contributed by General Dynamics in San Diego — kudos to Karl Meyers of G.D. A much larger quantity of AS-4/3501-5a graphite/epoxy laminate was donated by Rohr



Industries of Chula Vista, and special thanks goes to Norm Brink at Rohr for all of his advice and encouragement. The AS-4/3501-5a material was used in the studies of Chapters 3, 4, 5, and 7. I would also like to thank all of the members of the local ASM and SAMPE chapters for their encouragement and suggestions over the past several years.

I want to especially thank my friends and fellow graduate students. Without their camaraderie and support graduate life would have been a lot harder. Special thanks go to Michele Okihiro, my officemate for the last many years, for her sense of humor, good advice, and great desserts. I would also like to thank Ron George and Tom Herbers for their friendship over the years, and to each and every person I've played beach frisbee with during my time here.

I owe a special debt to my family, especially my parents, for all of their encouragement and love from day one. But the one person I want to thank most is my wife Jennifer — I couldn't have done it without her by my side.

## VITA

August 29, 1960	Born, Orlando, Florida, USA
August 1983	BS in Mechanical Engineering, Virginia Tech
1984-1985	Research Assistant, Florida Atlantic University
August 1986	MS in Ocean Engineering, Florida Atlantic University
1985-1991	Research Assistant, Scripps Institution of Oceanography University of California, San Diego
1991	Doctor of Philosophy in Oceanography, University of California, San Diego

## PUBLICATIONS

Sloan, F. E., Talbot, J. B., and Seymour, R. J., "Electrochemical Damage in Graphite/Epoxy Composites," Proc. First International Symposium on Environmental Effects on Advanced Materials, San Diego, June 1991, NACE, Houston, in press.

Seymour, R. J., and Sloan, F. E., "Pultrusion and Thermoforming of a Graphite-Thermoplastic Marine Cable," Proc. 31st SAMPE Symp., San Diego, April 1991.

Sloan, F. E., and Seymour, R. J., "Environmental Testing Using a Compliant Load-Frame," J. of Composite Materials, Vol 24, July 1990, pp. 727-738.

Hartt, W. H., and Sloan, F. E., "Fatigue of Welded Connections in Seawater," Proc. 1st OMAE Specialty Symposium on Offshore and Arctic Frontiers, ASME, New York, 1986, pp. 59-71.

## FIELDS OF STUDY

Major Field: Oceanography (Applied Ocean Science)

Studies in Corrosion and Electrochemistry:  
Professors M. T. Simnad and J. B. Talbot

Studies in Composite Materials:  
Professors H. Murakami, J. B. Kosmatka, and R. J. Seymour

Studies in Organic Chemistry:  
Professors B. H. Zimm, C. L. Perrin, and D. J. Faulkner

Studies in Marine Chemistry:  
Professors E. D. Goldberg and J. Gieskes

## **ABSTRACT OF THE DISSERTATION**

### **Investigations into the Effects of Long-Term Seawater Exposure on Graphite/Epoxy Composite Materials**

by

**Forrest E. Sloan**

Doctor of Philosophy in Oceanography

University of California, San Diego, 1991

Professor Richard J. Seymour, Chairman

The investigations documented here were intended to determine whether graphite-fiber-reinforced plastics can survive the highly aggressive seawater environment when used as structural materials in advanced ocean engineering designs. Two general effects of seawater exposure were identified as potentially life-limiting phenomena. The first effect is a weakening of the fiber-to-matrix bond caused by exposure of the interface to moisture. The second effect is the establishment of an electrolyte (seawater) around the conductive graphite fibers, thus allowing electrochemical reactions to take place. (The effects of static pressure, solar radiation and biological activity were not included in the present investigation).

The fiber/matrix interface bond is weakened as a result of exposure to a moist environment. However, for graphite/epoxy composites the bond does not generally fail in the absence of applied loading. When loads are applied the local effect is for the fiber to de-bond from the matrix. However, the effects on a larger scale are more complex, and may not be intuitive. For example, in the present study it was found that the weakened fiber/matrix bond actually increased the resistance of the material to fatigue and fracture.

Electrochemical degradation can occur as the result of stray-current corrosion or galvanic coupling. Stray-current damage is rapid, involves dissolution of the graphite reinforcing fibers, and can occur under relatively low current conditions. Galvanic coupling damage is a subtle localized corrosion phenomenon involving chemical attack of the polymer resin. Electrochemical damage is the result of interaction with species which form as intermediates in the oxygen reactions on the anode and cathode.

# **I COMPOSITE MATERIALS AND THE MARINE ENVIRONMENT**

## **1.1. INTRODUCTION**

The advantages of using fiber-reinforced composite materials have been widely recognized in many high-technology areas such as the aerospace, automotive, biotech, and sporting goods industries. High strength and stiffness coupled with low density and good corrosion resistance have largely overcome acceptance problems associated primarily with high initial cost.

Composites have been used for many years in the marine industry, primarily as boat-building materials, e.g. fiberglass-reinforced polyester. More recently, however, composites have been considered for more advanced applications where metals are undesirable because of their high density and tendency to corrode. For example, submarines operating at great depth require thick hulls to prevent collapse. Metal hulls are quite heavy and cannot be used in deepest-ocean manned vehicles because of the prohibitively large buoyancy required. As another example, consider deepwater designs for oil and gas recovery such as the guyed tower and the tension-leg platform. Lowering the deployment weight and maintenance costs are essential to make these deep water recovery operations economical. Composite materials can provide much more efficient designs while increasing system reliability.

A composite material can be defined as a combination of two or more distinct materials which act synergistically to produce a desired property or properties that is unobtainable from the constituent components. This definition encompasses such composites as concrete and steel-belted tires, and includes the mud bricks reinforced with straw made since prehistory. The strongest engineering composites, however, are materials which have been reinforced with continuous

high-strength fibers. Because of their growing economic and engineering importance, the present study will consider only composites of polymer matrix materials and continuous reinforcing fibers.

High-strength reinforcing fibers are far too brittle to act alone, and are typically laid down parallel to one another and bonded together in a plastic matrix. The fibers carry the load while the matrix distributes the load among the fibers and carries the load across individual fiber breaks. By stacking the resulting composite laminae (layers or plies) in different directions, a laminate can be created which exhibits superior structural properties in any number of directions. This ability to tailor the strength of the material to the expected magnitude and direction of the applied loads gives the engineer much greater flexibility in the design process.

Fiber-reinforced polymer composites are also attractive to ocean engineers because of their inherent resistance to electrochemical corrosion. Non-metals have the advantage of being essentially non-conducting, thus precluding the primary mode of attack for metals. However, the ocean is an extremely aggressive service environment, where wave-loading, biological activity, UV radiation, and hot/wet cycles can all act synergistically to cause unanticipated failure of a component. Non-metals such as reinforced polymers are less susceptible to electrochemical damage, but may be prime targets for biological activity and UV radiation.

In order to safely utilize the advanced capabilities of composite materials in the ocean, designers must recognize and understand the mechanisms of environmental degradation. Therefore obtaining knowledge of the damage modes inherent to seawater is the first step towards designing newer materials which would greatly extend the useful life of ocean engineering designs. The purpose of the following investigations has been to identify damage mechanisms which might lead to premature failure in structural composite members used in the ocean.

## **1.2. BACKGROUND**

### **1.2.1. Mechanical Properties of Composites**

Fiber-reinforced composite materials have impressive fiber-controlled properties when compared to common engineering metals, as listed in Table 1.1 and shown in Figs. 1.1 and 1.2 (Tsai, 1987; ASM, 1987; Smith, 1990). Specific (normalized with respect to density) tensile strength in the fiber direction is much higher for these materials, and this is the primary reason for their use. However, composites are highly anisotropic, and they are typically much weaker when loaded in a direction which is not parallel to the fibers. Specific transverse and shear properties are listed in Tables 1.2 and 1.3, and are shown in Figs. 1.3 and 1.4. These figures illustrate the inefficiency of matrix-controlled properties, and show why fiber-reinforced composites must be used carefully in design.

### **1.2.2. Constituent Materials in Composites**

A fiber-reinforced composite is actually composed of three distinct materials, the load-bearing fibers, the matrix material, and a "sizing" or "binding" agent that protects the fibers and ensures a good bond to the matrix. In a typical application, a matrix is selected based on environmental demands, while the fiber is chosen based on anticipated loading. The fiber manufacturer will usually supply fibers which are coated with a binding agent that is compatible with the chosen matrix resin.

#### **1.2.2.1. Reinforcing Fibers**

There are five major families of reinforcing fibers: glass, aramid, graphite, boron, and polyethylene. These fibers are listed along with important physical

properties in Table 1.4 (Tsai and Hahn, 1980; Halpin, 1984; Smith, 1990). The characteristics of each fiber family are listed in Table 1.5.

Glass fibers are undoubtedly the most common reinforcing material in use in composites. E-glass (electrical grade glass fibers) remains one of the strongest reinforcing fibers, and is available in many forms at very low cost. One disadvantage of glass reinforcement is a relatively low modulus, which can reduce the efficiency of the composite in high-strain applications by straining the matrix/fiber interface. Glass reinforced composites are therefore generally more fatigue sensitive than laminates with other types of reinforcements. E-glass fibers are also known to suffer from a long-term stress-corrosion mechanism in the presence of even small amounts of moisture (Mandell and Meier, 1983). Several grades of glass fibers are available which have special properties for specific applications, e.g. high strength (S, S2) or corrosion resistance (CR).

Boron fibers have a very high modulus and are therefore very good in applications where stiffness is essential. However, boron is a comparatively expensive material. Consequently boron-fiber-reinforced composites are used primarily in military and aerospace applications.

Aramid (aromatic polyamide) fibers have very high specific tensile strength and stiffness. The principal disadvantage of aramid fiber is a low resistance to buckling under compressive loading. Aramid fibers also tend to absorb moisture, which can lead to swelling and the formation of residual stresses. Composites reinforced with aramid fibers are able to absorb great amounts of energy, and are widely used in applications requiring protection against collisions and rough handling.

High-density polyethylene (HDPE) fiber properties are comparable to aramid properties, but the specific properties are higher due to a lower density.



These fibers have only recently been introduced, and have been used primarily in applications dominated by aramid such as ropes and ballistic protection.

Disadvantages include low transverse strength, low compressive strength, and a tendency to creep at relatively low temperatures. HDPE offers the unique property of flotation (specific gravity of 0.97).

Initially high costs and low elongation-to-failure precluded carbon (graphite) fibers from early marine use. However, their widespread use in the aerospace industry and emerging use in automobiles has led to a large manufacturing base and hence property improvements and rapidly falling costs. Graphite fibers can be obtained in a wide range of strength and stiffness, although the highest stiffness fibers remain extremely expensive. The high specific modulus of all graphite fibers makes them an excellent choice in fatigue. Graphite fibers are electrically conductive and this property can be put to good use, e. g. in resistance welding of thermoplastics. Electrical conductivity can also cause problems such as galvanic corrosion when used with structural metals.

The availability of many types of reinforcing fibers with widely varying properties can make the choice of any one type of reinforcement difficult. However, the advantage of designing with composites is that a single choice is unnecessary. By constructing a laminate with several distinct layers, the advantages of all of the fibers might be utilized. For example, it is common to see composites of graphite combined with covering plies of aramid or glass. The graphite provides stiffness while the glass and/or aramid provides protection against impact damage. The best properties of each material are used to create a composite with the advantages of both.

#### 1.2.2.2. Polymer Matrix Materials

In an aggressive environment such as seawater, selection of the matrix is of prime importance. Ideally the matrix will keep the fibers separate from the environment, and will not lose ductility or strength after long term exposure. These criteria suggest a polymer which forms a strong bond with the fibers, and one which does not absorb significant amounts of moisture. A high-temperature material is not necessary, as service temperatures in the ocean are unlikely to exceed 40°C.

Two broad classes of engineering plastics have been developed over the years, namely thermosets and thermoplastics. Thermosets such as epoxies and polyesters are specialty plastics which exhibit superior mechanical properties and are resistant to chemicals and high temperature environments. However, the manufacturing of thermosets involves volatile chemicals and complex high-temperature/high-pressure cure cycles. Production rates using reinforced thermosets are therefore relatively low. Thermoplastics, on the other hand, are easily molded by heating to the melt temperature, and are best utilized in high volume applications. Thermoplastics generally exhibit greater toughness than thermosets, but have lower strength and stiffness. As a result of the increasing demand for higher performance and lower manufacturing costs for aerospace parts, each of these polymer classes has moved in the direction of the other. For example, research in the thermosets area is aimed at simplifying cure cycles and improving ductility. Recently introduced thermoplastics exhibit higher modulus and better environmental resistance.

The most common industrial thermosetting resins are the polyesters, which are typical matrix materials for fiberglass components. Vinyl ester resins are used where higher toughness and greater chemical resistance is desired. For high-performance applications epoxies are used. Epoxies exhibit higher strength and

stiffness, greater environmental resistance and low cure shrinkage. Phenolic resins are used where resistance to fire damage is desired, e.g. strength retention at elevated temperatures and release of minimal toxic smoke. Mechanical properties of several thermosetting plastics are shown in Table 1.6 (Smith, 1990; May, 1988).

Recently several thermoplastic materials have been introduced as high performance composite matrices. These new thermoplastics have a semi-crystalline structure, producing a material with higher mechanical properties than many epoxies, and improved resistance to chemical attack. Polyetheretherketone (PEEK) has become one of the best known of these new thermoplastics because of its high modulus and strain-to-failure, complemented by excellent adhesion to graphite fibers. Polysulfone (PSF) exhibits environmental resistance and good engineering properties such as high modulus and ductility. Polyphenylsulfones and polyethersulfones(PES) are recent developments in this group. These polymers show good hydrolytic stability, but can be sensitive to common solvents, e.g. chloroform and ketones. Mechanical properties for several thermoplastics are shown in Table 1.7 (Smith, 1990; Fried, 1983).

### **1.2.3. Fiber-Reinforced Composites in the Marine Industry**

Composite materials have been used for many years in the marine industry. Several review articles have been published, most notably by Fried (1969) and Graner(1982). More recently an excellent text on the design of marine structures in composites has been published by Smith (1990). Also, a national conference on the subject was hosted by the National Research Council (Pipes, 1990).

The most common user of composite materials in the ocean today is the recreational boat owner. Small boats have been made from fiberglass laminates for decades, and more recently larger boats such as minesweepers have been constructed

in fiberglass. More expensive reinforcing materials such as aramid and graphite have been limited to high-performance racing boats and yacht hulls.

The two major sources for engineering applications of composites in the ocean have been the U. S. Navy and the offshore oil and gas industry. The Navy has been slowly adopting composites for years in weight- and corrosion-critical applications. The offshore industry has also begun to recognize the importance of composites, especially in designs for deep water exploration.

From the Navy standpoint, the emergence of cored, fibrous laminates (originally developed for aircraft) has encouraged a shift away from traditional shipbuilding materials. These lightweight laminate sandwich panels offer better impact resistance and fire retardation than heavier metal panels. For example, a program was begun at Ingalls shipbuilding to replace steel hatch doors with much stiffer composites, at a weight savings of nearly 50 percent for each hatch (Pegg and Reyes, 1986). A separate industry-sponsored study found that for a hypothetical 7000 ton destroyer, replacement of steel and aluminum in hull and superstructure ballistic protection, ship mast, and interior bulkheads resulted in a weight savings of nearly 350 tons (Crump and Riewald, 1983). This weight savings could result in increased mission capability and/or a reduction in ship size. Weight reduction in topside facilities also serves to shift the ship center of gravity downward, increasing the stability of the vessel. Current Navy research into composites in submarines concentrates not only on pressure hulls but on other weight saving areas such as drive shafts and engine mounts (Evans, 1990).

By choosing appropriate materials, structural laminates can be produced which are anywhere from opaque to transparent to sonar. Sonar domes for submarines and surface ships are now made primarily of composite laminates. The nonmetallic character of composites can also be beneficial, and is well suited for

mine countermeasure duty. Modern minesweepers such as the U.S. Navy's 57-meter Osprey-Class use all-composite hull and superstructure (Smith, 1990). Applications other than ships also benefit from the use of composites, e.g. shore facilities (Zarate, 1985).

The Navy, as well as the scientific research community, has a continuing interest in deep submergence vehicles. In order to withstand the severe compressive loads imposed by the high-pressure environment, thick hulls and related support structure are essential. However, these vehicles must also be relatively lightweight so that buoyancy requirements do not overtax propulsion systems. Early investigations have shown that in order to design a functional cylindrical vessel capable of surviving in the deepest ocean, only non-metallics such as fiber-reinforced plastics are feasible as hull materials (Hom, 1969; Graner, 1969). Many designs now exist for deep-submergence vehicles in composites (Garvey, 1990; Stachiw, 1990; Smith, 1990). The Navy's deepest diving submersible are currently all-metal designs, either spherical or ring-stiffened cylinders.

The primary driving force for the use of composites in the offshore oil and gas industry is weight. The higher the weight of a drilling or production platform, the larger the supporting structure or hull must be for adequate safety. Salama (1986) has estimated that the use of composite production separator tanks gives a weight savings of over 25 tons in a typical offshore application. Although these separators cost nearly twice as much as their steel counterparts, the cost savings in reduced hull size alone results in a net cost savings of over \$250,000. He also demonstrates that the replacement of 2000 ft long steel TLP tethers with graphite or aramid composites can save over 3300 tons in tether weight, which allows substantial reduction in hull displacement and hence reduces total project cost. A filament wound composite tubular is currently being field tested as a lightweight

marine riser (Sparks, 1986). Although driven by initial savings, the switch to composites will prove even more cost-effective as time goes on. Non-corroding composites will eliminate a portion of the millions of dollars spent annually by the petroleum industry on expensive corrosion and maintenance systems.

#### **1.2.4. Selection of Materials for Seawater Testing**

The composite material chosen for the present study consisted of graphite fibers in high-performance aerospace-grade epoxies. Graphite was chosen as the reinforcing material based on its superior overall performance as a structural material coupled with favorable projections for future costs. Fiberglass has already been studied extensively, while organic fibers lack sufficient compressive strength for consideration. Epoxy was selected as a relatively common matrix material for graphite fibers. Any attempt at a comprehensive study of different matrix materials would be prohibitive, as new and improved plastics are introduced frequently. Graphite/epoxy (Gr/Ep) composites enjoy an extensive test database in industry and government, and high-quality pre-fabricated samples of this material can be obtained at relatively low cost.

#### **1.2.5. Damage Mechanisms for Graphite/Epoxy in the Marine Environment**

Historically the most severe environmental damage to structures in the ocean has occurred in the splash zone. This is the area of any partially submerged component which is exposed to the high-energy air/seawater interface between high and low tide levels. This interface area experiences high moisture, salt, and thermal gradients as well as increased biological activity, solar radiation, and surface wave action. The splash zone is known to dramatically increase corrosion rates for metallic materials that are susceptible to corrosion in seawater.

Environmental damage to graphite/epoxy (Gr/Ep) in the ocean is also apt to be most severe in the splash zone. The most likely causes for damage in Gr/Ep exposed to splash zone conditions are:

1. Moisture absorption
2. Salinity
3. Galvanic corrosion
4. Wave loading (fatigue)
5. Ultraviolet radiation (sunlight)
6. Biological activity

Any program designed to investigate the long-term behavior of Gr/Ep in seawater should address all of these potential causes for damage and any possible synergistic damage mechanisms.

#### **1.2.5.1. Moisture Absorption**

The effects of water exposure on static properties in graphite/epoxy composites have been well-studied. Shen and Springer(1977) and others (Browning and Hartness, 1974; Judd, 1975) have correlated strength reduction in graphite/epoxy matrices with equilibrium water absorption. Fiber-dominated properties, such as tensile strength in the fiber direction, are unaffected by long-term water exposure. Properties that depend upon matrix or interface properties, however, e.g. transverse strength and shear strength, can be significantly affected. This moisture-induced degradation involves both reversible (upon drying) and irreversible components.

The reversible degradation mechanism is thought to involve matrix plasticization by absorbed moisture. Plasticization decreases the effectiveness of the matrix in spreading the applied load among the fibers, thus reducing the composite strength. Possible causes of moisture absorption and consequent plasticization are

H<sub>2</sub>O hydrogen bonding (i.e. proton exchange between water and hydrophilic sites within the resin) and dilution of free volume within the matrix. Several investigators (Fuller et al, 1979; Apicella and Nicolais, 1985) have concluded that water interacts with amine and hydroxyl sites, suggesting that interruption of weak intermolecular hydrogen bonding is one plasticization mechanism. Other studies (Jelinski et al, 1985; Boll et al, 1985) suggest that these specific interactions play no role and that water acts solely as a diluent to the polymer.

In any case, absorbed moisture plasticizes the matrix and lowers the glass-transition-temperature ( $T_g$ ) (Browning et al, 1977; DeIasi and Whiteside, 1978; Brinke, 1983). The  $T_g$  is the temperature below which the material reacts as a glassy solid. The material begins to soften at temperatures above  $T_g$ . This becomes important in aerospace applications where service temperatures can exceed a moisture-reduced  $T_g$ . The degree of water absorption and plasticization is dependent on resin chemistry and curing procedures (Danieley and Levy, 1981).

Whitney and Browning (1978) observed that moisture diffusion is actually a 2-stage process. After reaching the Fickian predicted maximum moisture content, additional absorption is thought to be caused by microcracking induced by residual or expansional strains. Residual stresses were also postulated as causing non-Fickian behavior via a stress-dependent diffusion coefficient. (Residual stresses within composite laminae are caused by different thermal and hygroscopic expansion coefficients between the fiber and the matrix.) The equilibrium water absorption of Gr/Ep composites is similarly increased by applied load, first as a result of volumetric expansion of the matrix (Marom and Broutman, 1981), then of migration through matrix microcracks (Whitney and Browning, 1978). Gillat and Broutman (1978) found that absorbed moisture lowered the matrix strength in a graphite/epoxy laminate, so that applied loads caused matrix cracking at lower stress



levels. The increased water content further lowers the matrix strength, and the result is a synergistic degradation of composites loaded in a wet environment.

Environmental cycling that causes repeated absorption/desorption increases composite water uptake as compared with simple absorption tests (Browning, 1978). One likely mechanism is matrix fatigue cracking caused by cyclic formation and/or relaxation of residual stresses. Most tests of this type are aimed at characterizing aircraft environmental loads, so thermal loads are also applied (e.g. temperature spikes). Observed cracking is therefore due to both cyclic residual stresses and thermal loads.

The static strength reduction associated with water absorption is found to be completely reversible upon drying for low-void-content unidirectional specimens (Judd, 1977) but not so for high-void-content (Hancox, 1981) or bidirectional specimens (Manocha et al, 1982). This suggests a more complicated irreversible damage mechanism where voids and/or matrix-rich interlaminar layers are present. Ashbee, et al (1967) have shown in early studies of water damage in polyester resins that impurities in the resin can cause irreversible microcracking as a result of osmotic action.

Complex adhesion mechanisms exist at the fiber/matrix interface, and determining causes for interface degradation is not simple. Kaelble et al (1974a,b) determined that water absorption causes an irreversible reduction in interface strength. The critical stress for crack propagation is predicted to decrease by 75 % in a graphite/epoxy. Kaelble suggests that matrices and fibers that are non-polar and exhibit an increased dispersion coefficient would be required for moisture-insensitive composite interfaces. Drzal et al (1982) has shown that the fiber-matrix "interface" is actually an interphase zone with as many as 7 distinct regions. These regions arise from evidence that the morphology and properties of the matrix and fiber are

different near the interface. Drzal (1986) discusses various changes that affect the interface in a comprehensive review article.

The studies presented here should be judged with some caution. Several different epoxy resin systems were used, and cure procedures varied. Also, many studies used boiling water to accelerate moisture absorption, an environment which is many times more damaging than room-temperature soaking. Temperatures above 50°C have been shown to cause unwanted post-cure reactions as well as thermal damage such as microcracking (Birger et al, 1989).

Perhaps a more effective method for accelerating moisture uptake is the use of high pressure. Although this study concentrated on likely splash-zone damage mechanisms, which would preclude high-pressure effects, Tucker (1989b) has reported a substantial increase in moisture uptake and related damage in a graphite/vinyl-ester composite subjected to high pressure seawater exposure. Other investigators (Letton and Bradley, 1990) report no significant changes in uptake or strength in epoxy resins and composites. Pressure effects are evidently highly dependent on resin-chemistry.

#### 1.2.5.2. Salinity

The additional effect of salt on immersed graphite/epoxy laminates has been the object of several empirical studies. Mazor and Broutman (1978) tested carbon fiber and graphite fiber composites which had been exposed to distilled water, air, and seawater for 11 years. Their results indicate that long-term water exposure causes significant and irreversible matrix and interface degradation, while fibers and fiber-dominated properties are unaffected. No specific effect of salt was noted. The data of Macander and Silvergleit (1977) show a slight decrease in the stress-rupture and fatigue strengths of unidirectional specimens exposed to seawater.

Monocha et al (1982) found that seawater or boiling water exposure weakly affected the flexural strength (a fiber-dominated property), but significantly degraded the matrix-dominated interlaminar shear strength (ILSS). Rege and Lakkad (1983) found that specimens soaked in hot 0.5M saltwater exhibited much greater strength reductions in flexure, ILSS, and compression as compared with specimens soaked in hot distilled water. As discussed previously, hot water studies may be misleading because of the damage caused by thermal stresses.

Exposure to salt does not appear to weaken graphite/epoxy matrices or interface bonds. Nakanishi and Shindo (1982) found that as the salinity of the environment increased from 4 to 23 percent (0.7 to 3.8 M), the equilibrium water content of the composite decreased. Their data also showed that decreases in flexural strength correlated with increases in equilibrium water content irrespective of salinity. Loos and Springer (1979) showed that moisture absorption was lower in saturated saltwater (NaCl) compared with exposure to distilled water. Rege and Lakkad (1983), however, found that exposure to low salinity (0.5 M) water substantially increased the equilibrium weight gain of their specimens. Although data seem to indicate a concentration effect (which may relate to the changing activity coefficients of the ions involved), any damage caused by salt alone would have to be limited to the polymer surface because of the low diffusivity of ions in polymers (Zaikov, 1988)

#### 1.2.5.3. Galvanic Corrosion

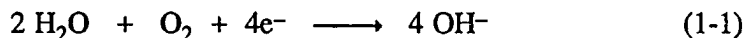
Because graphite is very high (noble) in the galvanic series, galvanic corrosion is likely to result when Gr/Ep is coupled to a metal in seawater. Conductivity of a dry laminate has been shown to be a tensor function of orientation (Tse et al, 1981), with coordinate property transformations typical of orthotropic

laminae. Belani and Broutman (1978) showed that conductivity perpendicular to the fiber direction decreases as the square root of the moisture content, being unaffected by moisture in the fiber direction. This effect is caused by matrix swelling, which decreases the random fiber contact that causes off-axis conductivity. Seawater absorption is likely to have a similar effect on bulk conductivity.

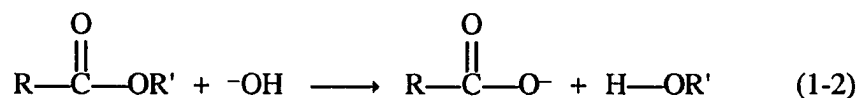
Limited work has been done in the area of galvanic effects of graphite composites electrically connected to metals. Brown and Coomber (1972) have shown that open circuit potentials between graphite-fiber-reinforced plastics and metals can vary significantly between resin systems, ranging from -300 to +300 mV (SCE). They also show that polarization occurs exclusively at the cathode and is oxygen diffusion controlled, as is the case for metal cathodes in seawater. Brown (1974) later found that an electrically insulating adhesive bond eliminated galvanic attack between a graphite-fiber composite and metals. However, specimens that were bolted and bonded (so that mating surfaces were insulated yet hard electrical contact was established) exhibited substantial localized corrosion of the metal near the edges of the composite. Fischer and DeLuccia (1976) investigated galvanic corrosion in seawater of a titanium and two aluminum alloys. An open-circuit-potential difference of 1.0v between graphite/epoxy and aluminum provided a driving force for significant corrosion problems, while the titanium couple was much less active. Hack and Macander (1983) considered the effect of graphite/epoxy on sacrificial zinc cathodic-protection-system anodes in seawater. Their results showed that the galvanic behavior of the Gr/Ep was similar to the Ni-Al bronze that the composite was to replace.

While galvanically coupling a metal to a graphite-fiber composite increases the corrosion rate of the metal, the effect on the composite has not been determined. At a graphite/polymer cathode, especially at the fiber/matrix/electrolyte interface,

oxygen will be reduced according to (Uhlig and Revie, 1985)



The shift in pH accompanied by the cathodic oxygen reaction could create conditions sufficient for hydrolysis of polymer linkages to occur, as suggested by Dougherty (1974). As an example, hydrolysis of ester linkages might result from a base-catalyzed saponification reaction (Pine et al, 1980):



(R represents a carbon chain). Damage in graphite/vinyl-ester cathodes has already been reported (Tucker et al, 1989a, 1990), but the mechanisms have not yet been identified.

Alternately, reductive degradation of the polymer may occur directly as a result of electron transfer to functional groups at the polymer/cathode interface. Shapoval(1985) and Pud(1984) have studied electrochemical reductive degradation (ECD) in several polymer systems. The mechanism is thought to be enhanced by electroactive centers such as aromatic rings and conjugated carbonyl and vinyl groups.

The breakdown of graphite-fiber/polymer interphase bonds under the influence of a corrosion current would be one case of a much more general problem. Other examples include so called "wood-electrolysis", i.e. the decay of wooden boat hulls near cathodic protection systems (Strasburg et al, 1982), premature metal/adhesive debonding when the metal is being protected against corrosion (Venables, 1983; Stevenson, 1985), and peeling/blistering of paints and coatings on cathodically protected ships and pipelines (Koehler, 1984; Dickie and Floyd, 1986; Leidheiser, 1981, 1983). Suspected damage mechanisms include (but are not limited to) breakdown of polymer linkages, debonding and dissolution of surface oxide

films, and blistering by electric-field-driven ion migration. All of these problems are a direct result of the cathodic reaction of an electrochemical cell.

#### 1.2.5.4. Wave Loading (Fatigue)

While there is considerable interest in the use of fiber composites in the ocean, most applications so far have been aimed towards improving the dry parts of ocean-going systems. There are few applications where composite laminates are actually exposed to the seawater environment. Consequently, little data exists which addresses the synergistic mechanisms associated with long term cyclic loading and seawater exposure on composite laminates.

Fatigue of composite materials in air has received considerable study over the last 20 years. As a result, the damage mechanisms and failure processes have been described in some detail, especially for tension-tension fatigue of graphite/epoxy laminates. In an excellent review article, Reifsneider et al (1983) divides the fatigue life of these laminates into three periods. During the first period microcracks form in the matrix material. These microcracks (and preexisting flaws) grow until a stable crack density (or characteristic damage state, CDS) is reached, which depends on the fiber orientation and constituent properties. The second period involves the coalescence of damage in the CDS to form larger areas of delamination and separation. The final phase is dominated by fiber fracture as delaminated areas lose their load-sharing ability and try to act independently. The worst possible damage and strength reduction occurs in laminates subjected to low-stress, high-cycle fatigue.

The added effects of water on the fatigue damage mechanisms in Gr/Ep are not well-understood. The fatigue study of Sumpson (1976) shows that cyclic loading of specimens in room temperature water results in only a slight decrease in

fatigue life versus room temperature air, as does elevated temperature testing (74°C) in air. There is, however, a sharp reduction in fatigue life for specimens subjected to 74°C water. The effect of room temperature water on fatigue life was found to be minor compared with loading history. Completely reversed loading ( $P_{\min} = -P_{\max}$ ) caused significantly lower fatigue life than simple cyclic loading ( $P_{\min} = 0$ ), whereas a combination of water and completely reversed loading resulted in no further life reduction.

The seawater fatigue testing of Macander et al (1979) showed no effect of saltwater on fatigue life up to 10 million cycles. However, because of the high frequency (10 Hz) and short presoak period (2 weeks) of these tests, this data cannot be extrapolated to long-term behavior. Sandifer (1982) conducted tension-tension fatigue tests on quasi-isotropic laminates (i.e. laminates with several plies each in the 0°, 45°, and 90° directions, to simulate isotropy in the plane of the fibers) in a seawater bath. He found no effect of seawater on fatigue strength, a result of the fiber-dominated properties of the quasi-isotropic specimens tested. Interestingly, he notes that all specimens failed at the water/air interface. Failures were associated with migration and accumulation of salt at delamination sites.

#### 1.2.5.5. Ultraviolet Radiation (Sunlight)

The sun's rays contain electromagnetic energy in a broad range of wavelengths, from 100 to 3000 nanometers. However, because of absorption by the atmosphere, only those with wavelengths above 290 nm reach the earth's surface. This corresponds to photon energies in the range 40 to 410 kJ/mole. The energy required to break single covalent bonds lies in the range 170 to 420 kJ/mole, corresponding to near-infrared (IR) wavelengths. Thus certain polymer bonds are susceptible to solar radiation damage (Pine, 1980; Cassidy and Aminabhavi, 1981).

A photochemical reaction is composed of three parts: (1) absorption of light to produce an electronically excited molecule, (2) primary photochemical processes that involve the excited molecule, and (3) secondary or "dark" reactions of the species produced in (2). A damaging primary photochemical reaction would be the formation of free radicals by homolytic cleavage of a polymer bond. Once a free radical is formed, secondary processes can occur such as chain scission, crosslinking, and oxidation (Roylance and Roylance, 1978).

UV radiation from natural sunlight can cause substantial degradation of a polymer fiber or matrix material. However, damage from UV would tend to be restricted to exposed surface areas, and could easily be prevented by using appropriate paints and coatings. A more serious consequence of UV radiation might be the high thermal load it creates on the part. The damage mechanisms behind UV damage seem to be well-understood, and in any case are not restricted to laminates in the ocean. This investigation will involve only indoor experiments, and will not consider damage caused by UV radiation.

#### **1.2.5.6. Biological Activity**

Several studies have concluded that fiber-reinforced plastics are too hard for common marine borers and worms to penetrate (Fried, 1969). Substantial growth typically occurs, especially in tropical areas, but this growth can be scraped away with little damage to the substrate. Although the evidence so far suggests that biological activity has little effect on composites, the remarkable patience and innovation of Mother Nature suggests that one day an organism will appear that thrives on reinforced plastics. Unreinforced engineering thermoplastics such as PVC have already come under extensive attack by marine borers, specifically in highly polluted harbors (Scott, 1989).



There are many inherent difficulties in trying to maintain and control the natural marine biota in the laboratory. There are also significant problems in monitoring corrosion experiments in-situ. Because of these difficulties, no attempt has been made in the present study to ascertain the effects of marine organisms on composite materials. The seawater used in the present tests has been sand-filtered to remove any macroorganisms. The microorganisms and larger forms that enter the tests as viable larva are assumed to have no effect on experimental results.

### 1.3. EXPERIMENTAL METHODS

Several authors cited above have shown that moisture or seawater has little effect on graphite fibers and fiber-controlled properties such as tensile strength and modulus. Any effect of prolonged exposure would therefore be best observed in experiments which test the matrix-controlled properties of the material. The experiments used in the present study have been designed to cause failure in the matrix or the fiber-to-matrix bond as much as possible.

A common method for determining environmental stability in composites is to break the material after it has been exposed to the environment for a fixed amount of time. However, this type of test may be unrealistic for these materials in an aggressive environment. Structural materials are loaded continuously in service, and damage grows from existing flaws under sustained static or fatigue loading. The effect of environment is typically to act synergistically with the applied load to increase the rate of damage growth. The experiments in this study have therefore tried to look at environmentally-enhanced damage growth as well as static strength loss after exposure. A fracture mechanics approach can be appropriate in certain applications (Friedrich, 1989). Specific details of the experiments used are presented in the individual chapters.

#### 1.4. SUMMARY

Composite materials are being used more and more in the marine environment wherever low-mass and corrosion resistance are essential. In order to safely utilize these materials in long-term applications in seawater it is essential that we identify and understand their degradation mechanisms. Graphite/epoxy is a commonly used high-performance composite material and has been chosen for further study into marine damage mechanisms in fiber-reinforced plastics.

A brief summary of marine applications of composite materials has been presented, followed by a survey of the literature involving likely damage mechanisms for composites used in surface waters (the splash zone). Moisture absorption and galvanic coupling are the most likely causes for degradation in this material in seawater. Experimental studies will therefore focus on matrix- or interface-controlled properties, which would be most affected by moisture absorption or electrochemical attack. Both static and fatigue experiments will be conducted if possible to help ascertain damage mechanisms.

TABLE 1.1. AXIAL PROPERTIES OF COMPOSITE LAMINATES

	Cost (\$/kg)	Density (g/cm <sup>3</sup> )	Modulus (GPa)	Strength (MPa)(Comp)	Specific Modulus	Specific Strength(Comp)
HS-Graphite/Epoxy	50-70	1.6	140-180	1500 (1500)	90-110	940 (940)
E-Glass/Epoxy	3-4	1.8	39	1060 (610)	22	590 (340)
Aramid/Epoxy	25-30	1.5	76	1400 (235)	51	930 (160)
Titanium	30-35	4.85	100	1300 (1300)	21	260 (260)
7079 T-6 Alum	6-7	2.7	72	470 (470)	27	170 (170)
Marine Plywood	2-4	0.6	7	40 (25)	12	67 (42)

TABLE 1.2. TRANSVERSE PROPERTIES OF COMPOSITE LAMINATES

	Density (g/cm <sup>3</sup> )	Modulus (GPa)	Strength (MPa)(Comp)	Specific Modulus	Specific Strength(Comp)
HS-Graphite/Epoxy	1.6	9-10.3	50 (250)	5.6-6.4	31 (160)
E-Glass/Epoxy	1.8	8.3	31 (120)	4.6	17 (67)
Aramid/Epoxy	1.5	5.5	12 (53)	3.7	8 (35)

TABLE 1.3. SHEAR PROPERTIES OF COMPOSITE LAMINATES

	Density (g/cm <sup>3</sup> )	Modulus (GPa)	Strength (MPa)	Specific Modulus	Specific Strength
Graphite/Epoxy	1.6	7.1-7.2	68-93	4.4-4.5	43-58
E-Glass/Epoxy	1.8	4.1	72	2.3	40
Aramid/Epoxy	1.5	2.3	34	1.5	23

TABLE 1.4. MECHANICAL PROPERTIES OF COMMON FIBER FAMILIES

	Diameter (micron)	Density (g/cm <sup>3</sup> )	Modulus (GPa)	Strength (GPa)	Specific Modulus	Specific Strength
Graphite	7	1.75	250-1000	2.2-4.5	140-570	1.3-2.6
Boron	100	2.6	410	3.5	160	1.4
E-Glass	16	2.55	72	2.4	28	0.94
S2-Glass	16	2.5	88	3.4	35	1.4
Aramid	12	1.44	120	2.8	83	1.9
Polyethylene	38	0.97	120	2.6	120	2.7

TABLE 1.5. CHARACTERISTICS OF FIBER FAMILIES

	Advantages:	Disadvantages:
Graphite	High modulus, high strength	Expensive, conducting
Boron	High modulus, high strength	Very expensive
Glass	Low cost, high strength	Low modulus, corrosion sensitive
Kevlar	High strength	Poor in compression, absorbs moisture
Polyethylene	Lightest weight	Poor in compression, creep sensitive

TABLE 1.6. MECHANICAL PROPERTIES OF THERMOSETTING PLASTICS

	Density, (g/cm <sup>3</sup> )	Modulus (GPa)	Strength (MPa)	Failure Strain (%)
Polyester (orthophthalic)	1.23	3.2	65	2
Polyester (isophthalic)	1.21	3.6	60	2.5
Vinyl Ester	1.12	3.4	83	5
Epoxy (DGEBA)	1.2	3.0	85	5
Epoxy (TGMDA)	1.3	4.0	100	1.2
Phenolic	1.15	3.0	50	2

TABLE 1.7. MECHANICAL PROPERTIES OF ENGINEERING THERMOPLASTICS

	Density, (g/cm <sup>3</sup> )	Modulus (GPa)	Strength (MPa)	Failure Strain (%)
High Density Polyethylene(HDPE)	0.95	1.0	30	600-1200
Polyamide	1.15	2.2	75	60
Polycarbonate	1.2	2.3	60	100
Polyphenylsulfone	1.3	2.1	72	60
Polyethersulfone (PES)	1.35	2.8	84	60
Polyetherimide (PEI)	1.3	3.0	105	60
Polyetheretherketone (PEEK)	1.3	3.7	100	50
Polyphenylsulfide (PPS)	1.34	3.3	75	3



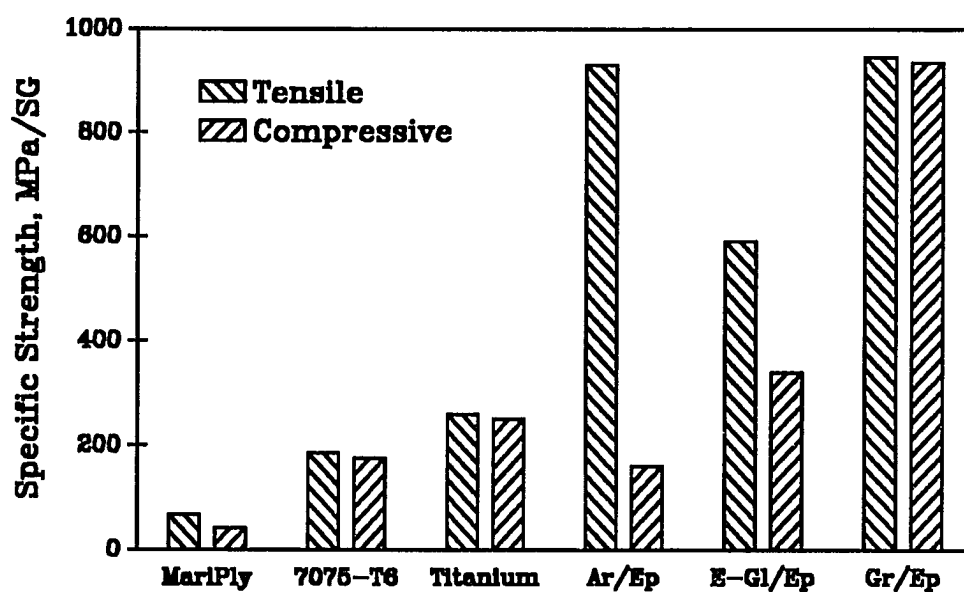


**Figure 1.1. Fiber-dominated tensile and compressive strength of composites and selected engineering materials.**

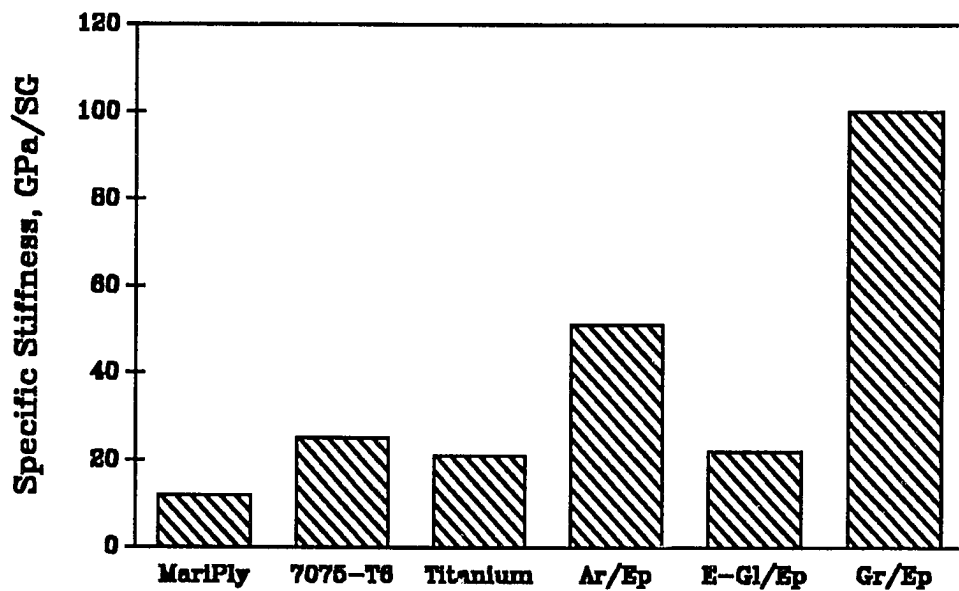


**Figure 1.2. Specific stiffness of composites and selected engineering materials. Figures 1.1 and 1.2 illustrate the superior fiber-dominated properties of composites.**

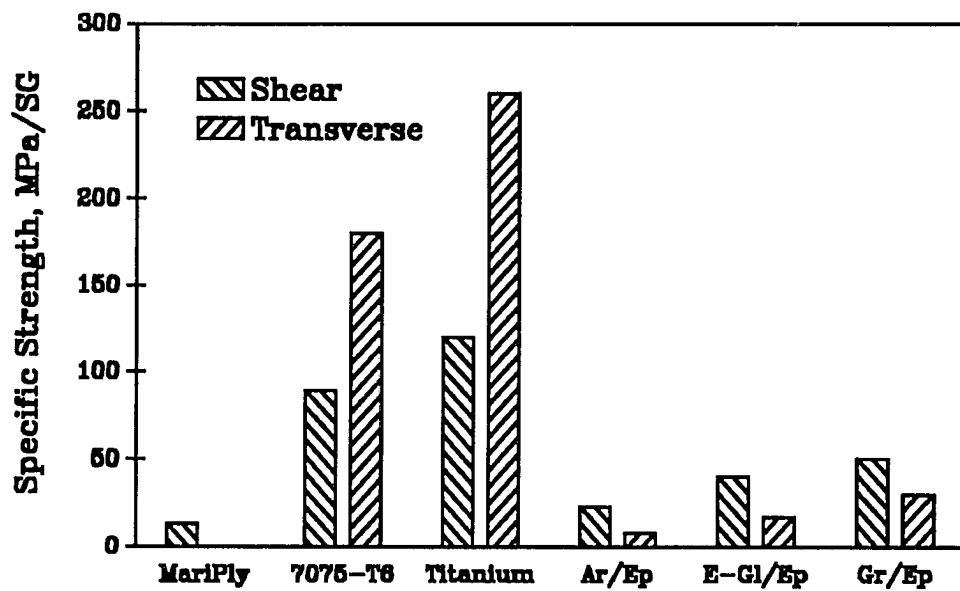


**Figure 1.3. Matrix-dominated shear and transverse strength of composites and selected engineering materials.**

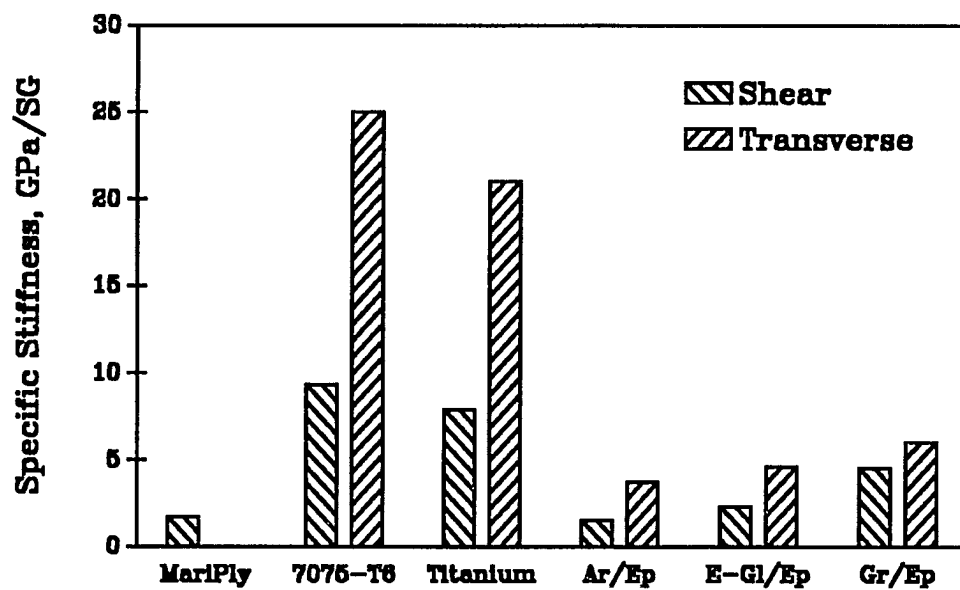


**Figure 1.4. Matrix-dominated stiffnesses of composites and selected engineering materials. Figures 1.3 and 1.4 illustrate the weak matrix-dominated properties of composites.**

## II EFFECT OF ENVIRONMENTAL CONDITIONS ON MOISTURE UPTAKE

### 2.1. INTRODUCTION

The simplest test of a materials resistance to environmental degradation is to expose that material to the environment of interest. Springer and co-workers (1981,1984) have conducted numerous investigations where composites were exposed to service environments and working fluids. Subsequent measurement of mechanical properties determined if changes had occurred during exposure.

The principal phenomenon associated with exposure of composite laminates to seawater is the diffusive uptake of moisture by the polymer matrix. Absorbed moisture can actually increase the strength of a composite by swelling the matrix slightly, thus relieving residual stresses which formed on cool-down from the curing process (Collins and Stone, 1985). However, moisture absorption can also cause weakening of the fiber-to-matrix bond and changes in matrix-controlled properties, e.g. shear modulus and transverse tensile strength. These effects are generally reversible upon drying, but the composite properties will be reduced in service. The amount of property degradation observed is typically a function of how much moisture is absorbed, so the equilibrium moisture level in the composite is an important parameter in design.

Another significant problem associated with moisture absorption is the accompanying depression of the glass-transition temperature ( $T_g$ ) of the matrix. Any large increase in temperature that exceeds the depressed  $T_g$  can cause irreversible damage (Browning, 1978). Composites used in submerged applications are unlikely to encounter thermal problems. However, in splash-zone applications there will be repeated cycles of cold submersion and hot sunlight exposure, raising the possibility of thermal damage. Again, the amount of moisture absorbed determines the extent

of damage.

In addition to moisture absorption, the noble electrochemical character of graphite fibers makes graphite/epoxy highly cathodic to most structural metals. Thus one possible effect of seawater exposure would be the cathodic polarization of the graphite/epoxy by a galvanically coupled metal. The corrosion rate of the metal would increase, but the effect on the graphite/epoxy is less clear. An increase in the amount of moisture absorbed would indicate some form of corrosion in the composite.

A simple experiment was begun to determine the long-term environmental stability of a graphite/epoxy laminate in seawater. The primary purpose of this investigation was to determine whether any ionic species or chemical element in seawater could attack the fiber or matrix of the composite. A secondary goal of the experiment was to determine the rate of moisture uptake by diffusion and the equilibrium moisture content of the material. A separate aim of the project was to determine what effect galvanic coupling might have on the material properties such as the equilibrium moisture content.

## 2.2. BACKGROUND

### 2.2.1. Moisture Uptake by Diffusion

The equations of mass transfer begin with the continuity equation,

$$\frac{\partial C_i}{\partial t} = -\nabla J_i + P_i \quad (2-1)$$

where  $C_i$  is the concentration of the migrating species,  $P_i$  is a production term, and  $J_i$  is the flux, given by

$$J_i = -D_i \nabla C_i \quad (2-2)$$

which is a statement of Fick's first law of diffusion. Plugging (2-2) into (2-1) with  $P_i=0$  and assuming that  $D_i$  is independent of position gives Fick's second law of

diffusion,

$$\frac{\partial C_i}{\partial t} = D_i \nabla^2 C_i \quad (2-3)$$

Consider now the composite plate of Fig. 2.1. Diffusion of moisture into the plate from any edge will initially be given by the 1-D form of equation (2-3), i.e.

$$\frac{\partial C}{\partial t} = D_x \frac{\partial^2 C}{\partial x^2} \quad (2-4)$$

This parabolic partial differential equation can be solved easily using Laplace transforms (Butkov, 1968), with solution

$$\frac{C(x,t) - C_{init}}{C_{max} - C_{init}} = 1 - \operatorname{erf}\left[\frac{x}{2\sqrt{D_x t}}\right] \quad (2-5)$$

Let  $m$  be the mass of the sample plate. The total absorbed mass of moisture will be given by integrating the mass flow rate over the elapsed time, i.e.

$$\text{absorbed mass, } \Delta m = \int_0^t (\text{flux, } J)(\text{area, } A) dt \quad (2-6)$$

Following the procedure of Shen and Springer (1976), substituting (2-5) into (2-2) and putting the result into (2-6) gives, for the 1-D case,

$$\Delta m = (\text{area}) (C_{max} - C_{init}) \left[ \frac{4D_x t}{\pi} \right]^{1/2} \quad (2-7)$$

or, considering now all sides of the plate,

$$\Delta m = 2 (C_{max} - C_{init}) \left[ \frac{4t}{\pi} \right]^{1/2} \left[ hw\sqrt{D_x} + lh\sqrt{D_y} + lw\sqrt{D_z} \right] \quad (2-8)$$

The percent moisture content  $M$  is defined by

$$M \equiv \frac{m_{total} - m_{dry}}{m_{dry}} = \frac{m_{init} + \Delta m - m_{dry}}{m_{dry}} = \frac{C}{\rho_{dry}} \quad (2-9)$$

where

$$\rho_{dry} = \frac{m_{dry}}{lwh} \quad (2-10)$$

so that equation (2-8) becomes

$$\frac{M(t) - M_{init}}{M_{max} - M_{init}} = \frac{4}{h} \left[ \frac{tD}{\pi} \right]^{1/2} \quad (2-11)$$

where  $D$  is the specimen diffusivity,

$$D = \frac{1}{4} \left[ \sqrt{D_{ztop}} + \sqrt{D_{zbot}} + 2\left(\frac{h}{l}\right)\sqrt{D_x} + 2\left(\frac{h}{w}\right)\sqrt{D_y} \right]^2 \quad (2-12)$$

If we now make the assumption that the top and bottom diffusivities are equivalent, i.e.  $D_{ztop} = D_{zbot} = D_z$ , this becomes

$$D = D_z \cdot \left[ 1 + \left( \frac{h}{l} \right) \sqrt{\frac{D_x}{D_z}} + \left( \frac{h}{w} \right) \sqrt{\frac{D_y}{D_z}} \right]^2 \quad (2-13)$$

so that  $D$  is the through-thickness diffusivity corrected for edge effects.

Assuming that diffusivity follows the coordinate transformations typical of a single composite ply gives

$$D_x = D_{11} \cos^2 \alpha + D_{22} \sin^2 \alpha \quad (2-14)$$

$$D_y = D_{11} \sin^2 \alpha + D_{22} \cos^2 \alpha \quad (2-15)$$

$$D_z = D_{22} \quad (2-16)$$

The longitudinal and transverse diffusivities come from micromechanics analysis (Shen and Springer, 1976), giving

$$D_{11} = (1 - \nu_f) \cdot D_m + \nu_f \cdot D_f \quad (2-17)$$

$$D_{22} = D_m \cdot (1 - 2\sqrt{\nu_f/\pi}) + D_m \cdot f(D_m/D_f) \quad (2-18)$$

where

$$f(D_m/D_f) = \frac{1}{B_o} \cdot \left( \pi - \frac{2}{\sqrt{B_1 \cdot B_2}} \cdot \ln \left| \frac{\sqrt{B_1 \cdot B_2} + B_1}{\sqrt{B_1 \cdot B_2} - B_2} \right| \right),$$

$$B_o = 2 \cdot \left( \frac{D_m}{D_f} - 1 \right), B_1 = B_o \cdot \sqrt{\nu_f/\pi} + 1, \text{ and } B_2 = B_o \cdot \sqrt{\nu_f/\pi} - 1.$$

For graphite/polymer composites,  $D_m \gg D_f$ , so these equations reduce to

$$D_{11} = (1 - \nu_f) D_m \quad (2-19)$$

$$D_{22} = (1 - 2\sqrt{\nu_f/\pi}) D_m \quad (2-20)$$

The subscripts 1 and 2 refer to directions parallel and perpendicular to the fibers in the plane of the ply. The subscripts x, y, and z refer to the laminate coordinate system. The subscripts m and f represent the matrix material and the fibers, respectively. For a laminate with  $n$  plies, each of thickness  $h_i$ , equations (2-14) and (2-15) become

$$D_x = D_{11} \sum_{i=0}^n \left[ \frac{h_i}{h} \right] \cos^2 \alpha_i + D_{22} \sum_{i=0}^n \left[ \frac{h_i}{h} \right] \sin^2 \alpha_i \quad (2-21)$$



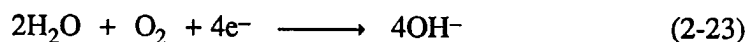
$$D_y = D_{11} \sum_{i=0}^n \left[ \frac{h_i}{h} \right] \sin^2 \alpha_i + D_{22} \sum_{i=0}^n \left[ \frac{h_i}{h} \right] \cos^2 \alpha_i \quad (2-22)$$

Equations (2-12) to (2-22) were put into the FORTRAN program DIFFUSE, which was used to calculate the theoretical initial diffusivity of the soaking specimens.

### 2.2.2 Formation of Calcareous Deposits

The tendency to form calcareous films at the cathode of a corrosion cell is the most important property of seawater in electrochemical studies. These films act to reduce corrosion rates by impeding the diffusion of oxygen to the cathode surface. Calcareous films can vary in composition and morphology depending on the conditions under which they form.

The principal electrochemical reaction at a cathode such as graphite in seawater is the oxygen reduction reaction (Uhlig and Revie, 1985),



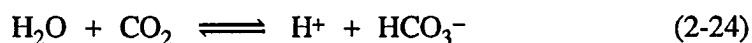
The generation of hydroxide ions raises the pH of the solution at the electrode surface. As the pH rises,  $\text{CaCO}_3$  and  $\text{Mg}(\text{OH})_2$  precipitate to form calcareous deposits at the cathode.  $\text{Ca}(\text{OH})_2$  and  $\text{MgCO}_3$  do not form because of their higher solubilities (Elbeik et al, 1986). Table 2.1 lists the most important constituent ions of seawater, along with their relative concentrations (Dexter and Culbertson, 1980).

The formation of calcareous films at cathodes in seawater was first observed by Sir Humphrey Davy more than 150 years ago (Davy, 1824). However, their beneficial effect in reducing corrosion rates was identified more recently (Humble, 1948). Today the offshore industry relies on the formation of calcareous deposits to reduce cathodic protection costs.

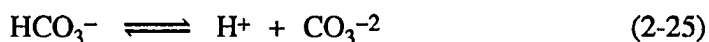
Because of the potential for reducing corrosion and related maintenance

costs in marine structures, calcareous deposits have been the subject of much recent study. Wolfson and Hartt (1981) studied the effects of water velocity on the morphology of calcareous films. England and Heidersbach (1981) studied the effects of deep water (high pressure) on film morphology. An extensive review of the literature relating to calcareous films was published by Hartt et al (1984). The effects of temperature on the Ca/Mg ratio of deposits were studied by Kunjapur et al (1987). Lin and Dexter (1988) investigated the effect of electrolyte temperature and magnesium ion concentration. The relative importance of cathodic potential, flow velocity, pH and temperature was investigated by Lee and Ambrose (1988).

The process of calcareous deposit formation and growth can be summarized from the studies cited above. As the pH rises near the cathode according to (2-23), two processes occur simultaneously. The most important occurrence is a shift in the equilibrium of the seawater carbonate system, given by



and



As hydroxyl ions are generated, this equilibrium is shifted to the right and more  $\text{CO}_3^{2-}$  becomes available for reaction. Eventually the solubility limit of calcium carbonate is exceeded, resulting in the precipitation of  $\text{CaCO}_3$ .

The second process which occurs is the direct formation of  $\text{Mg}(\text{OH})_2$ . This tends to decrease initially the magnesium ion concentration near the cathode surface. The formation of magnesium hydroxide (as well as calcium carbonate) is an important buffering mechanism, limiting the surface pH to around 9.5. This reaction is also important because of the complicating effects of  $\text{Mg}^+$  ions on calcareous growth, as discussed below.

The presence of magnesium ions significantly affects the formation of

calcium carbonate.  $\text{CaCO}_3$  has two stable forms, aragonite and calcite. Aragonite is a hard relatively dense form which becomes the dominant precipitate in warm waters (e.g.  $>25^\circ\text{C}$ ). Calcite is a softer, less dense deposit and is the stable precipitate at lower temperatures ( $<10^\circ\text{C}$ ). Magnesium ions tend to inhibit the nucleation of both aragonite and calcite crystals.  $\text{Mg}^+$  ions also inhibit the growth of calcite crystals, but has no similar effect on aragonite. The presence of  $\text{SO}_4^{2-}$  in seawater tends to decrease this effect by forming complexes with the magnesium ions.

Experimental evidence shows that the ability of calcareous deposits to limit corrosion currents is distinctly temperature dependent. Deposits which form in cold waters are generally not very protective and do not strongly inhibit current flow. On the other hand deposits which form in warmer waters are generally more protective and impede current flow.

This temperature dependence can be explained by the magnesium ion inhibition effect discussed above.  $\text{Mg}(\text{OH})_2$  forms initially at the cathode, thus depleting the near-surface solution of  $\text{Mg}^+$  ions long enough for  $\text{CaCO}_3$  crystals to precipitate without inhibition. In warm waters, these crystals are aragonite and can grow without interference from other ions. In the resulting films the ratio of precipitated calcium to magnesium ions gets larger as time goes on, indicating preferential precipitation of  $\text{CaCO}_3$ . In cold waters, however, the crystals are calcite, and their growth is inhibited by the presence of  $\text{Mg}^+$ . These films grow much more slowly, and their Ca/Mg ratios remain constant. The result is the formation of a dense protective film in warm waters, and a thin porous film in cold waters.

### 2.3. EXPERIMENTAL PROCEDURE

The absorption of moisture by graphite/epoxy laminates in seawater was investigated by immersion of sample coupons in aqueous solutions. T-300/934 graphite/epoxy (Gr/Ep) coupons were cut from an experimental 26-ply laminate donated for test by the Space Systems Division of General Dynamics in San Diego. The laminate had a proprietary quasi-isotropic tape-layup with single fiberglass cloth surface plies on the top and bottom. Nominal coupon dimensions for the simple soaking experiments were 13 x 63 x 3.6 mm. Coupons were cut using a water-cooled diamond saw.

Coupons for galvanic coupling experiments were cut slightly longer than the standard specimens, 90 mm, to accommodate a screw for electrical contact to the anode. Corrosion current and potential for the graphite/epoxy-magnesium (Gr/Ep-Mg) galvanic couple were measured using a high-impedance digital multimeter. Electrochemical potentials were measured with respect to the saturated calomel reference electrode (SCE).

Coupons were immersed in tapwater and fresh Pacific seawater in round tanks of approximately 2.0 liter capacity. Cathodically polarized specimens were exposed in similar tanks while attached to a single magnesium rod sacrificial anode, as shown in Fig. 2.2. Eight specimens were immersed in each tank for the soaking experiments, while 16 specimens were fixed to the corrosion rack.

For the first 40 days of the experiment, water was changed daily, and solution temperatures were kept at 40°C using aquarium heaters. The corrosion tank was stirred with a magnetic stirring bar so that water velocity near the specimens was approximately 5 cm/sec. Aeration was accomplished in the corrosion tanks by an aquarium bubbler.

After 40 days water was changed once-weekly (with some replenishment to

account for evaporation until tank covers were developed). After 100 days (and until the end of the experiment at 140 days) water was changed infrequently, stirring was discontinued, and temperatures were not controlled, cooling to ambient temperatures around 14-18°C. Aeration by bubbling continued until the end of the test.

The pH of each tank was measured infrequently during the experiment. Initial values of pH were 8.2 and 8.0 for the tap and seawater, respectively. Seawater pH was not observed to rise above 8.2 in the soak tank and 8.7 in the corrosion tank. Tapwater pH did not exceed 8.4. pH measurements were not made during the unheated phase of the experiment.

Weight changes were recorded periodically by removing the specimens from the tanks, drying with a paper towel and then weighing individually on a laboratory scale. The laboratory balance had a resolution of 0.5 milligram with an accuracy of  $\pm 1$  milligrams. Specimens were returned to their tanks immediately following weight measurement. At the end of the experiment, specimens were baked in a drying oven at 200°C for 8 hours on consecutive days until less than 5 mg (approximately 0.1% by weight) weight was lost in one day. This drying temperature was chosen arbitrarily and exceeded the curing temperature of the laminate (180°C).

A fourth group of specimens was kept in a desiccator during the period of the experiment. These specimens were baked along with the soaked specimens. The amount of water lost by these control specimens (as a percentage of initial weight) was assumed to be the amount of water present initially in all other specimens. In addition, the dry weight of the control specimens was taken as the reference weight for all specimens in the experiment. Calculation of weight gains from absorbed moisture were complicated by film formation in all of the tanks.

Surface films tended to form on all of the environmentally conditioned specimens. Very thin films formed on the specimens soaking in tapwater and seawater. SEM analysis of these films was done to determine morphology and composition of the films. There was extensive deposit formation on the galvanically coupled specimens. These deposits were later dried, collected analyzed by X-ray diffraction to determine their composition.

In order to determine how much moisture was absorbed by the galvanically-coupled specimens, the weight of the dry calcareous deposits had to be separated from the weight of any moisture absorbed in the deposits. For this purpose, four deposit-coated specimens were baked to remove all the water from both the specimen and the deposits. Subsequently the dried calcareous deposits were removed by scraping. Four additional specimens had their deposits removed with weak (0.5 molar) acetic acid before drying. By comparing the weights of the removed calcareous growth in these two sets of specimens, the amount of absorbed moisture in the deposits, and hence the specimens, could be determined.

## **2.4. RESULTS AND DISCUSSION**

### **2.4.1. Weight Gain Results**

Plots of percentage weight gain versus time are shown for the test coupons in Fig. 2.3 for the first 49 days of the experiment. The moisture uptake in the tapwater and seawater soaking tanks appears to follow initially a linear dependence between weight gain and the square root of time, as predicted by equation (2-11). The apparent diffusivity coefficients, based on the present tapwater and seawater data using (2-11) and the aspect ratio correction of (2-13), are compared with similar data by Loos and Springer (1979) in Table 2.2. The theoretical initial diffusivities are an order of magnitude smaller than those observed. This is most likely a result

of the fiberglass cover plies of the laminate. The theoretical prediction was based on diffusivity data obtained on unidirectional graphite/epoxy plies, and the diffusivities of the fiberglass surface plies are not known. Diffusivity was not calculated for the galvanically coupled specimens. The large increase in the weight of these samples was a result of heavy calcareous deposit formation.

The potentials and currents for the galvanically coupled specimens were monitored periodically during the experiment. The corrosion potential of the graphite-magnesium galvanic cell was stable during the experiment with an average value of -1.55V (SCE). The corrosion current for the individual specimens averaged 5.0 mA initially and dropped within a few days to a steady-state value around 0.2 mA, which is consistent with the current-limiting nature of calcareous deposits.

Film formation occurred on all of the exposed specimens. The calcareous film which formed on the galvanically coupled specimens was quite thick. For these specimens weight gain was dominated by calcareous growth. However, the films formed in the tapwater and seawater soaking experiments were comparatively thin. Thus it was assumed that weight gain in these specimens was primarily caused by moisture uptake.

The apparent diffusivity of the specimens might also have been affected by the film formation. The film which formed on the seawater specimens was much thicker than the film which formed on the specimens soaked in tapwater. However, the weight gain in the seawater specimens was observed to be less over time. This apparent anomaly is explained by considering the film as a barrier to moisture diffusion. Moisture diffusion was assumed to be the primary means of weight gain, and the thick biofilm which formed in seawater would have acted to impede this diffusion.

Final weight gain data for the soaking experiments are tabulated with the

corrosion experiments in Table 2.3. For the soaked specimens, the after-baking weights were found to be greater than the reference zero weight. This increase in dry weight is an indication of deposits formed on the surfaces of the soaked specimens. For the corrosion coupons, the after-baking weights with deposits removed were less than those of the in-air coupons. This is evidence for some additional mechanism causing weight loss in the electrochemical environment.

Results of the acid dissolution experiments are shown in Tables 2.4 and 2.5. These data show that part of the total moisture absorbed in the corrosion coupons is associated with the heavy calcareous films. This bound water is most likely accumulating within the porous deposits as well as in under-deposit blisters that were observed growing during the exposure period.

The summary data of Table 2.3 indicate a slight increase in the moisture uptake of the composite because of galvanic coupling. However, there was significant scatter in the dry weights of the deposits because of the inconsistent manner in which calcareous deposits grow and fall away. The large scatter in the dry deposit weights made any conclusions regarding galvanically-induced weight gain impossible.

Experimental error complicated the analysis of these results. Periodic (and futile) attempts were made early in the experiment to remove calcareous deposits by light scraping. This scraping skewed the weight gain data of Fig. 2.3, and could have caused the apparent weight loss shown in Table 2.3. Replacement of evaporated (ion-free) water by fresh tap- or seawater caused a salinity rise in the tanks at 40 days, when tanks began to be changed once weekly. This rise in salinity resulted in an increase in the rate of surface film formation, possibly as a result of an increase in dissolved ion activity. Because of this experimental error, no accurate assessment of film formation rates was attempted. Another major error was the high



drying temperature used (200°C), which exceeded the curing temperature (180°C) of the epoxy system. The high temperatures can cause post-cure reactions which release volatiles. The loss of volatiles represents a weight loss which might be misinterpreted as absorbed moisture being driven off in the drying process.

#### 2.4.2. Qualitative Chemical Analysis of Surface Films

Fig. 2.4 is a scanning electron microscope (SEM) micrograph of the surface of an unsoaked specimen. The area shown is a layer between adjacent plies and shows the rough surface left by the specimen cutting operation. This micrograph should be treated as a control for comparison with later micrographs.

Fig. 2.5 shows a particle clinging to the surface of a specimen soaked in tapwater, forming with other particles a thin tapwater film. An energy dispersive X-ray spectrometer (EDS) attachment to the SEM showed this tapwater film to consist of widely spaced calcareous aggregates along with particles which indicate the presence of sulfur. Sulfur is present in the water pipes in the laboratory as a result of bacteria, but it is possible that the EDS is detecting sulfur present in the organic matrix material of the underlying composite.

Fig. 2.6 shows the thin surface film deposited on the specimens soaking in seawater. The film seems to be an accumulation of particulate material and is 5-10 $\mu$ m thick. Fibers in the underlying graphite/epoxy surface can be seen through a crack in the film. The appearance of the film is consistent with the studies of Goldberg et al (1988), who found that uptake of particulate organic matter occurs after the formation of an organic biofilm. EDS analysis showed the dried film to be primarily calcareous, and is most likely composed of shell/exoskeleton biomaterials which passed through the packed-sand seawater filter.

Heavy calcareous deposits 200-500mm thick were formed on the

galvanically coupled specimens per the discussion of section 2.2.2. Visible white deposits formed on the specimen edges in less than 24 hours, because of the exposed conductive fibers concentrating the electrochemical reactions. These edge deposits were irregular, voluminous and quite adherent. Figure 2.7 is a photograph of the underside of an edge deposit, and reveals two distinct regions. The darker regions have a metallic "sparkle", while the lighter regions are dull. Figures 2.8 and 2.9 are SEM micrographs of the dark regions, which show complex formations of what appear to be fibrils, while Figs. 2.10 and 2.11 show the structure of the lighter regions. Both regions conform to the shape of the underlying cathode surface. The dark regions may be a residue of specimen scraping early in the experiment.

Calcareous growth was more subtle on the specimen faces, where corrosion currents were inhibited by the glass/epoxy cloth cover plies of the specimens. Here the growth was not visible during the initial portion of the experiment. After several weeks however a thin homogeneous film could be seen on the specimen faces. This delay represents the time required for moisture to diffuse through the glass/epoxy cover plies to the underlying conductive graphite/epoxy plies. Figure 2.12 is a photograph of the underside of a face deposit, which has crystallized in the form of the underlying laminate. (The laminate surface reflects the Teflon-coated fiberglass cloth bleeder/release fabric used in the laminate curing process.) Blisters (debonded areas) eventually formed under this film as shown in Fig. 2.13. These blisters accumulated fluids and caused some flaking away of the deposits. Figures 2.14 and 2.15 are SEM micrographs of the inside and outside surfaces, respectively, of a face deposit.

X-ray diffraction analysis of the calcareous films showed their composition to be primarily of aragonite ( $\text{CaCO}_3$ ), with some brucite ( $\text{Mg}(\text{OH})_2$ ). In addition, the film which formed on the specimen faces was somewhat ordered, i.e. the

aragonite platelets tended to lay down perpendicular to the c-axis of the orthorhombic unit cell. Figures 2.16a and 2.16b compare the XRD spectra of the face deposits to deposits which have been ground up to remove all orientation. The orientation of the face deposits (which were formed under lower current conditions) can be seen in the enhancements of the 002 and 012 peaks in the XRD spectra. These results may be significant in that the diffusive and thus current-limiting properties of calcareous deposits may be a function of the crystal orientation.

## 2.5. CONCLUSIONS

T-300/934 graphite/epoxy specimens exposed to fresh Pacific seawater absorb less than 1 percent moisture by weight. The moisture absorption rate in seawater is comparable to the rate of moisture absorption in tapwater. Thin surface films form both in seawater and in tapwater, complicating attempts to accurately measure the rate of moisture uptake by diffusion.

Galvanic coupling of the material to magnesium rod anodes causes the formation of thick calcareous deposits. These heavy deposits complicated attempts to determine the effect of galvanic coupling on moisture absorption. Although the data presented here show a slight increase in the moisture uptake under galvanic coupling conditions, large variations in the rates of formation and breaking away of these deposits prevents any conclusions from being made.

X-ray diffraction of the calcareous deposits formed on the faces of composite coupons shows a tendency for the material to lay down in a preferred crystal orientation. The protective properties of these deposits, which formed under relatively low electrical-current conditions, may be a function of the crystal orientation. Further study may reveal valuable structure/property relationships that could be utilized in cathodic protection schemes for metals in seawater.

The present study could have been improved by utilizing a standard method for determining moisture absorption rates in composites. Such a standard is presently under development by ASTM (1990). The present experiments would have also benefited from the use of continuously flowing seawater, which would have prevented several experimental errors that occurred. Possible variations on these experiments include (1) utilizing an artificial seawater mixture in moisture absorption experiments to avoid the formation of biofilms, and (2) the use of potentiostatic polarization and simple NaCl solutions to avoid the formation of calcareous films in simulated galvanic coupling experiments.

TABLE 2.1. PRINCIPLE CONSTITUENTS OF SEAWATER (@ 35 o/oo SALINITY)

Ion or Molecule	Concentration, g/kg sw
Na <sup>+</sup>	10.77
Mg <sup>+2</sup>	1.290
Ca <sup>+2</sup>	0.4121
K <sup>+</sup>	0.399
Sr <sup>+2</sup>	0.0079
Cl <sup>-</sup>	19.354
SO <sub>4</sub> <sup>-2</sup>	2.712
HCO <sub>3</sub> <sup>-</sup>	0.140
Br <sup>-</sup>	0.0673
B(OH) <sub>3</sub>	0.0257
F <sup>-</sup>	0.0013

TABLE 2.2 FICKIAN DIFFUSIVITY COEFFICIENTS IN T300/934 GRAPHITE/EPOXY (m<sup>2</sup>/sec)

Observed	Predicted
4.2 x 10 <sup>-12</sup>	0.38 x 10 <sup>-12</sup>

TABLE 2.3. SUMMARY OF MOISTURE ABSORPTION RESULTS  
(% Initial Weight)

Environment	Measured Parameters		Derived Parameters		
	Maximum Weight Gain mean (dev)	Weight After Baking mean (dev)	Deposit Weight mean (dev)	Water Uptake mean (dev)	Leaching Loss mean (dev)
Air	---	-2.13 (0.03)	---	---	---
Tapwater	0.98 (0.04)	-1.99 (0.04)	0.14 (0.05)	0.84(0.06)	---
Seawater	1.23 (0.06)	-1.77 (0.08)	0.36 (0.09)	0.87(0.10)	---
Seawater (Mg anode)	17.8 (1.3)	-2.81 (0.09)	15.0-16.9	1.1-1.5	0.68 (0.10)

TABLE 2.4. RESULTS OF WEIGHT REMOVAL OPERATIONS  
(% Initial Weight)

Specimen ID#’s	Removal Method	Maximum Weight Gain mean (dev)	Weight Lost in Operation a. mean (dev)	Weight Lost in Operation b. mean (dev)	Weight Lost in Operation c. mean (dev)
1-7	a. Bake b. Scrape c. Bake	16.9 (1.3)	4.04 (0.22)	15.0 (1.1)	0.72 (0.02)
9-11	a. Bake b. Acid c. Bake	19.3 (0.75)	4.38 (0.26)	16.9 (0.73)	0.74 (0.03)
12-14	a. Acid b. Bake	18.0 (0.48)	17.4 (0.52)	3.39 (0.06)	—

TABLE 2.5      DISTRIBUTION OF ABSORBED MOISTURE  
                                 (% Initial Weight)

Specimen ID#’s	Total Water mean (dev)	Initial Water* mean (dev)	Water Bound to Deposits mean (dev)	Water Absorbed by Gr/EP mean (dev)
1-7	4.77 (0.25)	2.13 (0.14)	1.56 (0.30)	1.1 (0.5)
9-11	5.13 (0.27)	2.13 (0.14)	1.52 (0.31)	1.5 (0.5)

\*Based on weight lost by control samples during high-temperature baking.  
Post-cure reactions and loss of volatiles may have caused this parameter  
to be overestimated.



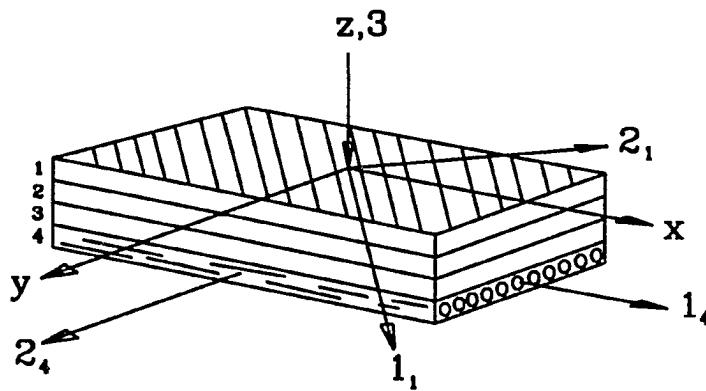


Figure 2.1. A laminate made up of distinct unidirectional composite plies. The x-y-z coordinate system is referenced to the laminate surroundings. The 1-2-3 coordinate system refers to the fiber and fiber-normal directions in each ply.

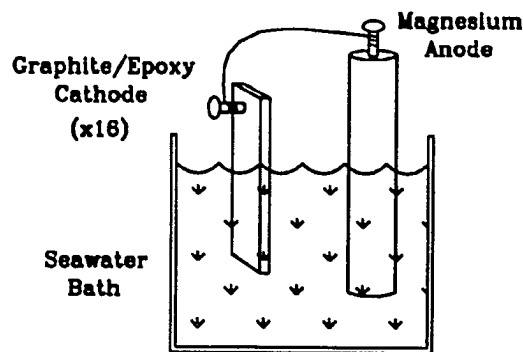


Figure 2.2. Schematic diagram of the cathodic polarization experiment. Sixteen graphite/epoxy specimens were connected to magnesium rod anodes in fresh (changed daily) seawater.

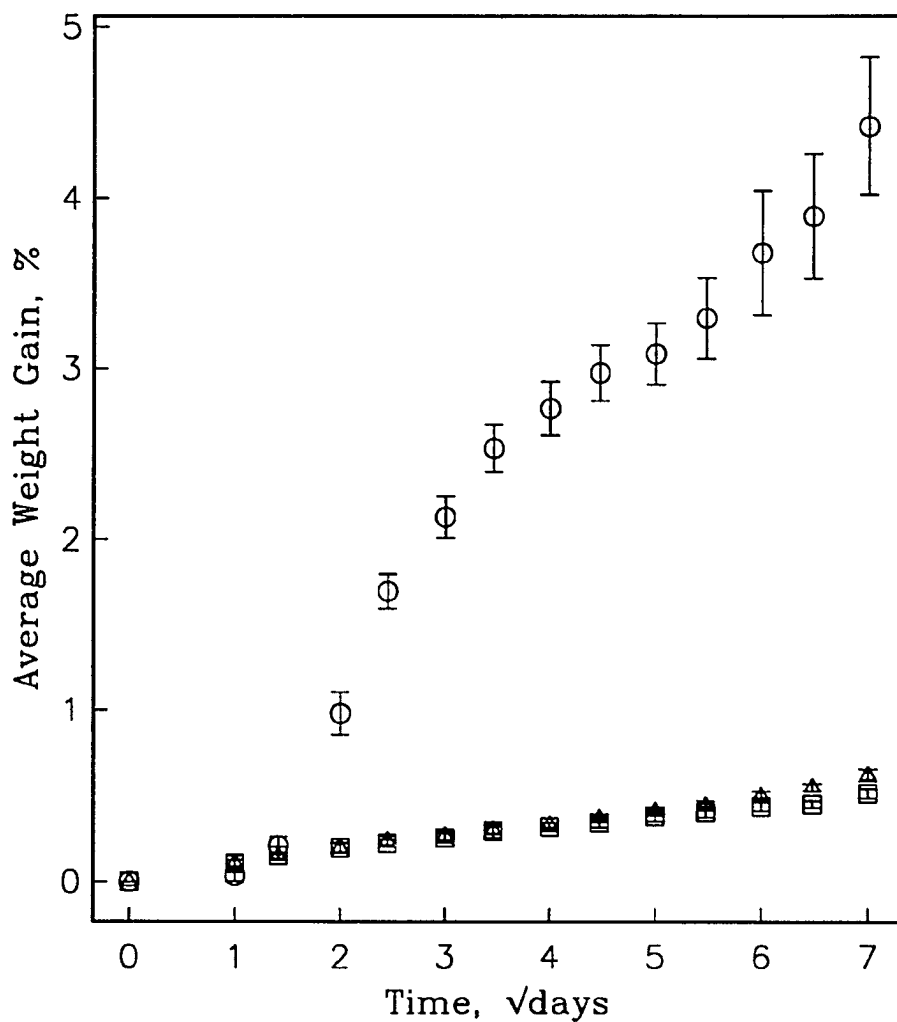


Figure 2.3. Moisture uptake in T300/934 Graphite/Epoxy Samples Exposed to Tapwater ( $\Delta$ ), Seawater ( $\Delta$ ) and Galvanic Coupling to Magnesium in Seawater(O).

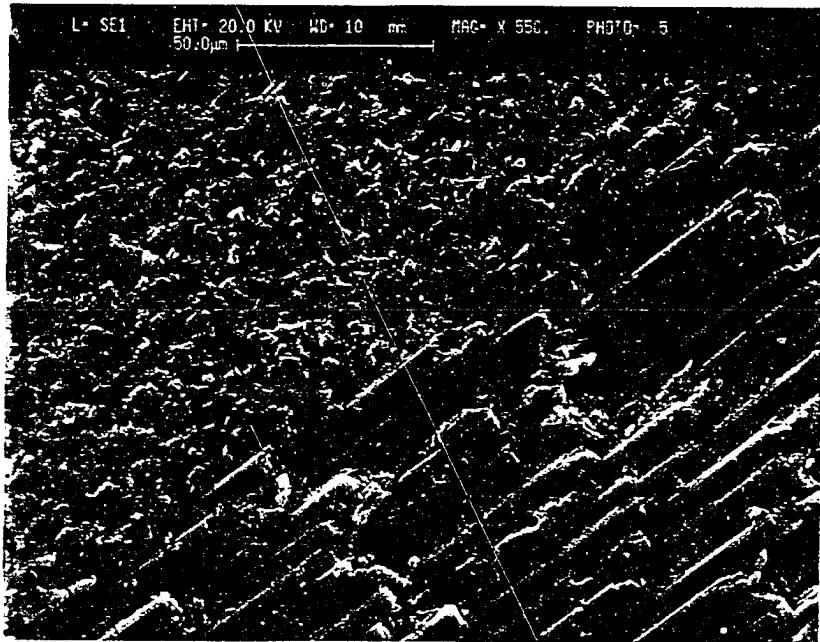


Figure 2.4. Scanning electron microscope (SEM) micrograph of the surface of an unsoaked specimen. Adjacent fiber layers are visible.

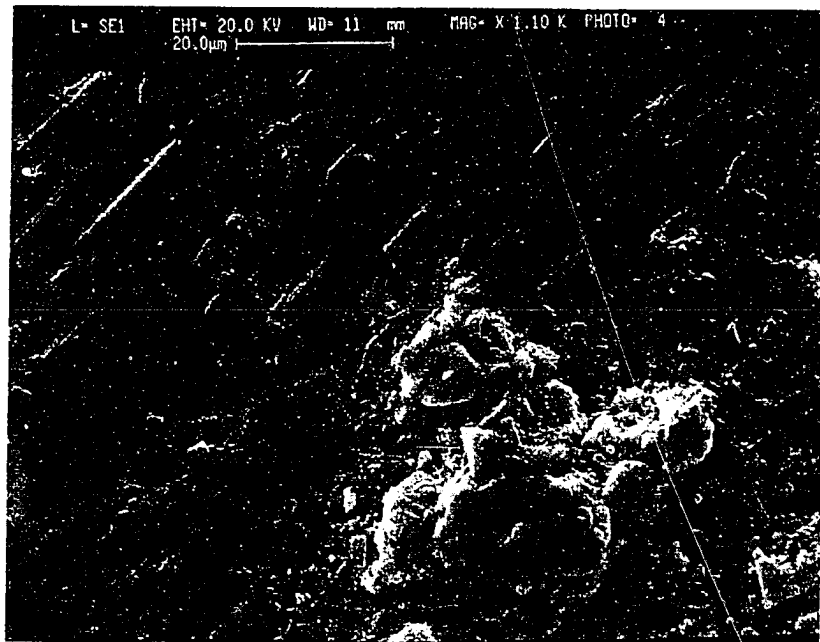


Figure 2.5. SEM micrograph of the surface of a specimen soaked in tapwater. A thin (less than 1 micrometer) film has formed on the specimen, as compared with Fig. 2.4. Several large clumps were also found clinging to the specimen, as shown here.

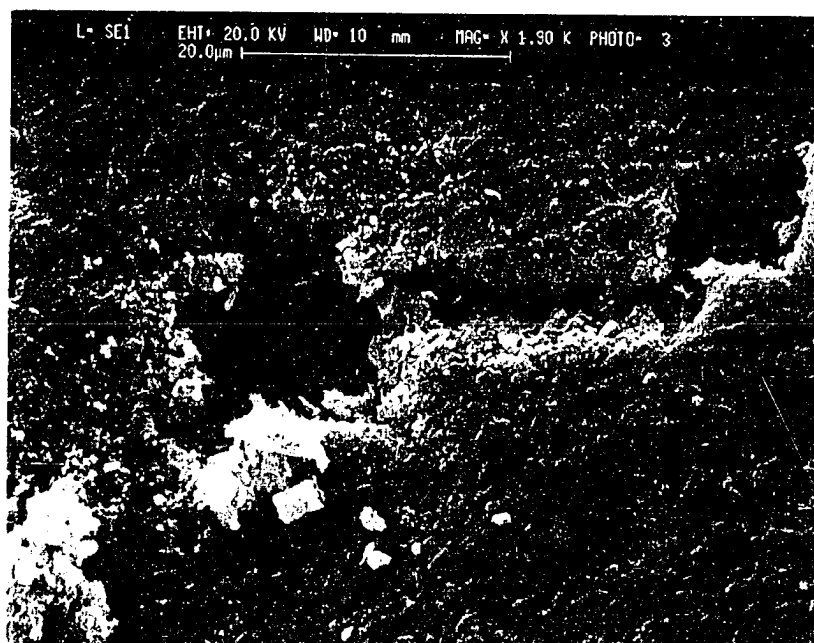


Figure 2.6. SEM micrograph of the relatively thick (5-10 micrometers) film which formed on the specimens soaking in seawater. This film is thought to be an accumulation of particulate matter which adhered to an organic biofilm.



Figure 2.7. Photograph of the underside of an electrochemically-formed calcareous deposit which formed on the edge of the laminate. The deposit has both dark and light-colored areas.

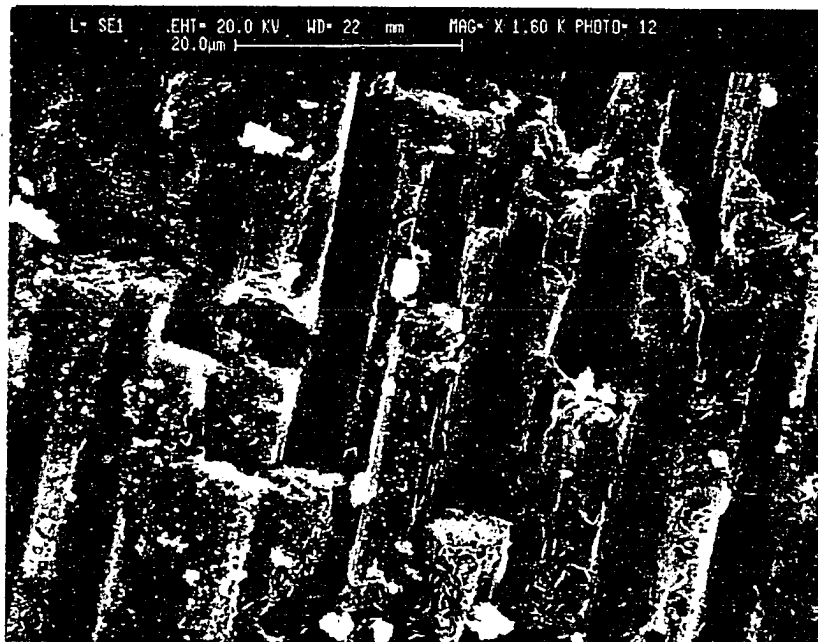


Figure 2.8. SEM micrograph of the underside of a calcareous edge deposit. This micrograph is from one of the dark areas seen in Fig. 2.7. The calcareous growth has taken the form of the underlying graphite/epoxy laminate.



Figure 2.9. Close-up micrograph of the broken fiber of Fig. 2.8. The underlying calcareous deposit seems to have a porous crystalline structure.



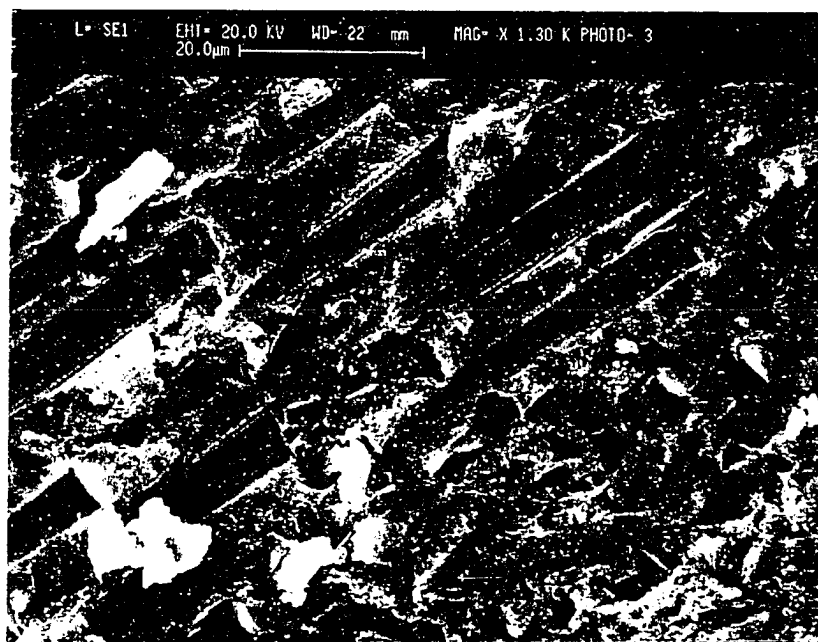


Figure 2.10. Micrograph of one of the light areas of Fig. 2.7. The light areas seem to have a finer structure than the dark areas. The crystal growth again follows the contours of the underlying specimen.

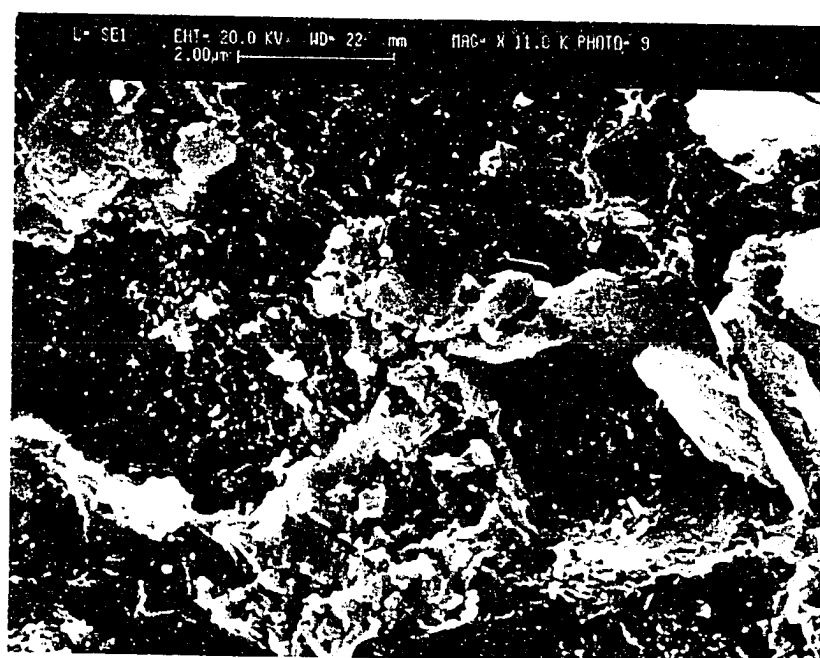


Figure 2.11. Close-up micrograph of Fig. 2.10. The much finer crystal size can be seen by comparing with Fig. 2.9.

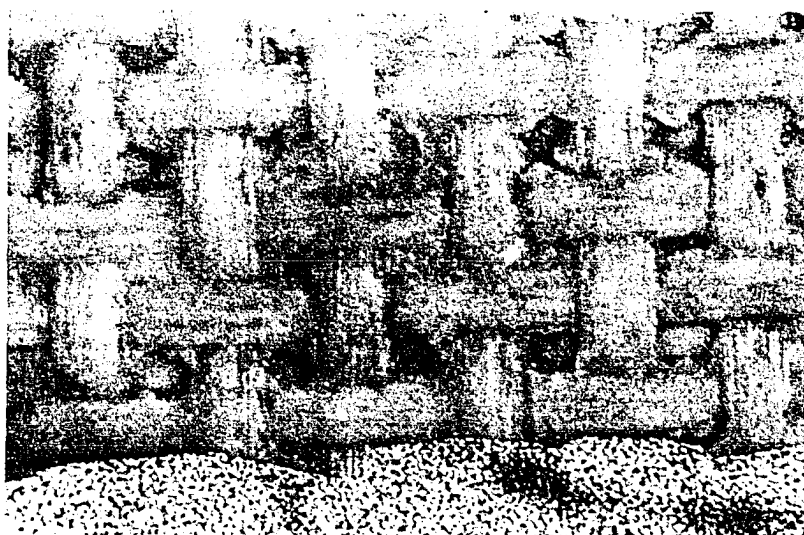


Figure 2.12. Photograph of the underside of a flake of calcareous deposit which formed on the face of the graphite/epoxy specimen. The flake has taken the form of the underlying laminate, which reflects the fiberglass cloth bleeder/release fabric used in the laminate curing process. Spacing between the fabric tows is approximately 1 mm.

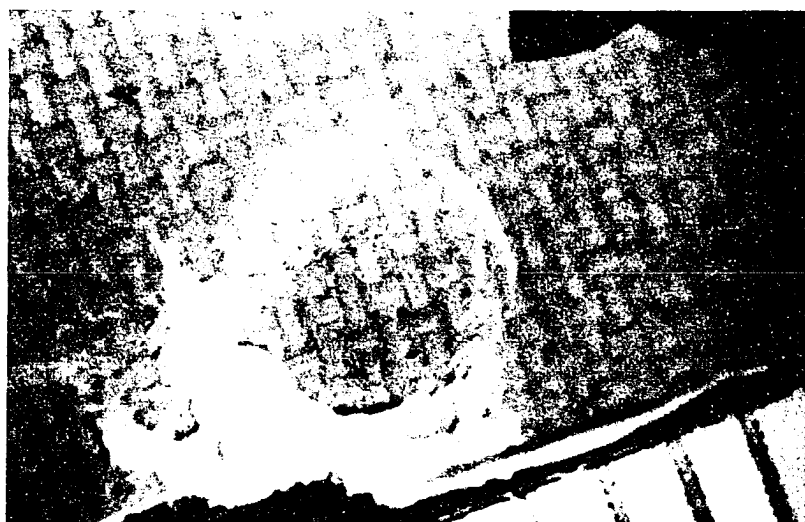


Figure 2.13. Photograph of the underside of a calcareous face deposit similar to that shown in Fig. 2.12. This flake had detached from the surface of the specimen, forming a "blister" in the calcareous coating. New deposits had begun to form in the occluded region beneath the detached film.

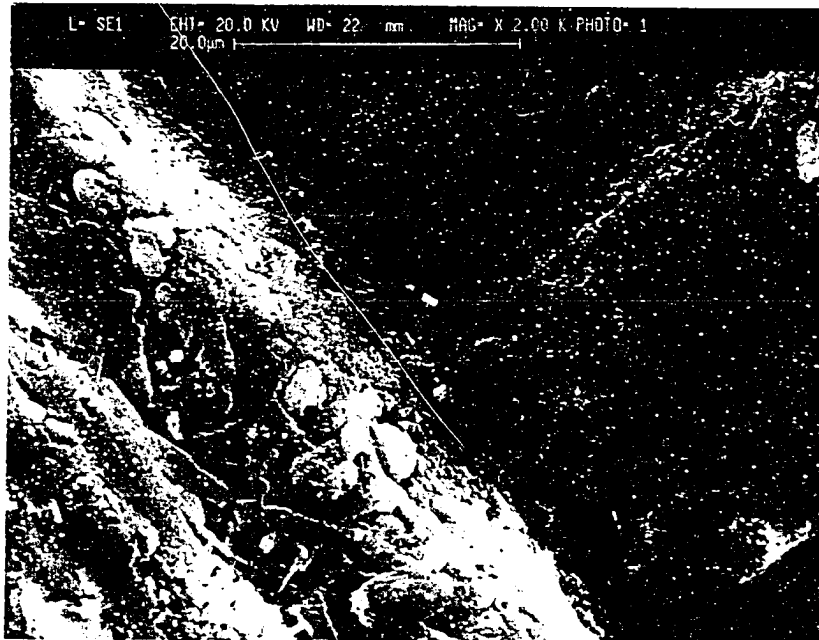


Figure 2.14. Close-up SEM micrograph of the flake shown in Fig. 2.12. The "intersection" is the impression left by the crossing of two fiberglass tows in the bleeder/release fabric.

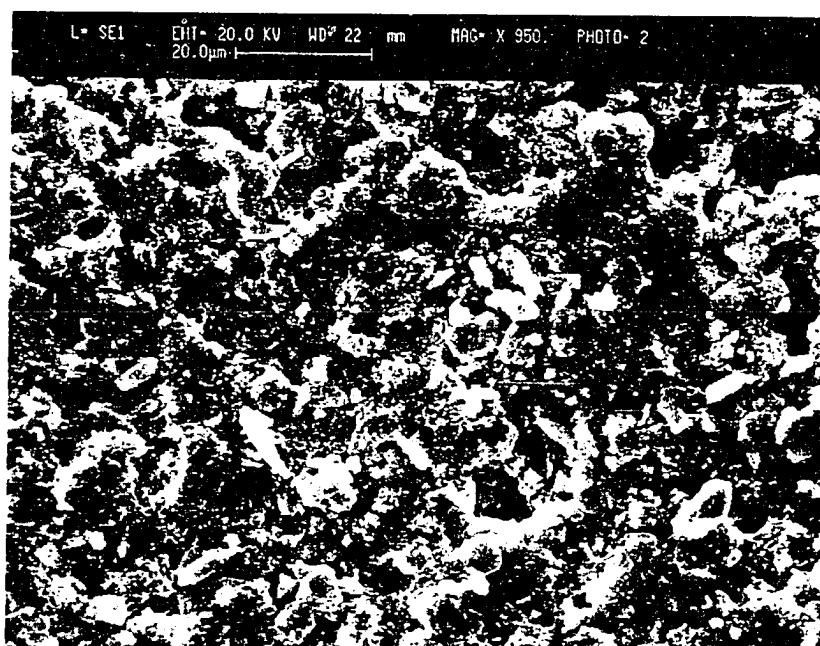


Figure 2.15. SEM micrograph of the outside surface of a face deposit similar to that shown in Fig. 2.14. No distinct patterns were discernible on the outside surfaces.

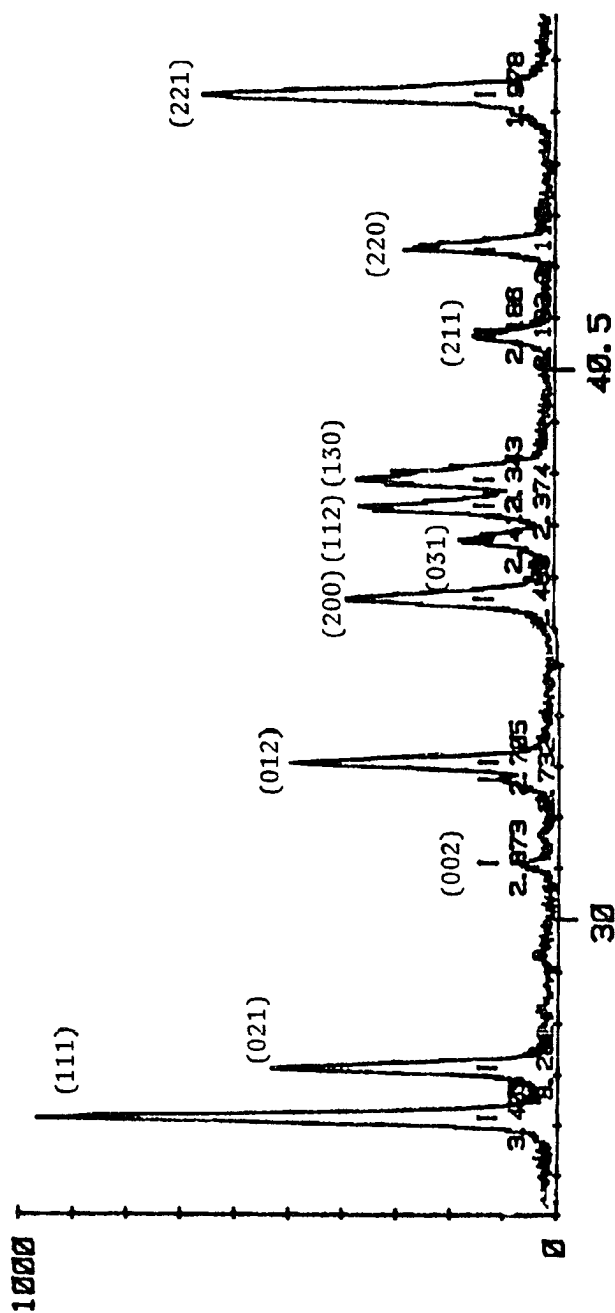


Figure 2.16a. X-ray diffraction spectra of a powdered sample of the calcareous film. The location and relative magnitude of the peaks clearly identified the material as aragonite  $\text{CaCO}_3$ , with traces of brucite,  $\text{Mg}(\text{OH})_2$ .

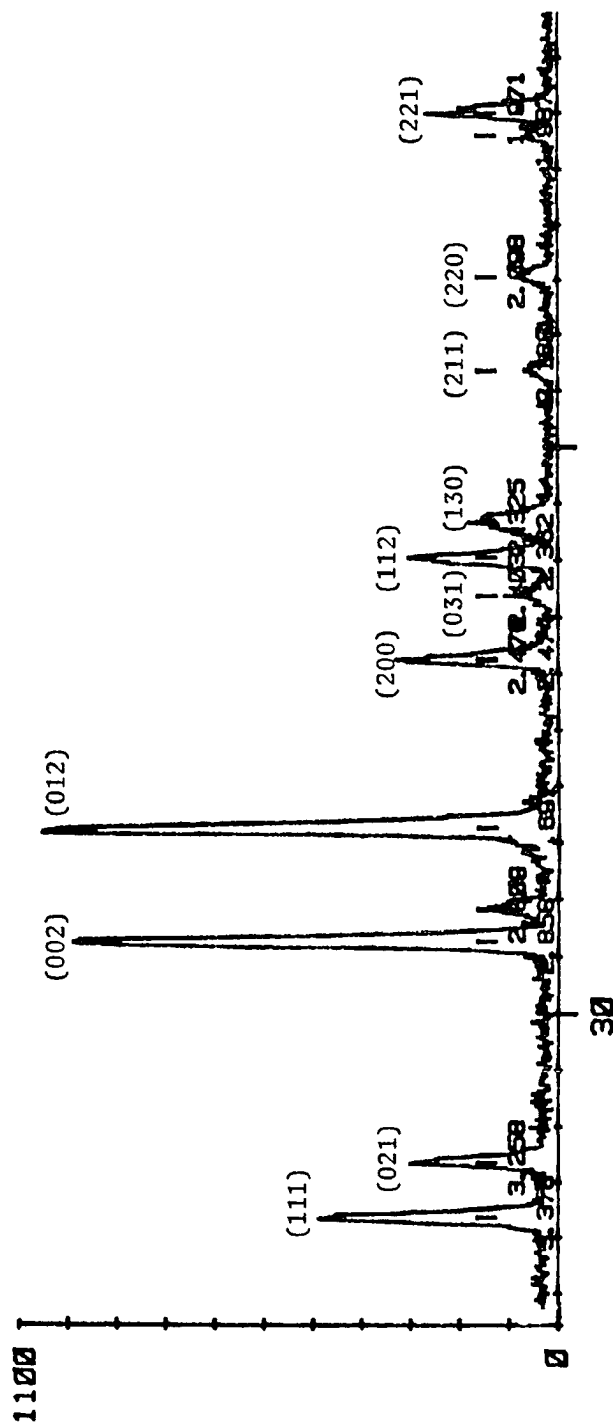


Figure 2.16b. X-ray diffraction spectra of a surface flake of the calcareous film. Note the large increase in the 002 and 012 peaks, which can be attributed to the preferred orientation of the aragonite during formation.



### **III THE EFFECT OF SEAWATER EXPOSURE ON SHEAR STRENGTH**

#### **3.1. INTRODUCTION**

One of the principal concerns of designers using composite materials in the marine environment is the effect of absorbed moisture on matrix-dominated properties such as transverse strength and shear strength. The matrix becomes plasticized by the absorbed moisture and is thus less able to support an applied load. This effect is usually small in epoxy matrices at room temperature, but becomes more apparent at elevated temperatures as a result of a depression in the glass-transition temperature (Browning, 1978). Fiber-dominated mechanical properties are not affected by moisture absorption.

The shear strength of a composite laminate is an important matrix-dominated property, and any reduction in strength caused by seawater exposure needs to be determined. The primary purpose of this investigation was thus to determine the effect of absorbed moisture on the shear strength of a unidirectional graphite/epoxy composite laminate tested at room temperature. Several experimental methods have been developed to ascertain shear properties in composites (Carlsson and Pipes, 1987; ASTM, 1987), but the simplest techniques involve the bending of beam samples. A secondary purpose of the study was to evaluate the effectiveness of the four-point beam-bending test method for determining moisture effects on shear strength and modulus.

#### **3.2. BACKGROUND**

##### **3.2.1. Shear Testing Using Composite Beam Specimens**

The commonly used standard method for determining shear strength involves fracturing short composite beam specimens in a 3-point bending fixture

(ASTM, 1984). This method is used as a comparative strength test in industry, but is not popular among researchers because of the tendency for failure to occur in a non-shear mode (Rosensaft and Marom, 1985). Browning et al (1983) suggested a 4-point bending method, shown in Fig. 3.1, to make failure in shear a more likely result of the test.

For a unidirectional composite beam loaded in the 4-point loading configuration the maximum tensile stress is given by

$$\sigma_{\max} = \frac{3PL}{4bh^2} \quad (3-1)$$

where  $P$  is the applied load,  $L$  is the span or length between the lower loading pins,  $b$  is the specimen width and  $h$  is the specimen thickness. The maximum shear stress is given by

$$\tau_{\max} = \frac{3P}{4bh} \quad (3-2)$$

By taking the ratio of (3-1) to (3-2) it can be shown that failure will occur in shear for specimens with

$$S \equiv L/h \leq \frac{\sigma_{\text{allow}}}{\tau_{\text{allow}}} \quad (3-3)$$

### 3.2.2. Compliance of a Symmetric Composite Beam including Shear

In most analyses of composite beams, e.g. in general laminate theory (Appendix A), it is assumed that deflections due to shear are negligible. This assumption is reasonable for beams which are long compared with their thickness. However, experiments designed to determine shear properties utilize specimens where shear effects are important, and these effects must be included in any analysis.

The present analysis utilizes Timoshenko beam theory, which includes the effect of shear as an additional term  $\phi$  in the expression for slope. The equations of Timoshenko beam theory can be derived using variational calculus, with the

result

$$E_x I (v'''' - \phi''') = p(x) \quad (3-4)$$

and

$$E_x I (v'''' - \phi''') = \frac{G_{xz} A \phi}{\alpha} = V(x) \quad (3-5)$$

where  $p(x)$  is the distributed load and  $V(x)$  is the shear load.  $E_x$  is the longitudinal stiffness of the beam,  $G_{xz}$  is the shear modulus,  $I$  is the moment of inertia,  $A$  is the cross-sectional area, and  $\alpha$  is the shear-correction factor of Timoshenko.

The deflection of a simply-supported beam under 4-point loading is shown schematically in Fig. 3.2. Only one half of the symmetrically loaded beam is shown for simplicity. For this case  $p(x)=0$ , which with (3-4) and (3-5) imply that  $V(x)$  is constant within each of the two sections shown in the figure. The result for a rectangular cross section where  $A=bh$  is

$$\phi = \frac{\alpha V}{G_{xz} bh} = \text{cnst} \quad (3-6)$$

The following boundary conditions are applied:

$$\begin{aligned} @x=0: & \quad v_1=0, (v_1'+\phi_1)=0, E_x I (v_1''-\phi_1')=PL/8 \\ @x=L/2: & \quad E_x I (v_2''-\phi_2')=0, E_x I (v_2''-\phi_2')=-P/2 \\ @x=L/4: & \quad v_1=v_2, (v_1'+\phi_1)=(v_2'+\phi_2) \end{aligned} \quad (3-7)$$

The results of applying the boundary conditions (3-7) to equations (3-4) and (3-5) can be used to define the compliance in two ways. If the deflection of the beam is measured at the center of the beam relative to the outer loading pins (i.e.  $v_2$  @  $x=L/2$ ), the compliance is

$$C_1 \equiv \frac{\delta_c}{P} = \frac{11L^3}{64E_x bh^3} \left[ 1 + \frac{8\alpha}{11} \left( \frac{E_x}{G_{xz}} \right) \left( \frac{h}{L} \right)^2 \right] \quad (3-8)$$

where  $\delta$  is the measured deflection and  $P$  is the applied load. If the deflection is measured at the inner loading pins relative to the outer loading pins (i.e.  $v_2$  @  $x=L/2$  minus  $v_2$  @  $x=L/4$ ), the compliance is

$$C \equiv \frac{\delta_i}{P} = \frac{L^3}{8E_x b h^3} \left[ 1 + \alpha \left[ \frac{E_x}{G_{xz}} \right] \left[ \frac{h}{L} \right]^2 \right] \quad (3-9)$$

The shear correction factor  $\alpha$  is generally assumed to be  $3/2$  for a beam free to deform under shear loading. The shear correction factors (the bracketed terms) of equations (3-8) and (3-9) are much more important in composite beams than in isotropic beams.  $E/G$  for isotropic materials is around 2.6, whereas  $E/G$  for composites can be as high as 35.

### 3.3. EXPERIMENTAL PROCEDURE

Four-point bending specimens were cut from panels of 30-ply unidirectional AS-4/3501-5a graphite/epoxy composite laminates. Specimens were cut in a water-cooled diamond saw to nominal dimensions 3.8 mm thick x 12 mm wide x 90 mm long. The specimens were cut with the reinforcing fibers parallel to the long dimension of the specimen.

Specimens were conditioned by hanging the specimens from racks suspended above tanks of fresh flowing Pacific seawater. Because of the small aspect ratio of the specimens (causing edge effects to appear in the diffusion equation) and the formation of surface films and biological growth on the specimens, the rate of moisture uptake by diffusion was not measured. Control specimens were kept in a separate laboratory (in ambient air) during the test period.

At the end of the conditioning period, test specimens were removed from the conditioning racks and tested to failure in a 4-point bending fixture similar to that of Fig. 3.1. An initial span-to-depth ratio ( $S$ ) of 12 was chosen in consultation with industry, but this was later increased to 16 as discussed below.

All testing was done in a Cortest constant-extension-rate tensile testing machine with a 50 kN load cell. This configuration had a resolution of 5 N and a

rated accuracy of  $\pm 0.5\%$  or 250 N. Crosshead displacement was monitored using a 7.5 mm stroke LVDT with a resolution of 2.5  $\mu\text{m}$ . Specimens were loaded at a nominal extension rate of 0.01 mm/min. Applied load and crosshead displacement data were collected and stored on an IBM PC-AT computer using Cortest data acquisition software. Deflection of the specimen was inferred from the movement of the loading crosshead. The load-deflection curve of the machine load-train was measured separately and subtracted from the specimen load-deflection data.

Specimens were tested immediately after being removed from the conditioning environment, i.e. no water loss occurred before testing. Specimens were weighed immediately after testing to determine the final "wet" weight. Specimens were then put into a drying oven at 100°C (210°F) to remove the absorbed moisture. Specimens were weighed daily during the drying period, and were removed when the change in weight over 24 hours was less than 5 milligrams (approximately 10 days). Weighing was performed in a laboratory balance with a resolution of 0.05 milligrams, and a rated accuracy of  $\pm 0.5$  milligram.

### **3.4. RESULTS AND DISCUSSION**

#### **3.4.1. Moisture Content of the Conditioned Samples**

The initial moisture content of the control specimens was 0.65% by weight, as determined by the weight lost during drying. The amount of moisture present in the samples after environmental conditioning was 1.0% as shown in Table 3.1. Samples absorbed approximately 0.35% moisture by weight during the 6-months of exposure to fresh flowing seawater. The final moisture content is in agreement with other studies (Loos and Springer, 1979; see also Chapter 2 of this text).

### 3.4.2. Non-Dimensional Data Analysis

In order to non-dimensionalize the data as much as possible, all deflection-load curves were converted to curves of apparent strain,  $\gamma_{app}$ , versus shear stress,  $\tau$ , where the apparent strain is defined here as

$$\gamma_{app} \equiv \frac{6\delta}{hS^3} \quad (3-10)$$

The beam deflection  $\delta$  is defined in (3-9) and  $S$  is the span-to-thickness ratio,  $L/h$ .

$\gamma_{app}$  has no physical meaning, but plotting the data in this manner gives a slope of  $E_s$ , where from (3-9)

$$E_s = E_x \cdot \left[ 1 + \alpha \left[ \frac{E_x}{G_{xz}} \right] \left[ \frac{h}{L} \right]^2 \right]^{-1} \quad (3-11)$$

The  $\gamma_{app}$ - $\tau$  curve for a typical control (dry) specimen is shown in Fig. 3.3. A theoretical curve is also shown based on (3-9) and literature values for  $E_x$  and  $G_{xz}$  (Tsai, 1987). All of the  $\gamma_{app}$ - $\tau$  plots were slightly non-linear, and there was a great deal of scatter in the initial slope data, as shown in Table 3.2.

### 3.4.3. Changes in Shear Strength

Because of the non-linear nature of the load-deflection curves observed in these tests, failure was defined in two ways, as shown in Fig. 3.3. The first failure definition was based on the standard offset method used to define yield in ductile metals. For these specimens yield was defined arbitrarily by a  $50 \times 10^{-6}$  offset in apparent strain from the initial slope of the  $\gamma_{app}$ - $\tau$  curve. The second failure definition was simply the maximum applied shear stress observed during the test.

The initial data was obtained using a span-to-depth ratio of 12, based on advice from industry. Most of the specimens tested in this configuration failed in compression under the loading pins. Consequently the span-to-depth ratio was increased to 16, which is the maximum allowed based on equation (3-3) and strength

data taken from Tsai (1987). The loading pins were still the initiation point of many failures, indicating that the shear strength was not being accurately measured in these tests.

The results of the failure analysis are shown in Table 3.3. The maximum shear stress data obtained using this test method is in general agreement with the literature value of 93 MPa for this material (Tsai, 1987). Neither of the failure definitions discussed above reveals any significant difference in the allowable shear stress between the wet and dry specimens. Thus the small amounts of moisture absorbed during the exposure period do not appear to have reduced the bending shear strength of the material in any way. Similar results have been reported by Birger et al (1989), who showed that moisture absorption below 50°C had little effect on strength or failure modes. Data scatter was most likely a result of premature compressive failure under the loading pins. A test procedure with a more consistent shear failure mode would be preferable.

The much lower failure strength defined by the offset method illustrates the non-linearity in the deflection-load curves obtained during this experiment. The most likely cause of this non-linearity is the non-standard method of determining the specimen deflection. Mounting a deflection gauge under the specimen mid-span and using equation (3-8) would have been a more direct and accurate means of determining the specimen deflection.

#### 3.4.4. Changes in Shear Modulus

Table 3.2 shows that the measured values of the shear-corrected stiffness  $E_s$  were in general agreement with values calculated using equation (9) and literature data for  $E_x$  and  $G_{xz}$ . The data shows a slight increase in the shear-corrected stiffness (and hence the shear modulus) with moisture absorption. This result was not

expected, and cannot be explained adequately with the present data.

In an attempt to explicitly determine  $E_x$  and  $G_{xz}$ , data taken under similar conditions but different span-to-depth ratios ( $S \equiv L/h$ ) were compared. Assuming that  $E_x$  remains constant, taking the ratio of the  $\gamma$ - $\tau$  slopes ( $E_s$  as defined above) gives an expression in the unknown quantity  $E_x/G_{xz}$ . Substituting  $E_x/G_{xz}$  back into (3-11) with a known  $E_s$  will give a value for  $E_x$ , then  $G_{xz}$  is determined. A similar method for determining moduli in a 3-point bending test is discussed by Fischer et al (1981). The calculated values for  $E_x$  and  $G_{xz}$  under these assumptions are shown in Table 3.4 along with literature data for this material (Tsai, 1987).

Attempts to determine values of longitudinal and shear moduli were unsuccessful. The scatter in the stiffness ( $E_s$ ) data were considerable, and calculated  $E_x$  and  $G_{xz}$  data were substantially different from literature values. Based on these results it must be concluded that changes in shear modulus cannot be determined using the 4-point bending test method as configured here. The large ratio of  $E_x$  to  $G_{xz}$  in this material makes determination of the moduli difficult, as small scatter in  $E_x$  leads to large scatter in  $G_{xz}$ . However, an inadequate experimental method also contributed to the poor results in this case. The specimen deflection should have been measured at mid-span, as discussed above. Also, a correction should have been included for the effects of loading pin indentation, as discussed by Fischer et al (1981). Finally, data should have been taken at several span-to-depth ratios, spaced farther apart than 12 and 16.

Several specimens had to be discarded because of dimensional irregularities. Cutting the specimens by hand (with a guide) in the diamond saw led to inconsistent specimen widths. More importantly, specimens cut from near the edges of the parent laminate were up to 20% thinner than those cut from the center. Specimens cut from larger laminates should always be checked for dimensional



consistency (especially thickness) before testing begins.

### 3.5. CONCLUSIONS

AS-4/3501-5a graphite/epoxy test coupons absorbed 1% of moisture by weight after 6 months of exposure to fresh flowing Pacific seawater at room temperature and one atmosphere pressure. This is in agreement with previous studies. The present test method produced strength and stiffness results consistent with literature data, but was unable to distinguish any effect of absorbed moisture on the bending shear strength of the material. Scatter in the strength data was caused by premature compression failure of many specimens under the loading pins, as well as inconsistent specimen dimensions.

The present test method was also unable to accurately determine shear and tensile modulus of the material because of extensive scatter in the bending stiffness data. Consequently no changes could be detected in the shear modulus of the material as a result of moisture absorption. Direct measurement of the specimen deflection and correction for indentation effects would have improved the accuracy of this test method. Bending-shear tests on unidirectional composite laminates are not recommended for monitoring changes in shear modulus — deflection of unidirectional specimens is dominated by tensile modulus.

TABLE 3.1. MOISTURE CONTENT OF TESTED SAMPLES

As Received		After 6-Month Seawater Soak		Literature Data
mean	dev	mean	dev	
0.65	(0.05)	1.0	(0.04)	1.2-1.4 (saltwater)

TABLE 3.2. SHEAR-MODIFIED BENDING STIFFNESS,  $E_s$ 

Conditioning Environment	As-Conditioned (L/h=16)		Dried (L/h=16)		Dried (L/h=12)	
	mean	(dev)	mean	(dev)	mean	(dev)
Literature Data	124.	---	124.	---	114.	---
Air Storage	125.6	(15.4)	127.8	(9.1)	125.0	(10.0)
Seawater Soak	150.3	(10.4)	143.5	(9.3)	130.5	(11.7)

TABLE 3.3. SHEAR STRESS AT FAILURE

Conditioning Environment	As-Conditioned (L/h=16)		Dried (L/h=16)		Dried (L/h=12)	
	mean	(dev)	mean	(dev)	mean	(dev)
Literature Data ( $\tau_{\max}$ )	---	---	93.0	---	93.0	---
Air Storage ( $\tau_{\max}$ )	88.7	(4.2)	91.5	(3.8)	101.2	(3.8)
Air Storage ( $\tau_{\text{offset}}$ )	81.0	(2.7)	80.0	(1.7)	81.0	(5.3)
Seawater Soak ( $\tau_{\max}$ )	91.6	(3.1)	94.6	(4.6)	96.3	(3.0)
Seawater Soak ( $\tau_{\text{offset}}$ )	79.6	(1.7)	82.8	(4.2)	78.4	(2.9)

TABLE 3.4. CALCULATED TENSILE AND SHEAR MODULUS

	Dry Data	Wet Data	Literature
Tensile, $E_x$	126	185	138
Shear, $G_{xz}$	450	5	7.1

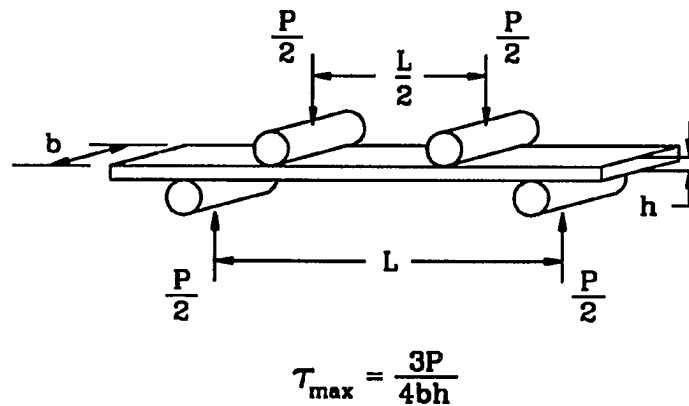


Figure 3.1. Schematic of the four-point bending test configuration. The mode of failure depends on the ratio of the span ( $L$ ) to the thickness ( $h$ ).

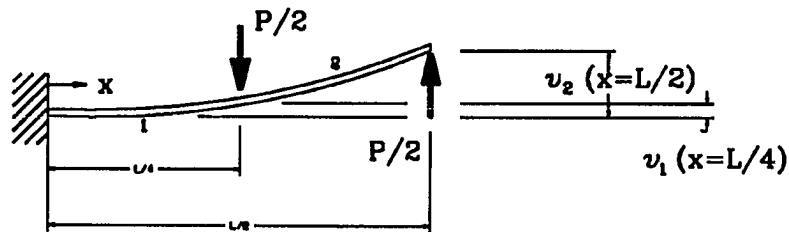


Figure 3.2. Diagram showing a beam deflecting under four-point loading. For analysis purposes only one half of the symmetric beam is considered.

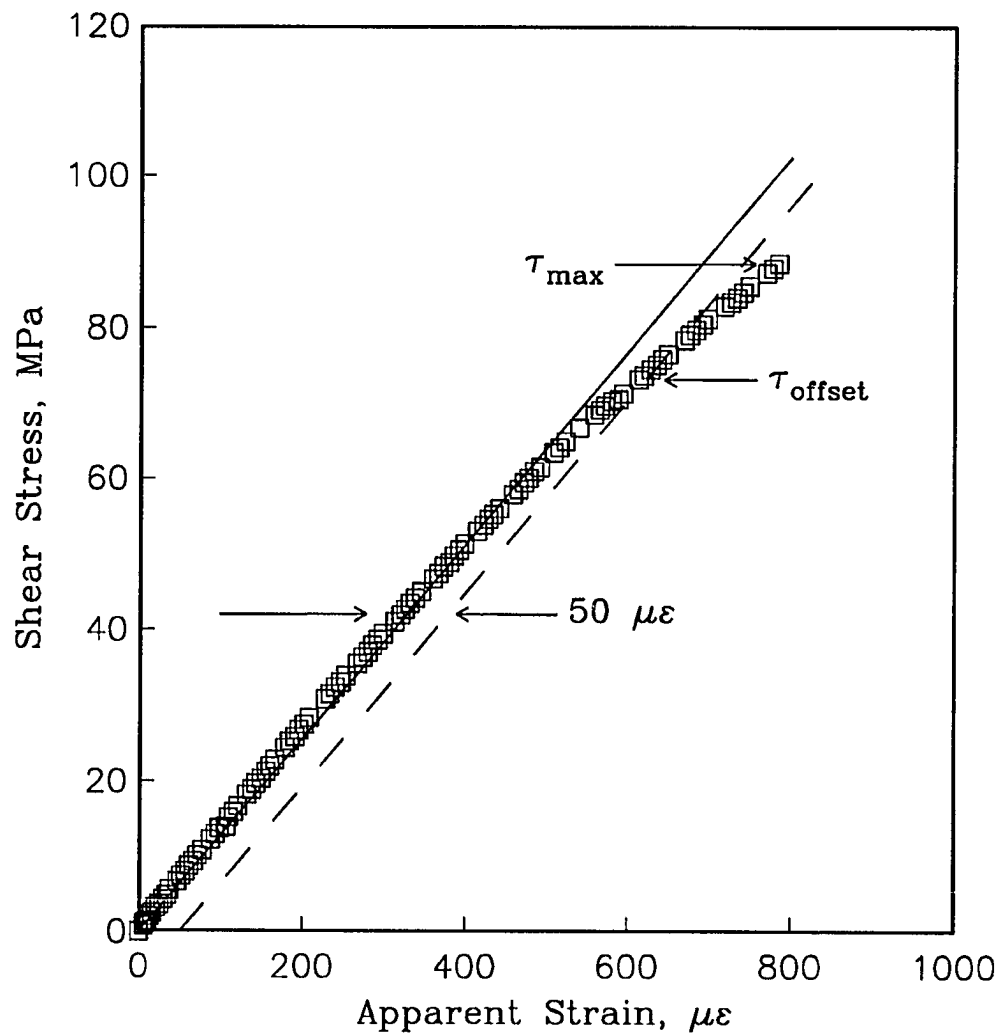


Figure 3.3. Typical apparent strain versus shear stress data for the four-point bending test. The  $50\mu\epsilon$  offset and  $\tau_{\max}$  failure criteria are illustrated.

## **IV THE EFFECT OF SEAWATER EXPOSURE ON MODE I INTERLAMINAR CRACK GROWTH**

### **4.1. INTRODUCTION**

Fatigue failure in fiber-reinforced composite materials typically results from the growth of delamination cracks which appear early in the life of the component (Reifsneider et al, 1983). The rate of growth of delamination cracks is thus of primary importance in estimating the service life of composite components. Several investigators have monitored the rate of delamination crack growth in laminates under fatigue loading (Ramkumar and Whitcomb, 1985; Hojo et al, 1987). However, mechanical loading and an aggressive environment such as seawater nearly always act synergistically to produce fatigue damage which would not occur under mechanical loading or environmental exposure alone. Several studies have addressed the effect of environment on fatigue properties (Sandifer, 1982, Sumsion, 1976, Macander et al, 1979), but few have investigated delamination growth during environmental exposure.

The fracture strength of composite materials can be strongly affected by exposure to hot/wet environments (Russell and Street, 1985; Garg and Ishai, 1985), a result of plasticization of the matrix. Fracture strength may also be a function of the crack length, specifically where fibers bridge the crack tip as in unidirectional laminates (Johnson and Mangalgiri, 1987). These effects are an important consideration in fatigue because the rate of damage growth is a function of the resistance of the material to fracture as well as the applied loading (Russell and Street, 1988).

The compliant load-frame (CLF) has recently been introduced (Sloan and

Seymour, 1990) as a simple linear-elastic fracture mechanics (LEFM) test method which relates observed crack growth to changes in the threshold strain-energy release rate,  $G_{\text{thres}}$  of the tested material. Linear-elastic material properties and self-similar crack growth are essential assumptions of LEFM and the CLF technique, but composites do not necessarily behave in this manner (Friedrich, 1989; Dharan, 1978). The effects of hot/wet environments and crack bridging discussed above could adversely affect the CLF test method.

Because of its simplicity and low cost, the CLF technique was selected for this investigation into the effects of seawater exposure on Mode I delamination of graphite/epoxy laminates. Double-cantilever-beam (DCB) test specimens cut from unidirectional AS-4/3501-5a graphite/epoxy laminates were chosen for the present study. There were two goals of this investigation. The first goal was to examine the effects of seawater exposure on Mode I crack growth rates and fracture strength in graphite/epoxy. The second goal was to determine the effectiveness of the CLF test method in monitoring environmental effects in a unidirectional composite laminate.

## 4.2. EXPERIMENTAL PROCEDURE

### 4.2.1. Specimen Preparation

Double-cantilever-beam (DCB) specimens were cut from panels of 30-ply unidirectional AS-4/3501-5a graphite/epoxy. Nominal specimen dimensions were 20 mm wide by 250 mm long by 3.8 mm thick. Brass-plated steel piano hinge was cut and bonded to the specimens using a two-part adhesive (Loctite). Mating surfaces were abraded and cleaned with a solvent prior to bonding. The edges of the specimens were stained with thinned typewriter correction fluid as an aid in crack length determination. Crack length was determined visually, with the aid of reference lines drawn at 80, 90, 100, 110, and 120 mm from the hinge pins. A 25

mm embedded Kapton-tape insert served as a crack initiator. Specimens were pre-cracked by loading in a fixed-displacement manner until the desired starting crack length of 80 mm was reached.

#### 4.2.2. Compliance Determination

The compliance of a DCB specimen which obeys linear-elastic beam theory has been derived previously (Whitney et al, 1982)

$$C = \frac{2a^3}{3EI} \quad (4-1)$$

where  $a$  is the crack length of the specimen and  $EI$  is the flexural rigidity of one arm of the split cantilever. However, because of rotation at the crack tip, hinge effects, and other effects not accounted for in the derivation of (4-1), compliance data for fiber-reinforced composites often does not follow this equation. In this case the compliance can be approximated as

$$C = M \cdot a^m \quad (4-2)$$

Six as-received specimens were used to determine the empirical parameters  $M$  and  $m$  of equation (4-2). These specimens were loaded to fracture in a screw-driven constant-extension-rate tensile tester as shown in Fig. 4.1. Load and deflection data were obtained from a 250 N resistance-bridge load cell and a  $\pm 25$  mm LVDT mounted on the crosshead. Crack-opening displacement (COD) was inferred by correcting the measured crosshead displacement using the load-deflection curve generated for the loading train alone. Specimens were loaded at a crosshead speed of 0.5 mm/min and unloaded at 2.5 mm/min. Data was collected using an IBM PC-AT computer with a Dataq DM-100 data acquisition card and a BASIC data collection program. A least-squares method was used to determine the parameters  $m$  and  $M$  which best fit the observed compliance data.



#### 4.2.3. Experimental Matrix

Specimens were loaded in air and in seawater, and were loaded statically for 60 days or fatigued for 30 days, as shown in Table 4.1. After the exposure period the specimens were loaded to failure in the tensile test machine of Fig. 4.1 to determine the effect of environmental conditioning on the fracture behavior. Several of the conditioned specimens were kept in their environments but were unloaded and allowed to relax for 30 days before fracture testing, to remove any viscoelastic effects. Other specimens were dried at the end of the conditioning period while being held at the maximum observed displacement, to remove absorbed moisture without being relaxed. A minimum of four specimens were tested under each set of loading and environmental conditions. Crack growth rates were monitored in selected fatigue specimens.

#### 4.2.4. Environmental Conditioning

To initiate the static load experiments, specimens were loaded in a fixed-displacement load frame until audible and visible crack extension occurred. The resulting critical specimen deflection  $\delta_c$  was recorded. Specimens were then loaded in a compliant load-frame (Fig. 4.2) using an extension spring sized according to the crack growth stability criterion derived previously (Sloan and Seymour, 1990). When the critical deflection was reached, the loading nut of Fig. 4.2 was locked, and the crack tip was immersed in the environment of interest. Corrosion-fatigue experiments were started in a similar manner, and were run at a load-ratio of 0.5 and a frequency of 0.5 Hz. Cyclic load was applied by a cyclic displacement of the loading bolt.

Crack length and applied load were monitored periodically during the

experiments to determine the applied strain-energy release rate  $G$ , given by (Whitney et al, 1982)

$$G = \frac{P^2}{2b} \cdot \frac{dC}{da} \quad (4-3)$$

or, using (4-2),

$$G = \frac{P^2}{2b} \cdot \text{mMa}^{m-1} \quad (4-4)$$

where  $b$  is the specimen width. Crack length was measured relative to reference marks on the specimens using a 7X optical loupe, giving a resolution of 0.1 mm. The applied load was inferred from the deflection of the loading spring, which was calibrated in the tensile tester of Fig. 4.1.

#### 4.2.5. Test Environment

Specimens were conditioned in both seawater and in laboratory air. The laboratory is in a building near the ocean and the inside environment is not controlled. The air temperature ranged from 16 to 27 °C (60 to 80 °F), with a humidity range of approximately 20 to 70 percent. The fresh flowing natural Pacific seawater used in these experiments is pumped continuously from the pier at the Scripps Institution of Oceanography. The temperature of the water ranged from approximately 13 to 21 °C. This seawater is sand-filtered only, so some types of algae and other organisms (e.g. sea-squirts) were introduced during the experiments as viable larva. No attempt was made to counter the effects, if any, of these organisms.

#### 4.2.6. Fracture Testing

At the end of the environmental conditioning period, the specimens were

loaded to fracture in the same tensile testing apparatus used in the compliance experiments. Compliance and critical strain-energy release rate data from the conditioned specimens were compared with the control specimens using equations (4-2) and (4-3) to determine the effects of environmental exposure. Selected specimens were loaded to near-fracture and examined for signs of non-colinear crack growth. Other specimens were sectioned after fracture for examination of fracture surfaces in the scanning electron microscope (SEM).

### 4.3. RESULTS AND DISCUSSION

The most significant phenomenon which occurred during fatigue testing was the appearance of reinforcing fibers bridged across the crack tip in the fatigue specimens. Fiber bridging, as observed by others (Johnson and Mangalgi, 1987; Russell and Street, 1988), decreases the compliance of the test specimens by holding the cantilevered beams together. Because the bridged fibers have to be broken, fiber bridging also increases the resistance of the material to fracture,  $G_R$ .

#### 4.3.1. Compliance Results

The compliance versus apparent crack length data from the six control specimens are shown in Fig. 4.3. The empirical parameters  $M$  and  $m$  were calculated as 0.401 and 2.78, respectively. This departure from beam theory (i.e.  $m=3$ ) is most likely a result of hinge effects and rotation about the crack tip.

The empirical compliance parameters  $m$  and  $M$  depend primarily on the elastic constants of the component materials of the composite, which can in general change as a result of environmental exposure. The stiffness of unidirectional DCB specimens is dominated by the reinforcing fibers and so should be unaffected by the environment. Figure 4.4 shows the compliance of the conditioned specimens along

with the curve fit to the control data. The data shows that the compliance decreases slightly, in response to the fiber bridging discussed above.

The change in compliance caused by crack bridging changes the parameter  $dC/da$  used in equation (4-3) to calculate  $G$ . Russell and Street (1988) introduced a higher-order term to empirically account for the effects of fiber bridging on  $C$  and  $G$  during crack growth. In this study the effect of crack bridging on compliance was assumed to be minor and was not accounted for in the determination of  $G$ .

#### 4.3.2 Results of Fracture Testing

Figure 4.5 plots the fracture resistance  $G_R$  of the as-received specimens (calculated using (4-4) at critical load) versus the crack length. No definite dependence on crack length was noted, indicating that crack bridging during fracture testing was minimal. No noticeable fiber bridging was observed during these tests.

Table 4.2 shows the results of the fracture testing after specimens were conditioned according to Table 4.1. The fracture resistance,  $G_R$ , increased dramatically in many cases, showing the strong influence of loading history and absorbed moisture on the fracture toughness. Data scatter was substantial and may have been a result of crack-length dependence under fatigue conditions. The large scatter is more likely a reflection of the random nature of fiber bridging. During the fracture tests it became apparent that the primary cause for the increase in fracture resistance was bridging of individual fibers across the crack tip. Figure 4.6 is a photograph of a fatigue specimen from a separate experiment which had been cycled at constant  $\Delta G$  in seawater for 6 months. Because of the extensive fiber bridging observed during these experiments, the data of Table 4.2 should be used for comparative purposes only.

#### 4.3.3. Crack Growth Results

Mode I crack growth rate data from the monitored fatigue specimens is shown in Figs. 4.7 and 4.8. The cracks in the specimens fatigued in air grew continuously during the test. However, the rate of crack growth dropped steadily, even though the CLF test method maintained a constant apparent  $\Delta G$  as shown in Fig. 4.9. Linear-elastic fracture mechanics would predict a relatively constant crack growth rate under constant  $\Delta G$  conditions, assuming that the resistance of the material to fracture,  $G_R$  remained constant.

The effect of simultaneous exposure to seawater on crack growth is dramatic. The data show that crack growth rates drop almost immediately to a level 5 times lower than the in-air data. Again, the crack growth rate should remain constant under these constant- $\Delta G$  conditions, indicating that the resistance of the material to fracture,  $G_R$ , is increasing in response to fiber bridging.

#### 4.3.4. SEM Analysis

SEM micrographs of static and fatigue fracture surfaces near the crack tip are shown in Figs. 4.10 to 4.14. The control (static fracture, in-air) samples exhibited typical Mode I fracture surfaces for unidirectional laminates, with evidence of occasional fiber pull-out as shown in Fig. 4.10. The samples fatigued in air displayed an easily distinguishable transition from static fracture to fatigue crack growth, as shown in Fig. 4.11. The fractured crack surfaces were relatively smooth and suggested crack growth primarily through the matrix. Fatigue crack growth seemed to more closely follow the fiber/matrix interface. A reverse transition occurs when the fatigued specimens are pulled apart (Fig. 4.12).

A large number of broken and semi-detached fibers were seen just behind the crack tip in specimens fatigued in seawater, evidence of fiber/matrix debonding

(Fig. 4.13). In addition, large areas of Mode II fracture marks (hackles) were observed near the crack tip in these specimens (Fig. 4.14). These marks suggest that a great deal of fracture energy was absorbed in fiber pullout parallel to the fracture surface, an indication of bridged fibers (Fig. 4.14). Evidence of debonded and bridged fibers suggests a weakened fiber/matrix interface bond. The conclusion that moisture significantly weakens the fiber/matrix interface bond is consistent with work by Kaelble and coworkers (1974a, 1974b) and more recently by Tsotsis and Weitsman (1990).

#### 4.3.5. Discussion

The most important question to be answered from the experiments described here is "What causes the dramatic increase in fracture resistance,  $G_R$  ?". Three possible mechanisms have been suggested — (1) matrix plasticization by moisture absorption, (2) viscoelastic effects under static loading, and (3) fiber bridging as a result of a weakened fiber/matrix bond. A moisture-plasticized matrix allows more energy to be absorbed within the matrix during crack growth (Kinloch, 1985). Stress-relaxation during static loading of the crack tip could also increase the apparent fracture energy (Kinloch, 1985). Bridging of debonded fibers increases the fracture surface area and requires fracture of the bridged fibers for crack growth to occur, as discussed by Johnson and Mangalgiri (1987). These three phenomena might also act synergistically to increase the fracture energy at the crack tip.

Important conclusions can be reached from comparison of selected data sets in Table 4.2. For example, comparisons between the as-conditioned and the relaxed data imply that viscoelasticity has little or no influence on post-conditioning fracture strength. Also, the fracture resistance of specimens which were soaked in seawater, but not mechanically loaded, was more than twice that of dried control samples.

This trend is in agreement with Garg and Ishai (1985) and others, as shown in Table 4.3. This increase disappeared upon drying, indicating that no permanent damage was caused by the exposure to moisture alone. (Dried samples were in fact more brittle than as-received control samples, which illustrates the importance of using carefully dried specimens to determine the critical energy levels to be avoided in service. If threshold strengths are determined on samples that are moist to some degree, a negative safety factor will result for laminates used in an arid environment.)

The increase in  $G_R$  which accompanies moisture absorption has been attributed to matrix plasticization (Garg and Ishai, 1985). But a weakening of the fiber/matrix bond could also cause such an increase by allowing fiber/matrix bridging on a scale much smaller than that seen in Fig 4.6. The absorbed moisture would weaken the interfacial bond but would not break it in the absence of an applied load. In this case the effect would appear during wet testing but would be reversible upon drying.

Crack-tip plasticization is a reasonable explanation for the rapid drop in crack growth rates which occurred during seawater exposure. This hypothesis can be tested by a simple calculation. If we assume that the crack is initially running solely through the epoxy, we can estimate the size of the plastic zone from LEFM assumptions. The plastic zone radius for an isotropic material can be approximated by (Collins, 1981)

$$r_p \cong \left(\frac{1}{2\pi}\right)\left(\frac{K_c}{\sigma_y}\right)^2 \quad (4-5)$$

For the 3501 epoxy, typical values are  $K_c = 1.0 \text{ MPa} \cdot \text{m}^{1/2}$  (Russell and Street, 1985) and  $\sigma_y = 10 \text{ MPa}$  (May, 1988). This gives  $r_p \cong 1 \text{ mm}$  and is not realistic for composites. However, for a fiber-reinforced material, a more appropriate plastic zone size would be a few fiber diameters, e.g. three graphite fiber diameters or

approximately 20  $\mu\text{m}$ . For moisture diffusing in epoxy, the diffusivity,  $D$ , is on the order of  $10^{-13} \text{ m}^2/\text{sec}$  (Zaikov, 1988), so the time for plasticization of the crack tip should be on the order of

$$t \approx \frac{r_p^2}{D} = 4000 \text{ secs.} \quad (4-6)$$

If the crack growth rate is initially greater than the rate of plasticization by moisture diffusion, then the crack tip region should never be plasticized. For the present data the initial crack growth rate is about  $5 \times 10^{-8} \text{ m/sec}$ , compared with an approximation of the plasticization rate,

$$\frac{r_p}{t} \approx \frac{20 \times 10^{-6} \text{ m}}{4 \times 10^3 \text{ sec}} = 5 \times 10^{-9} \text{ m/sec, } \ll 5 \times 10^{-8}. \quad (4-7)$$

Thus the crack growth rate is initially an order of magnitude higher than the rate of plasticization by diffused moisture. Under these assumptions the matrix around the crack tip could never be plasticized, because the crack would grow faster than the moisture could diffuse. The conclusion would have to be that some other factor besides plasticization was at work in stalling the crack growth. Based on the present experiments that factor is most likely micro-scale fiber bridging caused by a weakened fiber/matrix interface.

Fiber debonding plays an important role in the reduction of Mode I crack growth rates in seawater, as discussed above. Therefore fiber debonding is likely to be a major reason for the increase in the Mode I fracture resistance of this material under wet conditions. This conclusion is supported by the data of Russell and Street (1985), who showed that although the fracture *resistance* of DCB specimens was a function of moisture content, the fracture *toughness* was independent of moisture. Fracture toughness was defined in that study as the initial fracture resistance of the specimen, measured at the resin-rich crack-starter insert where no fibers are present. The data can only be explained by interaction between the absorbed moisture and



the reinforcing fibers.

Another important question to be answered by these experiments is "Is exposure to seawater during fatigue loading more damaging than fatigue loading in air?". The answer, however, depends on one's definition of "damage". This study has shown that Mode I delamination cracks growing in seawater tend to self-arrest much more rapidly than those in air, because of a weakened fiber/matrix interface at the crack tip. Alternately, examination of the fatigue damage zones shows that although the seawater has caused the total 2-dimensional damage zone (i.e. the crack) growth to decrease, the 3-dimensional damage zone has spread beyond the apparent crack tip more so than in air. Paradoxically, the growth of a 3-dimensional damage zone is aided by seawater, but the result is an increase in the apparent fracture strength of the material.

These experiments demonstrate that the compliant load-frame (CLF) test method is an effective technique for studying the physical mechanisms of damage growth in unidirectional graphite/epoxy, even though crack growth is not self-similar in this material. However, the relationship between  $G_{\text{thres}}$  and the crack length derived previously (Sloan and Seymour, 1990) no longer applies. The resistance of this material to crack growth increased on exposure to the environment, rather than decreased as was assumed.

#### 4.4. CONCLUSIONS

The effects of seawater exposure on Mode I delamination crack growth and subsequent fracture strength in unidirectional AS-4/3501-51 graphite/epoxy have been investigated using the compliant load-frame (CLF) test method. The CLF test method is a simple and effective technique for establishing conditions of stable crack growth in which damage evolution mechanisms can be compared in different

environments.

Fatigue crack growth in unidirectional graphite/epoxy in air is accompanied by bridging of the crack tip by individual fibers. Fiber-bridging increases the fracture surface area and tends to hold the crack together, increasing the fracture resistance  $G_R$  of the material. The primary effect of seawater is to weaken the fiber/matrix interface bond, causing an increase in the amount of fiber bridging that was observed. Crack growth rates in seawater were a factor of 5 lower than in air, and dropped immediately upon exposure to seawater. This slowdown was initially attributed to plasticization of the matrix, but simple comparisons of crack growth rates with typical diffusion rates indicate that micro-scale fiber bridging must be a major factor.

Exposure to seawater alone, without applied loading, also increases the Mode I fracture resistance of this material. This effect is completely reversible upon drying. The increase in fracture resistance was thought to be caused largely by plasticization of the matrix material at the crack tip. However, the results of the crack-growth-rate experiments suggest that micro-scale fiber bridging plays a significant role.

TABLE 4.1. ENVIRONMENTAL CONDITIONING TEST MATRIX  
(Number of Data Points)

Test Condition	Environmental Loading Conditions					
	30-Day Fatigue		60-Day Static		No-Load	
	Air	Seawater	Air	Seawater	Air	Seawater
As-conditioned	7	7	4	4	55	4
+ 30-day Relax or + 10-day Dry	7	6	---	4	---	---
	---	3	4*	4	4	4

\* After conditioning plus 30-day relaxation period plus 10-day drying period. Other specimens received either the relaxation or the drying after the initial conditioning, but not both.

TABLE 4.2. EFFECT OF ENVIRONMENT ON MODE I FRACTURE  
RESISTANCE,  $G_R$  (J/m<sup>2</sup>)

Test Condition	Environmental Conditioning					
	30-Day Fatigue		60-Day Static		No-Load	
	Air mean (dev)	Seawater mean (dev)	Air mean (dev)	Seawater mean (dev)	Air mean (dev)	Seawater mean (dev)
As-conditioned	289 (24)	376 (26)	208 (22)	287 (36)	148 (16)	251 (21)
+ 30-day Relax	279 (14)	352 (30)	---	323 (48)	---	---
+ 10-day Dry	---	251 (17)	140 (15)	258 (31)	120 (11)	111 (11)

TABLE 4.3. EFFECT OF MOISTURE ON MODE I FRACTURE RESISTANCE,  $G_R$ , FROM DCB TESTING (J/m<sup>2</sup>)

Reference	Material	Dry $G_R$	Wet $G_R$	Change, %
Garg & Ishai, '85	T300/934	103	129	+25
Russell & Street, '85	AS/3501	175	200	+15
Wilkins, '81	AS/3501	130	168	+29
Present Data	AS/3501	120	250	+100

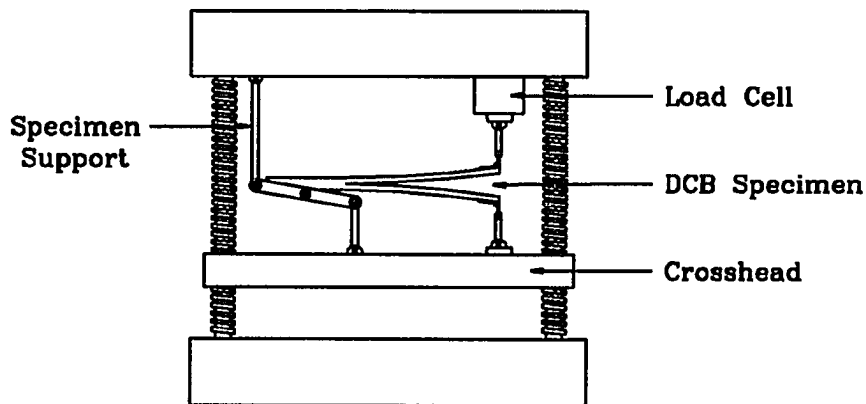


Figure 4.1. Constant-extension-rate tensile tester used to determine the fracture resistance of the double-cantilever-beam (DCB) test specimens.

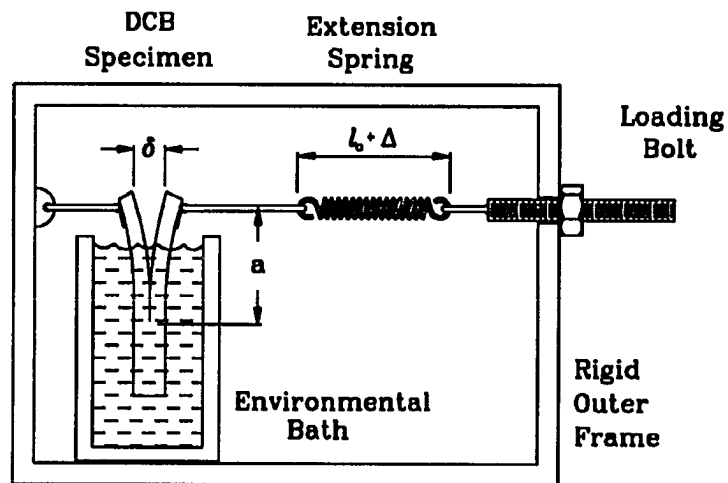


Figure 4.2. A compliant load-frame used for static loading of double-cantilever-beam specimens during environmental exposure. Fatigue experiments were performed using similar load-frames by cyclic displacement of the loading bolt.

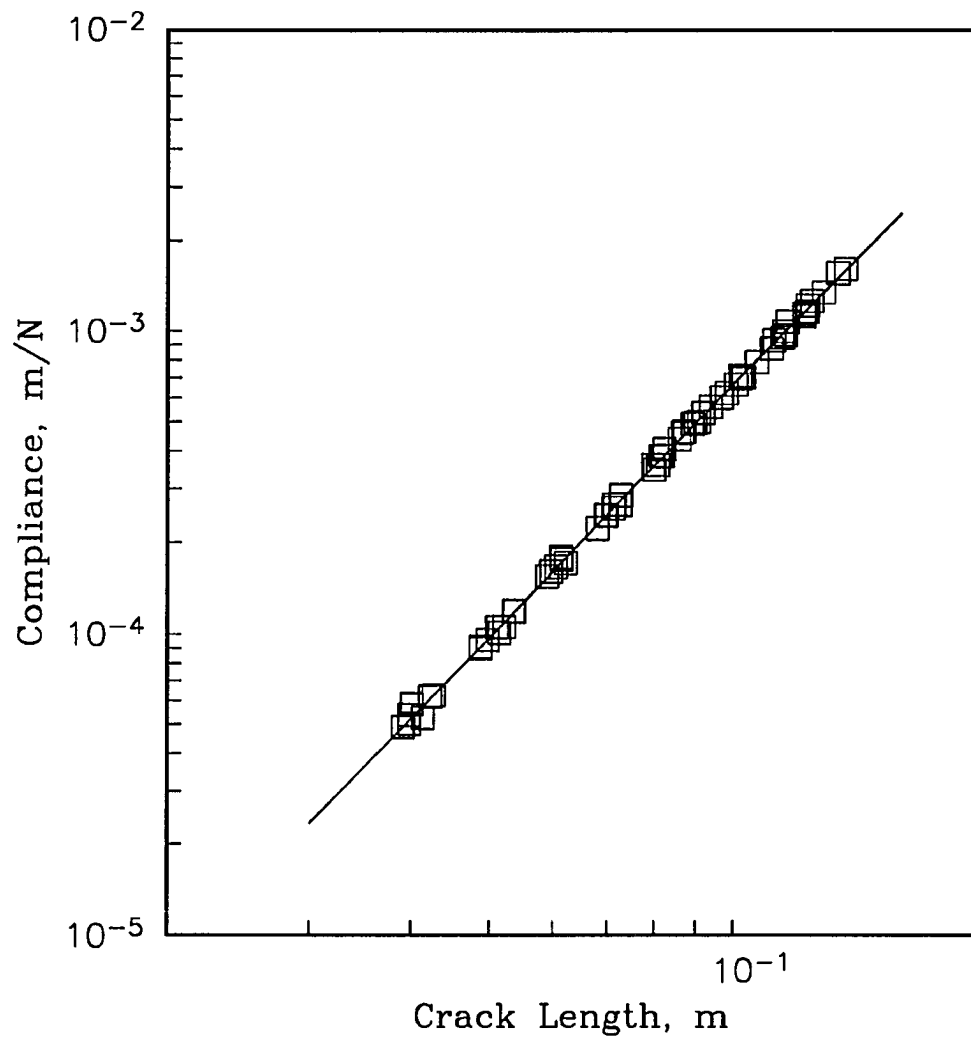


Figure 4.3. Compliance data of DCB specimens cut from as-received AS4/3501 laminates. The straight-line curve-fit parameters were used to calculate the applied strain-energy release rate,  $G$ .

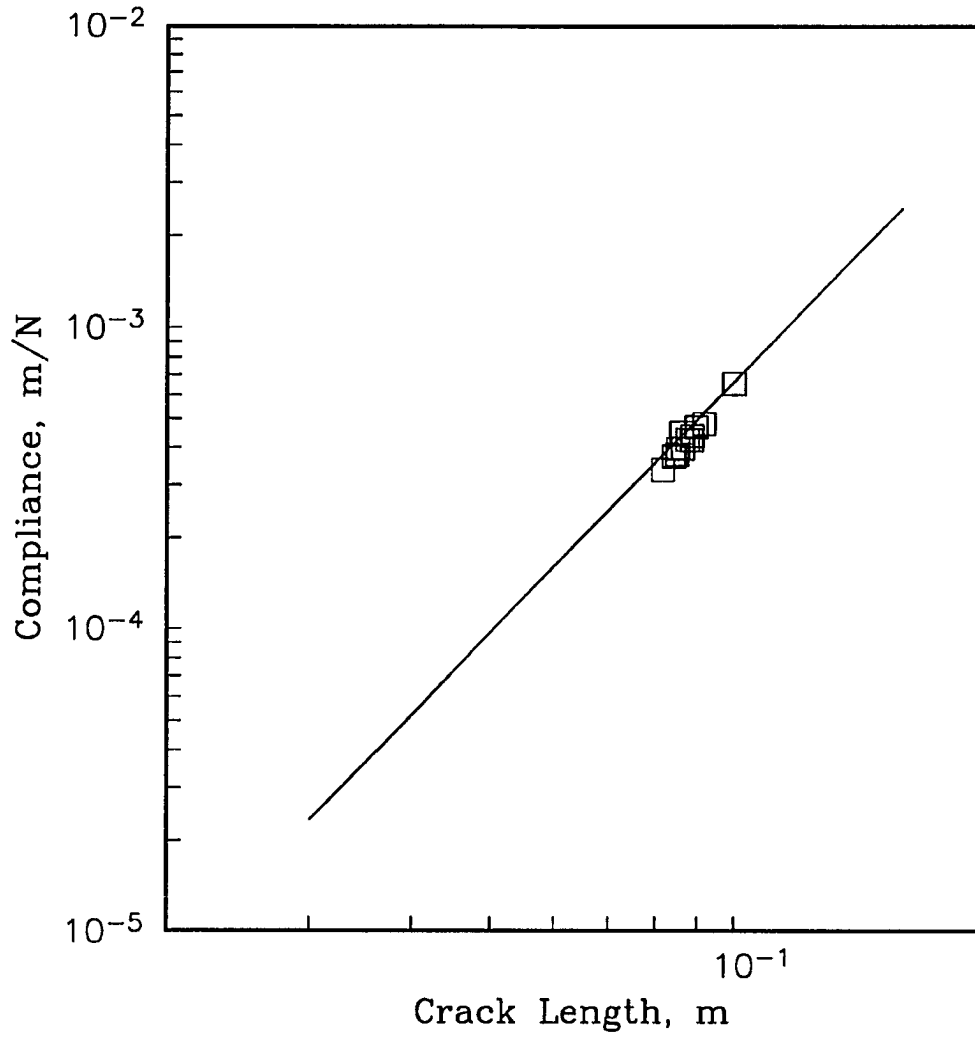


Figure 4.4. Compliance data of seawater-fatigued DCB specimens. The decrease observed compared with as-received data (straight line) is attributed to fiber bridging of the crack tip.

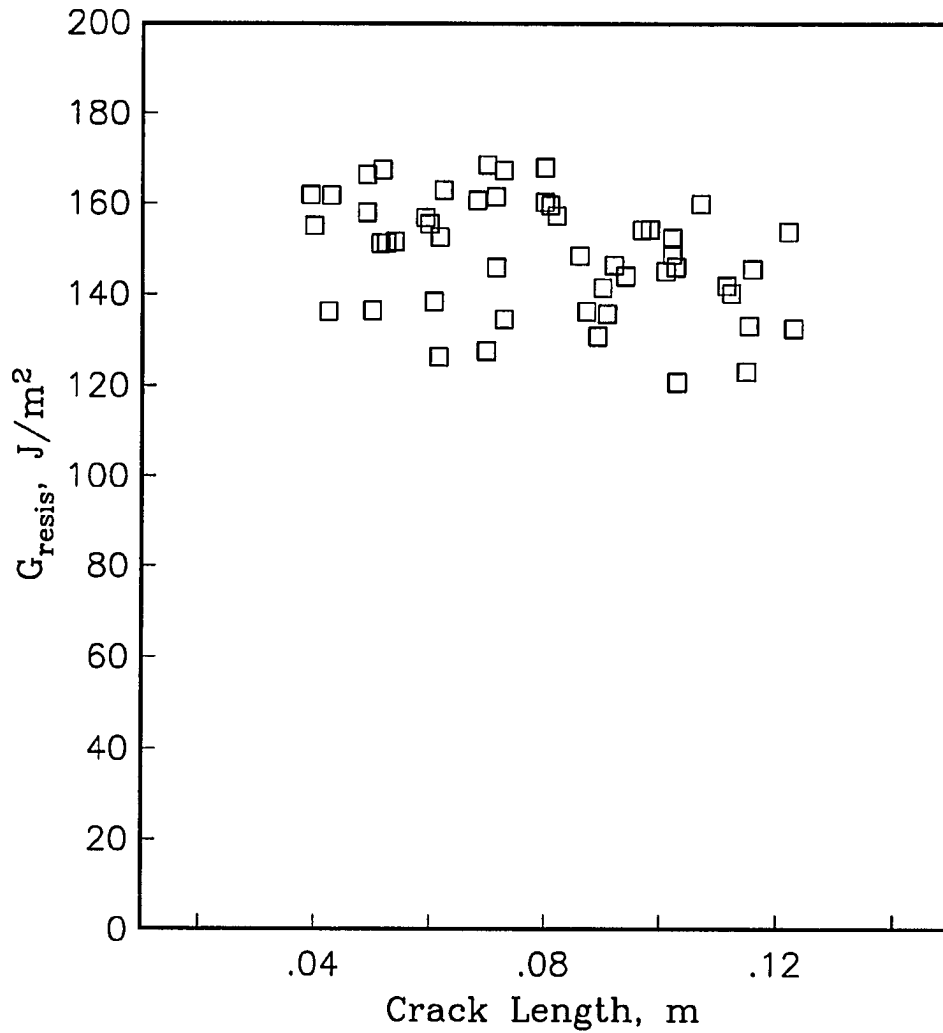


Figure 4.5. Fracture resistance as a function of crack length for the as-received material. Data scatter was significant, and no definite trend could be determined.



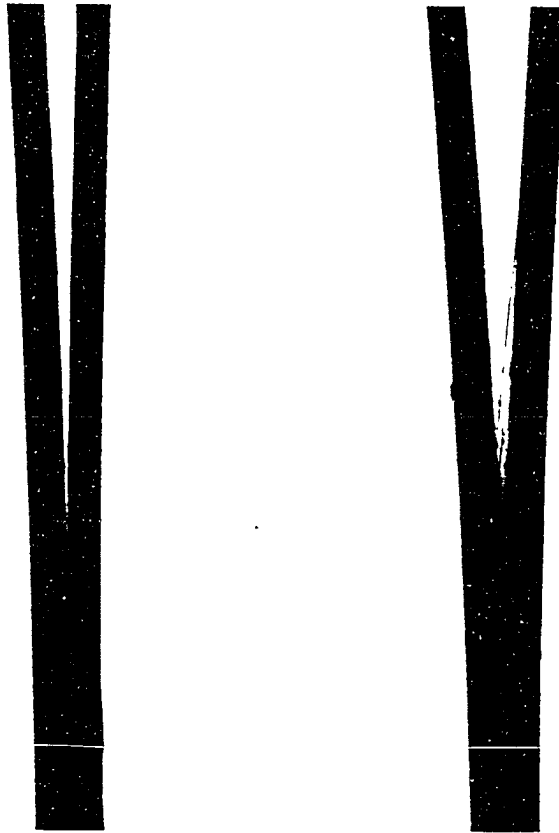


Figure 4.6. Double-cantilever-beam specimens which show the extensive crack-tip bridging which occurred in samples fatigued in seawater (right photo). The specimen on the left is a control specimen which was not fatigued.

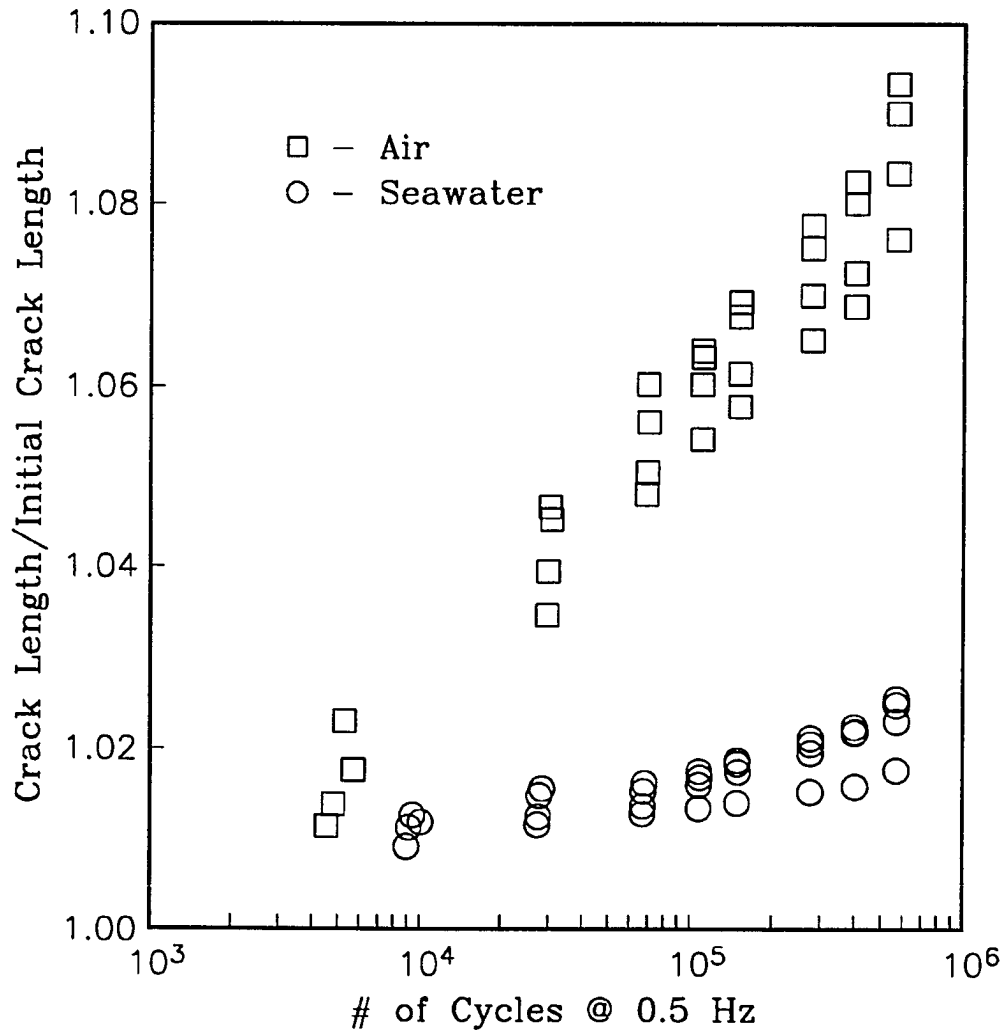


Figure 4.7. Total crack growth (normalized wrt initial crack length) during fatigue loading. Crack growth was much greater in air than in seawater.

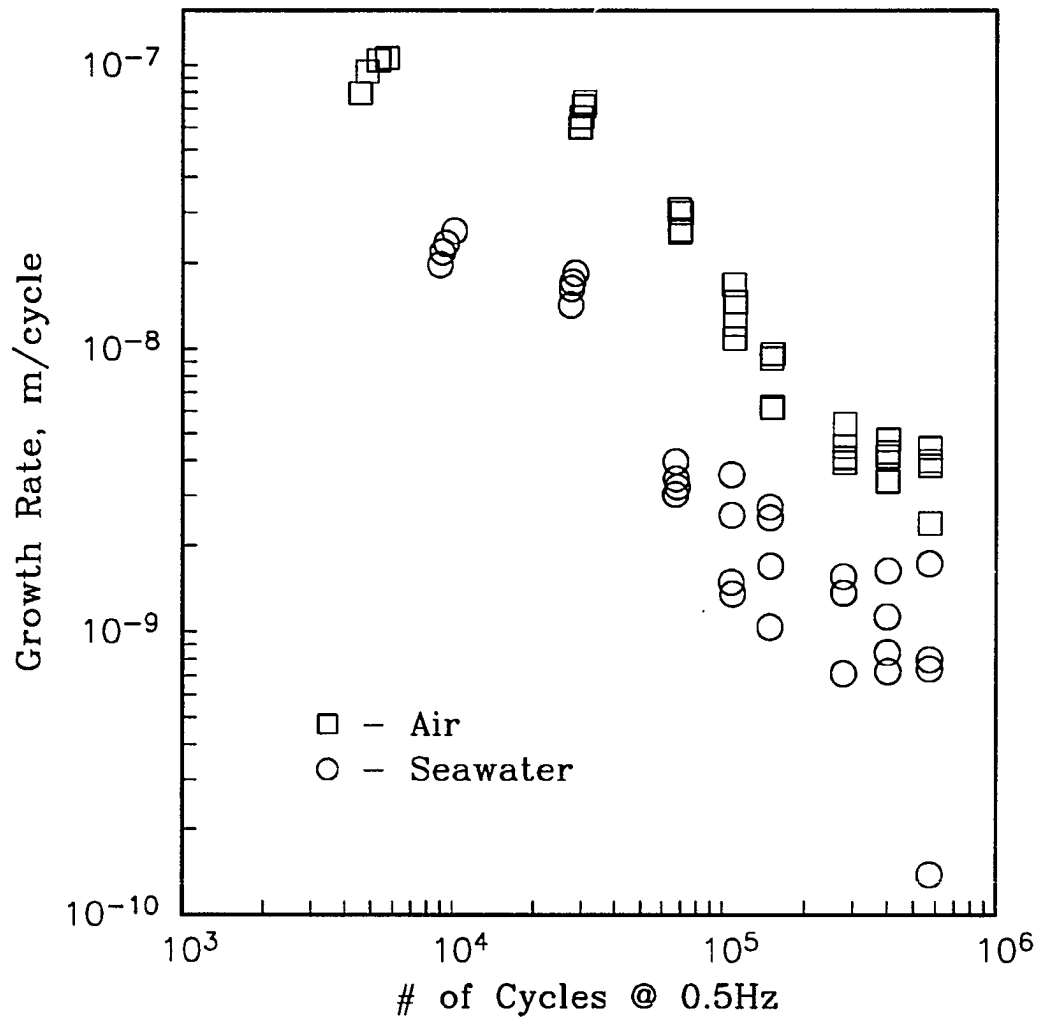


Figure 4.8. Crack growth rates in air and in seawater dropped steadily during the test. Growth rates in seawater dropped immediately to a level more than 5 times lower than growth rates in air.

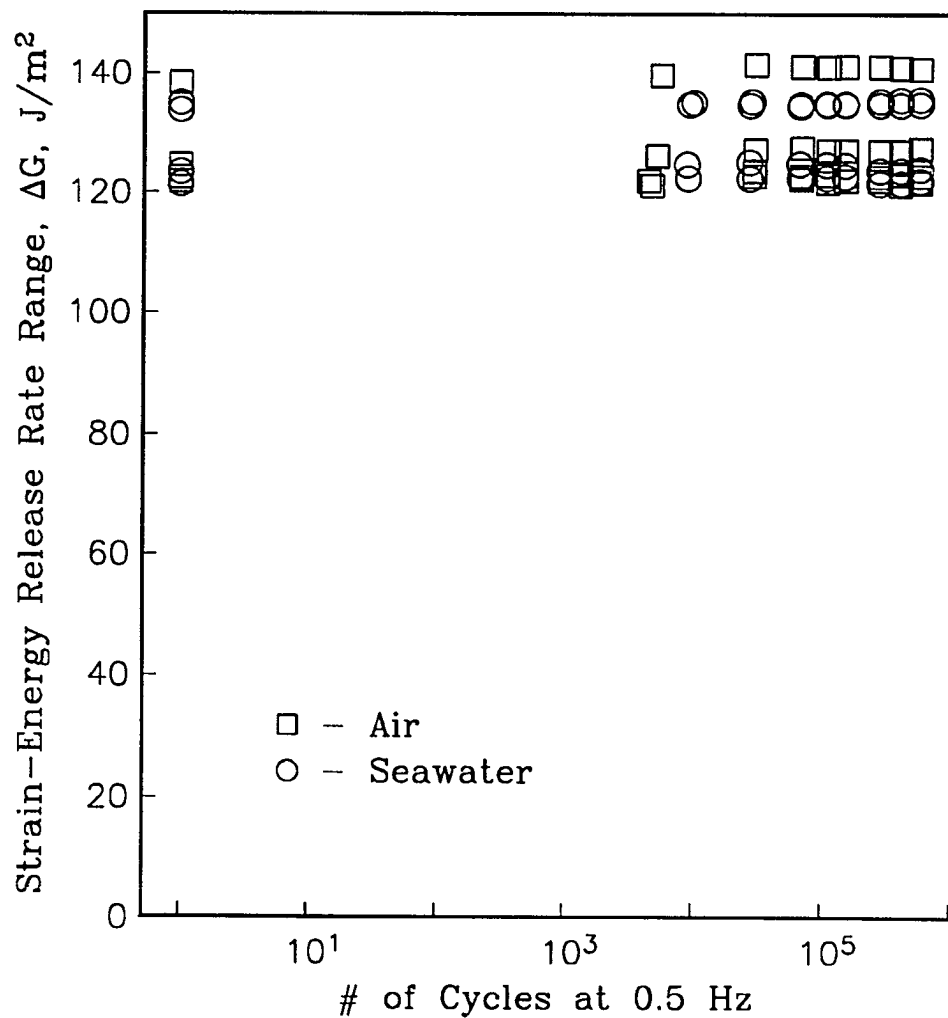


Figure 4.9. Energy applied to the crack tip during the crack growth experiments. The calculated value of  $\Delta G$  remains constant only if compliance changes such as those of Figure 4.4 are neglected.

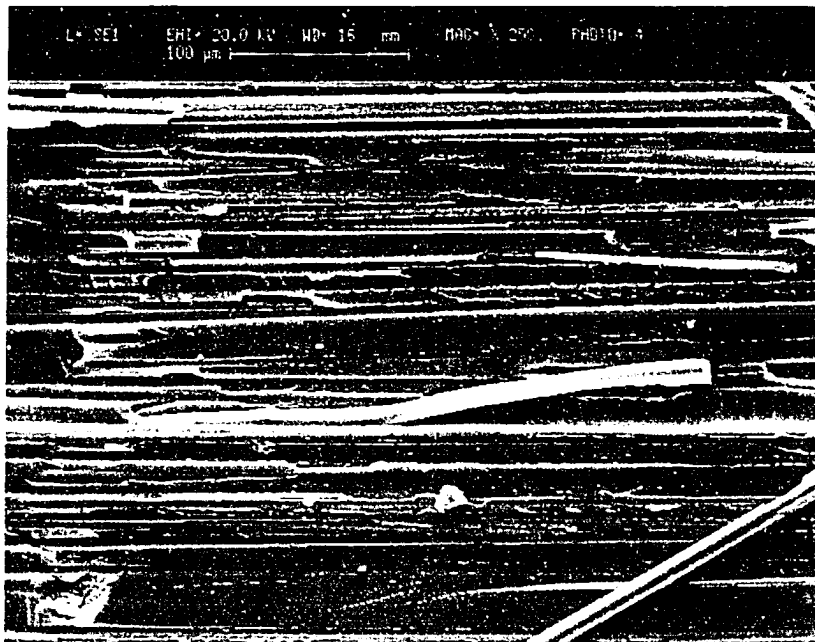


Figure 4.10. Scanning electron microscope (SEM) micrograph of a Mode I fracture surface in graphite/epoxy, which shows a partially detached fiber.



Figure 4.11. SEM micrograph of the transition from static fracture to fatigue crack growth. Crack growth was accompanied by fatigue markings perpendicular to the fiber surfaces. Failure seemed to follow the fiber/matrix interface during fatigue growth, unlike static fracture. Crack growth is from top to bottom in this photo.

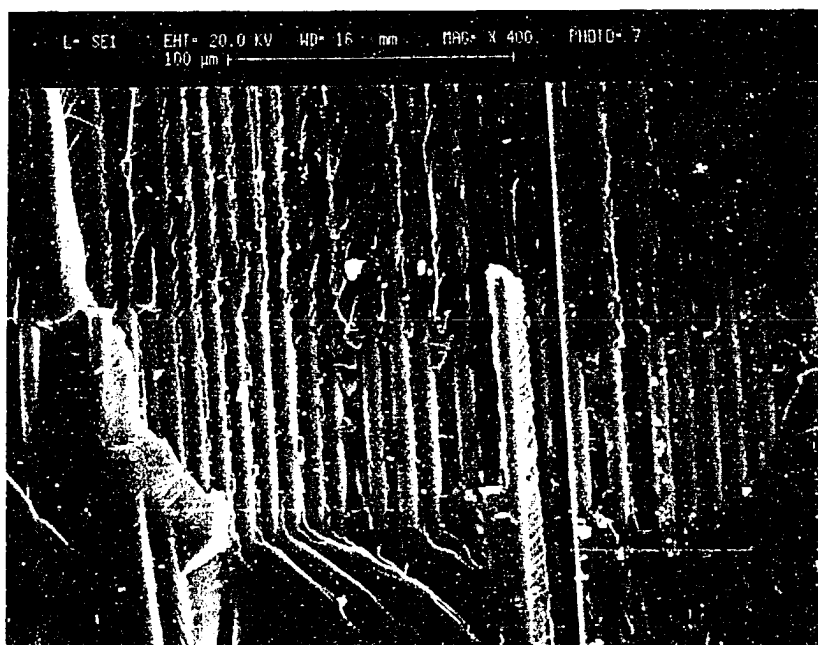


Figure 4.12. SEM micrograph of the transition from fatigue crack growth to static fracture. In most areas the transition was similar to that shown in Fig. 4.11, except in reverse. Crack growth is from top to bottom in this photo.

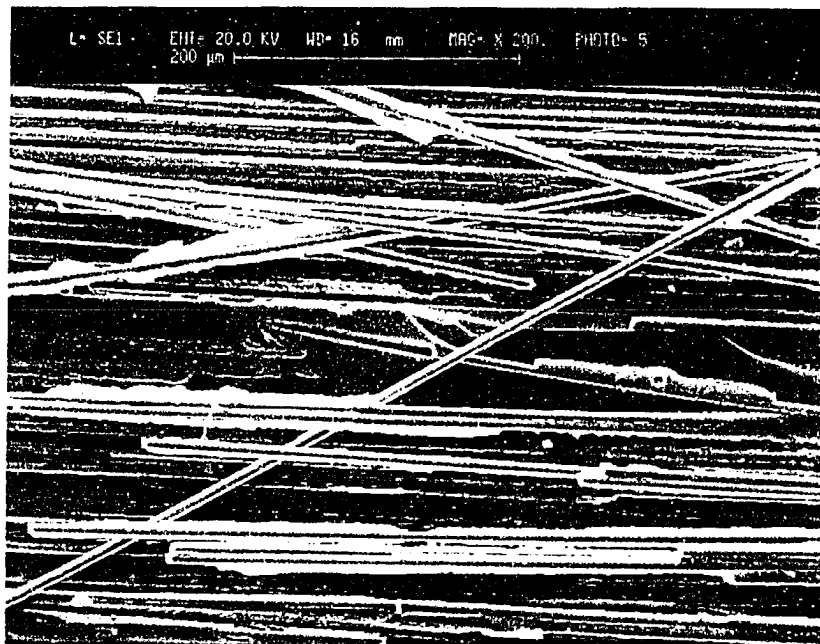


Figure 4.13. A large number of fibers were partially debonded from the fracture surface behind the crack tip in specimens fatigued in seawater. This is further evidence of extensive fiber bridging during the experiment. Crack growth is from right to left in this photo.





Figure 4.14. At the tip of the crack in specimens fatigued in seawater, Mode II fracture markings (hackles) were extensive. These markings are caused by pull-out of bridged fibers during fracture tests at the end of the fatigue experiment.

## **V ANODIC POLARIZATION (STRAY-CURRENT) DAMAGE**

### **5.1. INTRODUCTION**

The conductive nature of graphite coupled with the presence of a low-resistivity electrolyte (seawater) can cause electrochemical reactions to occur at the surface of a graphite-fiber-reinforced composite. For example, electrical current flowing out of the composite into the electrolyte could cause inadvertent "stray current" damage. For this case, from the standpoint of electrochemical corrosion, graphite should behave like a metal. Metals oxidize and corrode when a current passes out of the material (an anodic current). Thus there is good reason to expect that similar damage mechanisms will be observed when such currents are passed by the graphite fibers, i.e. fiber dissolution under anodic currents. Anodic dissolution of the load-bearing graphite fibers would, of course, have catastrophic results. The purpose of this study is thus to investigate the possibility of anodic polarization (stray-current) damage in graphite/epoxy composite materials.

### **5.2. BACKGROUND**

#### **5.2.1. Anodic Polarization (Stray Current Corrosion)**

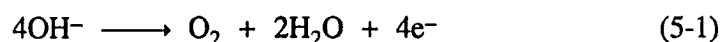
When current in an electrical system flows along a path other than the one originally intended, unanticipated corrosion damage typically results. This is referred to as "stray-current" damage, and is often seen in underground metal piping networks near metropolitan electric rail systems. Current used to power the rail system inadvertently passes into the piping system where a path of lesser resistance occurs. The point of exit of this "stray" current is where unexpected corrosion damage takes place (Uhlig and Revie, 1985).

Stray-current corrosion of graphite/epoxy is unlikely to occur in practice. Graphite is somewhat less conductive than metals and so would tend not to be the path of least resistance in a stray-current situation. However, millions of dollars are spent each year repairing damage caused by unanticipated stray-current corrosion, so the possibility of damage in graphite-reinforced systems should not be ignored.

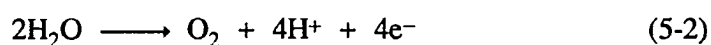
### 5.2.2. Oxygen Evolution on Carbon and Graphite

The electrochemical properties of graphite have been the subject of several exhaustive reviews, most notably by Randin (1974) and more recently by Kinoshita (1988). A major conference (Yeager, 1984) has also been devoted to this subject. Sloan and Seymour (1990) have summarized these reviews as they pertain to electrochemical damage mechanisms in graphite.

As the potential of carbon is increased from its rest potential, oxygen can be evolved from hydroxyl ions and from water in the oxygen/water reactions (Uhlig and Revie, 1985),

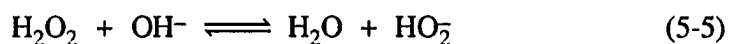
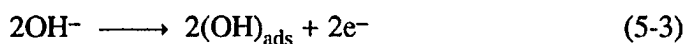


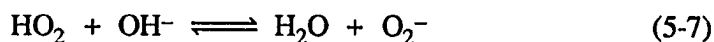
for alkaline solutions, and



for neutral/acidic solutions.

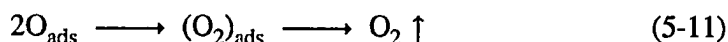
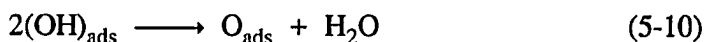
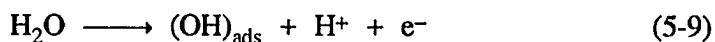
Several mechanisms have been suggested for oxygen evolution from hydroxyl ions on graphite, and all involve peroxide intermediates, e.g. (Randin, p. 53)





The  $\text{O}_2$  which evolves originates in the peroxide, and the evolution mechanism does not involve breaking the O-O bond (Kinoshita, p. 362)

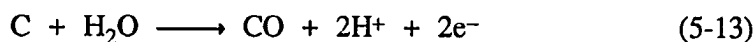
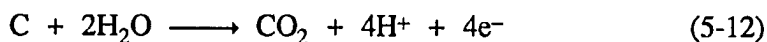
For oxygen evolving directly from water, the proposed mechanism involves adsorption of atomic oxygen at the anode surface, i.e. (Kinoshita, p. 369)



with reaction (5-10) as the slow step.

### 5.2.3. Oxidation of Carbon/Graphite

The principal chemical equations describing the corrosion of graphite in aqueous solutions are given by Pourbaix (1974),

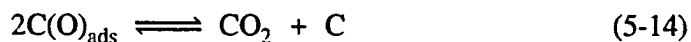


These reactions are energetically favorable, and they predict that carbon should dissolve in water under most conditions. However, the high overpotentials (i.e. activation energies) for these reactions make carbon relatively inert in natural waters at normal temperatures and pressures.

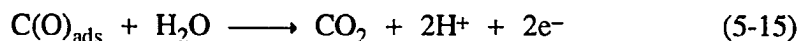
Experimental observations of anodic corrosion in aqueous solutions suggest that the corrosion of graphite is a result of interaction with evolved species (Randin, p. 52). In alkaline electrolytes where oxygen evolves from hydroxyl ions, corrosion of carbon anodes is not observed, whereas corrosion is rapid in neutral/acidic solutions where oxygen evolves from water. In general, rapid degradation of carbon anodes has been associated with potentials near or above the oxygen evolution

potential of reaction (5-2). Graphite anodes degrade at similar potentials, but less actively because the graphite is more ordered and has fewer edge-planes to be attacked.

These experimental observations can be explained by the mechanisms of oxygen evolution described previously, coupled with the nature of the adsorbed species in each case. The evolution of oxygen from hydroxyl ions occurs with the adsorption of molecular oxygen, i.e.  $O_2$ . This molecule is not reactive with carbon, and the evolved oxygen does not corrode the anode surface. However, the evolution of oxygen from water involves the adsorption of atomic oxygen,  $O_{ads}$ . Atomic oxygen is highly reactive and can cause direct combustion of the graphite surface, either by a chemical pathway,

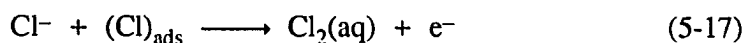


or an electrochemical pathway,

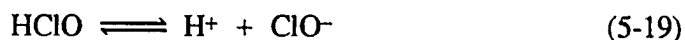
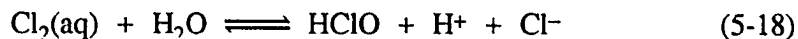


(Randin, p. 53).

Other reactions can also degrade a graphite anode. For example, in solutions containing chloride (e.g. seawater), formation of chlorine ( $Cl_2$ ) can occur at the anode, i.e.



with formation of active chlorine ( $ClO^-$ )



Active chlorine can then chemically attack the carbon surface (Kinoshita, p. 338). However, active chlorine is much less aggressive than atomic oxygen, and chlorine evolution occurs at the expense of oxygen evolution. Thus corrosion rates of carbon

anodes are highest in solutions of relatively low salinity such as seawater, and are dominated by oxidation from evolved oxygen.

The oxidation of carbon and graphite produces  $\text{CO}_2$  and  $\text{CO}$ , along with a surface oxide film and a dark soluble organic corrosion product thought to be a derivative of humic acid (Randin, Kinoshita). Of course the relative amounts and compositions of these corrosion products will depend on the environmental parameters such as salinity, temperature, pH, and potential. The concurrent evolution of several gases, formation of surface oxides, and the production of soluble corrosion products make standard electrochemical monitoring techniques inadequate by themselves for determining reaction kinetics. Collection and analysis of corrosion products (gases and solubles) are essential for a complete analysis of the oxidation process in carbon anodes.

### 5.3. EXPERIMENTAL PROCEDURE

Graphite/epoxy electrodes were cut from 30-ply unidirectional AS-4/3501-5a laminates and washed in distilled water. Electrode coupons had dimensions 13 x 76 x 3.8 mm, with fibers running in the long dimension. Specimen electrical contact was made by drilling and tapping a hole for a 4-40 screw in one end of the coupon. An alligator clip was used to grip the screw, thus holding the specimen in place and providing electrical connection.

A Pine Instruments scanning potentiostat was used to obtain anodic scans of potential vs. current on graphite/epoxy coupons. The counter electrode was a Corning platinum electrode, and potentials were measured with respect to a saturated calomel reference electrode (SCE). Initial potential scans were made from 0 to 900 mV (SCE) and back to 0 mV, repeated 5 times. Scanning rate was 1.0 volts/minute. The electrolyte used was 0.5M NaCl at room temperature.

Anodic polarization experiments to simulate stray-current conditions were conducted up to six weeks using simple potentiostats (Baboian, 1979) as shown in Fig. 5.1. The electrolyte used was 0.5 molar NaCl in 0.5 liter beakers. Initial pH for the solution was approximately 7.0. Current and potential in the circuit were recorded periodically, but no attempt was made to maintain electrolyte conditions. Both specimens (anode and cathode) were inspected daily for evidence of degradation such as matrix cracking. Corrosion of the specimens was typically accompanied by the formation of dark soluble oxidation products, so electrolyte clarity was also monitored (visually) during the test.

At the end of each of the stray-current experiments, coupons were removed from the electrolyte and placed in a drying oven at 100°C for 8 hours to remove absorbed moisture. The exposed ends of selected specimens were then cut away and sputter-coated with a 0.5 nm layer of gold prior to inspection in a scanning electron microscope (SEM). A specimen which had not been polarized was also prepared as a control sample.

#### 5.4. RESULTS AND DISCUSSION

Figure 5.2 shows the results of the anodic potential scans on the graphite/epoxy coupons. The equilibrium potential of the graphite/epoxy is unstable and lies between 0 and 100mV (SCE). Scans between 0 and +900mV begin to show signs of irreversibilities when repeated. This data may be indicative of the formation of a surface oxide film which would contribute a growing IR-drop to the potential scan.

The steady-state corrosion currents observed in the long-term stray-current experiments are plotted as a function of applied potential in Fig. 5.3. The instruments used here were not accurate enough to measure currents near the equilibrium potential, but the data shown in Fig. 5.3 supports the increase in current observed in Fig. 5.2 at potentials between 500 and 600 mV (SCE).

Specimens subjected to long-term anodic polarization in these experiments were observed to swell and crack extensively, and the accompanying electrolyte turned a yellowish brown color. Figure 5.4 shows the conditioning times which passed before visual detection of (1) crack-initiation or (2) electrolyte discoloration by corrosion products. Matrix cracking seems to occur at potentials above about 600mV, which corresponds to the potential of steep current increase shown in Figs. 5.2 and 5.3. Discoloration of the electrolyte was not observed below 900mV. The distinct potential levels identified with the onset of cracking and discoloration suggest that separate damage mechanisms are involved. However, visual monitoring of the electrolyte clarity could not have detected minute amounts of corrosion products, which could have been present at samples conditioned between 600 and 900 mV. The swelling and cracking of all samples oxidized above 600 mV suggests a corrosion reaction, with formation of a corrosion product a likely consequence.

Figures 5.5 and 5.6 are SEM micrographs of control specimens which were not anodically polarized and so show no oxidation damage. The micrographs of Figs. 5.7 and 5.8 are from a specimen polarized to 750 mV (steady-state corrosion current  $\approx 10 \mu\text{A}/\text{cm}^2$ ) for 14 days. Substantial micro-cracking has occurred, but there is no visual indication of fiber dissolution. Figures 5.9 and 5.10 show damage in a specimen polarized to 1900 mV (current  $\approx 1000 \mu\text{A}/\text{cm}^2$ ) for 3 days. This specimen was on the verge of disintegration, and areas of possible fiber dissolution were observed. Cracking was most pronounced along the mid-plane of the



specimens. This may have been caused by better electrical contact from the screw at the specimen mid-plane, or it may have been the result of residual stresses formed in laminate fabrication.

The 550-600 mV potential determined for initiation of damage can be identified with the potential for oxygen evolution of equation (5-2) from the Nernst equation, (Uhlig and Revie, 1985)

$$E = E_o + \left(\frac{RT}{nF}\right) \cdot \ln(K) \quad (5-20)$$

or, at pH=7, 25°C, and  $pO_2=0.2$ ,

$$E = 1.229 + (0.0592/4)\log(0.2) - 0.0592(7)$$

$$E = 0.80 \text{ V (NHE) or } 0.56 \text{ V (SCE)}$$

Thus oxygen evolved at the anode is the most likely agent responsible for degradation of the graphite/epoxy anode.

The oxidation of graphite by anodic polarization has been widely studied, primarily to find ways of extending the service lives of graphite anodes. In addition, oxidation of graphite fibers has been used in industry as a means of altering the strength of graphite-fiber reinforced composites (Proctor and Sherwood, 1983). Neffe (1987) has suggested that anodic oxidation be used as a quality control check for reinforcing fibers.

The organic matrix may also be oxidized by anodic reaction products. For example, the atomic oxygen evolved at a graphite-fiber anode might directly attack the polymer carbon chain or the interface bonds between the graphite and the matrix. The mechanisms and severity of oxidation damage in polymers are well-established but have not been considered in this study.

## 5.5. CONCLUSIONS

The quasi-metallic behavior of graphite-reinforced plastics suggest that electrochemical damage (i.e. corrosion) may result when these materials are used with metals in the marine environment. The experiments reported here show that anodic polarization (stray-current corrosion) can significantly damage graphite-reinforced plastics, even at current levels as low as  $1 \mu\text{A}/\text{cm}^2$ . Atomic oxygen which forms as an intermediate in the oxygen evolution reaction is the most likely agent for attack of the graphite fibers.

Graphite-fiber-reinforced plastics should be electrically isolated from metals (e.g. fasteners and fittings) when used in seawater service. Fiberglass or organic-fiber plies and sealer coatings are used extensively in the aerospace industry and would be apply equally to marine applications. However, few insulating materials remain intact for more than a few years. For long term protection a program of periodic corrosion-potential monitoring would be advisable. These precautions would largely preclude electrochemical damage such as the stray-current corrosion discussed here.

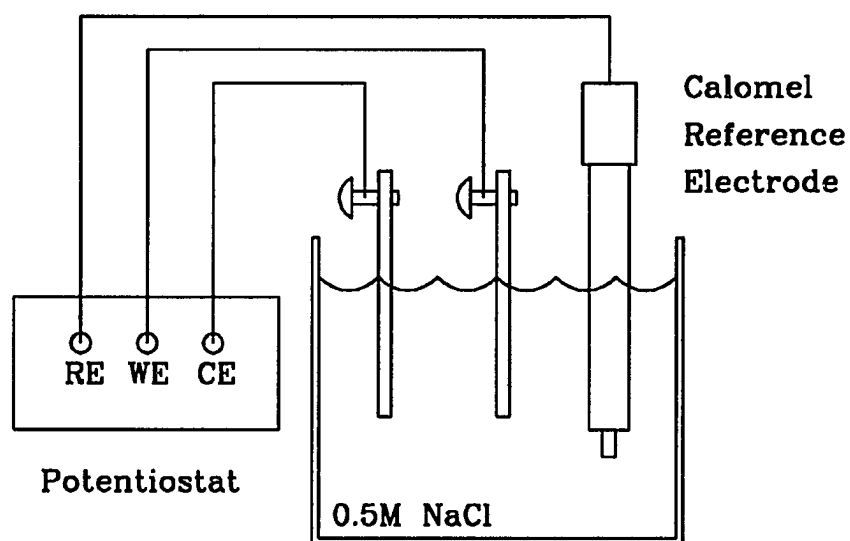


**Figure 5.1.** Anodic polarization experiment using simple potentiostat circuit. Graphite/epoxy coupons were used both as anode and as cathode.

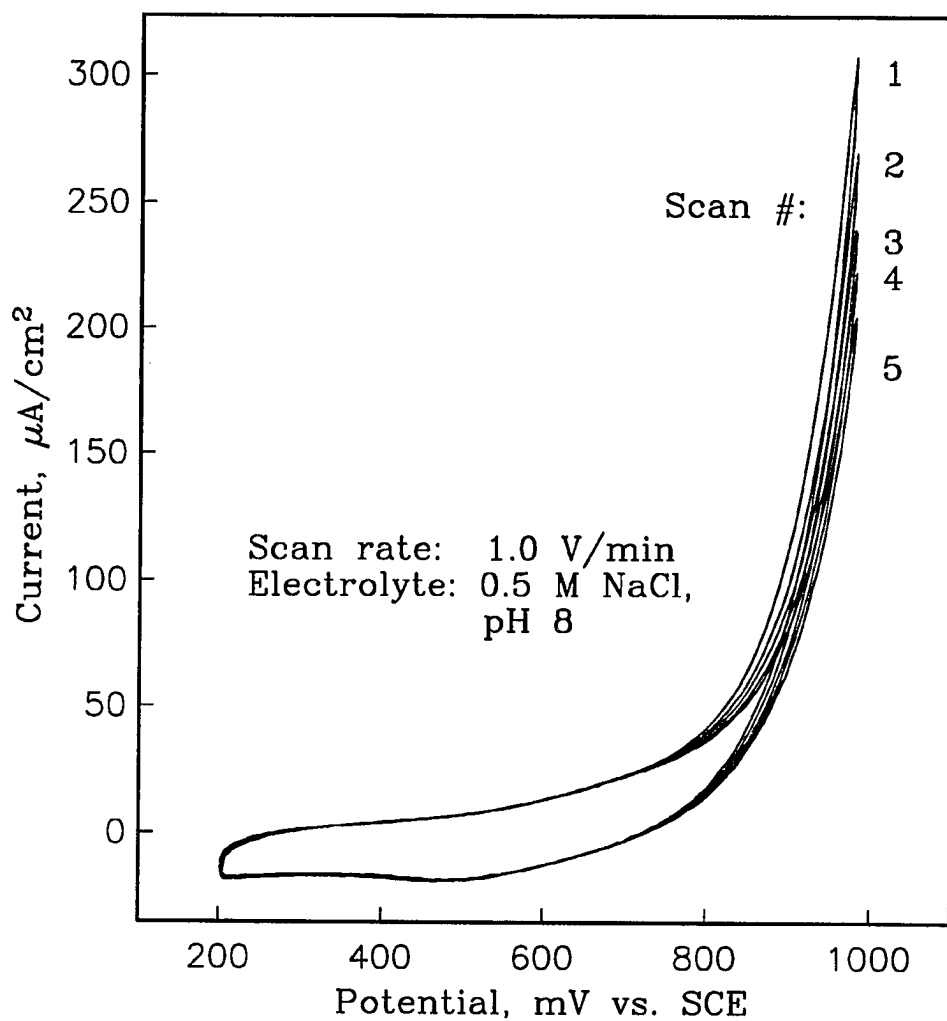


Figure 5.2. Anodic polarization scans on AS4/3501 graphite/epoxy. The decrease in the anodic current from the first scan to the fifth scan suggests the formation of a surface corrosion film.

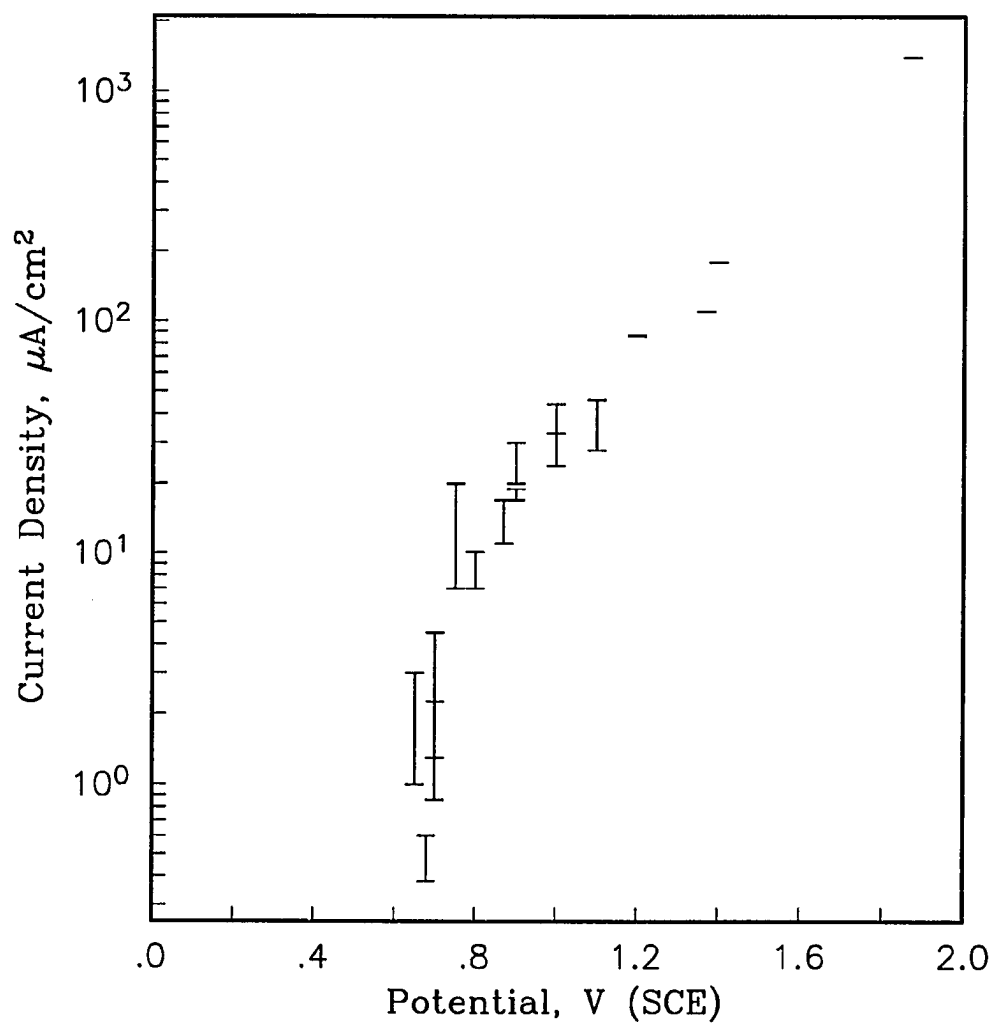


Figure 5.3. Steady-state current as a function of applied potential in long-term anodic polarization experiments. Current rises rapidly above 600 mV.

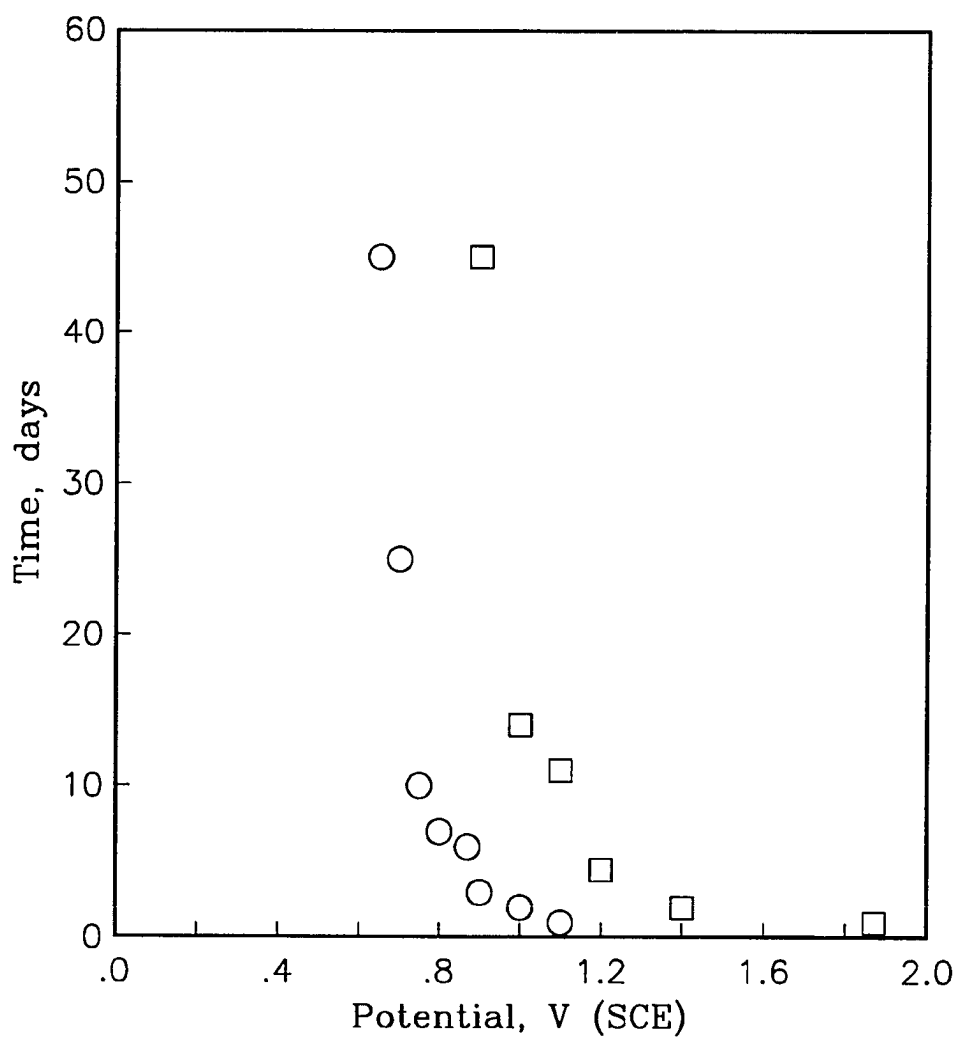


Figure 5.4. Time elapsed before the observation of matrix cracking (○) and electrolyte discoloration (□) during anodic polarization of graphite/epoxy.



Figure 5.5. Scanning electron microscope (SEM) micrograph of the surface of a graphite/epoxy specimen. This sample was not anodically polarized, and this figure should be used as a control for comparison with Figs. 5.7 and 5.9.

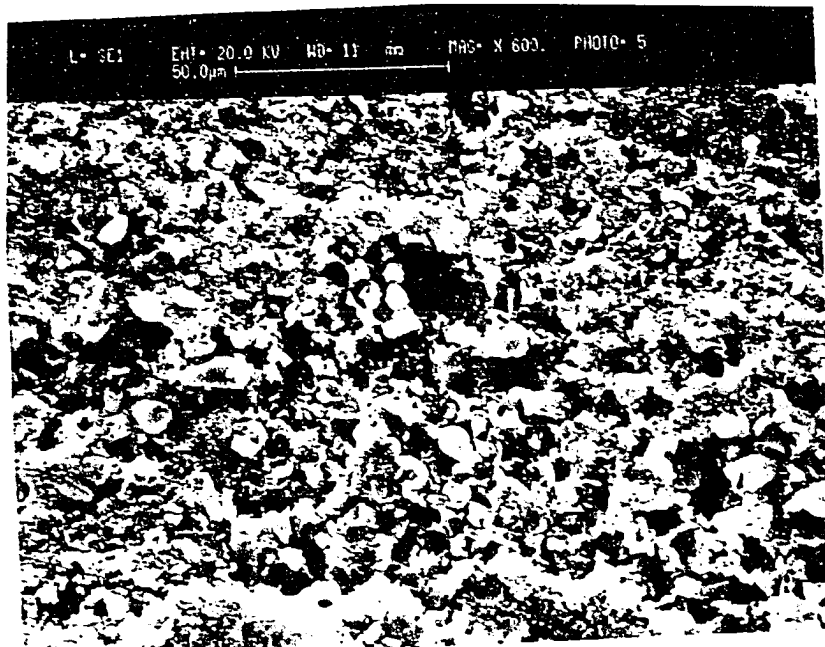


Figure 5.6. Close-up view of the control specimen of Fig. 5.5.



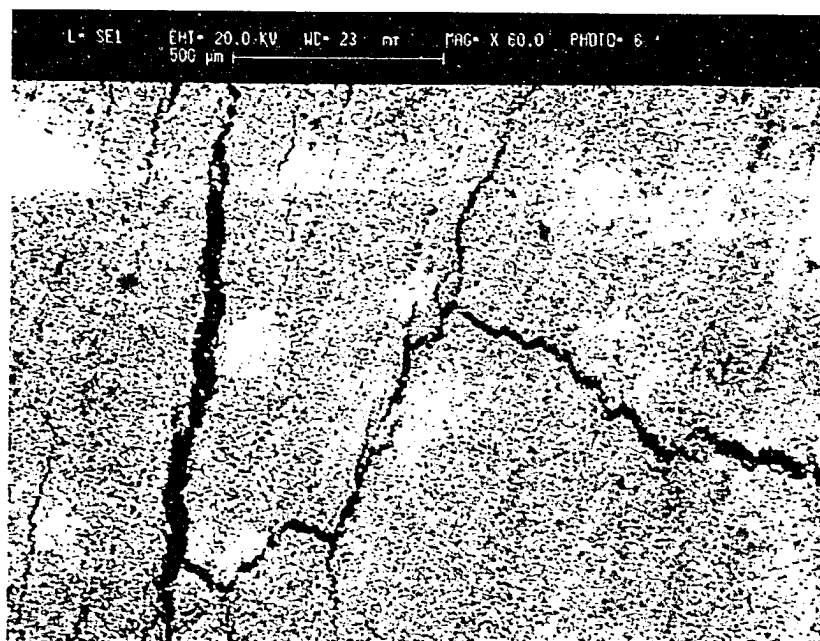


Figure 5.7. SEM micrograph of the surface of an anodically polarized graphite/epoxy specimen. This sample was held at a potential of 750 mV (SCE) for 14 days. The steady-state current in the sample was approximately 10 microamperes per square centimeter.

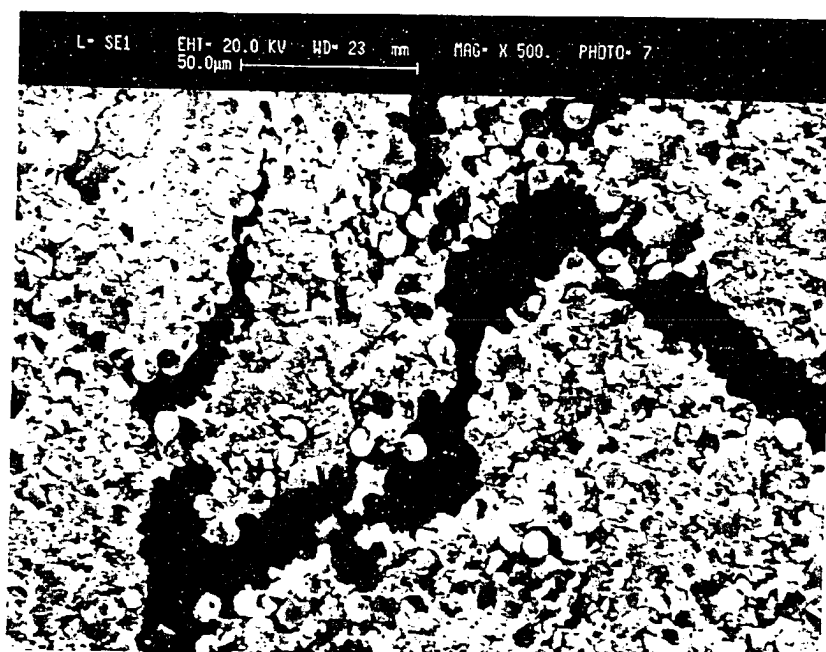


Figure 5.8. Close-up view of the anodically polarized specimen shown in Fig. 5.7. Extensive and random cracking occurs throughout the specimen. There is no evidence of fiber dissolution.

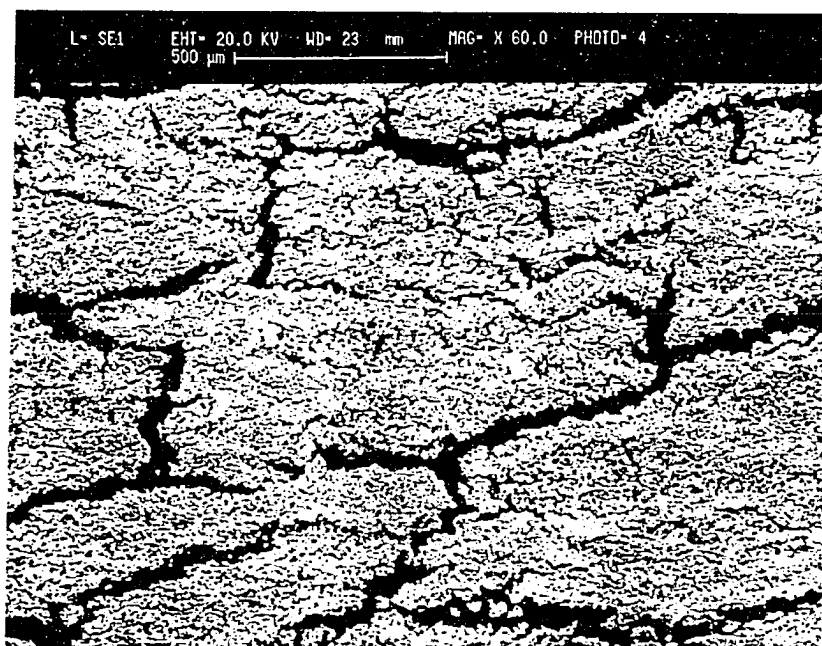


Figure 5.9. SEM micrograph of the surface of an anodically polarized graphite/epoxy specimen. This sample was held at a potential of 1900 mV (SCE) for 3 days. The steady-state current in the sample was approximately 1000 microamperes per square centimeter.

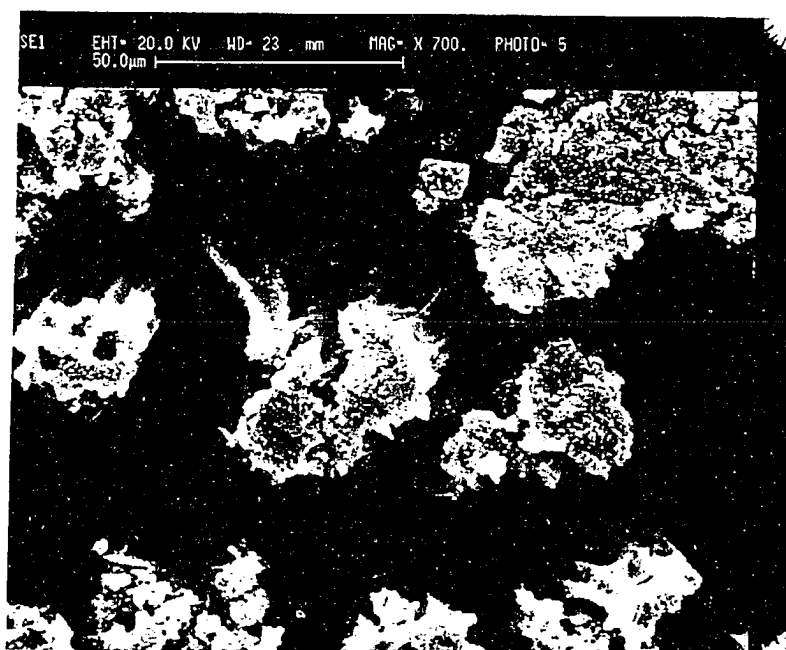


Figure 5.10. Close-up view of the anodically polarized specimen shown in Fig. 5.9. The specimen has nearly disintegrated, and areas like the one shown here suggest that fiber dissolution has occurred.

## **VI CATHODIC POLARIZATION (GALVANIC COUPLING) DAMAGE**

### **6.1. INTRODUCTION**

Graphite behaves as a metal in an electrochemical sense, and has a very noble rest potential. In other words, graphite lies very high in the galvanic series, and will be cathodic to most structural metals. Metallic materials tend to debond from polymers and adhesives when used as cathodes in an electrochemical cell. Thus there is good reason to expect that similar damage will be observed in graphite/epoxy cathodes, i.e. graphite fibers debonding from the polymer matrix. Cathodic debonding of the fibers from the matrix would of course affect mechanical properties such as stiffness and shear strength. Because the conductive graphite fibers continue into the interior of the composite, any substantial debonding reaction would also dramatically increase the surface area of the matrix available for moisture absorption. The purpose of this study is thus to investigate the possibility of cathodic polarization (galvanic coupling) damage in graphite/epoxy composite materials.

### **6.2. BACKGROUND**

#### **6.2.1. Galvanic Coupling Damage in Graphite-Fiber-Reinforced Plastics**

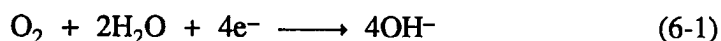
Galvanic coupling of metals to graphite-reinforced plastics is known to increase corrosion rates in structural alloys, e.g. aluminum or stainless steel. However, the effect on the graphite/polymer cathode is more subtle. A recent German study concluded that the high pH generated at the graphite cathode damaged the composite matrix material, as reported by Donaldson (1989). Tucker (1989, 1990) has observed damage to graphite-reinforced polyesters galvanically coupled to steel. The exact damage mechanisms remain unclear. The shift in pH

accompanied by the cathodic reaction (oxygen reduction) could create conditions sufficient for hydrolysis of polymer linkages to occur. A similar example is "wood-electrolysis", i.e. the decay of fiberglass and wooden boat hulls near metal fittings being cathodically protected (Strasberg et al, 1982).

### 6.2.2. Cathodic Reactions on Carbon and Graphite

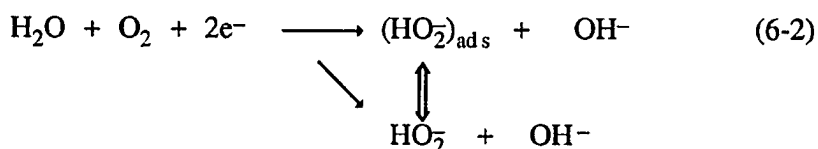
The electrochemical properties of graphite have been the subject of several exhaustive reviews, most notably by Randin (1974) and more recently by Kinoshita (1988). A major conference (Yeager, 1984) has also been devoted to this subject. A summary of these reviews regarding electrochemical damage in graphite has been presented previously (Sloan and Seymour, 1990).

The overall oxygen reduction reaction at a cathode in natural waters is given by (Uhlig and Revie, 1985)

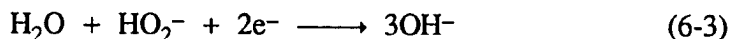


There are two accepted pathways for the reduction of oxygen at a cathode (Yeager, 1984): (1) the peroxide 2-electron pathway, and (2) the direct 4-electron pathway.

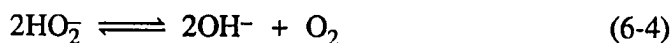
The peroxide pathway goes as



followed either by electro-reduction of peroxide,



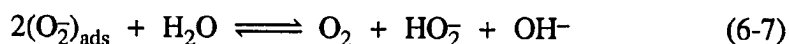
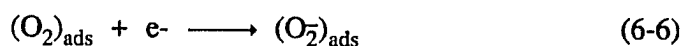
or catalytic decomposition,



The direct 4-electron pathway (6-1) occurs in a similar process. Here the peroxide which forms as an intermediate remains adsorbed until reduced and never

enters into solution. The two pathways can, in general, occur in parallel, and the amount of peroxide introduced into solution depends on the electrode and electrolyte conditions.

Experimental evidence supports the peroxide pathway for  $O_2$  reduction on graphite with adsorption of molecular oxygen, i.e. (Kinoshita, p. 362)

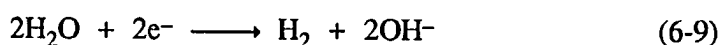


Rotating disk studies show that the reaction is first order in oxygen, and the slope of the  $1/i_L$  vs  $\omega^{-1/2}$  curve corresponds to the Levich equation for a 2-electron process (Randin, p. 58). Furthermore,  $^{18}O$  isotope tagging has shown that oxygen in the adsorbed peroxide molecule originates from gaseous oxygen (Yeager, 1984). This is analogous to the mechanism discussed in Chapter 5 for oxygen evolution from hydroxide. Tafel slope evidence suggests that equation (6-6) is the slow or rate-determining step in the reaction.

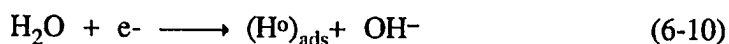
At sufficiently negative potentials, hydrogen will be evolved at the cathode according to the reactions (Uhlig and Revie, 1985)



for acid solutions, and



for neutral/alkaline solutions. For discharge from water, the commonly assumed reaction mechanisms are discharge (DeLucia, 1988)



followed by recombination



and/or desorption



Tafel slope evidence supports the mechanism of fast discharge, with desorption the slow (rate-determining) step, which agrees with data from metals.

### 6.2.3. Graphite Degradation by Excess Peroxide

If the breakdown of peroxide in the 2-electron  $\text{O}_2$  reduction reaction of equations (6-2) to (6-4) occurs rapidly enough, the overall reaction is indistinguishable from the 4-electron pathway. For carbon and graphite, breakdown of peroxide occurs initially at moderately high rates. However this catalytic activity decreases steadily, eventually resulting in a build-up of peroxide, in porous regions of the cathode as well as in any electrolyte that is isolated from the bulk. This high peroxide concentration can produce  $\text{O}_2\cdot$  and  $\text{OH}\cdot$  radicals which will degrade the electrode surface (Yeager, 1984). For graphite fibers, possible regions of isolated electrolyte include porous areas between graphite fibrils and pre-existing flaws in the fiber structure.

### 6.2.4. Formation of Calcareous Films

The tendency to form calcareous films at the cathode of a corrosion cell is one of the most important properties of seawater in electrochemical studies (see Chapter 2). The generation of hydroxide ions by the oxygen reduction reaction (6-1) raises the pH of the solution at the electrode surface. The pH rise shifts the equilibrium of the  $\text{H}_2\text{CO}_3/\text{HCO}_3^-/\text{CO}_3^{2-}$  system to the right, and  $\text{CaCO}_3$  and  $\text{Mg}(\text{OH})_2$  precipitate to form calcareous deposits at the cathode (Hartt et al, 1984). pH values of 9 to 10 have been calculated for normal surfaces with no film formation (Wolfsson and Hartt, 1981). Calcareous film formation and debonding can result in occluded volumes of electrolyte where ion concentrations can exceed those near the



surface of the film. Under-film values of 10 to 10.5 have been calculated where hydrogen is not evolved (Dexter and Lin, 1991). Other ionic species such as perhydroxyl ion may also be concentrated under calcareous films. Calcareous films tend to limit oxygen ( $O_2$ ) diffusion, and thus will also tend to limit perhydroxyl ion ( $HO_2$ ) diffusion.

### 6.3. EXPERIMENTAL PROCEDURE

As part of an earlier experiment investigating the effects of galvanic currents on moisture uptake, sixteen graphite/epoxy coupons were exposed to seawater heated to 40°C while attached to a single Mg rod anode, as shown in Fig. 6.1. The rest potential of the resulting corrosion cell was stable at -1550 mV SCE. Eight similar specimens were soaked under the same conditions with no exposure to magnesium, and eight additional specimens were kept in a desiccator as a control. The details of this experiment are detailed elsewhere, along with the results of moisture uptake and surface film analysis (see Chapter 2).

All specimens were cut from a 26-ply quasi-isotropic T300/934 graphite/epoxy laminate which had fiberglass surface plies. Specimen dimensions were 13 mm wide x 90 mm long x 3.6 mm thick. At the end of the preconditioning period, all of the samples were baked at 200°C on consecutive days to drive out the absorbed moisture.

After the specimens were dried and weighed they were stored in a desiccator. After remaining in storage for several months, each specimen was tested to failure in a 4-point bending mode as shown in Fig. 6.2. This procedure was chosen to ensure failure by shear, as discussed in Chapter 3. Testing was done on a Cortest constant-extension-rate tensile machine with a 5 kN load cell. After being tested to failure in the bending fixture, two specimens from each conditioning group

were split along their fracture surfaces. These surfaces were then examined in the scanning electron microscope (SEM).

## 6.4. RESULTS AND DISCUSSION

### 6.4.1. Experimental Results

The 4-point bending shear strength data are shown in Fig. 6.3, where the maximum computed shear strength data is presented as a Weibull failure distribution. The effect of simple seawater soaking on shear strength was negligible except for a slight increase in the data scatter (i.e. a decrease in the Weibull slope). However, specimens attached to magnesium anodes lost approximately 30 percent of their original strength.

While the strength loss observed after galvanic coupling is substantial, it is primarily a result of the small specimen size. Analysis of the resulting fracture surfaces (discussed below) showed that the observed strength loss was caused by localized corrosion. Delaminated areas extending in from the specimen edges reduced the effective width of the specimens by between 10 and 40%, roughly matching the observed loss of strength.

Two fracture surfaces from each of the three exposure groups were examined and photographed in the SEM. Figure 6.4 shows the fracture surface of a control sample. The "hackle" formations are characteristic of Mode II fracture, as discussed elsewhere (Johannesson and Blikstad, 1985; Smith and Grove, 1987), and were typical of this quasi-isotropic sample. The samples soaked in seawater alone had fracture surfaces similar to the control samples.

Overall the fracture surfaces of the galvanically coupled (corroded) samples had features similar to the control samples. However, semi-circular degraded areas were found along the edges of these samples, similar to that shown in Fig. 6.5.

Within these areas the fracture surfaces showed a significantly different type of damage, as shown in Figs. 6.6 and 6.7. Extensive debonding of the fibers from the matrix can be observed, with fracture of the matrix between the fibers. In the interior of these specimens, outside of the corroded areas, the fracture surfaces were similar to the controls, as shown in Fig. 6.8. The shapes of these regions and their proximity to the edges of the specimens suggest a localized damage mechanism that spreads slowly from the edge. The estimated rate of damage growth observed in these tests is approximately 6-8 millimeters per year. Damage growth in laminates under static or fatigue loading while being galvanically coupled could be much higher. Mechanical and chemical damage mechanisms often act synergistically to accelerate damage in stress-corrosion-cracking and corrosion-fatigue situations.

#### 6.4.2. Chemical Attack of the Epoxy Resin

Three potentially harmful species are evolved at the surface of the graphite cathode: hydrogen, hydroxyl and perhydroxyl ions. Atomic hydrogen ( $H^0$ ) is known to embrittle metals, and was evolved copiously in these experiments. However, direct chemical attack of the polymer by atomic hydrogen is unlikely. Hydroxyl ions ( $OH^-$ ) are also evolved rapidly at these potentials, but aerospace-grade composite matrix epoxies are thought to be stable in high pH solutions (Levy et al, 1979).

Perhydroxyl ions ( $HOO^-$ ) are evolved according to (6-2), and the perhydroxyl ion is hundreds of times more reactive as a nucleophile than hydroxyl (Schirmann and Delavarenne, 1979). Because the perhydroxyl ion is highly reactive, it will catalytically decompose into oxygen and hydroxyl according to (6-3) and (6-4), so reactions with the polymer would have to be rapid. For example, in the presence of an electrophilic center such as an ester bond the perhydroxyl ion can

react before decomposition has time to occur (Schumb et al, 1955; Schirmann and Delavarenne, 1979). Although catalytic breakdown of peroxide on graphite occurs rapidly at first, the reaction slows down steadily, eventually resulting in a build-up of peroxide in porous regions of the cathode. This high peroxide concentration can produce  $O_2^{\cdot-}$  and  $OH^{\cdot}$  radicals which would degrade the graphite surface as well as the polymer (Yeager et al, 1984).

A damage mechanism that involves perhydroxyl ions might have been enhanced by the calcareous films which formed on these specimens in seawater. Calcareous films are known to reduce the oxygen reduction rate (and so reduce the formation of perhydroxyl) by inhibiting the diffusion of oxygen to the cathode surface. However, the same film would inhibit the diffusion away of potentially damaging perhydroxyl ions.

## 6.5. CONCLUSIONS

T-300/934 graphite/epoxy laminates were coupled with magnesium anodes to form a galvanic cell in 40°C seawater. After 140 days these specimens were fractured in a 4-point bend test fixture. The results showed a 30 percent decrease in the apparent shear strength as compared with control samples soaked in seawater with no galvanic coupling. Scanning electron microscopy (SEM) inspection of the fracture surfaces revealed the damage to be localized corrosion which caused a reduction in the effective widths of the test coupons.

Nucleophilic attack of the epoxy matrix material is the most likely mechanism for chemical degradation of the polymer matrix. Hydroxyl and perhydroxyl ions have been suggested as possible agents of nucleophilic attack. Hydroxyl ion is abundant at the cathode, but high pH solutions are not thought to attack graphite/epoxy. Perhydroxyl ion is highly reactive and is known to attack

many organic compounds, but would tend to catalytically decompose. Damaging concentrations of perhydroxyl and hydroxyl can also build up behind the low-permeability calcareous film that forms under cathodic polarization conditions in seawater. Further analysis of the polymer systems involved is required before conclusions can be reached regarding damage mechanisms.

As suggested in Chapter 5, graphite-fiber-reinforced plastics should be electrically isolated from metals (e.g. fasteners and fittings) when used in seawater service. Fiberglass or organic-fiber plies and sealer coatings can be used to provide effective insulation from other materials. However, few materials retain their insulating properties for more than a few years because of wear, chemical breakdown, or electrolyte absorption. For long term protection a program of periodic corrosion-potential monitoring should be instituted. Careful monitoring would identify cathodic polarization sites early so that galvanic corrosion damage could be stopped or mitigated.

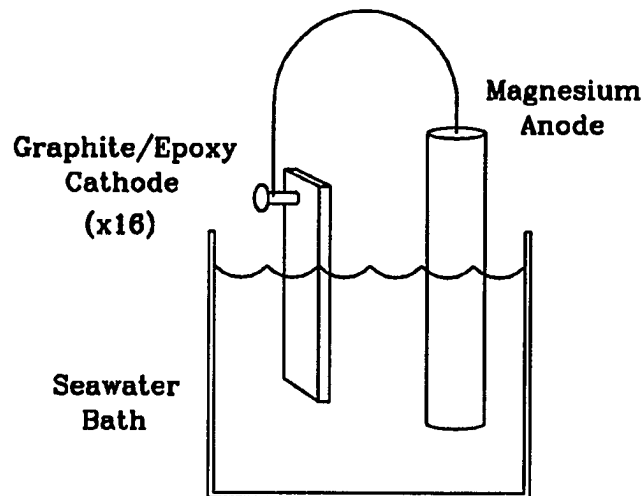
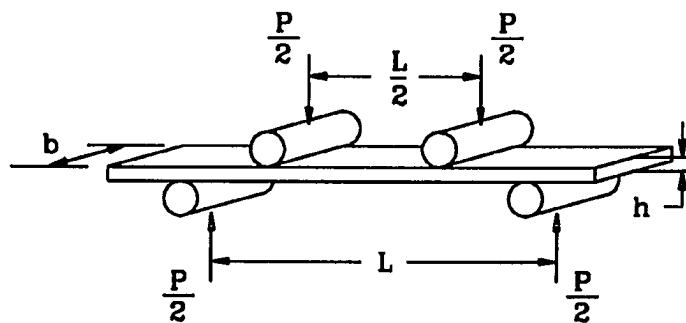


Figure 6.1. Cathodic polarization experiment. Graphite/epoxy test coupons were coupled to magnesium rod anodes in 40 °C seawater for up to 140 days.



$$\tau_{\max} = \frac{3P}{4bh} ; \quad \frac{L}{h} \leq \frac{\sigma_{\max}}{\tau_{\max}} \quad \text{for shear failure}$$

Figure 6.2. Schematic diagram of the four-point bending test used to determine the shear strength of environmentally conditioned graphite/epoxy samples. Details of this test have been presented in Chapter 3.

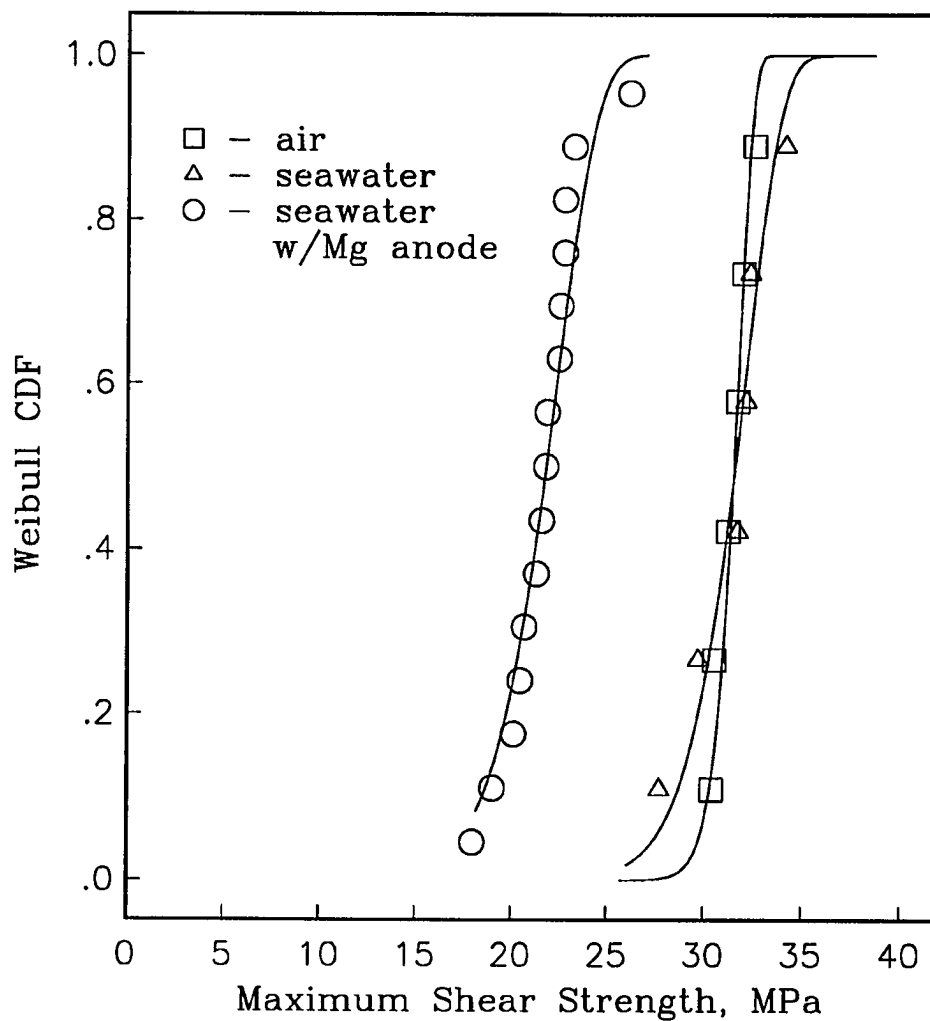


Figure 6.3. Weibull distribution of shear strength data for environmentally conditioned graphite/epoxy (T300/934) samples. Galvanic coupling to magnesium significantly lowered the shear strength of these 26-ply quasi-isotropic laminate test coupons.

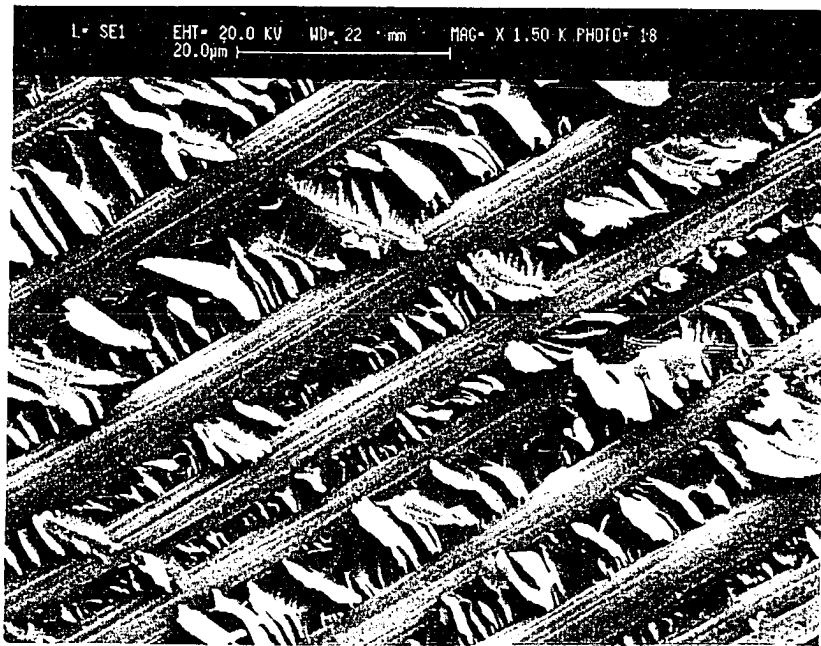


Figure 6.4. Scanning electron microscope (SEM) micrograph of the Mode II fracture surface of a control specimen. This figure shows the Mode II "hackle" markings which are typical of Mode II fracture in quasi-isotropic laminates.



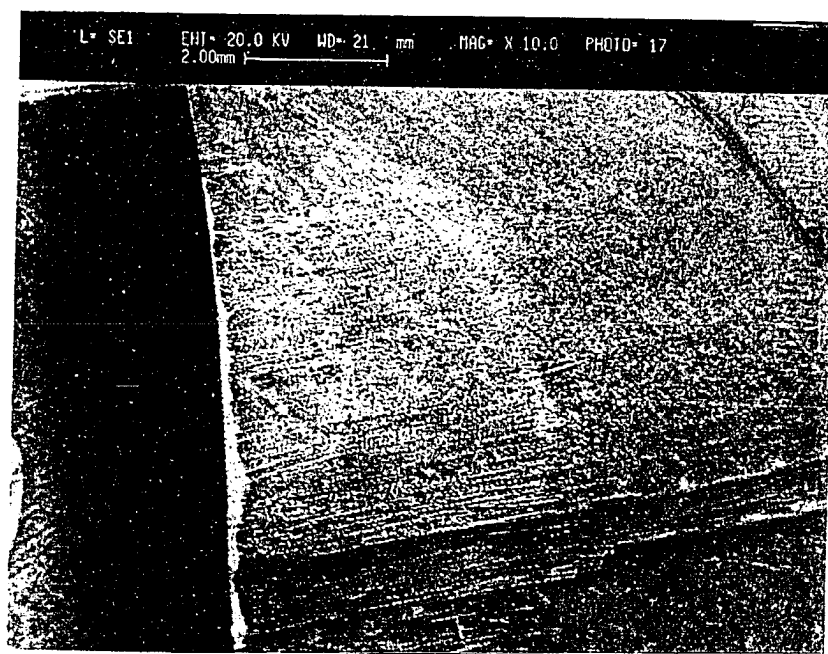


Figure 6.5. SEM micrograph of a degraded area on the edge of a cathodically polarized specimen. Degraded areas could be found along the edges of the galvanically coupled samples.

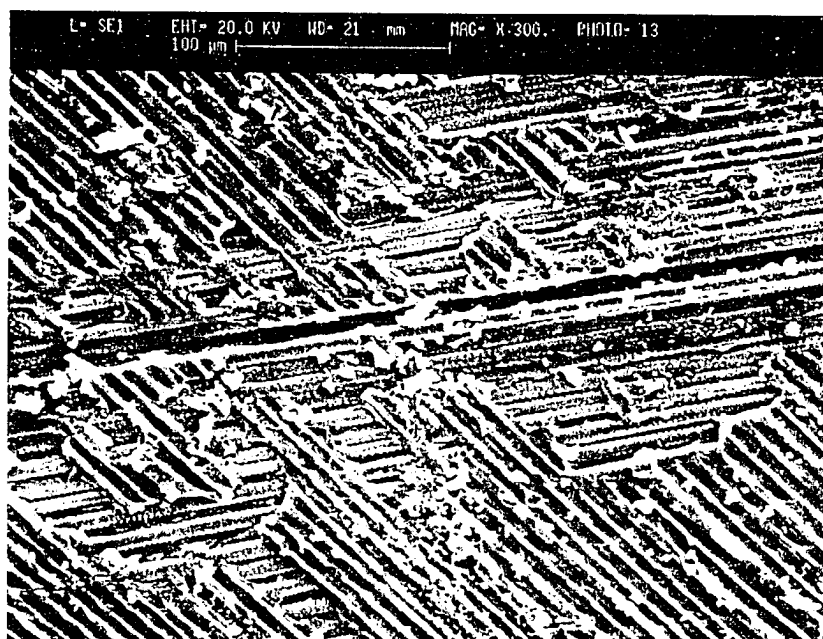


Figure 6.6. SEM micrograph of the damaged area shown in Fig. 6.5. Fibers appear to be completely detached from the surrounding matrix.

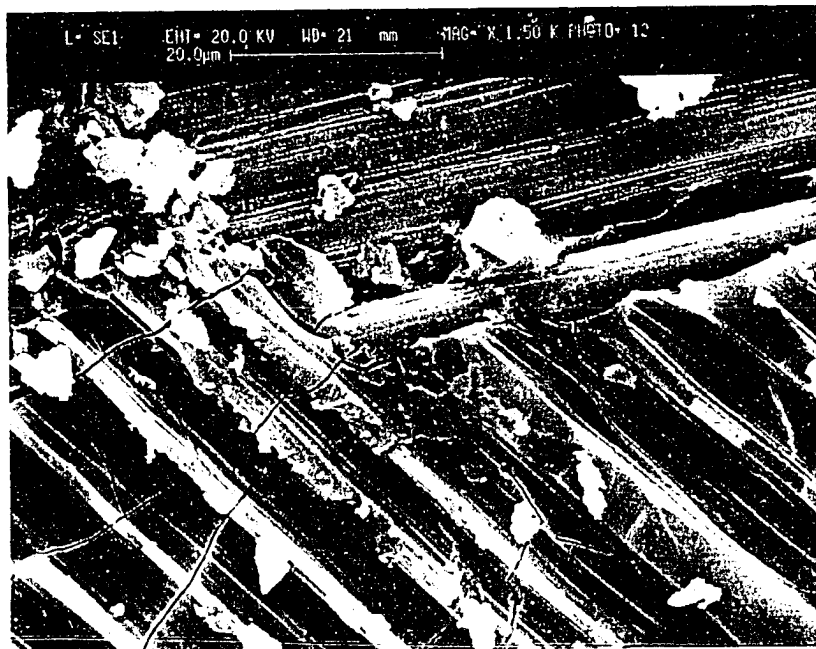


Figure 6.7. Close-up view of the cathodically polarized specimen shown in Fig. 6.6. This figure should be compared with the typical Mode II fracture surface of the control sample, shown in Fig. 6.4.

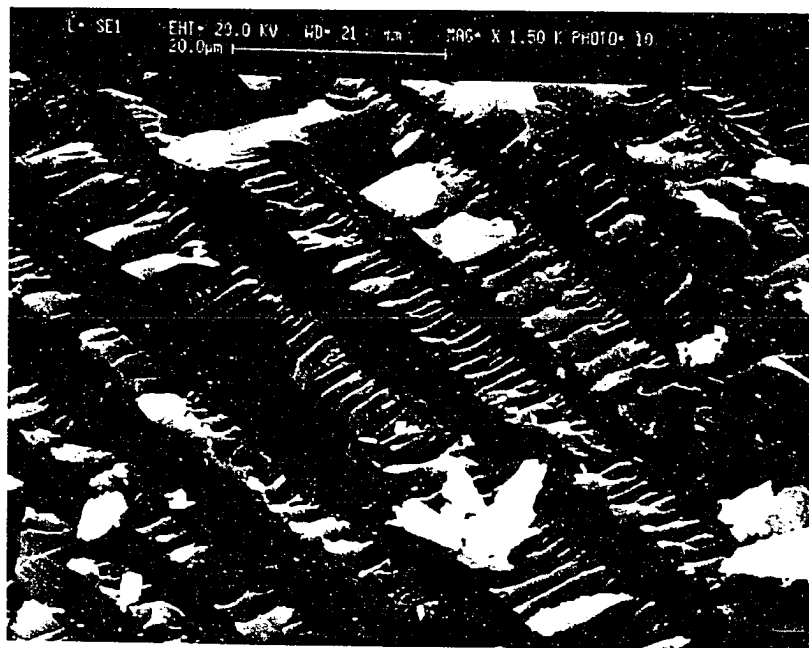


Figure 6.8. SEM micrograph of the interior of the sample shown in Figs. 6.5 to 6.7. In the interior of the cathodically polarized specimens, away from the edges, fracture surfaces were typical of Mode II fracture in quasi-isotropic samples. This photo compares well with Fig. 6.4.

## VII CATHODIC POLARIZATION DAMAGE MECHANISMS

### 7.1. INTRODUCTION

Galvanic coupling of graphite/epoxy laminates with magnesium anodes has resulted in a localized corrosion phenomenon that degrades the epoxy matrix (see Chapter 6). A review of the literature suggests that both hydroxyl and perhydroxyl ions which are evolved as a result of oxygen reduction could have contributed to this degradation. The purpose of the following experiments was to try and distinguish which of the two ions is responsible for the observed cathodic polarization (galvanic coupling) damage in graphite/epoxy.

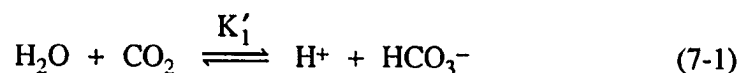
The activities of the suspected ions is a strong function of the pH of the solution in which the reaction takes place. pH directly determines the activity of the hydroxyl ion, but also determines whether hydrogen peroxide exists as  $\text{H}_2\text{O}_2$  or as the more active perhydroxyl ion ( $\text{HOO}^-$ ). Thus the first goal of this investigation was to determine, both theoretically and experimentally, the pH level behind a calcareous film where hydrogen is being evolved. Concurrently, graphite/epoxy samples would be exposed to high pH solutions and checked for signs of chemical attack. The second goal was to verify that hydrogen peroxide is evolved at graphite cathodes using well-established electrochemical test methods. At the same time graphite/epoxy samples would be exposed to various hydrogen peroxide solutions. Following the exposure studies, the third goal was to use Fourier-transform infrared (FTIR) spectroscopy on corroded graphite/epoxy samples, to identify the chemical bonds in the epoxy matrix that were affected. The knowledge gained from these investigations should help to identify the most likely damage mechanisms.

## 7.2. BACKGROUND

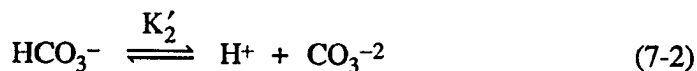
### 7.2.1. pH Levels Under a Calcareous Film

Many different models have been presented to derive the pH level at surfaces under cathodic polarization conditions. Winkelmann (1959) considered only  $H^+$  and  $HO^-$  ions in his model, and used the dissociation constant of water  $K_w$  to derive an equation for  $C_{H^+}$  in terms of  $C_{HO^-}$ . He then integrated across the diffusion layer, deriving a quadratic expression for the hydroxide concentration at the surface of the cathode. A slightly different approach was taken by Engell & Forchhammer (1965) who simply assumed that oxygen was completely reduced at the cathode surface. This implied that the diffusive flux of hydroxide away from the surface had to be 4 times greater than the diffusive flux of oxygen towards the surface. By considering convective fluid flow they derived a relation between the convective mass transfer coefficients and the diffusion coefficients. The pH at the surface of a cathode in freshwater under oxygen reduction conditions (but no hydrogen evolution) was calculated at 10.9. Wolffson and Hartt (1981) used a similar analysis to calculate initial surface pH values between 11 and 11.3. A review of several models of electrode-surface pH was presented by Kuhn and Chan (1983).

These models predict pH values at the surface of bare electrodes that are at least one pH unit higher than that measured in seawater electrolytes. As discussed by Engell and Forchhammer (1965) and by Dexter and Lin (1991), the models above ignore the buffering capacity of the carbonate system in seawater, which removes large quantities of hydroxide to convert bicarbonate to carbonate ion. The equilibrium equations of the carbonate system are given by



and



where  $K'_1$  and  $K'_2$  are the equilibrium constants of carbonic acid in seawater. The model presented recently by Dexter and Lin (1991) includes the effects of carbonate buffering as well as the effect of a surface film. Dexter and Lin's model is the most complete seen in the literature thus far, and has been used as the basis for the construction of the model presented here. The present model complements that of Dexter and Lin by presenting the model on more formal electrochemical grounds, thus eliminating the need for terms representing oxygen reduction and hydrogen evolution.

The formal equation which describes the movement of ionic or suspended species in a fluid must account for (a) migration under the influence of an electric field (for ions), (b) diffusion caused by concentration gradients, and (c) convection by bulk fluid movements.

$$\vec{N}_j = -z_j U_j F C_j \nabla \phi - D_j \nabla C_j + C_j \vec{v} \quad (7-3)$$

i.e. (flux) = (migration) + (diffusion) + (convection),

where  $\vec{N}_j$  is the flux of the  $j^{\text{th}}$  species,

$\nabla \phi$  is the potential gradient

$C_j$  is the species concentration

$D_j$  is the species diffusivity

$\vec{v}$  is the fluid velocity vector

$z_j$  is the charge on the ion

$U_j$  is the mobility of the ion

and

$F$  is Faraday's constant

The other governing equations include the definition of the current density

in an electrolyte (for ionic species),

$$\vec{i} = F \cdot \sum_j z_j \vec{N}_j \quad (7-4)$$

and the continuity equation,

$$\frac{\partial C_j}{\partial t} = -\nabla \cdot \vec{N}_j + R_j \quad (7-5)$$

where  $R_j$  is a production/consumption term.

In order to simplify the present analysis, only 1-D steady-state conditions are considered with no production/consumption. Thus the divergence of the flux  $\vec{N}_j$  goes to zero (i.e. there is a constant flux) and the derivative terms in (7-3) are taken with respect to  $x$  only. It is also assumed that the high salt concentration in seawater (e.g. NaCl ions) forms a supporting electrolyte so that  $\nabla\phi = 0$ , and that the fluid is static such that  $\vec{v} = 0$ . The resulting flux equation is

$$\vec{N}_j = -D_j \frac{\partial C_j}{\partial x} \quad (7-6)$$

As another simplification the concentration gradient is linearized, giving

$$\vec{N}_j = -\frac{D_j}{\delta} \Delta C_j \quad (7-7)$$

where  $\delta$  is the distance across a diffusion barrier or a diffusion layer and  $\Delta C$  is the concentration difference. Equation (7-4) now becomes

$$\vec{i} = -F \sum_j z_j \frac{D_j}{\delta} \Delta C_j \quad (7-8)$$

The model of Dexter and Lin is based on a balance of charge and carbon fluxes at the interface between a filmed cathode and the bulk fluid diffusion layer. Using equation (7-8) and the sign convention of Figure 7.1, the charge-flux balance equation can be written as

$$\frac{i_{app}}{F} = N_{OH,f} + N_{HCO_3,d} + 2N_{CO_3,f} - N_{OH,d} - N_{HCO_3,f} - 2N_{CO_3,d} \quad (7-9)$$

In other words, the charge flux towards the film less the charge flux away from the film must be balanced by the applied current. (The contribution of hydrogen ions has been neglected.) This is an alternate form of the charge balance equation



presented by Dexter and Lin, who use an oxygen flux term instead of the applied current term. The inclusion of hydrogen evolution into the present model follows automatically as simply an increase in the applied current. Terms involving uncharged species such as oxygen and hydrogen are not necessary for the completeness of the model.

The carbon balance comes from the continuity equation, again using the sign convention of Figure 7.1,

$$N_{\text{CO}_2,\text{d}} + N_{\text{HCO}_3,\text{d}} + N_{\text{CO}_3,\text{f}} - N_{\text{CO}_2,\text{f}} - N_{\text{HCO}_3,\text{f}} - N_{\text{CO}_3,\text{d}} = 0 \quad (7-10)$$

The subscripts d and f in equations (7-9) and (7-10) represent the fluid diffusion layer and the calcareous film, respectively, e.g. the flux of  $\text{CO}_3^{2-}$  through the fluid diffusion layer is given by

$$N_{\text{CO}_3,\text{d}} = \frac{D_{\text{CO}_3,\text{d}}}{\delta_{\text{d}}} \cdot (C_{\text{CO}_3,\text{b}} - C_{\text{CO}_3,\text{i}}) \quad (7-11)$$

The subscripts b and i represent the bulk fluid and the film/fluid interface, the boundaries of the fluid diffusion layer. The boundaries of the calcareous film will be represented by the subscripts i and s, where s stands for the cathode surface.

The concentrations of the species in (7-9) and (7-10) must now be written in terms of the hydrogen ion activity, a. The hydroxide ion is related to a through the dissociation constant of water,  $K_w'$ , i.e.

$$C_{\text{OH}} = \frac{K_w'}{a} \quad (7-12)$$

For the carbon species, the concentration can be written in terms of the hydrogen ion activity and the titration alkalinity, TA, giving (Dexter and Lin, 1991)

$$C_{\text{CO}_2} = \frac{a^2 \cdot \text{TA}}{K'} \quad (7-13)$$

$$C_{\text{HCO}_3} = \frac{a \cdot K_1' \cdot \text{TA}}{K'} \quad (7-14)$$

$$C_{\text{CO}_3} = \frac{K_1' \cdot K_2' \cdot \text{TA}}{K} \quad (7-15)$$

where

$$K \equiv a \cdot K_1' + 2 \cdot K_1' \cdot K_2' \quad (7-16)$$

$K_1'$  and  $K_2'$  were defined in (7-1) and (7-2). The titration alkalinity TA is a measure of the acid-neutralizing capacity of the solution, and is assumed constant for seawater.

The assumptions inherent in writing (7-13) through (7-14) are important to the accuracy of the model and must be discussed further. The titration alkalinity can be expressed for seawater as (Stumm and Morgan, 1981)

$$TA = CA + BA + [OH^-] - [H^+] \quad (7-17)$$

where CA is the carbonate alkalinity and BA is the borate alkalinity (other minor seawater constituents have been ignored). The fundamental assumption used here is that the titration alkalinity TA is equivalent to the carbonate alkalinity CA. This assumption is commonly made for seawater pH near 8.0, and is fairly accurate. However, as the pH rises, the contributions from BA and hydroxide become more important. The resulting errors could adversely affect the model, especially at pH levels above 10.

Substituting equations (7-11) through (7-16) into (7-9) and (7-10) gives two equations in  $a_i$  and  $a_s$ , i.e.

$$\begin{Bmatrix} a_i^2 \\ a_i \\ 1 \end{Bmatrix}^T \begin{bmatrix} A_{11} & A_{12} & A_{13} \\ A_{21} & A_{22} & A_{23} \\ A_{31} & A_{32} & A_{33} \end{bmatrix} \begin{Bmatrix} a_s^2 \\ a_s \\ 1 \end{Bmatrix} = 0 \quad (7-18)$$

and

$$\begin{Bmatrix} a_i^2 \\ a_i \\ 1 \end{Bmatrix}^T \begin{bmatrix} B_{11} & B_{12} & B_{13} \\ B_{21} & B_{22} & B_{23} \\ B_{31} & B_{32} & B_{33} \end{bmatrix} \begin{Bmatrix} a_s^2 \\ a_s \\ 1 \end{Bmatrix} = 0 \quad (7-19)$$

where the A's and B's are complicated functions of the environmental constants described above.  $a_s$  and  $a_i$  represent the activity of the hydrogen ion at the cathode surface and at the film surface, respectively, and can be converted to pH by taking the negative of the log of the activity.

The complete solution to (7-18) and (7-19) involves a 10<sup>th</sup> order polynomial in  $a_i$ , and is not easily solved. Following the suggestion of Dexter and Lin, the terms involving  $\text{CO}_2$  flux in equation (7-10) have been ignored as negligible for  $\text{pH} > 8$ . This assumption gives  $B_{i1} = B_{1i} = 0$ , allowing (7-19) to be solved for  $a_i$  in terms of  $a_s$ . Substituting this solution back into (7-18) leads to a fourth-order polynomial in  $a_s$ , which has only one real, positive root. This solution technique has been used to solve for  $a_s$  and  $a_i$  in the Fortran program PHCALC.

The environmental constants used in the calculation of pH in PHCALC are listed in Table 7.1. The diffusivities of ions in bulk electrolytes were taken from various texts (e.g. Newman, 1973). The diffusivities of ions through calcareous films is largely unknown, although there is some evidence that the bulky deposits formed at high current densities offer little resistance to diffusion (Hartt et al, 1984). A common approach is to let the film diffusivity be some fraction of the bulk diffusivity, such that  $D_f = D_b \cdot \phi$ , as done by Dexter and Lin. Rather than estimate the value of  $\phi$ , this parameter was allowed to vary in the present model, along with the film thickness. The diffusion layer thickness was assumed to be 0.02 cm. Other constants were taken from texts on marine chemistry (e.g. Stumm and Morgan, 1981).

#### 7.2.2. Investigation of Oxygen Reduction Using a Rotating Ring-Disk Electrode

The reduction of oxygen on a cathode is a very important electrochemical reaction for many natural and industrial processes, and has been thoroughly investigated. One experimental method which is particularly useful in studying oxygen reduction on cathodes is the rotating ring-disk electrode or RRDE.

### 7.2.2.1. Theory of Rotating Disk and Rotating Ring-Disk Electrodes (Filinovsky and Pleskov, 1984)

According to equation (7-3), ions move in solution in response to electric fields, convective flow, and concentration gradients. Consider now the rotating disk electrode shown schematically in Figure 7.2. The standard assumptions of an indifferent electrolyte, steady-state conditions, and constant diffusivity give (in cylindrical coordinates, with no angular dependence)

$$v_r \frac{\partial C_i}{\partial r} + v_z \frac{\partial C_i}{\partial z} = D_j \cdot \left[ \frac{1}{r} \cdot \frac{\partial}{\partial r} \left( r \frac{\partial C_i}{\partial r} \right) + \frac{\partial^2 C_i}{\partial z^2} \right] \quad (7-20)$$

For a rotating disk, convective flux dominates the diffusive flux in the radial direction. Also, near the disk surface ( $z$  approaching zero) the species concentration is independent of the radius, giving

$$v_z \frac{\partial C_i}{\partial z} = D_j \cdot \frac{\partial^2 C_i}{\partial z^2} \quad (7-21)$$

Hydrodynamic analysis of the rotating disk gives a series solution of  $v_z$ ,

$$v_z = -a_0 \omega^{3/2} \eta^{-1/2} z^2 + \dots \quad (7-22)$$

where  $a_0$  is an empirical constant, which holds true for small  $z$ . Substituting (7-22) into (7-21) and solving gives the result

$$\frac{C_b - C(z)}{C_b - C_s} = 1 - \gamma \left[ \frac{1}{3} ; \left[ \frac{z}{a_0 D_j^{1/3} \omega^{-1/2} \eta^{1/6}} \right]^3 \right]^{1/\Gamma(1/3)} \quad (7-23)$$

where  $C_b$  is the bulk concentration and  $C_s$  is the surface concentration. The diffusion boundary layer thickness can now be arbitrarily defined as the value of  $z$  at which this solution has a value of .005, i.e. the distance from the disk where the concentration reaches 99.5% of the bulk. This definition gives

$$\delta_d = 1.61 D^{1/3} \eta^{1/6} \omega^{-1/2} \quad (7-24)$$

which for a typical solution is around  $5 \times 10^{-3}$  cm. When compared with a typical shear boundary layer of around  $10^{-1}$  cm, we see that diffusion is the dominant mass transfer mode at the disk surface.

Because the diffusion and hydrodynamic boundary layers can be separated, the flux to the disk surface can be expressed as the linearized diffusion flux, i.e.

$$N_j = D_j \cdot \frac{\partial C_j}{\partial z} \Big|_{z=0} \cong D_j \cdot \frac{(C_b - C_s)}{\delta_d} \quad (7-25)$$

Thus the current becomes

$$i = nFN_j = nFD(C_b - C_s)/\delta_d,$$

or

$$i = 0.62nF(C_b - C_s)D^{2/3}\eta^{-1/6}\omega^{1/2} \quad (7-26)$$

The limiting current is that which drives the surface concentration to zero, thus giving the Levitch equation,

$$i_L = 0.62nFC_bD^{2/3}\eta^{-1/6}\omega^{1/2} \quad (7-27)$$

The most important consequence of the rotating disk analysis is the linear relationship between the limiting current and the square root of the rotation rate.

Figure 7.3 shows the rotating ring-disk electrode or RRDE, consisting of a disk electrode surrounded by a ring electrode which is insulated from the disk. The RRDE is used primarily to investigate the reaction kinetics of multi-stage chemical reactions such as oxygen reduction. As an example, consider a two-stage electrode reaction occurring on the central disk



If the rate  $k_2$  of the second reaction is not high enough, some of the intermediate product  $B$  will be introduced into the solution and carried to the ring. If it is assumed that  $B$  is completely oxidized on the ring, i.e.



then by measuring the reaction rate  $k_3$  the relative amount of  $B$  that is reduced according to (7-29) can be determined.

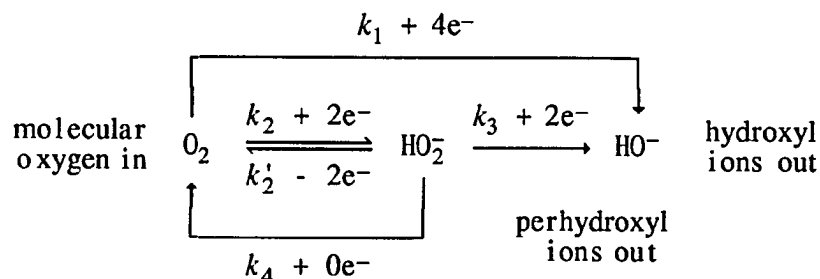
The ring current can be at most a fraction of the disk current, depending on the collection efficiency of the RRDE,  $N_{rde}$ , i.e.

$$I_r = I_d \cdot \left(\frac{n_r}{n_d}\right) \cdot N_{rde} \quad (7-31)$$

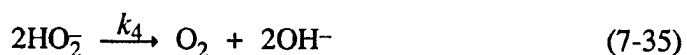
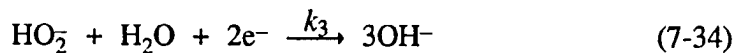
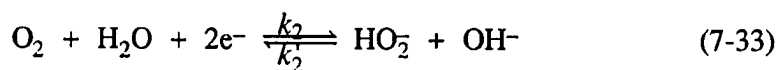
The efficiency  $N$  is a function only of the geometry of the ring-disk combination, and ranges from around 0.2 to 0.5. Note that the ring current will be directly proportional to the disk current and is not a function of the rotation speed,  $\omega$ .

#### 7.2.2.2. Oxygen Reduction (Tarasevich et al, 1983)

The oxygen reduction reaction in alkaline environments involves several competing reactions, which can be represented schematically:



These reactions can also be written conventionally,



The expressions involving  $HO_2^-$  can also be written using the form  $H_2O_2$  with addition of  $H^+$  where appropriate.

The rate of oxygen diffusion to the disk surface must be equivalent to the rate of consumption (to  $HO^-$  and  $HO_2^-$ ) less the rate of  $HO_2^-$  decomposition. Also, the rate of perhydroxyl formation must equal the rate of consumption plus the rate of diffusion away from the disk surface. A flux balance of the species involved gives

$$D_A \cdot (C_A^b - C_A^s) / \delta_A = (k_1 + k_2) \cdot C_A^s - (k_2' + \frac{k_4}{2}) \cdot C_B^s \quad (7-36)$$

and

$$k_2 \cdot C_A^s = (k_3 + k_4 + k_2') \cdot C_B^s + D_B C_B^s / \delta_B \quad (7-37)$$

where A=oxygen, B=perhydroxyl.

The current on the disk is the result of charge transfer reactions, therefore

$$I_d = \pi d^2 \cdot F \cdot [(4k_1 + 2k_2) \cdot C_A^s + (2k_3 - 2k_2') \cdot C_B^s] \quad (7-38)$$

The diffusive transport of perhydroxyl ion away from the disk is the product of the disk area and the perhydroxyl flux, i.e.

$$A_d \cdot N_B = \pi d^2 \cdot D_B \cdot C_B^s / \delta_B \quad (7-39)$$

thus the total current collected at the ring will be

$$I_r = 2 \cdot F \cdot (\pi d^2 \cdot D_B \cdot C_B^s / \delta_B) \cdot N_{rde} \quad (7-40)$$

where  $N_{rde}$  is the collection efficiency. Solving equations (7-36) and (7-37) for  $C_A$  and  $C_B$ , then substituting into (7-38) and (7-40), it can be shown that

$$\frac{I_d}{I_r} = \left\{ \frac{2k_1+k_2}{k_2} + \left[ \left( \frac{2k_1+k_2}{k_2} \right) (k_3+k_4+k_2') + (k_3-k_2') \right] \cdot \frac{\delta_B}{D_B} \right\} \cdot N_{rde}^{-1} \quad (41)$$

where

$$\delta_B = 1.61 D_B^{1/3} \eta^{1/6} \omega^{-1/2} \quad (7-42)$$

from the Levitch equation. By introducing the limiting current for oxygen reduction at the disk,

$$I_{L,A} = 4F \cdot \pi d^2 \cdot D_A C_A^b / \delta_A \quad (7-43)$$

it can also be shown that

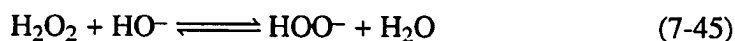
$$\frac{I_{L,A} - I_d}{I_r} = \left\{ 1 + 2 \cdot \left[ \frac{(k_3+k_4+k_2')}{k_2} \cdot \left( \frac{D_A}{D_B} \right)^{2/3} \right] + \frac{2}{k_2} \left( \frac{\delta_A}{D_A} \right)^{-1} \right\} \cdot N_{rde}^{-1} \quad (7-44)$$

Because  $\delta_B$  and  $\delta_A$  are proportional to  $\omega^{-1/2}$ , the left sides of equations (7-41) and (7-44) can be measured at several different  $\omega$ 's and plotted as function of  $\omega^{-1/2}$  and  $\omega^{+1/2}$ , respectively. The slope and intercepts of the resulting curves will give 4 equations in the 5 unknown rate constants. More information is required to

solve for the 5 unknown rate constants. Typically additional information is obtained from experimental conditions, or some assumption is made regarding one of the rate constants.

### 7.2.3. Properties of Hydrogen Peroxide

Hydrogen peroxide is an important part of many chemical, electrochemical, and industrial processes and has been the subject of periodic review, most recently by Schirmann and Delavarenne (1979). The reactivity and stability of  $\text{H}_2\text{O}_2$  is strongly influenced by the pH of the solution. For example, in alkaline solutions the perhydroxyl ion ( $\text{HOO}^-$ ) is produced according to the equilibrium reaction



with a pK near 11.6. The perhydroxyl ion has a reactivity more than 100 times greater than the hydroxide ion, and is especially active as a nucleophile.

Pourbaix (1974) presents a complete discussion of the stability of  $\text{H}_2\text{O}_2$  solutions using a pH-E diagram, as reproduced in Figure 7.4. The equilibrium pH between  $\text{HOO}^-$  and  $\text{H}_2\text{O}_2$  is shown as line (1). In the region above line (2),  $\text{H}_2\text{O}_2$  is stable and water is oxidized according to (7-34). In the region below line (4), hydrogen peroxide is again stable, and oxygen is reduced according to (7-33,  $k'_2$ ). Between lines (2) and (4) hydrogen peroxide is doubly unstable and decomposes according to (7-35).

These stability regions are immediately applicable to the RRDE analysis discussed previously. For oxygen reduction on a cathode in seawater, only reactions occurring below line (4) need be considered. Thus the reaction constants  $k'_2$  and  $k_4$  can be assumed to be zero. This simplification leads to a solution for the remaining reaction constants  $k_1$ ,  $k_2$ , and  $k_3$ .



#### 7.2.4. FTIR Analysis of Graphite/Epoxy Composites

Advances in computing hardware have made FTIR (Fourier-Transform InfraRed) spectroscopy a low-cost and relatively easy-to-use analytical tool in the chemical analysis of polymers. The theory and experimental techniques of FTIR spectroscopy have been the subject of many texts, e.g. Colthup et al (1990). Several standard techniques now exist for specimen preparation and IR exposure, and the use of a particular technique depends on the physical and chemical properties of the specimen to be analyzed as well as the amount of sample available. The FTIR analysis of composite materials has been the subject of several review articles (Young and Chang, 1986; Cole et al, 1988a,b).

The most common FTIR analysis techniques are simple transmittance, multiple internal reflectance, and diffuse reflectance. The transmission technique is perhaps the most convenient, in which a small amount (2-3%) of powdered sample is mixed with an IR-invisible salt (e.g. KBr). The mixture is then pressed into a solid pellet which is then exposed to the IR beam. The chemical bonds within the sample absorb the beam energy at specific wavelengths, thus producing a spectrum of absorbance which helps to identify the chemical structure. Traditional reflectance techniques place a KBr or similar crystal between two identical samples, and the IR signal reflects back and forth between the two samples before exiting. This multiple-reflectance increases the signal-to-noise ratio of the final spectrum. More recently a diffuse-reflectance (DRIFT) technique has become popular, in which an IR signal is simply reflected from the surface of an unprepared sample. The DRIFT technique has the advantage of requiring little or no sample preparation.

Unreinforced epoxy matrix materials have been studied extensively using FTIR techniques. Levy et al (1979) studied degradation in epoxy resins subjected to stress, temperature, and moisture using an internal reflectance technique. Similarly,

Luoma and Rowland (1986) studied the environmental degradation of an aerospace epoxy matrix using a weatherometer and internal reflectance FTIR.

Problems arise, however, in the FTIR analysis of matrix materials reinforced with graphite fibers because of the strong broad-band absorption of infrared by graphite. Young and Chang (1986) found pressed-pellet transmission spectra of powdered graphite/polymer composites unsatisfactory because of poor spectrum quality. Cole et al (1988a) found that DRIFT techniques worked best if the direction of the IR beam coincided with the fiber direction, thus minimizing reflectance from the fibers. DRIFT was found to be useful in evaluating graphite/epoxy prepregs, in which the fibers are covered with a thin layer of partially-cured epoxy, and reflection from the underlying fibers can easily be minimized by proper sample orientation. The principal challenge of using FTIR techniques with fully-cured graphite-reinforced plastics is the minimization of undesirable signals resulting from the presence of the graphite fibers.

### **7.3. EXPERIMENTAL PROCEDURE**

#### **7.3.1. pH of Galvanically Coupled Samples**

45 coupons were cut from 30-ply unidirectional AS-4/3501-5a graphite/epoxy laminates. Coupons were cut 13 mm wide x 90 mm long x 3.8 mm thick, with the fiber direction parallel to the length. These specimens were gripped on one end with a brass clip and suspended above a tank of free-flowing Pacific seawater. The clips were connected electrically to a magnesium alloy anode during the experiment to produce galvanic corrosion. 15 specimens were connected to each magnesium anode, and the anodes were replaced when depleted.

After more than one year under these conditions, large amounts of calcareous films had formed on the suspended ends of the specimens. This growth

was concentrated at the tips of the specimens where the ends of the unidirectional fibers were exposed. Typical dimensions of the calcareous formations were 10 mm thick x 20 mm wide x 10-25 mm long, extending down from the end of the suspended coupons. These deposits were irregular, and were marked by holes which evidently served as a pathway for the hydrogen gas which was evolved slowly but continuously during these experiments.

In order to sample the pH beneath these deposits, the Cardy pH measurement system (from Cole-Parmer Scientific) was used. The measurement procedure using this system was as follows:

- (a) Carefully break off (without crushing) the calcareous deposit to expose the underside of the deposit
- (b) Wipe the underside of the deposit with sampling sheets provided by Cardy
- (c) transfer the sampling sheet to the pH measurement unit and add deionized water to obtain a stable pH reading.

This method of surface pH measurement is relatively new, and its absolute accuracy has not been independently verified, although measurements of liquid pH standards were accurate and repeatable.

#### 7.3.2. High pH Exposure Study

To determine the effects of high pH on graphite/epoxy, sample coupons were soaked in 0.5 molar NaCl solutions of pH = 10 for one year and pH = 12 for 8 months. pH was periodically monitored in the solutions and was adjusted by the addition of dilute NaOH or HCl solutions. At the end of the exposure period samples were examined for visible signs of degradation.

### 7.3.3. Rotating Ring Disk Study

The RRDE experiments described here utilized a graphite/epoxy disk in concert with a platinum ring. The graphite/epoxy disk was cut from a 30-ply unidirectional AS-4/3501-5a laminate as shown in Fig. 7.5, so that the graphite reinforcing fibers were normal to the face of the electrode. Specimens were cut as rectangular strips from the parent laminate, then turned down to the proper diameter in a lathe (graphite dust was collected by vacuum during machining). Disks were then cut from the resulting rods in a water-cooled diamond cutoff saw. The surfaces of the disks were polished and rinsed in distilled water before mounting on the RRDE.

The interchangeable disks used in this study were 3.83mm (0.151in) in diameter (this dimension was limited by the thickness of the parent laminate). The inside and outside diameters of the fixed platinum ring were 7.50 mm and 8.50 mm. The theoretical collection efficiency of this geometry was 21.8%. The collection efficiency of this geometry was also determined experimentally, based on the procedure recommended by Pine Instruments. The experimentally determined collection efficiency using a platinum disk of this size was 22.1%.

All experiments were performed on a Pine Instruments AFRDE4 Potentiostat using a Pine ASR Analytical Rotator and Speed Control. Data was collected using a Hewlett-Packard Model 7090A Data Acquisition and Plotting System in buffer capture mode. The data was then transferred to an IBM PC with a National Instruments GPIB-PC2A IEEE-48 instrumentation interface card. Current and potential were sampled using this configuration at collection rates ranging from 0.5 to 2 samples per second. The electrolyte used in the experiments was 0.5 M NaCl adjusted to pH 8.0.

#### 7.3.4. H<sub>2</sub>O<sub>2</sub> Exposure Study

In an effort to ascertain the effects of H<sub>2</sub>O<sub>2</sub> exposure in graphite/epoxy, two long-term soaking experiments were started in conjunction with the high pH exposure study of section 7.3.2. In the first experiment AS-4/3501-5a graphite/epoxy coupons were exposed to a 5% solution of H<sub>2</sub>O<sub>2</sub> for a period of one year. In the second experiment similar specimens were exposed to a solution of HOO<sup>-</sup>, which was prepared by adding H<sub>2</sub>O<sub>2</sub> to a high-pH solution. However, this solution proved to be unstable as will be discussed later.

#### 7.3.5. FTIR Analysis

FTIR spectra of the T300/934 graphite/epoxy samples (which were corroded during the experiments of Chapter 6) were first acquired using the diffuse reflectance (DR) method. DR-FTIR spectra were obtained using a BioRad Model UMA 300A spectrometer with a DR-FTIR microscope accessory that allows the IR signal to be reflected from specific areas of the sample. This micro-sampling feature allowed spectra from the corroded fracture surfaces of the sample to be acquired separately from the control areas of the sample. However, because of extensive interference from the randomly oriented and exposed graphite fibers on the fracture surfaces, spectra obtained using this method were unusable.

Standard transmittance spectra were obtained for both the T-300/934 and the AS-4/3501-5a graphite/epoxy systems using a Perkin-Elmer Model 1600 FTIR spectrometer. Powder samples were removed from cured laminate coupons using a milling machine with a 6 mm end-mill turning at approximately 800 rpm, using a depth-of-cut of 0.05 to 0.1 mm. For corroded coupons, powder samples were obtained by scraping visibly degraded areas by hand. The resulting powder was collected and ground further in a mortar and pestle to achieve a particle size of

approximately 100  $\mu\text{m}$ . All tools used in sample preparation were cleaned thoroughly with alcohol before and after use.

Ground graphite/epoxy powder from control samples was dried overnight at 60 °C under vacuum, then mixed with dry IR-grade KBr powder to get a mixture of approximately 3-5% graphite/epoxy. The powder mixture was then pressed to form a KBr disk which was then exposed to the IR beam. IR spectra were obtained in ratio mode, i.e. the absorbance of the sample was compared to the absorbance of a control beam to minimize the effects of atmospheric gases in the sample chamber such as  $\text{CO}_2$  and  $\text{H}_2\text{O}$ . As discussed earlier, the signal-to-noise ratio for these spectra were too low to be of use because of the large amount of graphite (70-80% by weight) in the composite powder.

Because of the poor spectra produced by the graphite/epoxy powders, a method for separating the graphite from the epoxy was sought. Gravity separation is the simplest technique, where the graphite/epoxy powder is stirred into a solution which has a specific gravity (SG) between that of graphite and epoxy. This solution could then be centrifuged to separate the two components. Graphite has a specific gravity of around 1.75, whereas epoxy is around 1.3. Fluids were thus sought with specific gravity between near 1.5. Two common solvents were tried initially, chloroform (SG=1.5) and carbon tetrachloride (SG=1.6). However, these solvents presented containment problems as well as the possibility of altering the IR signal by reacting with the epoxy samples.

High-density salt solutions were tried next, specifically solutions of zinc chloride ( $\text{ZnCl}_2$ ) and zinc bromide ( $\text{ZnBr}_2$ ). Zinc chloride is a toxic material and was found to be unstable in solution. However, zinc bromide is much less toxic, and was completely stable in solution. Thus solutions of SG 1.5 were produced by mixing  $\text{ZnBr}_2$  powder with distilled water until the SG (as measured using standard

hydrometers) reached the desired level. (Note that zinc salts dissolve exothermically, and specific gravity is sensitive to temperature. Solutions should be allowed to cool to room temperature before measuring the specific gravity.)

To prepare epoxy samples for FTIR analysis, graphite/epoxy powder samples were mixed with solutions of SG=1.50  $\text{ZnBr}_2$  and then centrifuged. The portion of the sample that remained in solution or floated to the top was poured off and filtered. The sample thus obtained was dried at 60 °C under vacuum for 24 hours. The dried samples were then used in making KBr disks for FTIR analysis.

## 7.4. EXPERIMENTAL RESULTS

### 7.4.1. pH Under a Calcareous Film

The results of the theoretical model of pH levels under a calcareous film are shown in Figures 7.6 and 7.7. The model shows that pH levels under calcareous films can approach 12 during continuous cathodic polarization. The output of the model depends strongly on the factor  $\phi/\delta_f$ , i.e. the film diffusivity factor divided by the film thickness. The theoretical effect of varying  $\phi/\delta_f$  are also shown in the figures.

The experimentally determined pH values are also shown in Figure 7.7. This data is presented as a histogram in Figure 7.8, and shows that the data is not normally distributed. The lower modes near 8.8 and 9.7 have been rejected as experimental error, and 11.3 has been chosen as the most likely estimator of the under-film pH.

The bulky calcareous deposits which formed during the present experiments provide little resistance to diffusion, thus the factor  $\phi$  should be around 1.0. The minimum thickness of the calcareous film is half of the specimen width or nearly 0.20 cm. Thus for these experiments  $\phi/\delta_f$  is approximately 5.0. The theoretical pH

model significantly overestimates the under-film pH compared with the experimental data. This error most likely results from ignoring the hydroxide concentration in the titration alkalinity term of the model. The additional hydroxide term would act as a buffering factor and so bring the calculated pH closer to the observed values.

#### 7.4.2. Rotating Ring Disk Study

The results of the rotating ring-disk investigation of oxygen reduction kinetics are shown in Figures 7.9 and 7.10, and are tabulated in Table 7.2. The data of Figures 7.9 and 7.10 have been fitted to a straight line to fit the linear model, although the data clearly is not linear. The non-linearity of the data might be attributed to many error sources not accounted for in the model, e.g. impurities in the test solution, failure to precondition the electrode, hydrogen evolution, and changes in solution pH.

The relative magnitudes of the rate constants  $k_1$  and  $k_2$  indicate that a large proportion of the oxygen reduction reaction goes through a hydrogen peroxide intermediate state. In addition, the rate of  $H_2O_2$  reduction on the disk ( $k_3$ ) was found to be negligible. Thus hydrogen peroxide will be present and available for reaction at a graphite/epoxy cathode under galvanic coupling conditions. The high pH levels found in the previous section (11.3) compared with the dissociation constant of hydrogen peroxide (11.6) indicates that a significant portion of the  $H_2O_2$  will be present in the form of the perhydroxyl ion.

#### 7.4.3. Long-term Exposure Experiments

Exposure to high pH levels (10 and 12) had little or no visible effect on AS-4/3501-5a graphite/epoxy samples. However, exposure to the 5 % solution of  $H_2O_2$  had a substantial effect. After one year of exposure samples were showing



bare fiber "hair", indicative of matrix dissolution. The  $\text{H}_2\text{O}_2$  solution was only slightly discolored. Interestingly, when the waste  $\text{H}_2\text{O}_2$  solution was poured into a high-pH solution (waste from the high-pH experiments), the solution turned a bright yellow. This is indicative of the presence of amine groups or conjugated alkene groups in the degradation products of the  $\text{H}_2\text{O}_2$  experiment.

Attempts to create a solution of perhydroxyl ions by adding  $\text{H}_2\text{O}_2$  to high pH solutions failed because of the instability of hydrogen peroxide. The rest potential of the graphite/epoxy surfaces put the solution into the doubly-unstable region of Figure 7.4. The result was an immediate and copious production of oxygen on the surface of the samples, which gradually diminished until after a few days only a high-pH solution was left.

#### 7.4.4. FTIR Analysis

FTIR spectra of the graphite/epoxy specimens are presented in Figures 7.11-7.18. Figure 7.11 shows the spectrum of a graphite/epoxy sample in which the graphite was not separated from the epoxy prior to analysis. The extensive noise in the spectra can be attributed to strong broad-band absorption by the graphite fibers, as demonstrated by the spectrum of graphite cloth shown in Figure 7.12. Figure 7.13 is the spectrum of 3501-5a epoxy which has been separated from the graphite/epoxy control sample using the procedure described earlier. Interference from the graphite has been largely eliminated. All subsequent epoxy spectra are taken on epoxy samples which were removed from fully-cured graphite/epoxy laminates.

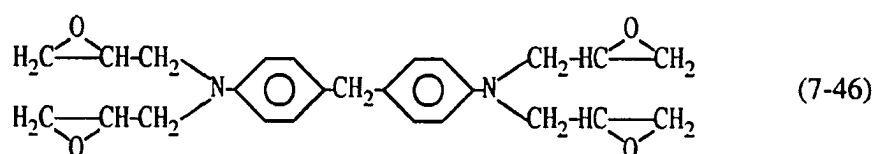
Figure 7.14 is the FTIR spectrum of the 3501-5a after exposure to a pH = 12 solution for 8 months. There is no evidence of chemical attack. Figure 7.15 is the spectrum of 3501 after exposure to 5 %  $\text{H}_2\text{O}_2$  for 12 months, and shows

substantial changes. Figure 7.16 is the spectrum from a control sample of 934 epoxy, and shows a structure similar to the 3501, with the exception of two new peaks. These peaks were attacked under cathodic polarization conditions as shown by the spectrum of Figure 7.17. The effect of high-temperature baking on the FTIR spectrum of 934 epoxy is shown in Figure 7.18. A complete analysis of these spectra is presented in the next section.

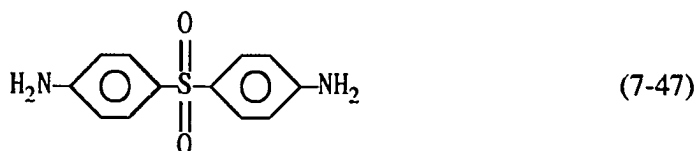
## 7.5. DISCUSSION

The experimental results presented thus far show that both the hydroxyl ion and hydrogen peroxide (and thus the perhydroxyl ion) are present during cathodic polarization of graphite/epoxy. One or both of these agents is responsible for the observed damage in the 934 epoxy. However, although both suspects have been placed at the scene of the crime, it remains to establish motive, i.e. to identify which chemical damage mechanisms would be favored under these conditions. For this purpose the structure of the cured epoxy must be established, then chemical bonds which might serve as sites for attack can be identified.

Both the 934 and the 3501 epoxy formulations begin with Ceiba-Geigy MY-720, which consists primarily of tetraglycidyl diaminodiphenyl methane (TGDDM) (May, 1983; Kong, 1989).



The TGDDM epoxy systems are typically crosslinked using the bifunctional crosslinking agent diaminodiphenylsulfone (DDS)



The principal curing reaction in the TGDDM/DDS system is nucleophilic attack of the epoxy groups of TGDDM by the amino groups of DDS, resulting in primary and secondary alcohol formation. The hydroxyl groups then attack other epoxy groups to add ether-bonds to the cross-linking network. The additional reaction of the secondary amines in the once-reacted DDS is not favored at normal curing temperatures, but will occur as a post-cure reaction at higher temperatures (Gupta et al, 1983).

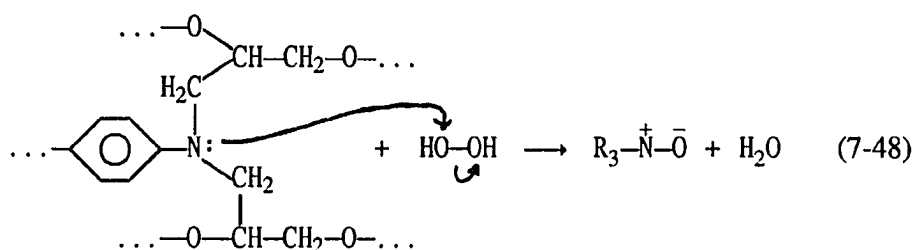
Table 7.3 lists the major FTIR spectral peaks which have been associated with the cured TGDDM/DDS epoxy system, along with their structural assignments (Levy et al, 1979; Luoma and Rowland, 1986; Colthup et al, 1990). All of these peaks can be found in the FTIR spectra presented in Figures 7.13 to 7.18. Table 7.4 lists extraneous bands which have also been found in these spectra. Most have been identified and are associated with corrosion or post-cure reactions as discussed below.

The present study has focused on determining whether hydroxide or hydrogen peroxide was responsible for the corrosion of a TGDDM/DDS epoxy matrix (Fiberite 934) under galvanic coupling conditions. Figure 7.13 is the FTIR spectrum of a control sample of a similar TGDDM/DDS epoxy system, Hercules 3501-5a. All of the peaks are identified in Table 7.3. The spectrum of a sample of 3501-5a exposed to a solution of pH = 12 for 8 months is shown in Figure 7.14. No significant differences in the spectra can be detected, strong evidence that high pH solutions have no effect on TGDDM/DDS epoxies.

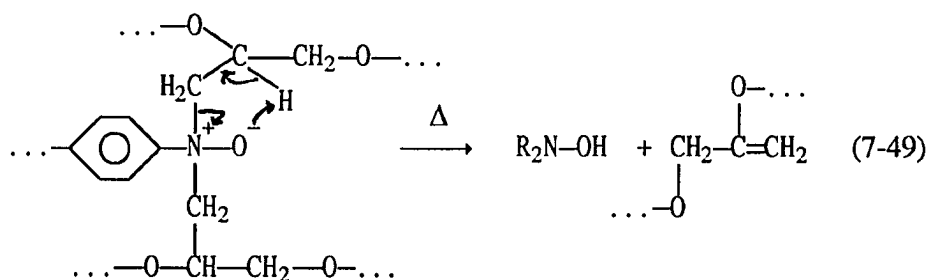
The spectrum of Figure 7.15 was taken from a sample of 3501-5a which was exposed to a solution of 5 % H<sub>2</sub>O<sub>2</sub> for one year. This spectrum shows significant changes compared with the control, primarily the marked reduction of the 1514 peak. The 1514 absorption peak which decreased in intensity comes from the

semi-circle stretch of the para-substituted phenyl groups of TGDDM and DDS. The frequency and intensity of this peak are dependent on the ring substituents, implying that a substituent of the phenyl groups has been altered. Two broad peaks also appear near 1650 and 1290  $\text{cm}^{-1}$  in the corroded sample. The 1650 peak is generally associated with C=C and C=N groups but can also be attributed to primary amine  $\text{NH}_2$  deformation. The 1290 peak is associated with the primary amine (C-N stretch) and suggests that the 1650 peak is also attributable to the formation of a primary amine. A smaller peak appears in the spectra near 1720 as a shoulder of the 1650 peak. Peaks in this region are normally attributed to carbonyl C=O stretch.

The secondary and tertiary amines of the DDS and TGDDM are the most likely sites for attack of the cured epoxy by hydrogen peroxide. For example, the tertiary amines of TGDDM can be oxidized by hydrogen peroxide, as discussed by March (1985):



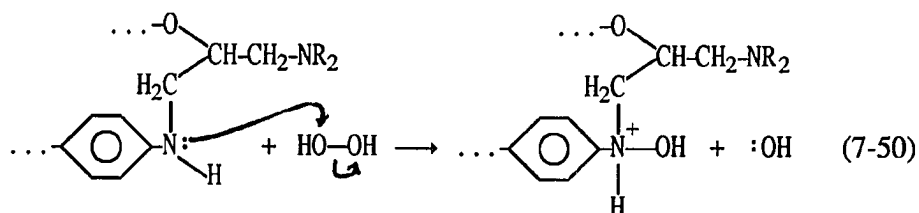
The formation of the amine oxide could be followed by a Cope elimination which would form vinyl compounds, i.e. (March, 1985)



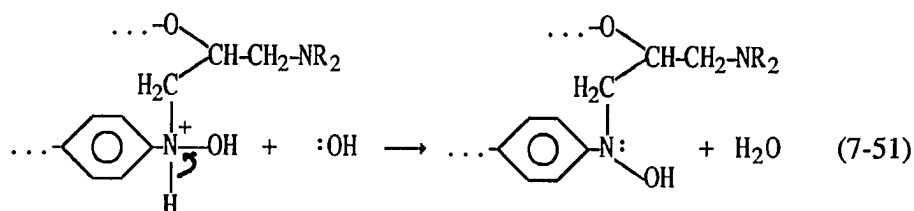
thus accounting for the 1650 C=C peak in the FTIR spectra. However, the Cope elimination generally proceeds with the addition of heat, i.e. the activation energy is

relatively high. Thus this reaction is not likely to have occurred under the present room-temperature conditions.

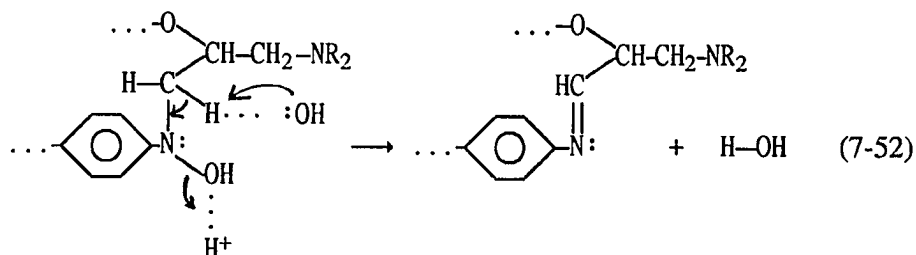
Attack of the secondary amines which formed on crosslinking the DDS with the TGDDM is more favored under the present conditions. Hydrogen peroxide would first form the amine hydroxide, i.e.



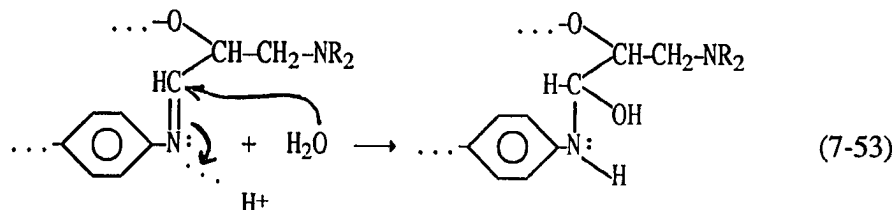
then



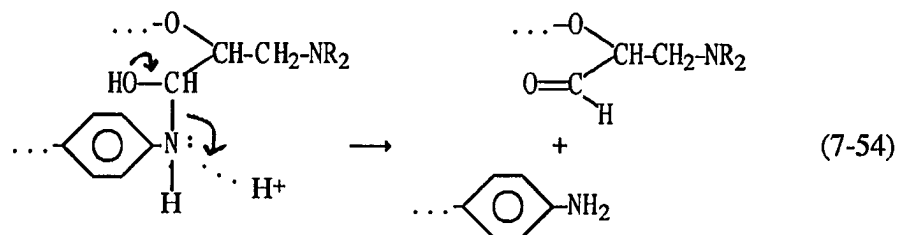
Under slightly acidic (or basic) conditions hydrolysis of the amine hydroxide would then occur,



followed by hydrolysis

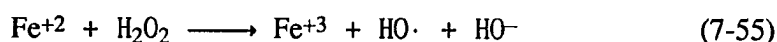


and finally formation of the aldehyde, i.e.

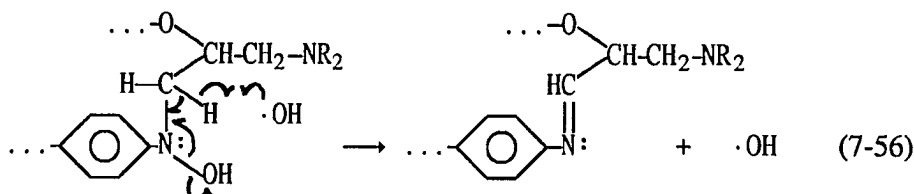


This mechanism would account for all of the peaks which appeared in the FTIR spectra, and would proceed under room temperature conditions.

A third possible damage mechanism involves attack by free radicals, which form as a result of interaction between hydrogen peroxide and metal ion impurities in the solution, e.g.



Hydroxide radicals tend to randomly abstract hydrogen atoms, e.g.

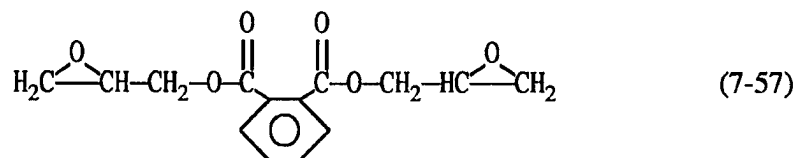


In this case the chain would be ruptured as in equations (7-53) and (7-54). A similar radical damage mechanism might involve other portions of the polymer.

The observed changes in the FTIR spectra of Figs. 7.13 and 7.15 support the hypothesis of attack of the secondary amine groups of the cured DDS. However, the similarities between reactions (7-52) and (7-56) make definite conclusions regarding specific mechanisms difficult. The  $\text{H}_2\text{O}_2$  exposure experiment could have been improved by the inclusion of an exposure test in which a kelating agent such as EDTA was added to the solution to prevent the formation of hydroxide radicals.

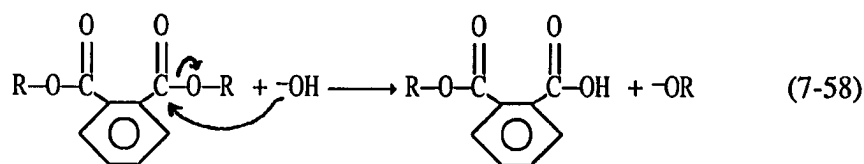
The 934 epoxy, also a TGDDM/DDS resin system, was corroded where hydroxide and hydrogen peroxide were being produced. The logical conclusion based on the results of the exposure experiments discussed above would be that

$\text{H}_2\text{O}_2$  is the agent responsible for damage. However, the control spectrum of the 934 TGDDM/DDS epoxy shown in Figure 7.16 contains extra peaks in the vicinity of 1285 and 1715 when compared with the 3501 epoxy control spectrum. These peaks have been identified as originating in a phthalate, namely diglycidyl *o*-phthalate (DGOP),



which is added to the TGDDM/DDS in the 934 system as a diluent. As discussed by Kong (1986), the 934 formulation consists of 63.2 weight % TGDDM as the primary epoxy constituent. 11.2 % DGOP is added as a diluent to lower the viscosity and improve fiber wet-out. 25.3% DDS is added as the principal crosslinking agent, and 0.4% of the  $\text{BF}_3$  complex is added as a polymerization catalyst.

The spectrum of the corroded 934 specimen is shown in Figure 7.17. The phthalate peaks have been sharply reduced, with little change in the remaining peaks. Thus attack of the phthalate group is indicated. There is no indication of peroxide attack of the secondary DDS amines as discussed above. The most likely mechanism for the observed 934 degradation is a saponification of the ester bonds in the DGOP (March, 1985), i.e.



Ester hydrolysis could have been caused by  $\text{H}_2\text{O}_2$  as well as hydroxide. However, the products of the hydrolysis would have been lost in the test solution (i.e. the seawater electrolyte), or would have been lost during the drying process as volatiles.

Using the analytical tools of this experiment it is not possible to distinguish which ion was responsible for ester hydrolysis. Given the much higher concentrations of hydroxide, and the lack of evidence of attack of the amine groups by hydrogen peroxide, the suggested damage mechanism for cathodic polarization damage in 934 epoxy is saponification of ester bonds in the phthalate additive DGOP.

Analysis of the corroded 934 spectrum is complicated by the effects of the high temperature (200 °C) baking which occurred immediately following the galvanic coupling exposure. Figure 7.18 is the spectrum of a control specimen which was baked under the same conditions as the corroded sample. Comparison with the unbaked control spectrum of Figure 7.16 shows an increase in the intensity of several peaks, along with the appearance of a new peak at 1375. The changes in the peak intensities is most likely a result of post-cure reactions. For example the new peak appears in the spectral region of tertiary amines, and probably resulted from the post-cure reaction of the secondary amines of the partially-reacted DDS.

The analytical methods used in the present experiment could have been improved in several ways. No effort was made in the present experiments to resolve amine peaks in the 2500-3500  $\text{cm}^{-1}$  because of atmospheric moisture in the samples. By drying the KBr at higher temperatures and pressing the KBr pellets under vacuum, interference from water could be reduced. Also, the spectra shown in these experiments were composed of 16 scans per spectrum, with a resolution of 4  $\text{cm}^{-1}$ . Higher resolution scans (e.g. 1  $\text{cm}^{-1}$ ) might have made peak identification more rapid and more accurate.



## 7.6. CONCLUSIONS

The purpose of the present study was to ascertain the most likely cause of damage in a T-300/934 graphite/epoxy composite material which corroded as a result of galvanic coupling to magnesium in seawater. Hydroxyl and/or perhydroxyl ions were suspected of causing the damage.

Rotating ring disk data has been presented which shows that a significant amount of oxygen is reduced to hydrogen peroxide on a graphite cathode, and that the resulting  $\text{H}_2\text{O}_2$  is not immediately reduced to hydroxide. Also, a theoretical analysis of the pH levels behind a calcareous film showed that pH in excess of 11.3 is likely for the cathodic polarization levels encountered in the galvanic couple. Under these high-pH conditions a significant portion of the hydrogen peroxide would exist as the perhydroxyl ion, which is hundreds of times more reactive as a nucleophile than hydroxyl.

A gravity separation technique has been demonstrated which greatly increases the signal-to-noise ratio of graphite/epoxy FTIR transmission spectra. FTIR spectra obtained using this technique indicate that hydroxide ion in high pH solutions has no effect on TGDDM/DDS graphite/epoxy matrix resins. However, dilute solutions of hydrogen peroxide significantly degrade these polymers by attacking the secondary amine of the cured DDS crosslinker.

The cathodic polarization damage which occurred in the 934 epoxy was found to result from ester hydrolysis of phthalate resin diluents which are part of the 934 epoxy formulation. There is no evidence to suggest that hydrogen peroxide participated in the cathodic polarization damage of the 934 resin. However, ester hydrolysis initiated from hydrogen peroxide is indistinguishable from ester

hydrolysis initiated by hydroxide alone, at least for the experimental methods utilized in this study.

Polymer composite matrix resins that are to be used in marine applications where galvanic coupling to metals is a possibility should not include hydrolyzable linkages such as esters. Composite materials, including graphite-fiber-reinforced plastics, are very likely to come into contact with metals during marine service because of the universal use of structural metals such as steel. Although sealer coatings and fiberglass or organic-fiber insulating plies are effective isolation techniques, these preventative measures will break down over time. By avoiding matrix resins that are susceptible to high pH environments, the damage caused by cathodic polarization can largely be eliminated. Polyester is an extreme example of a hydrolyzable matrix resin.

TABLE 7.1. ENVIRONMENTAL PARAMETERS USED IN pH MODEL

Parameter	Value	Comment/Reference
Bulk Diffusivities, $D_b$ :	$\times 10^5 \text{ cm}^2/\text{sec}$	
OH	5.3	Newman
HCO <sub>3</sub>	1.1	Newman
CO <sub>3</sub>	1.0	Assumed
Film Diffusivity Factor, $\phi$ :		
$D_f = \phi \times D_b$	$0 < \phi < 1$	Model Parameter
Diffusion Layer Thickness:		
$\delta_d$	0.020 cm	Dexter and Lin
Calcareous Film Thickness:		
$\delta_f$	0.2 cm max	Model Parameter
Equilibrium Constants:		
Water:		
pK <sub>w</sub> '	13.7	Stumm and Morgan
Carbonic Acid:		
pK <sub>1</sub> '	6.03	Stumm and Morgan
pK <sub>2</sub> '	9.18	Stumm and Morgan
Hydrogen Activity, pH:	8.00	Assumed
Alkalinity, TA:	2.47 meq/liter	Stumm and Morgan

TABLE 7.2. RESULTS OF RRDE EXPERIMENTS

Disk Potential (mV SCE)	$(I_d/I_r)$		$(I_{d,1}-I_d)/I_r$		$k_1$	$(\times 10^3)$ $k_2$	$k_3$
	slope	intcpt	slope	intcpt			
-800	2.18	26.2	0.0219	1.46	9.1	3.8	0.000
-900	16.9	27.5	0.0198	1.45	10.7	4.2	0.003
-1000	35.5	28.8	0.0246	1.42	9.1	3.4	0.007

TABLE 7.3. FTIR BAND ASSIGNMENTS IN CURED TGDDM/DDS EPOXY  
(Levy et al, 1979; Luoma and Rowland, 1986; Colthup et al, 1990)

Wavenumber cm-1	Position	Origin	Remarks
560	Sulfone	DDS	Scissors deformation, strong
690/718	Phenyl	TGDDM/DDS	Sextant bending, mass sensitive
802/820	Phenyl	TGDDM/DDS	C-H wag for ortho-sub
1013	Phenyl	TGDDM/DDS	Sextant stretch, weak
1075	Ether	Cured Epoxy	C-O stretch, ether or alcohol
1104	Sulfone	DDS	Strong, sharp
1141	Sulfone	DDS	Strong, symmetric stretch
1188	Amine	TGDDM	Weak, tertiary amine
1228	Amine	TGDDM	Weak, tertiary amine
1280	Amine	DDS	Secondary amine of cured DDS
1340	Amine	TGDDM	Tertiary amine C-N stretch
1452	Chain	TGDDM	Aliphatic C-H stretch
1514	Phenyl	TGDDM/DDS	Semi-stretch, substituent-sensitive
1594	Phenyl	TGDDM/DDS	Quad-stretch, less sensitive

TABLE 7.4. ASSIGNMENT OF EXTRANEEOUS BANDS IN FTIR SPECTRA

Wavenumber cm-1	Suspected Position	Suspected Origin	Remarks
668	CO <sub>2</sub>	Lab Air	Air entrained in KBr disk
1280	Phthalate	DGOP	Ester C-O stretch, overlaps amine
1290	Amine	DDS	Primary amine C-N stretch
1375	Amine	DDS	Tertiary DDS amine in baked 934
1385	CO <sub>2</sub>	Lab Air	Air entrained in KBr disk
1654	Amine	DDS	Primary amine NH <sub>2</sub> deformation
1716	Phthalate	DGOP	Ester C=O stretch
1720	See text	Chain	Aldehyde C=O stretch

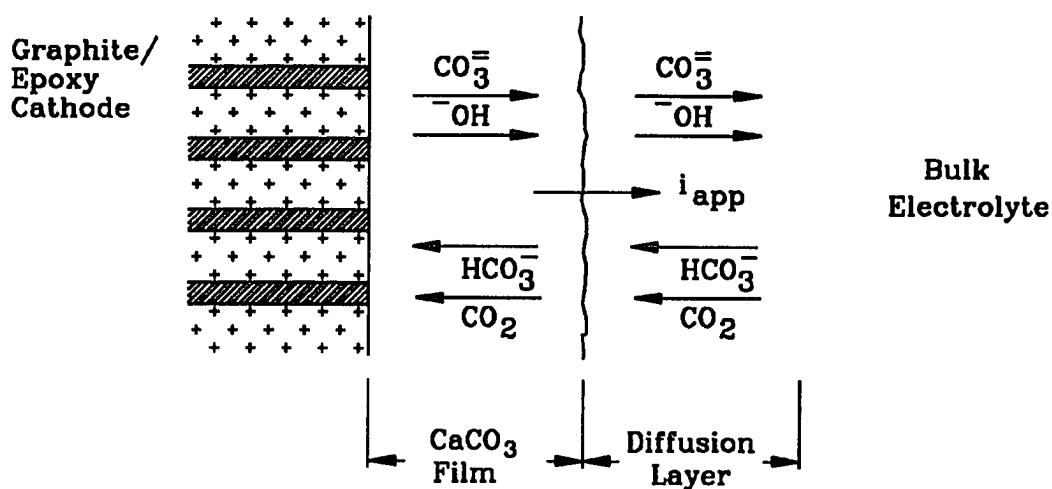


Figure 7.1. Ion fluxes at a surface film. The charge flux to the film less the charge flux away from the film must be balanced by the applied current.

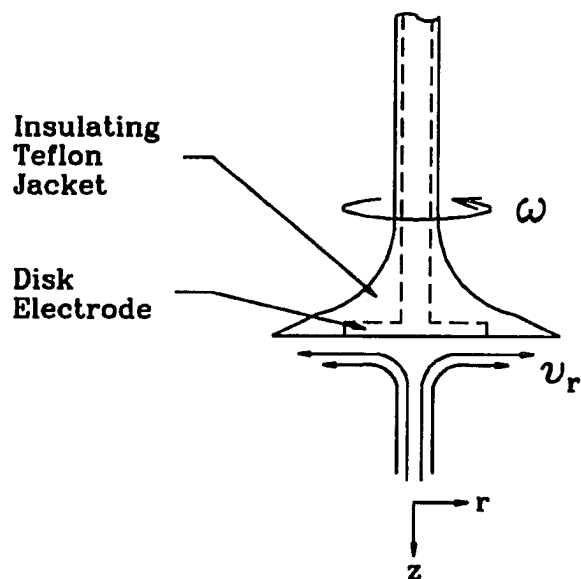
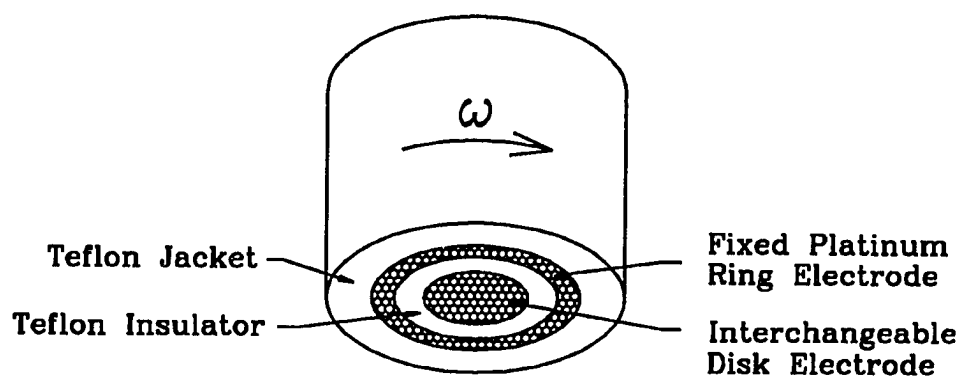
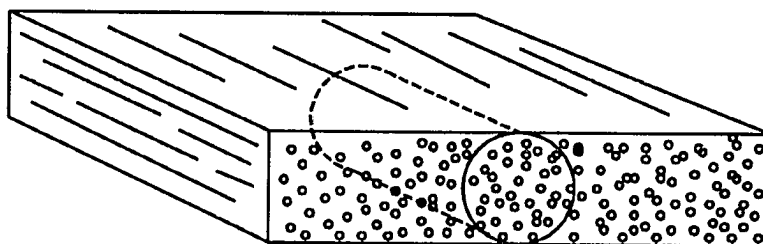


Figure 7.2. The rotating disk electrode. The diffusion-limited current on the disk is proportional to the rate of rotation.



**Figure 7.3.** The rotating ring-disk electrode. By applying different potentials to the ring and the disk, kinetics of the reactions occurring at the disk can be studied.



**Figure 7.5.** The graphite/epoxy disk electrode as part of the parent laminate. The laminate was first cut into square cross-section strips, then each strip was turned down to the proper diameter in a lathe.

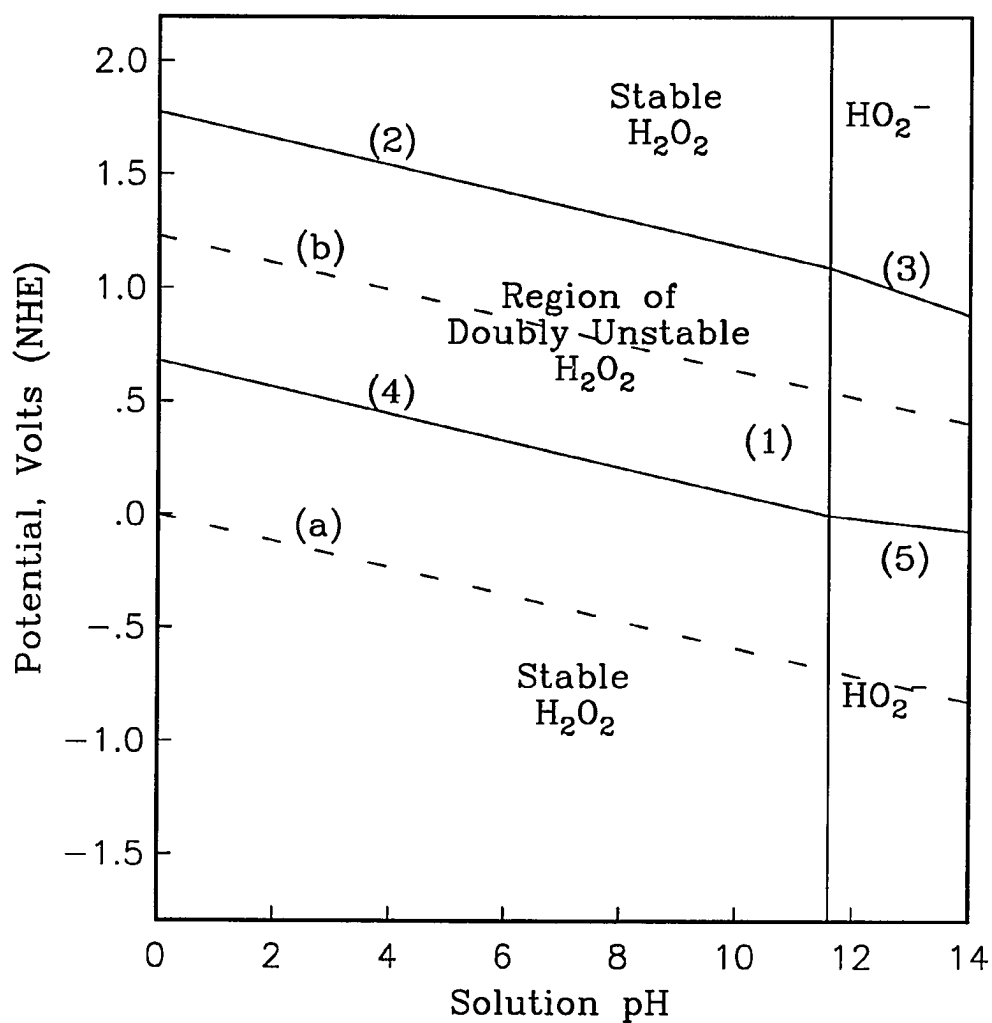


Figure 7.4. Pourbaix diagram for hydrogen peroxide. Hydrogen peroxide will decompose into oxygen and water in the region between lines (2) and (4).

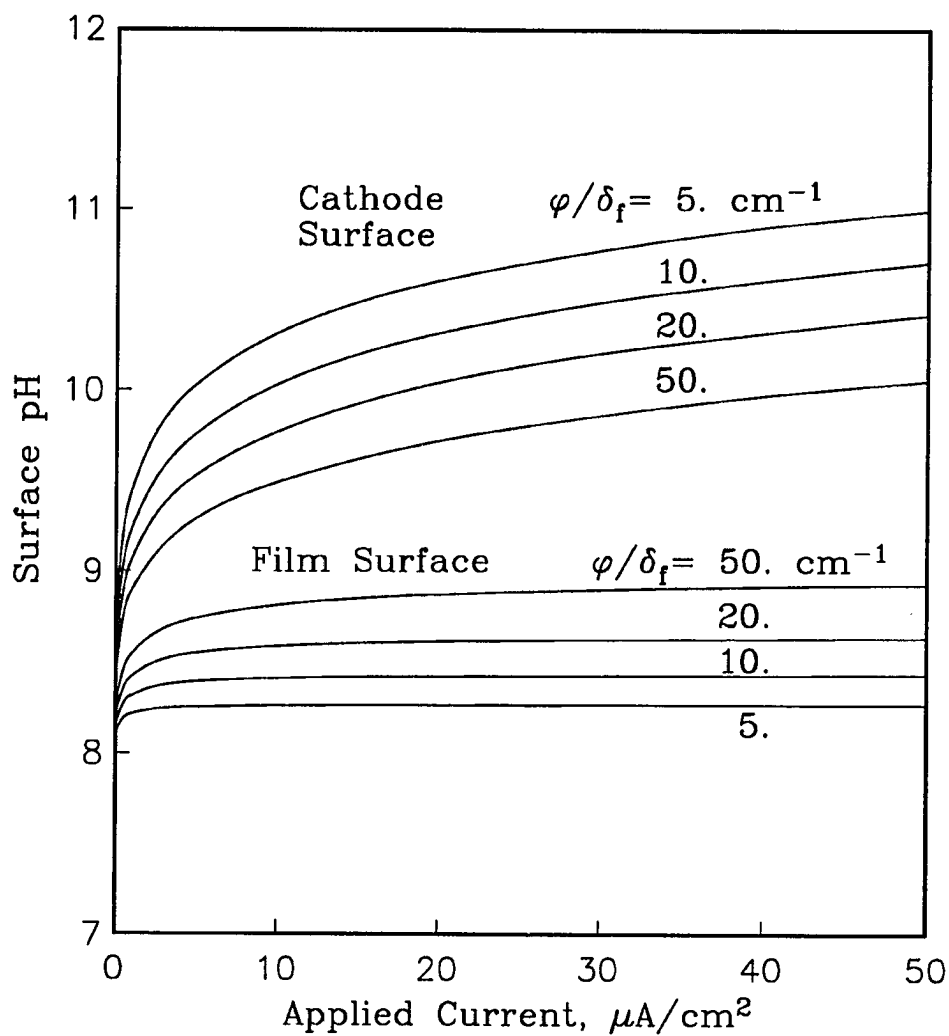


Figure 7.6. Theoretical pH under a calcareous film. The model is sensitive to the film diffusivity factor  $\varphi$  (dimensionless) and the film thickness  $\delta_f$  (cm).



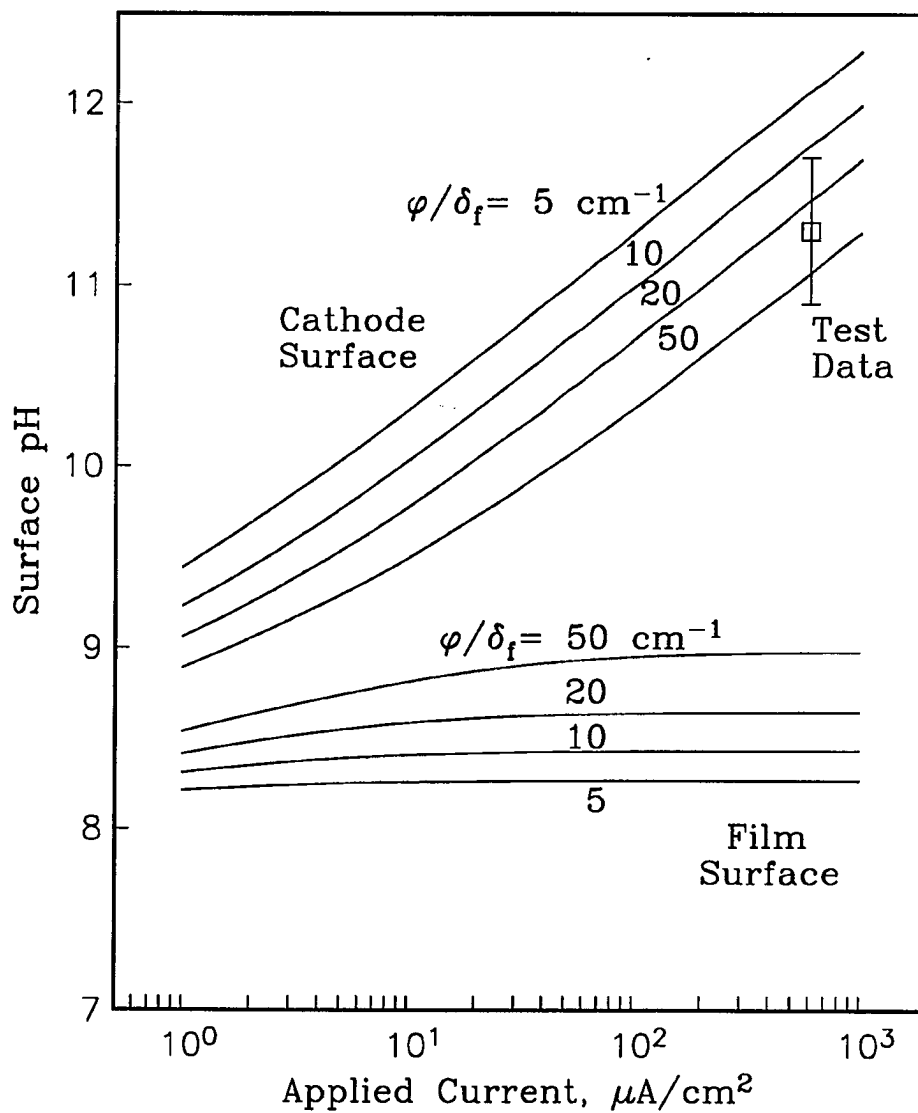


Figure 7.7. Theoretical pH under a calcareous film with experimental data. The model overestimates the pH as compared to the data ( $i_{\text{app}} = 600 \mu\text{A}/\text{cm}^2$ ,  $\phi/\delta_f = 5 \text{ cm}^{-1}$ ).

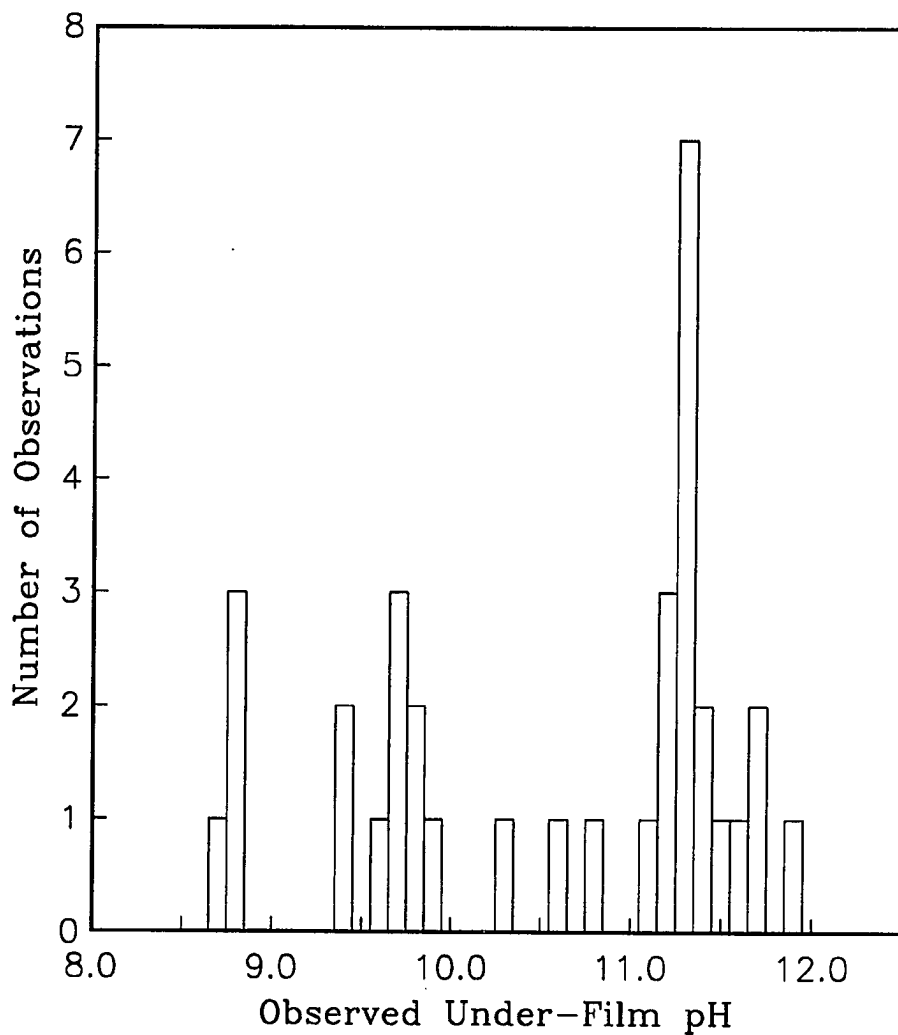


Figure 7.8. Histogram of the under-film pH data. The data exhibited a multi-modal distribution, and the largest mode (11.3) was chosen as the most likely estimator of the under-film pH.

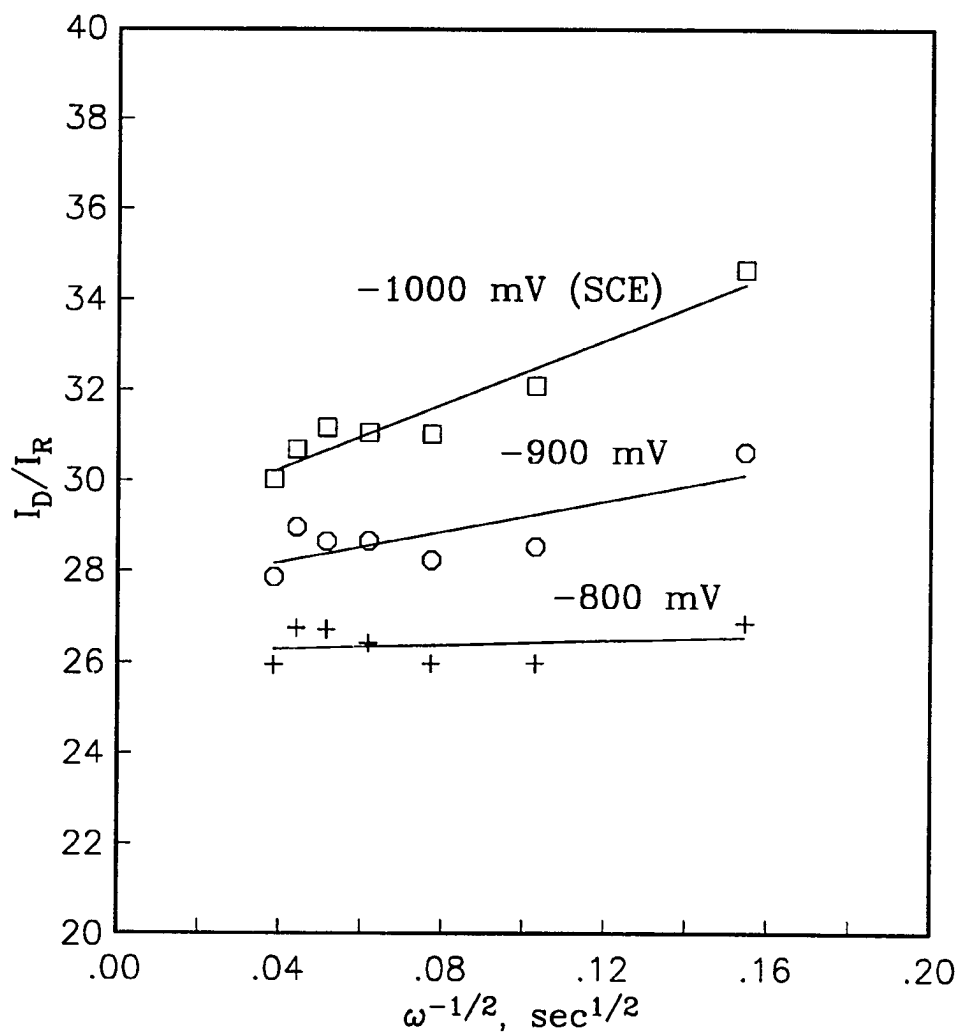


Figure 7.9. Disk-to-ring current ratio as a function of rotation rate for the rotating ring-disk experiments. The data of Figures 7.9 and 7.10 determine the kinetic rate constants  $k_1$ ,  $k_2$ , and  $k_3$ .

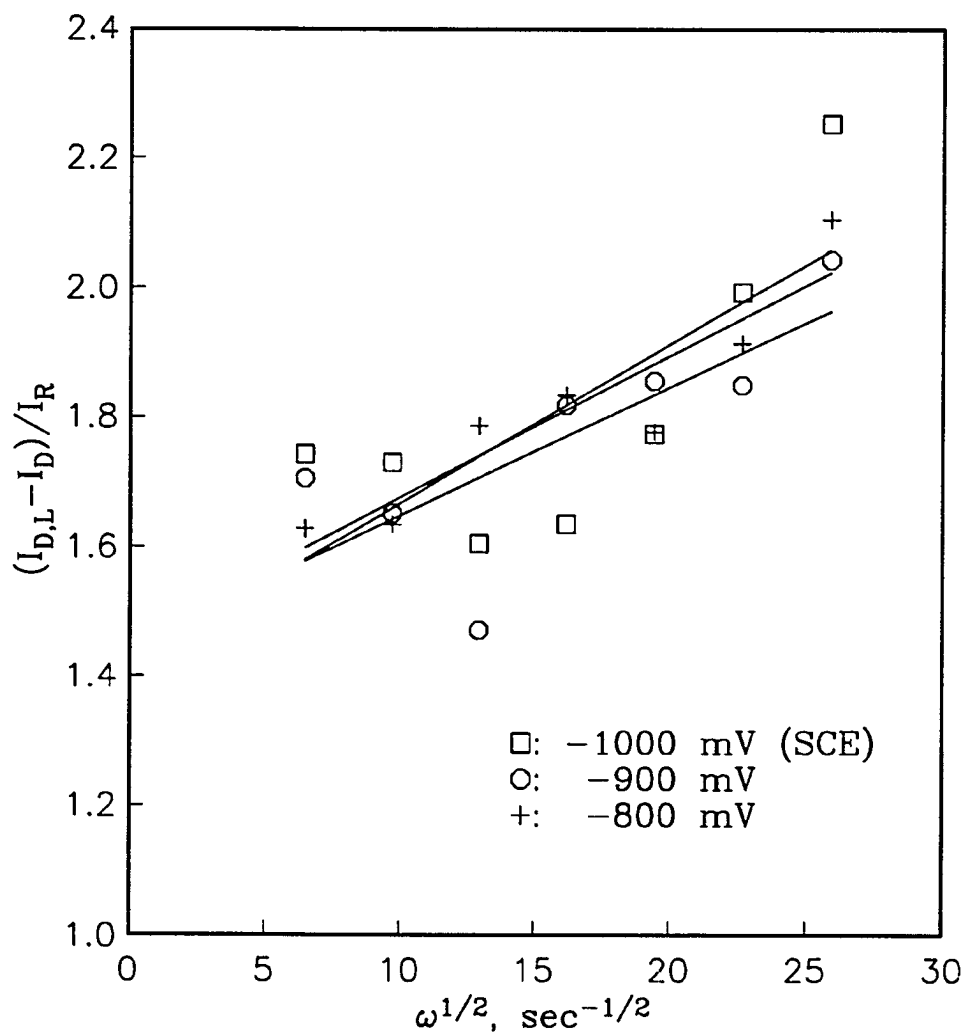


Figure 7.10. Disk-to-ring current ratio as a function of rotation rate for the rotating ring-disk experiments. The data of Figures 7.9 and 7.10 determine the kinetic rate constants  $k_1$ ,  $k_2$ , and  $k_3$ .

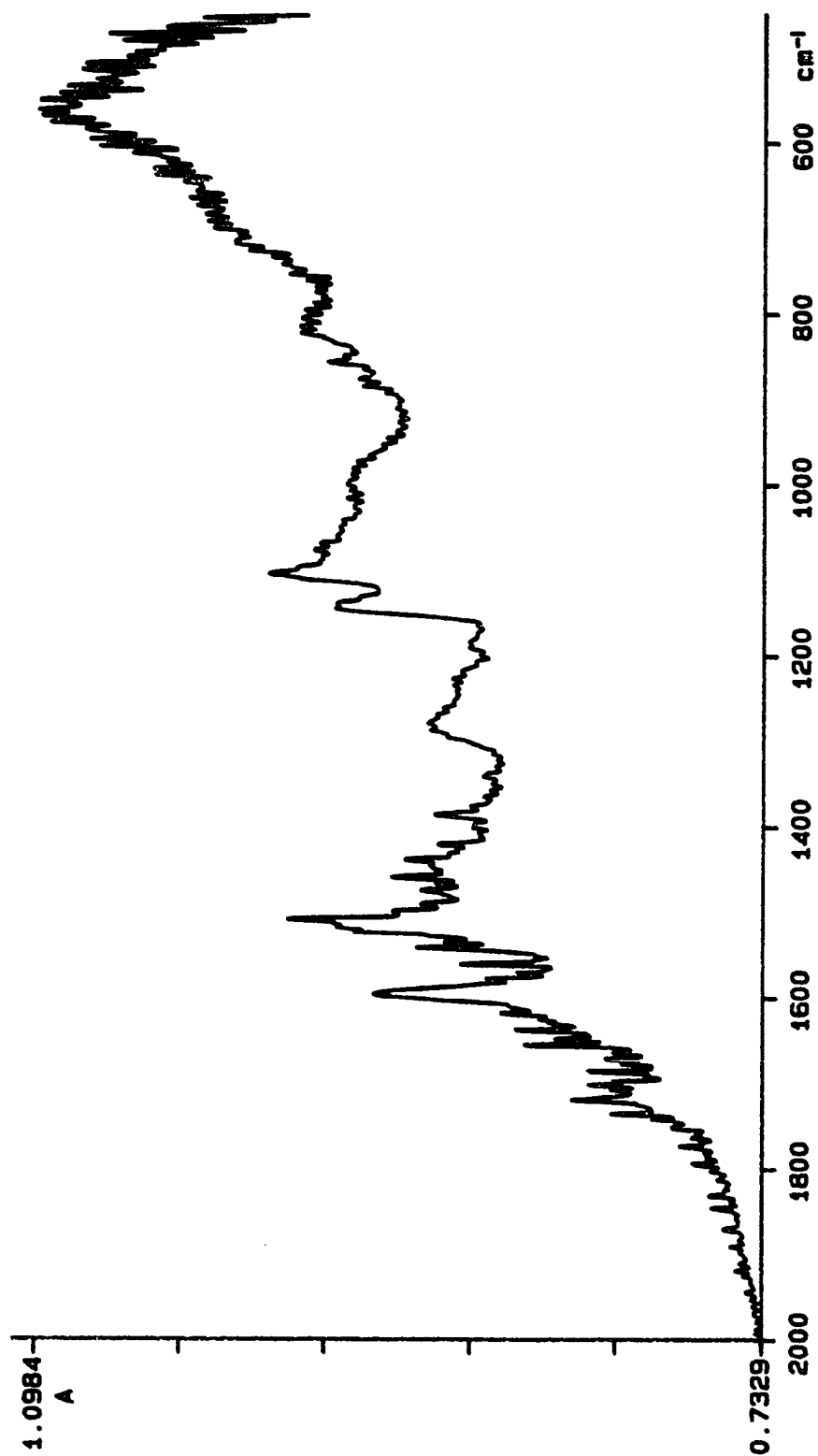


Figure 7.11. FTIR spectrum of a powdered graphite/epoxy sample. Strong broad-band absorption by the graphite obscures peaks which are attributable to the cured epoxy polymer.

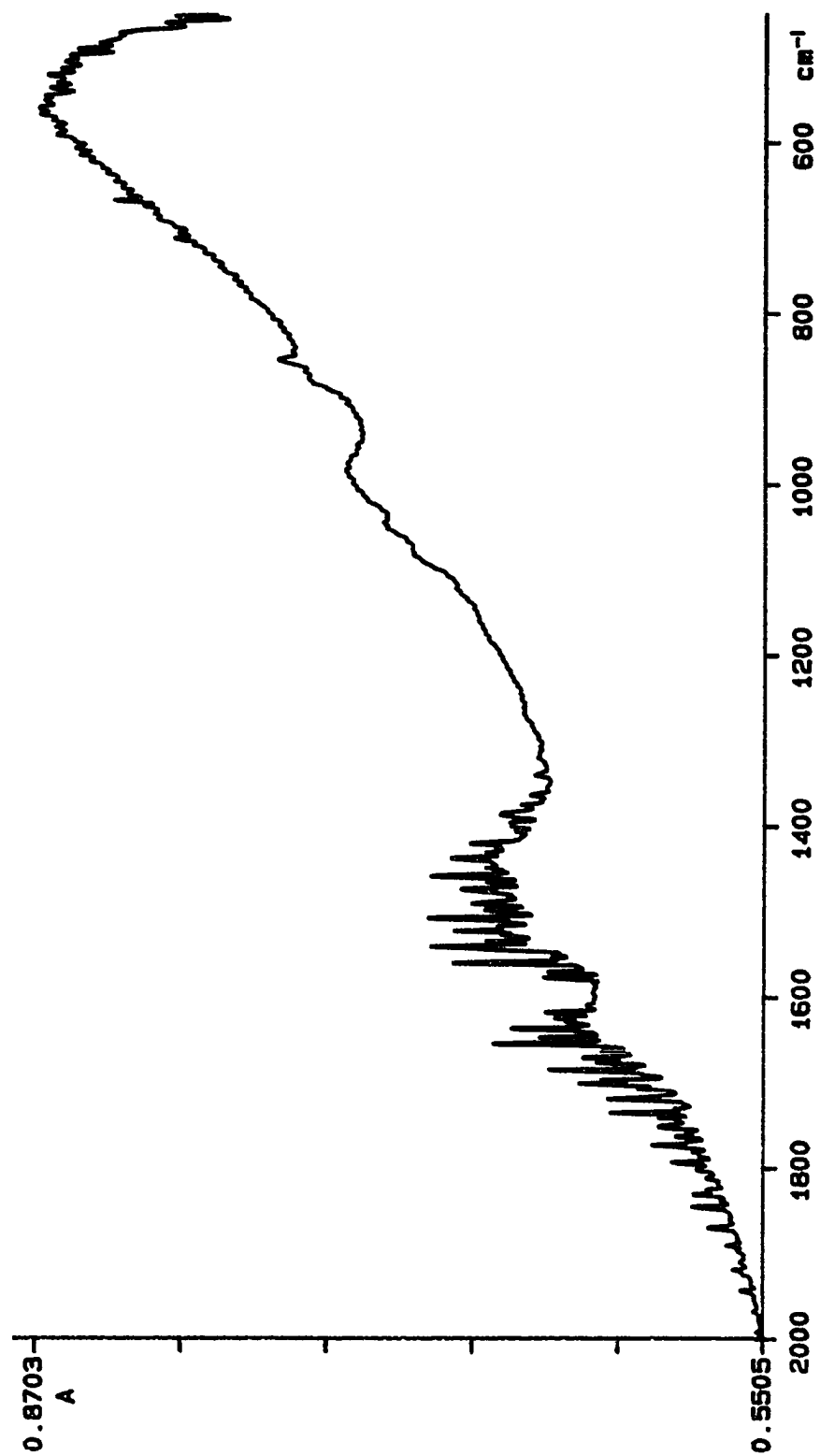


Figure 7.12. FTIR spectrum of ground graphite fibers taken from a sample of graphite cloth. The broad-band absorption of graphite is evident.

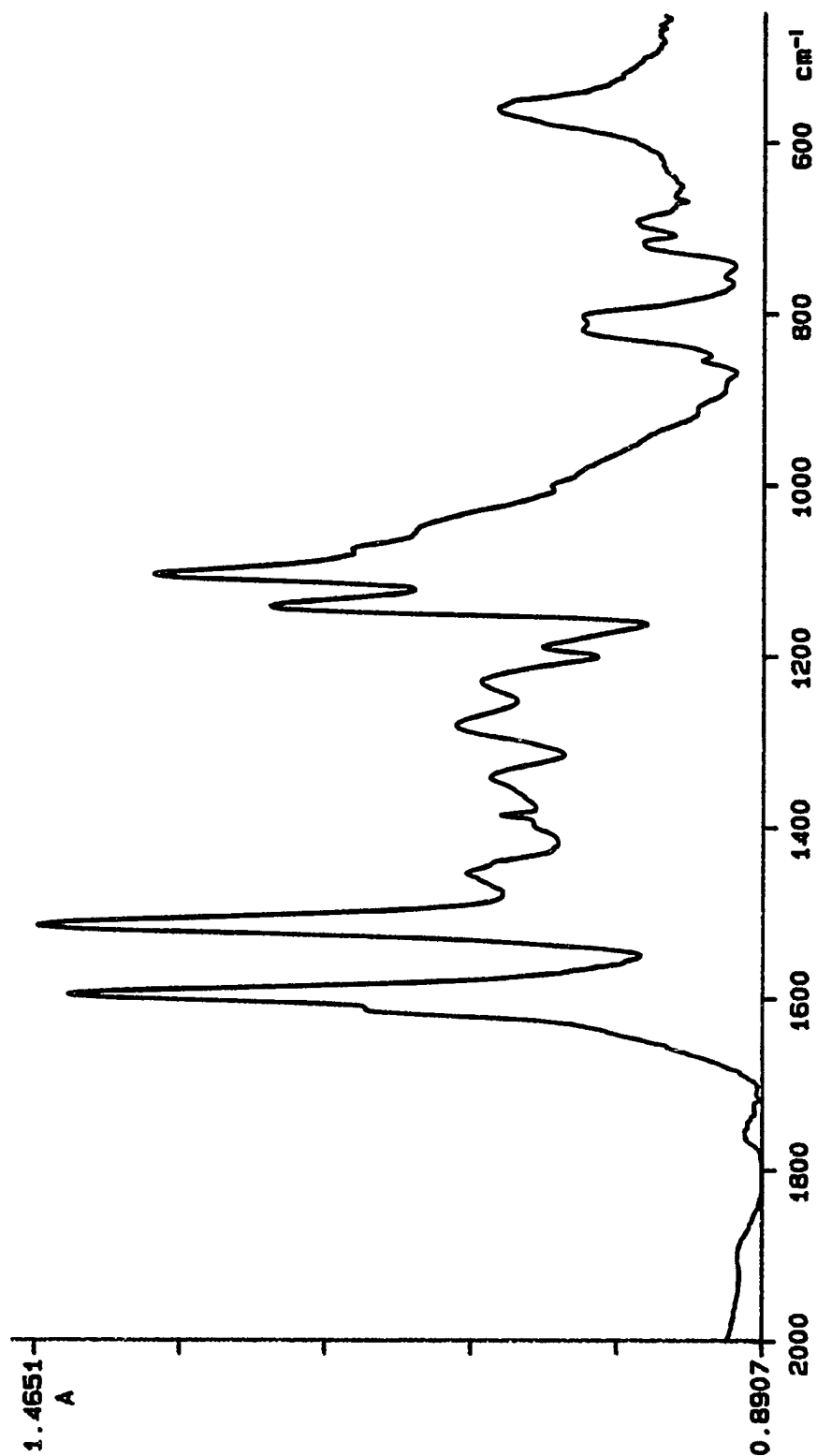


Figure 7.13. FTIR spectrum of cured 3501-5a epoxy which has been separated from the graphite fibers of AS-4/3501-5a graphite/epoxy using a gravitational separation technique. The expected TGDDM/DDS peaks are now clearly identifiable in the separated epoxy.

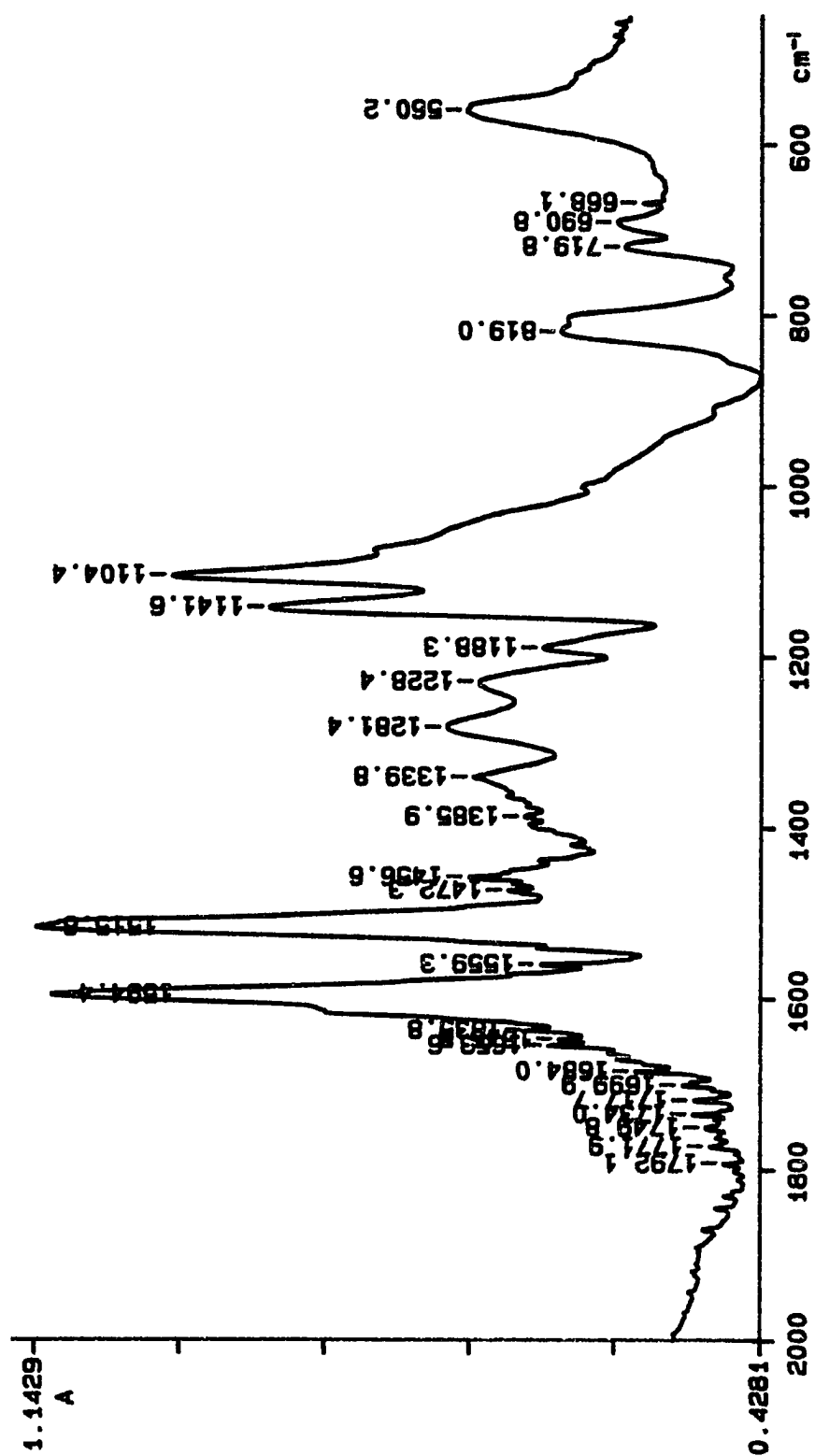


Figure 7.14. FTIR spectrum of 3501-5a epoxy from graphite/epoxy specimens soaked in a pH 12 solution for 8 months. No significant changes from the control spectrum are evident.



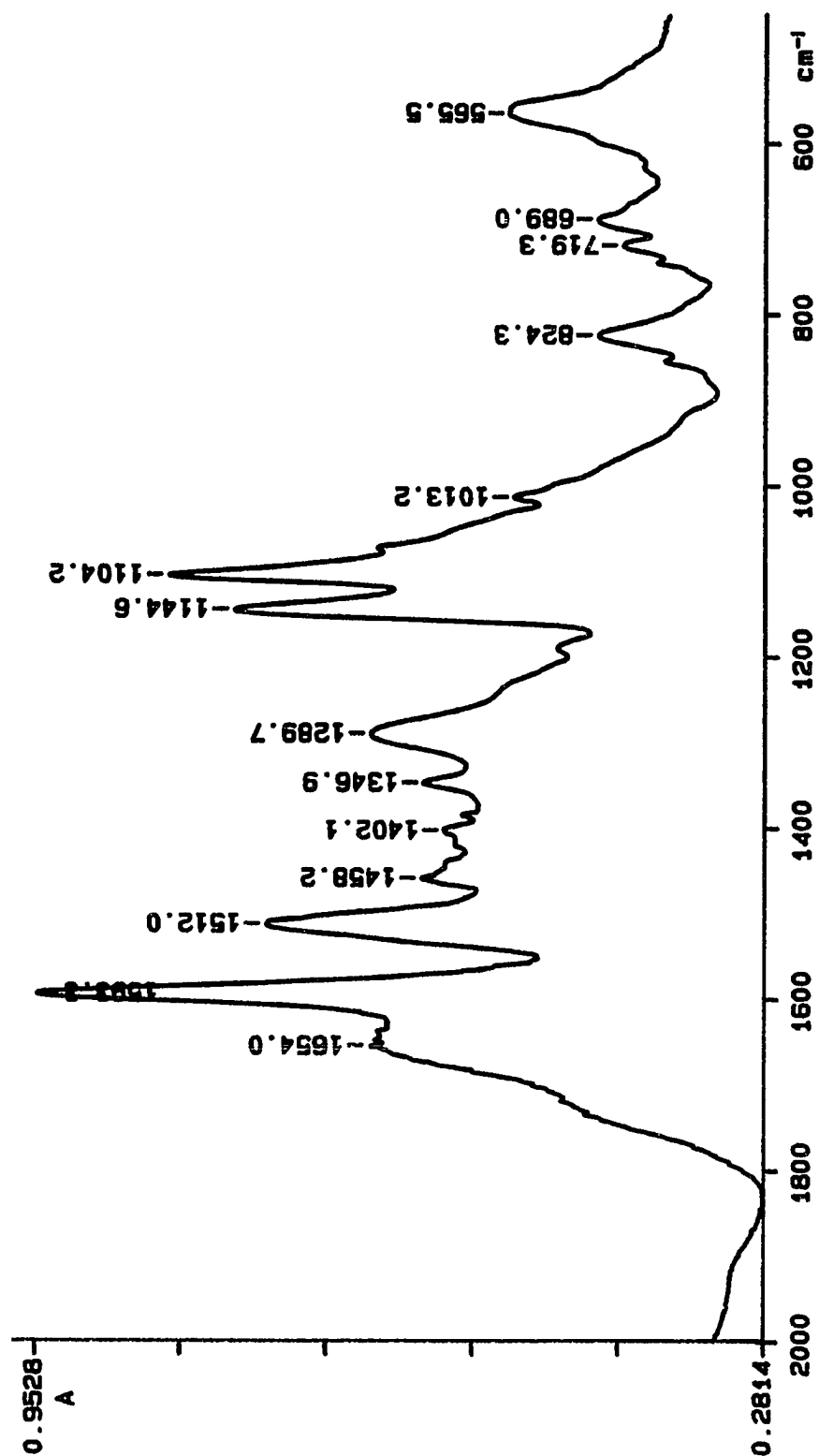


Figure 7.15. FTIR spectrum of 3501-5a epoxy from graphite/epoxy specimens soaked in a 5%  $\text{H}_2\text{O}_2$  solution for 12 months. Substantial changes have occurred in the chemical structure of the epoxy.

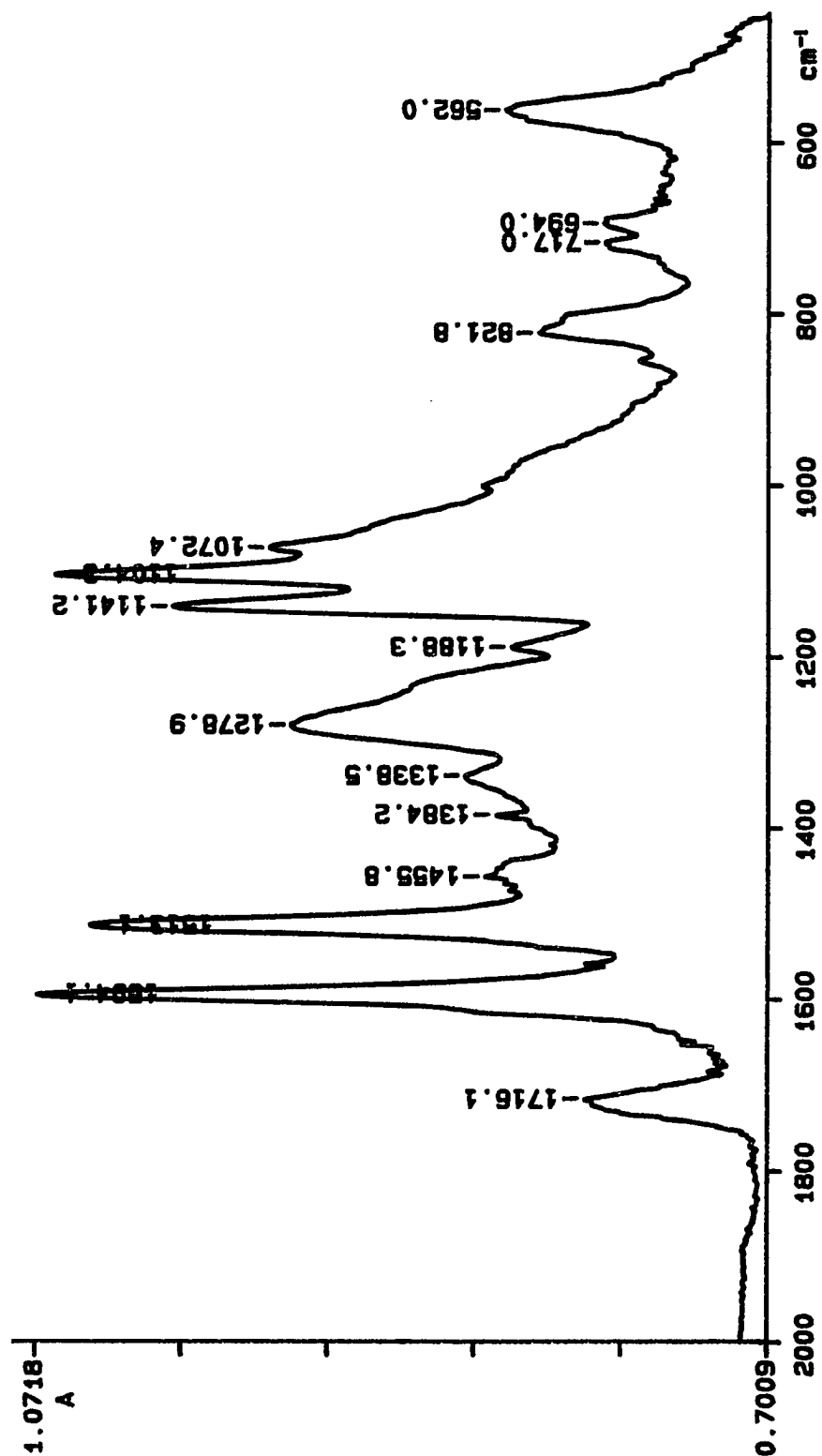


Figure 7.16. FTIR spectrum of cured 934 epoxy which has been separated from a T-300/934 graphite/epoxy sample. Several peaks are present which cannot be attributed to the TGDDM/DDS system. These peaks correspond to the C=O and C-O bonds of the phthalate epoxy additive DGOP.

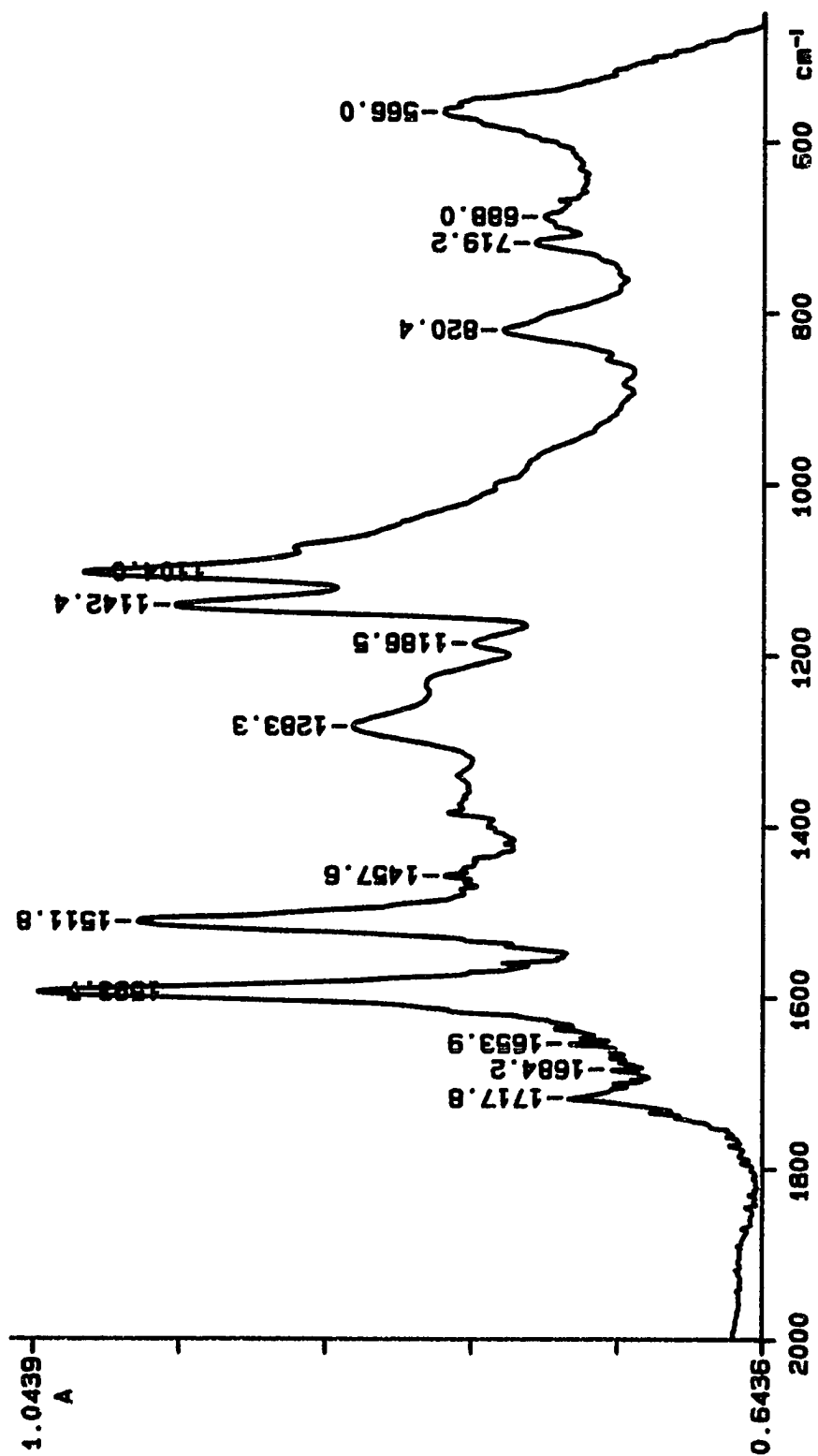


Figure 7.17. FTIR spectrum of 934 epoxy taken from samples corroded under cathodic polarization conditions. The phthalate ester bonds have been preferentially attacked, suggesting that ester hydrolysis is the damage mechanism.

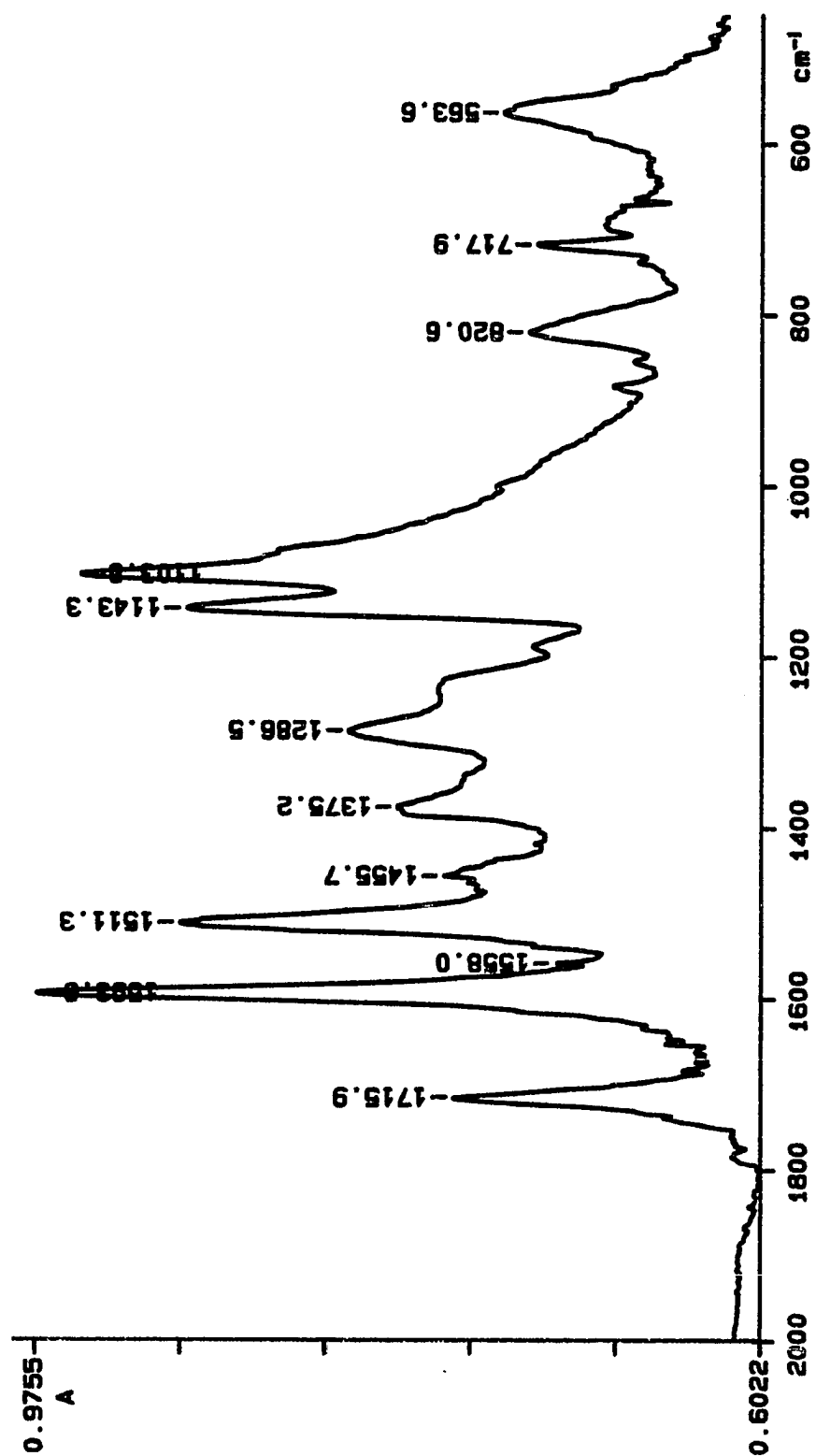


Figure 7.18. FTIR spectrum of 934 epoxy which has been baked at 200°C. Changes in the spectrum compared with control spectra suggest that post-cure reactions have occurred such as the reaction of the DDS secondary amines to form tertiary amines.

## VIII SUMMARY AND RECOMMENDATIONS

### 8.1. INTRODUCTION

The story is often told of the very first "ship" made with composite materials — a small fiberglass skiff built in a New York boat yard for the U.S. Navy. This footnote to history wound up at the bottom of the East River glued firmly to its mold because no one had thought to use mold release. Today small boats are made almost exclusively of fiberglass composites, and the Navy is using fiberglass in a variety of applications, including entire ships (e.g. minesweepers). Future marine structures will continue to use composites, replacing metals in many weight or corrosion critical applications.

Because fiberglass is widely used in many industries, there is a large volume of literature on the environmental degradation of fiberglass composite materials in moist environments. Although great strides have been made in protecting glass against chemical attack, the fact remains that water is a powerful solvent that will chemically attack glass fibers. This limits the long-term applications of fiberglass materials in wet environments.

Because of the long term risks inherent in using glass reinforcing fibers, advanced graphite, aramid, and polyethylene reinforced composite materials are emerging as possible replacements. These materials are much stronger and stiffer than glass on a per-weight basis, and in many applications cost savings due to mass reduction far outweigh any outlays caused by increased material costs. However, in order to utilize these materials confidently in the marine environment, more studies are needed which characterize the long-term effects of seawater exposure. The purpose of this dissertation has thus been to help to characterize these effects in a single composite, namely the graphite-fiber-reinforced epoxies utilized by the

aerospace industry. Many of the damage mechanisms identified in this report are equally applicable to other fiber/matrix composite systems.

## **8.2. SUMMARY**

The degradation which was observed in these studies was generally one of two types: moisture-induced or electrochemically-induced (damage caused by static pressure, solar radiation, and/or biological activity was not included in the present study). Chapters 2 through 4 concentrated on the moisture-induced changes, while Chapters 5 through 7 dealt with electrochemical damage. The first chapter presented a survey of applicable literature involving the use of and the damage mechanisms associated with composite materials in the marine environment.

### **8.2.1. The Effect of Moisture on Static Properties**

Composite materials are damaged by exposure to moist environments because the polymer matrix tends to absorb moisture from the surroundings. This moisture moves through the polymer via diffusion, and weakens the fiber-to-matrix bond of the material. However, the rate of moisture diffusion in polymers is quite small ( $10^{-13}$  m<sup>2</sup>/sec) at typical seawater temperatures, as shown in Chapter 2, and for thick composites equilibrium absorption times can exceed many years. For this reason, short-term soaking of graphite/epoxy composite test samples in water is not likely to cause changes in the mechanical properties of the samples unless the samples are quite small. This result has been confirmed by the work discussed in Chapter 3, as well as by many other investigators.

Test specimens that are small enough to allow rapid equilibrium are generally too small for mechanical testing, thus accelerated testing is preferred. The easiest way to accelerate the diffusion reaction is to raise the energy of the system

by raising the temperature. For this reason many investigators over the years have subjected test materials to boiling water. Studies have recently proven what was long suspected — that the damage caused by moisture absorption and the damage caused by exposure to boiling water are quite different, and is much more severe for boiling water. Composites used in environmental tests should never be exposed to water in excess of 50°C unless the service environment is to be that severe. The temperature at which the specimens are dried also needs to be monitored to ensure that the  $T_g$  of the matrix is not exceeded and post-cure reactions are not induced.

### 8.2.2. The Inadequacy of Static Testing

The above discussion has assumed that changes in mechanical properties can be determined from samples loaded after exposure to the test environment. This is the most common method for determining environmental resistance data in composites, and has been used for many years. This has led to a large (and growing) database of environmental resistance data that, unfortunately, is essentially useless for most applications.

Imagine that a new alloy of steel is being considered for use in structural members on an offshore platform. A consulting engineer is hired to determine if the steel is safe to use in seawater. The consultant soaks samples of the steel for one year, performs a static test, and declares the steel undamaged by the effects of seawater exposure. The consultant's conclusions would of course be completely invalid, having ignored the well-known effects of fatigue and corrosion-fatigue on the useful life of this material. Yet this is the type of data that is repeatedly presented to support the idea that composite materials are safe for use in the marine environment.

When structural members made of composite materials are deployed in ocean engineering applications, they are going to be introduced into a severe combination of environmental attack and fatigue loading. An aggressive environment and fatigue loading always act synergistically to produce damage that is greater than either could produce alone. For this reason static property testing following environmental exposure cannot be expected to reveal damage mechanisms which are applicable to damage accumulation models in composites deployed in the real world. A dry fatigue test should be run at the very least, and a full-scale wet fatigue test in the service environment would be the best (albeit impractical in most cases).

### 8.2.3. Monitoring Damage in Composites

Damage accumulation in composites occurs as the result of simultaneous growth of microcracks which occur throughout the material. This is in contrast with metals, which generally exhibit the establishment early in the fatigue life of a single dominant crack or fracture. Thus whereas a fracture-mechanics-based damage accumulation model, e.g. the Paris crack growth law (which relates the growth dynamics of a single crack to the state of stress at the crack tip), can be used with great success in metals, its applicability to composites is questionable.

Damage-mechanics modeling (which defines "damage" as an intrinsic function of some measurable quantity, e.g. stiffness) is a better approach (Poursartip et al, 1982; Talreja, 1985; Weitsman, 1987), but general models of fatigue and corrosion-fatigue in composites remain elusive. More research in this area is needed, especially in non-destructively sensing damage progression.



#### 8.2.4. Delamination Growth in a Moist Environment

Some of the most interesting work in this study involved monitoring delamination crack growth in unidirectional graphite/epoxy laminates fatigued in seawater. Double-cantilever-beam specimens were chosen for these tests because of their frequent use in the literature on Mode I fracture and fatigue testing. Specimens were loaded with tension springs to provide a region of stable damage growth during the tests. The results of these tests (detailed in Chapter 4) were complicated by the appearance of numerous reinforcing fibers which bridged across the arms of the double-cantilever specimen. These bridged fibers greatly increased the resistance of the material to crack growth. The primary effect of moisture exposure was to weaken the fiber-to-matrix bond so that more fibers were bridged. In this case the weakened interface bond actually increased the resistance of the material to fracture and fatigue.

Although the present study showed that Mode I damage growth is slowed down substantially under moist conditions, the results are not generally applicable to fatigue of graphite/epoxy composites. The fiber-bridging that was observed can be attributed to the unidirectional lay-up used in the test specimens. The same result may not be obtained in bi-directional lay-ups, or when using graphite/epoxy cloth plies. Also, fiber-bridging is a phenomenon that would appear primarily in Mode I loading. There is evidence that Mode II fracture resistance of graphite/epoxy decreases after moisture absorption (Garg and Ishai, 1985). A more complete picture of fatigue behavior in composite laminates would be generated by repeating the studies of Chapter 4 using cloth-ply laminates and/or using a Mode II fatigue configuration.

### 8.2.5. Electrochemical Damage Mechanisms in Graphite/Epoxy

Graphite will conduct electricity, not nearly as well as a metal but well enough to allow current to flow in an electrochemical cell. Thus graphite-reinforced plastics may be susceptible to the same types of electrochemical (i.e. corrosion) damage that metals are. Metals tend to dissolve under anodic polarization conditions and tend to debond from polymers when cathodically polarized. Thus there is good reason to expect that graphite fibers will behave similarly.

Anodic polarization of graphite/epoxy could result from stray electrical currents, as discussed in Chapter 5. Graphite/epoxy coupons exhibited extensive oxidation damage when subjected to anodic currents of as low as  $1 \mu\text{A}/\text{cm}^2$ . The experimental evidence suggests that the graphite fibers are directly attacked by atomic oxygen which is adsorbed at the graphite surface during the oxygen evolution reaction.

Cathodic polarization of graphite/epoxy can easily occur in seawater as the result of galvanic coupling to structural metals. The studies of Chapter 6 showed that galvanic coupling of T-300/934 graphite/epoxy to magnesium can cause localized corrosion damage, with a penetration rate of approximately 5 mm/year. The chemical species most likely to have caused the damage were the hydroxyl and perhydroxyl ions which are evolved at the cathode during oxygen reduction. Chapter 7 detailed studies aimed at identifying the mechanisms by which these two ions might attack an epoxy matrix, and which was involved in the attack of a 934 epoxy matrix. The evidence presented there suggested that the ester bonds of the epoxy additive DGOP were attacked by the hydroxide ion under the high pH conditions at the cathode surface.

Graphite/epoxy composites are similar to metals in that they are susceptible to electrochemical damage, i.e. corrosion. However, graphite-reinforced polymers do not dissolve as a result of electron transfer (as in metals, i. e.  $M \rightarrow M^+ + e^-$ ). Rather, they are attacked by chemical species such as atomic oxygen and perhydroxyl ion that are evolved in the oxygen evolution (anodic) and oxygen reduction (cathodic) reactions.

There are several methods that can be used to minimize electrochemical damage in graphite-fiber-reinforced plastics. The simplest method would be to electrically isolate the composite, through the use of sealer coatings or by using fiberglass or organic-fiber insulation plies as surface plies in the layup of the laminate. However, over long periods of time isolation schemes will fail, typically by erosion, cracking, or by chemical breakdown. Furthermore, the use of coatings and insulation layers complicates the already complex job of joining composites and metals, and reduces the structural efficiency of the design. A more direct method of minimizing the effects of galvanic coupling would be to utilize polymer matrices that are not susceptible to attack by hydroxide. Examples of polymers that would not be susceptible include most thermoplastics as well as many epoxy formulations. Examples of susceptible resins include polyesters and polyimides. When resin formulations are to be used, all additives (such as the DGOP used in 934) should be checked for susceptibility. In any case, an effective safeguard against the effects of galvanic corrosion is periodic inspection to monitor the electrochemical potential of structural elements. By monitoring the corrosion potential of the structure, areas experiencing unexpected galvanic polarization can be identified and proper corrective actions taken.

### 8.3. CONCLUSIONS

The investigations documented here were intended to determine whether graphite-fiber-reinforced plastics can survive the highly aggressive seawater environment when used as structural materials in advanced ocean engineering designs. Two general effects of seawater exposure have been identified as possible life-limiting phenomena. The first effect is a weakening of the fiber-to-matrix bond caused by exposure of the interface to moisture. The second effect is the establishment of an electrolyte (seawater) around the conductive graphite fibers, thus allowing electrochemical reactions to take place. (The effects of static pressure, solar radiation and biological activity were not included in the present investigation).

The fiber/matrix interface bond is weakened as a result of exposure to a moist environment. However, for graphite/epoxy composites the bond does not generally fail in the absence of applied loading. When loads are applied the local effect is for the fiber to de-bond from the matrix. However, the effects on a larger scale are more complex, and may not be intuitive. For example, in the present study it was found that the weakened fiber/matrix bond actually increased the resistance of the material to fatigue and fracture.

Electrochemical degradation can occur as the result of stray-current corrosion or galvanic coupling. Stray-current damage is rapid, involves dissolution of the graphite reinforcing fibers, and can occur under relatively low current conditions. Galvanic coupling damage is a subtle localized corrosion phenomenon involving chemical attack of the polymer resin. Electrochemical damage is the result of interaction with species which form as intermediates in the oxygen reactions on the anode and cathode.

## LIST OF REFERENCES

- Apicella, A. and Nicolais, L., "Effect of Water on the Properties of Epoxy Matrix and Composite," in *Epoxy Resins and Composites I*, K. Dusek, Ed., *Advances in Polymer Science Series*, No 72, Springer-Verlag, New York, 1985, pp. 69-77.
- Ashbee, K. H. G., Frank, F. C., and Wyatt, R. C., "Water Damage in Polyester Resins," *Proceedings of the Royal Society A*, Vol. 300, 1967, pp. 415-419.
- ASM International, *Engineered Materials Handbook, Vol. 1, Composites*, Metals Park, Ohio, 1987.
- ASTM Standard Test Method for Apparent Interlaminar Shear Strength of Parallel Fiber Composites by Short Beam Method, D2344-84, American Society for Testing and Materials, Philadelphia, 1984.
- ASTM Standards and Literature References for Composite Materials*, American Society for Testing and Materials, Philadelphia, 1987.
- ASTM, "Proposed Standard Test Method for Moisture Absorption Properties and Conditioning of Polymeric-Matrix Composite Materials," Committee D30.04, R. Fields, Chairman, American Society for Testing and Materials, Philadelphia, 1989.
- Babolian, R., McBride, L., Langlais, R., and Haynes, G., "Effect of Modern Electronics on Corrosion Technology," *Materials Performance*, Vol. 18, No. 12, 1979, pp. 40-44.
- Belani, J. G. and Broutman, L. J., "Moisture Induced Resistivity Changes in Graphite-Reinforced Plastics," *Composites*, Vol. 9, No. 4, October 1978, pp. 273-277.
- Birger, S., Moshonov, A., and Kenig, S., "The Effects of Thermal and Hygrothermal Ageing on the Failure Mechanisms of Graphite-Fabric Epoxy Composites Subjected to Flexural Loading," *Composites*, Vol. 20, No. 4, July 1989, pp. 341-348.
- Boll, D. J., Bascom, W. D., and Motiee, B., "Moisture Absorption by Structural Epoxy Matrix Carbon-Fiber Composites," *Composites Science and Technology*, Vol. 24, 1985, pp. 253-273.
- Brinke, G. ten, Karasz, F. E., and Ellis, T. S., "Depression of Glass Transition Temperatures of Polymer Networks by Diluents," *Macromolecules*, Vol. 16, 1983, pp. 244-249.
- Brown, A. R. G. and Coomber, D. E., "Behavior of Couples of Aluminum and Plastics Reinforced with Carbon Fibre in Aqueous Salt Solutions," *British Corrosion Journal*, Vol. 7, September 1972, pp.232-235.
- Brown, A. R. G., "The Corrosion of CFRP-to-Metal Couples in Saline Environments," Presented at the International Conference on Carbon Fibres, their Place in Modern Technology, London, February 1974, Paper No. 35, The Plastics Institute, Inc.

Browning, C. E. and Hartness, J. T., "Effects of Moisture on the Properties of High-Performance Structural Resins and Composites," *Composite Materials: Testing and Design (Third Conference)*, ASTM STP 546, American Society for Testing and Materials, 1974, pp. 284-302.

Browning, C. E., "The Mechanisms of Elevated Temperature Property Losses in High Performance Structural Epoxy Resin Matrix Materials After Exposure to High Humidity Environments," *Polymer Engineering and Science*, Vol. 18, No. 1, January 1978, pp. 16-24.

Browning, C. E., Abrams, F. L., and Whitney, J. M., "A Four-Point Shear Test for Graphite/Epoxy Composites," *Composite Materials: Quality Assurance and Processing*, ASTM STP 797, C. E. Browning, Ed., American Society for Testing and Materials, 1983, pp. 54-74.

Browning, C. E., Husman, G. E., and Whitney, J. M., "Moisture Effects in Epoxy Matrix Composites," *Composite Materials: Testing and Design (Fourth Conference)*, ASTM STP 617, American Society for Testing and Materials, 1977, pp. 481-496.

Butkov, E., *Mathematical Physics*, Addison-Wesley, 1968.

Carlsson, L. A., and Pipes, R. B., *Experimental Characterization of Advanced Composite Materials*, Prentice-Hall, 1987.

Cassidy, P. E. and Aminabhavi, T. M., "Enhanced Environmental Degradation of Plastics," *Journal of Macromolecular Science -- Reviews in Macromolecular Chemistry*, Vol. C21 No. 1, 1981, pp. 89-133.

Cole, K. C., Noel, D., and Hechler, J.-J., "Applications of Diffuse Reflectance Fourier-Transform Infrared Spectroscopy to Fiber-Reinforced Composites," *Polymer Composites*, Vol. 9, No. 6, December 1988, pp. 395-403.

Cole, K. C., Pilon, A., Noel, D., Hechler, J.-J., Chouliotis, A., and Overbury, K. C., "Comparison of Infrared Spectroscopic Methods for the Quantitative Analysis of Epoxy Resins Used in Carbon-Epoxy Composite Materials," *Applied Spectroscopy*, Vol. 42, No. 5, 1988, pp. 761-769.

Colins, J. A., *Failure of Materials in Mechanical Design*, Wiley, New York, 1981.

Collings, T. A., and Stone, D. E. W., "Hygrothermal Effects in CFRP Laminates: Stresses Induced by Temperature and Moisture," *Composites*, Vol. 16, No. 4, October 1985, pp. 307-316.

Colthup, N. B., Daly, L. H., and Wiberley, S. E., *Introduction to Infrared and Raman Spectroscopy*, 3rd Ed., Academic Press, 1990.

Crump, W. A. and Riewald, P. G., "Lighter and Stronger Ships," *Proceedings, U. S. Naval Institute*, September 1983.

Danieley, N. D. and Long, E. R., "Effects of Curing on the Glass Transition Temperature and Moisture Absorption of a Neat Epoxy Resin," *Journal of Polymer Science: Polymer Chemistry Edition*, Vol. 19, 1981, pp. 2443-2449.

Davy, H., "On the Corrosion of Copper-sheeting by Sea-water, and on Methods of Preventing this Effect; and on their Application to Ships of War and other Ships," Philosophical Transactions of the Royal Society of London, Series A, 1824, pp. 151-158.

DeIasi, R. and Whiteside, J. B., "Effect of Moisture on Epoxy Resins and Composites," Advanced Composite Materials -- Environmental Effects, ASTM STP 658, J. R. Vinson, Ed., American Society for Testing and Materials, 1978, pp. 2-20.

DeLuccia, J. J., "Electrochemical Aspects of Hydrogen in Metals," Hydrogen Embrittlement: Prevention and Control, ASTM STP 962, L. Raymond, Ed., American Society for Testing and Materials, Philadelphia, 1988, pp. 17-34.

Dexter, S. C. and Lin, S-H., "Calculation of Seawater pH at Polarized Metal Surfaces with Calcareous Deposits and Biofilms," Corrosion/91, National Association of Corrosion Engineers, Houston, Paper Number 499.

Dexter, S.C. and Culberson, C., "Global Variability of Natural Sea Water," Materials Performance, Vol. 19, No. 9, September 1980, pp. 16-28.

Dharan, C. K. H., "Fracture Mechanics of Composite Materials," Journal of Engineering Materials and Technology, Vol. 100, July 1978, pp. 233-247.

Dickie, R. A., and Floyd, F. L., Eds., *Polymeric Materials in Corrosion Control*, American Chemical Society, Washington, D.C., 1986, ACS Symposium Series No. 322.

Donaldson, P., "Stop the Rot," Aerospace Composites and Materials, Vol. 1, No. 4, 1989, pp. 19-23.

Dougherty, R. H., "Carbon Fiber for Maritime Structures," Presented at the Los Angeles Section, Society of Naval Architects and Marine Engineers, February 14, 1974.

Drzal, L. T., "The Interphase in Epoxy Composites," in Epoxy Resins and Composites II, K. Dusek, Ed., Advances in Polymer Science Series, No. 75, Springer-Verlag, New York, 1986, pp. 1-32.

Drzal, L. T., Rich, M. J., and Lloyd, P. F., "Adhesion of Graphite Fibers to Epoxy Matrices: I. The Role of Fiber Surface Treatment," Journal of Adhesion, Vol. 16, 1982, pp. 1-30.

Elbeik, S., Tseung, A.C.C., and Mackay, A.L., "The Formation of Calcareous Deposits during the Corrosion of Mild Steel in Sea Water," Corrosion Science, Vol. 26, No. 9, 1986, pp. 669-680.

Engell, H.-J. and Forchhammer, P., Corrosion Science, Vol. 5, 1965, pp. 479-488 (in German).

England, H. R. and Heidrich, R. H., "The Effects of Water Depth on Cathodic Protection of Steel in Seawater," 1981 Offshore Technology Conference, Paper No. 4154, pp. 379-384.

Evans, T., "The Submarine Perspective," National Conference on the Use of Composite Materials in Load Bearing Marine Structures, Arlington, Virginia, Sept. 26, 1990, National Research Council.

Filinovsky, V. Yu., and Pleskov, Yu. V., "Rotating Disk and Ring-Disk Electrodes," in *Comprehensive Treatise of Electrochemistry, Volume 9, Electrodes: Experimental Techniques*, Plenum Press, New York, 1984.

Fischer, P. and DeLuccia, J. J., "Effects of Graphite/Epoxy Composite Materials on the Corrosion Behavior of Aircraft Alloys," *Environmental Effects on Composite Materials*, ASTM STP 602, American Society for Testing and Materials, 1976, pp. 50-66.

Fischer, S., Roman, I., Harel, H., Marom, G., and Wagner, H. D., "Simultaneous Determination of Shear and Young's Moduli in Composites," *Journal of Testing and Evaluation*, JTEVA, Vol. 9, No. 5, Sept. 1981, pp. 303-307.

Fried, J. R., "Polymer Technology--Part 7: Engineering Thermoplastics and Specialty Plastics," *Plastics Engineering*, Vol. 39, No. 5, May 1983, pp. 35-44.

Fried, N., "Marine Applications," in *Handbook of Fiberglass and Advanced Plastics Composites*, G. Lubin, Ed., Van Nostrand Reinhold, New York, 1969.

Friedrich, K., Ed., *Application of Fracture Mechanics to Composite Materials*, Composite Material Series, No. 6, Elsevier, New York, 1989.

Fuller, R. T., Sherrow, S., Fornes, R. E., and Memory, J. D., "Hydrogen Exchange Between Water and Epoxy Resin," *Journal of Applied Polymer Science*, Vol. 24, 1979, pp. 1383-1385.

Garg, A. and Ishai, O., "Hygrothermal Influence on Delamination Behavior of Graphite/Epoxy Laminates," *Engineering Fracture Mechanics*, Vol. 22, No. 3, 1985, pp. 413-427.

Garg, A. C., "The Fracture Toughness of Some Graphite Fibre-Reinforced Epoxy Laminates," *Composites*, Vol. 17, No. 2, April 1986, p. 141.

Garvey, R. E., "Composite Hull for Full-Ocean Depth," *Marine Technology Society Journal*, Vol. 24, No. 2, 1990, pp. 49-58.

Gillat, O. and Broutman, L. J., "Effect of an External Stress on Moisture Diffusion and Degradation in a Graphite-Reinforced Epoxy Laminate," *Advanced Composite Materials -- Environmental Effects*, ASTM STP 658, J. R. Vinson, Ed., American Society for Testing and Materials, Philadelphia, 1978, pp. 61-83.

Goldberg, E.D., Koide, M., Bertine, K., Hodge, V., Stallard, M., Martincic, D., Mikac, N., Branica, M., and Abaychs, J.K., "Marine Geochemistry - 2: Scavenging Redux," *Applied Geochemistry*, Vol. 3, 1988, pp. 561-571.

Graner, W. R., "Marine Applications," in *Handbook of Composites*, G. Lubin, Ed., Van Nostrand Reinhold, New York, 1982.



- Graner, W. R., "Reinforced Plastics for Deep-Submergence Application," *Ocean Engineering*, Vol. 1, 1969, pp. 353-372.
- Gupta, A., Cizmecioglu, M., Coulter, D., Liang, R. H., Yavrouian, A., Tsay, F. D., and Moacanin, J., "The Mechanism of Cure of Tetraglycidyl Diaminodiphenyl Methane with Diaminodiphenyl Sulfone," *Journal of Applied Polymer Science*, Vol. 28, 1983, pp. 1011-1024.
- Hack, H. P. and Macander, A. B., "The Effect of Cathodic Protection on Graphite Fiber-Epoxy Composite in Natural Sea Water," *Materials Performance*, March 1983, pp. 16-20.
- Halpin, J. C., *Primer on Composite Materials: Analysis*, Technomic Publishing Co., Lancaster, Pennsylvania, 1984.
- Hancox, N. L., "The Influence of Voids on the Hydrothermal Response of Carbon Fibre Reinforced Plastics," *Journal of Materials Science*, Vol. 16, 1981, pp. 627-632.
- Hartt, W. H., Culberson, C. H. and Smith, S. W., "Calcareous Deposits on Metal Surfaces in Seawater -- A Critical Review," *Corrosion*, Vol. 40, No. 11, November 1984, pp. 609-618.
- Hojo, M., Tanaka, K., Gustafson, C. G., and Hayashi, R., "Effect of Stress Ratio on Near-threshold Propagation of Delamination Fatigue Cracks in Unidirectional CFRP," *Composites Science and Technology*, Vol. 29, 1987, pp. 273-292.
- Hom, K., "Composite Materials for Pressure Hull Structures," *Ocean Engineering*, Vol. 1, 1969, pp. 315-324.
- Humble, R.A., "Cathodic Protection of Steel in Sea Water with Magnesium Anodes," *Corrosion*, Vol. 4, No. 7, July 1948, pp. 358-370.
- Jelinski, L. W., Dumais, J. J., Cholli, A. L., Ellis, T. S., and Karasz, F. E., "Nature of the Water-Epoxy Interaction," *Macromolecules*, Vol. 18, 1985, pp. 1091-1095.
- Johannesson, T. and Blikstad, M., "Fractography and Fracture Criteria of the Delamination Process," *Delamination and Debonding of Materials*, ASTM STP 876, W.S. Johnson, Ed., American Society for Testing and Materials, Philadelphia, 1985, pp. 411-423.
- Johnson, W. S., and Mangalgiri, P. D., "Investigation of Fiber Bridging in Double Cantilever Beam Specimens," *Journal of Composites Technology and Research*, Vol. 9, No. 1, Spring 1987, pp. 10-13.
- Judd, N. C. W., "Absorption of Water into Carbon Fibre Composites," *The British Polymer Journal*, Vol. 9, No. 1, March 1977, pp. 36-40.
- Judd, N. C. W., "The Effect of Water on Carbon Fibre Composites," Presented at the 30th Anniversary Technical Conference of the Reinforced Plastics/Composites Institute, 1975, Section 18-A, The Society of the Plastics Industry, Inc.

Kaelble, D. H., Dynes, P. J., and Cirlin, E. H., "Interfacial Bonding and Environmental Stability of Polymer Matrix Composites," *Journal of Adhesion*, Vol. 6, 1974, pp. 23-48.

Kaelble, D. H., Dynes, P. J., Crane, L. W., and Maus, L., "Interfacial Mechanisms of Moisture Degradation in Graphite-Epoxy Composites," *Journal of Adhesion*, Vol. 7 1974, pp. 25-54.

Kinloch, A. J., "Mechanics and Mechanisms of Fracture of Thermosetting Epoxy Polymers," *Epoxy Resins and Composites I*, K. Dusek, Ed., *Advances in Polymer Science Series*, No. 72, Springer-Verlag, New York, 1985, pp. 45-67.

Kinoshita, K., *Carbon -- Electrochemical and Physicochemical Properties*, Wiley-Interscience, New York, 1988.

Koehler, E. L., "The Mechanism of Cathodic Disbondment of Protective Organic Coatings -- Aqueous Displacement at Elevated pH," *Corrosion*, Vol. 40, No. 1, January 1984, pp. 5-8.

Kong, E. S.-W., "Physical Aging in Epoxy Matrices and Composites," in *Advances in Polymer Science Series*, No. 80, Springer-Verlag, Berlin, 1986.

Kuhn, A. T. and Chan, C. Y., "pH Changes at Near-Electrode Surfaces," *Journal of Applied Electrochemistry*, Vol. 13, 1983, pp. 189-207

Kunjapur, M. M., Hartt, W. H., and Smith, S. W., "Influence of Temperature and Exposure Time Upon Calcareous Deposits," *Corrosion*, Vol. 43, No. 11, 1987, pp. 674-679.

Lee, R. U., and Ambrose, J. R., "Influence of Cathodic Protection Parameters on Calcareous Deposit Formation," *Corrosion*, Vol. 44, No. 12, 1988, pp. 887-891.

Leidheiser, H., Ed., *Corrosion Control by Organic Coatings*, National Association of Corrosion Engineers, Houston, 1981.

Leidheiser, H., Jr., "Towards a Better Understanding of Corrosion Beneath Organic Coatings," *Corrosion*, Vol. 39, No. 5, May 1983, pp. 189-201.

Letton, A., and Bradley, W., "Studies in Long Term Durability of Composites in Seawater," *Proceedings, Use of Composite Materials in Load-Bearing Marine Structures*, National Research Council, September 25-26, 1990.

Levy, R. L., Fanter, D. L., and Summers, C. J., "Spectroscopic Evidence for Mechanochemical Effects of Moisture in Epoxy Resins," *Journal of Applied Polymer Science*, Vol. 24, 1979, pp. 1643-1664.

Lin, S. H. and Dexter, S. C., "Effects of Temperature and Magnesium Ions on Calcareous Deposition," *Corrosion*, Vol. 44, No. 9, 1988, pp. 615-622.

Loos, A. C. and Springer, G. S., "Moisture Absorption of Graphite-Epoxy Composites Immersed in Liquids and in Humid Air," in *Environmental Effects on Composite Materials*, G. S. Springer, Ed., Technomic, 1981, pp. 34-50.

- Loos, A. C., and Springer, G. S., "Moisture Absorption of Graphite-Epoxy Composites Immersed in Liquids and in Humid Air," *Journal of Composite Materials*, Vol. 13, 1979, pp. 131-147.
- Luoma, G. A., and Rowland, R. D., "Environmental Degradation of an Epoxy Resin Matrix," *Journal of Applied Polymer Science*, Vol. 32, 1986, pp. 5777-5790.
- Macander, A. and Silvergleit, M., "The Effect of the Marine Environment on Stressed and Unstressed Graphite/Epoxy Composites," *Naval Engineers Journal*, Vol. 89, No. 4, August 1977, pp. 65-72.
- Macander, A., Silvergleit, M., and Edelstein, H. P., "Marine Durability of a Graphite/Epoxy Composite Subjected to Static and Fatigue Loading," *Mechanical Behavior of Materials, Proceedings of the Third International Conference*, August 20-24, 1979, Cambridge, England, Pergamon Press, New York, 1979, pp. 333-343.
- Mandell, J. F. and Meier, U., "Effects of Stress Ratio, Frequency, and Loading Time on the Tensile Fatigue of Glass-Reinforced Epoxy," *Long-Term Behavior of Composites*, ASTM STP 813, T. K. O'Brien, Ed., American Society for Testing and Materials, Philadelphia, 1983, pp. 55-77.
- Manocha, L. M., Bahl, O. P. and Jain, R. K., "Performance of Carbon Fibre Reinforced Epoxy Composites under Different Environments," *Progress in Science and Engineering of Composites*, T. Hayashi, K. Kawata and S. Umewaka, eds., *International Conference on Composite Materials -- IV*, Tokyo, 1982, pp. 957-964.
- March, J., *Advanced Organic Chemistry: Reactions, Mechanisms, and Structure*, 3rd Ed., Wiley, New York, 1985.
- Marom, G., and Broutman, L. J., "Moisture in Epoxy Resin Composites," *Journal of Adhesion*, Vol. 12, 1981, pp. 153-164.
- May, C. A., Ed., *Epoxy Resins: Chemistry and Technology*, Marcel Dekker, New York, 1988.
- Mazor, A. and Broutman, L. J., "Effect of Long-Term Water Exposure on Properties of Carbon and Graphite Fiber-Reinforced Epoxies," *Polymer Engineering and Science*, Vol. 18, No. 5, April 1978, pp. 341-349.
- Nakanishi, Y. and Shindo, A., "Deterioration of CFRP and GFRP in Salt Water," *Progress in Science and Engineering of Composites*, T. Hayashi, K. Kawata and S. Umewaka, Eds., *International Conference on Composite Materials -- IV*, Tokyo, 1982, pp. 1009-1016.
- Neffe, S., "Effect of Anodic Oxidation of Pan-Based Carbon Fibers on the Morphological Changes of their Surfaces," *Carbon*, Vol. 25, No. 6, 1987, pp. 761-767.
- Newman, J. S., *Electrochemical Systems*, Prentice-Hall, 1973.
- Pegg, R. L. and Reyes, H., "Composites Promise Navy Weight, Tactical Advantages," *Sea Technology*, Vol. 27, No. 7, July 1986, pp. 31-34.

Pine, S. H., Hendrickson, J. B., Cram, D. J., and Hammond, G. S., *Organic Chemistry*, 4th Ed., McGraw-Hill Book Company, New York, 1980.

Pipes, R. B., Chairman, National Conference on the Use of Composite Materials in Load Bearing Marine Structures, National Research Council, Arlington, Virginia, September 25-26, 1990.

Pourbaix, M., *Atlas of Electrochemical Equilibria in Aqueous Solutions*, National Association of Corrosion Engineers, Houston, 1974.

Poursartip, A., Ashby, M. F., and Beaumont, P. W. R., "Damage Accumulation During Fatigue of Composites," *Scripta Metallurgica*, Vol. 16, 1982, pp. 601-606.

Proctor, A. and Sherwood, P. M. A., "X-Ray Photoelectron Spectroscopic Studies of Carbon Fibre Surfaces -- II. The Effect of Electrochemical Treatment," *Carbon*, Vol. 21, No. 1, 1983, pp. 53-59.

Pud, A. A., Shapoval, G. S., Tomilov, A. P., and Yatsimirskaya, T. S., "Electrochemical Reductive Degradation of Polyethylene Terephthalate," *Teoreticheskaya i Eksperimental'naya Khimiya*, Vol. 20, No. 5, September-October 1984, pp. 584-589.

Ramkumar, R. L., and Whitcomb, J. D., "Characterization of Mode I and Mixed-Mode Delamination Growth in T300/5208 Graphite/Epoxy," *Delamination and Debonding of Materials*, ASTM STP 876, W. S. Johnson, Ed., American Society for Testing and Materials, Philadelphia, 1985, pp. 315-335.

Randin, J.P., "Carbon," in *The Encyclopedia of Electrochemistry of the Elements*, Allen J. Bard, Ed., Volume VII, Marcel-Dekker, New York, 1976.

Rege, S. K. and Lakkad, S. C., "Effect of Salt Water on Mechanical Properties of Fibre Reinforced Plastics," *Fibre Science and Technology*, Vol. 19, No. 4, 1983, pp. 317-324.

Reifsnider, K. L., Schulte, K., and Duke, J. C., "Long-Term Fatigue Behavior of Composite Materials," *Long-Term Behavior of Composites*, ASTM STP 813, T.K.O'Brien, Ed., American Society for Testing and Materials, Philadelphia, 1983, pp. 136-159.

Rosensaft, M., and Marom, G., "Evaluation of Bending Test Methods for Composite Materials," *Journal of Composite Technology and Research*, Vol. 7, No. 1, Spring 1985, pp. 12-16.

Roylance, D., and Roylance, M., "Weathering of Fiber-Reinforced Epoxy Composites," *Polymer Engineering and Science*, Vol. 18, No. 4, March 1978, pp. 249-254.

Russell, A. J., and Street, K. N., "A Constant  $\Delta G$  Test for Measuring Mode I Interlaminar Fatigue Crack Growth Rates," *Composite Materials: Testing and Design (Eighth Conference)*, ASTM STP 972, J. D. Whitcomb, Ed., American Society for Testing and Materials, Philadelphia, 1988, pp. 259-277.

- Russell, A. J., and Street, K. N., "Moisture and Temperature Effects on the Mixed-Mode Delamination Fracture of Unidirectional Graphite/Epoxy," *Delamination and Debonding of Materials*, ASTM STP 876, W. S. Johnson, Ed., American Society for Testing and Materials, Philadelphia, 1985, pp. 349-370.
- Salama, M. M., "Lightweight Materials for Deepwater Offshore Structures," OTC Paper No. 5185, Offshore Technology Conference, Houston, May 1986.
- Sandifer, J. P., "Effects of Corrosive Environments on Graphite/Epoxy Composites," *Progress in Science and Engineering of Composites*, T. Hayashi, K. Kawata and S. Umewaka, eds., International Conference on Composite Materials -- IV, Tokyo, 1982, pp. 979-986.
- Schirmann, J.-P., and Delavarenne, S. Y., *Hydrogen Peroxide in Organic Chemistry*, Edition et Documentation Industrielle (EDI), Paris, 1979.
- Schumb, W. C., Satterfield, C. N., and Wentworth, R. L., *Hydrogen Peroxide*, American Chemical Society Monograph Series, Reinhold, New York, 1955.
- Scott, P. J. B., "Biodeterioration of Plastics in the Sea," *Materials Performance*, October 1989, pp. 52-53.
- Shapoval, G. S., Pud, A. A., Zamotayev, P. V., and Kachan, A. A., "Degradation of Some Carbon-Chain Polymers by Electrochemical Reduction," *Polymer Science USSR*, Vol. 27, No. 10, 1985, pp. 2427-2431.
- Shen, C. H. and Springer, G. S., "Effects of Moisture and Temperature on the Tensile Strength of Composite Materials," *Environmental Effects on Composite Materials*, G. S. Springer, Ed., Technomic, 1981, pp. 79-93.
- Shen, C.-H., and Springer, G. S., "Moisture Absorption and Desorption of Composite Materials," *Journal of Composite Materials*, Vol. 10, 1976, p. 2.
- Sloan, F. E. and Seymour, R. J., "Environmental Testing Using a Compliant Load-Frame," *Journal of Composite Materials*, Vol. 24, No. 7, July 1990, pp. 727-738.
- Sloan, F. E., and Seymour, R. J., "Electrochemical Degradation Mechanisms in Graphite-Fiber-Reinforced Epoxy Composite Materials," University of California, San Diego, SIO Reference Series No. 90-16, April 16, 1990.
- Smith, B. W. and Grove, R. A., "Determination of Crack Propagation Directions in Graphite/Epoxy Structures," *Fractography of Modern Engineering Materials: Composites and Metals*, ASTM STP 948, J. E. Masters and J. J. Au, Eds., American Society for Testing and Materials, Philadelphia, 1987, pp. 154-173.
- Smith, C. S., *Design of Marine Structures in Composite Materials*, Elsevier Applied Science, New York, 1990.
- Sparks, C., "Lightweight Composite Production Risers for a Deep Water Tension Leg Platform," *Proceedings of the Offshore Mechanics and Arctic Engineering (OMAE) Conference*, Tokyo, April 1986.

Springer, G. S., Ed., *Environmental Effects on Composite Materials*, Technomic, 1981.

Springer, G. S., Ed., *Environmental Effects on Composite Materials, Volume 2*, Technomic, 1984.

Stachiw, J. D., "Pressure Resistant Ceramic Housings for Deep Submergence Unmanned Vehicles," *Marine Technology Society Journal*, Vol. 24, No. 2, pp. 59-62.

Stevenson, A., "On the Durability of Rubber/Metal Bonds in Seawater," *International Journal of Adhesion and Adhesives*, Vol. 5, No. 2, April 1985, pp. 81-91.

Strasburg, W. M., Peterson, M. H., and Pinto, J. E., "Deterioration of Wooden Hull Planking by Cathodic Protection Systems," *Materials Performance*, Vol. 21, No. 9, September 1982, pp. 14-16.

Stumm, W. and Morgan, J. J., *Aquatic Chemistry*, 2nd Ed., Wiley-Interscience, New York, 1981.

Sumsion, H. T., "Environmental Effects on Graphite-Epoxy Fatigue Properties," *Journal of Spacecraft*, Vol. 13, No. 3, March 1976, pp. 150-155.

Talreja, R., "A Continuum Mechanics Characterization of Damage in Composite Materials," *Proc. R. Soc. Lond. A*, Vol. 399, 1985, pp. 195-216.

Tarasevich, M. R., Sadkowski, A., and Yeager, E., "Oxygen Electrochemistry," in *Comprehensive Treatise of Electrochemistry, Volume 7, Kinetics and Mechanisms of Electrode Processes*, Plenum Press, New York, 1983.

Tsai, S. W. and Hahn, H. T., *Introduction to Composite Materials*, Technomic Publishing Co., Lancaster, Pennsylvania, 1980.

Tsai, S. W., *Composites Design*, 4th Ed., Think Composites, Dayton, Ohio, 1988.

Tse, K. W., Moyer, C. A., and Araj, S., "Electrical Conductivity of Graphite Fiber-Epoxy Resin Composites," *Materials Science and Engineering*, Vol. 49, 1981, pp. 41-46.

Tsotsis, T. K., and Weitsman, Y., "Energy Release Rates for Cracks Caused by Moisture Absorption in Graphite/Epoxy Composites," *Journal of Composite Materials*, Vol. 24, May 1990, pp. 483-496.

Tucker, W. C. and Brown, R., "Blister Formation on Graphite/Polymer Composites Galvanically Coupled with Steel in Seawater," *Journal of Composite Materials*, Vol. 23, 1989, pp. 389-395.

Tucker, W. C., and Brown, R., "Moisture Absorption of Graphite/Polymer Composites Under 2000 Feet of Seawater," *Journal of Composite Materials*, Vol. 23, August 1989, pp. 787-797.

Tucker, W. C., Brown, R., and Russell, L., "Corrosion Between a Graphite/Polymer Composite and Metals," *Journal of Composite Materials*, Vol. 24, 1990, pp. 92-102.

Uhlig, H. H. and Revie, R. W., *Corrosion and Corrosion Control*, 3rd Ed., John Wiley & Sons, New York, 1985.

Venables, J. D., "Adhesion and Durability of Metal/Polymer Bonds," *Adhesion* 7, K. W. Allen, Ed., Applied Science Publishers, New York, 1983.

Weitsman, Y., "Coupled Damage and Moisture-Transport in Fiber-Reinforced, Polymeric Composites," *International Journal of Solids and Structures*, Vol. 23, No. 7, 1987, pp. 1003-1025.

Whitney, J. M., and Browning, C. E., "Some Anomalies Associated with Moisture Diffusion in Epoxy Matrix Composite Materials," *Advanced Composite Materials -- Environmental Effects*, ASTM STP 658, J. R. Vinson, Ed., American Society for Testing and Materials, Philadelphia, 1978, pp. 43-60.

Whitney, J. M., Browning, C. E., and Hoogsteden, W., "A Double Cantilever Beam Test for Characterizing Mode I Delamination of Composite Materials," *Journal of Reinforced Plastics and Composites*, Vol. 1, October 1982, pp. 297-313.

Winkelmann, D., *Korrosion (Weinheim)*, Vol. 11, 1959, p. 58 (in German).

Wolfson, S. L. and Hartt, W. H., "An Initial Investigation of Calcareous Deposits Upon Cathodic Steel Surfaces in Sea Water," *Corrosion*, Vol. 37, No. 2, February 1981, pp. 70-76.

Yeager, E., Molla, J. A., and Gupta, S., "The Electrochemical Properties of Graphite and Carbon," in *The Electrochemistry of Carbon, Proceedings of the Workshop*, August 17-19, 1983, Case-Western Reserve University, The Electrochemical Society, *Proceedings* Vol. 84-5, 1984.

Young, P. R., and Chang, A. C., "FTIR Characterization of Advanced Materials," *SAMPE Quarterly*, Vol. 17, No. 4, July 1986, pp. 32-39.

Zaikov, G. E., *Diffusion of Electrolytes in Polymers*, Utrecht, The Netherlands, VSP, 1988.

Zarate, D. A., "Composite Materials Technology Assessment: Waterfront Shore Facilities and Amphibious Advanced Base Applications," 1985, Naval Civil Engineering Lab, TM 52-85-08, Port Hueneme, California.

## APPENDIX A: GENERAL LAMINATE THEORY

### A.1. General Laminate Theory

Engineering design of composite laminates begins with the unidirectional composite lamina or ply, which is modeled as a transversely isotropic material in plane stress. For this condition, stress is related to strain by the matrix  $[Q]$ , i.e.

$$\begin{Bmatrix} \sigma_1 \\ \sigma_2 \\ \tau_{12} \end{Bmatrix} = \begin{bmatrix} Q_{11} & Q_{12} & 0 \\ Q_{21} & Q_{22} & 0 \\ 0 & 0 & Q_{66} \end{bmatrix} \begin{Bmatrix} \epsilon_1 \\ \epsilon_2 \\ \gamma_{12} \end{Bmatrix} \quad (\text{A-1})$$

(A reduced indicial notation is used, where in the coordinate system 1-2, the 1-axis follows the fiber direction while the 2-direction lies normal to the fibers in the plane of the ply). Recall that for an isotropic material (i.e. one whose properties are independent of orientation), the elastic behavior of the material depends on only two constants,  $E$  and  $\nu$ . Hooke's law for the plane stress condition is

$$\begin{aligned} Q_{11} &= Q_{22} = E/(1-\nu^2) \\ Q_{12} &= Q_{21} = \nu Q_{11} \\ Q_{66} &= E/2(1+\nu) = G \end{aligned} \quad (\text{A-2})$$

For a unidirectional fiber-reinforced ply, the components of the Hooke's law or  $Q$ -matrix become

$$\begin{aligned} Q_{11} &= E_{11}/(1-\nu_{12}\nu_{21}) \\ Q_{22} &= E_{22}/(1-\nu_{12}\nu_{21}) \\ Q_{12} &= Q_{21} = \nu_{12}Q_{22} \quad (\nu_{21} = \nu_{12}\frac{E_{22}}{E_{11}}) \\ Q_{66} &= G_{12} \end{aligned} \quad (\text{A-3})$$

There are now four independent elastic constants:  $E_{11}$  and  $E_{22}$ , the stiffness in the fiber and fiber-normal directions, respectively, the shear modulus,  $G_{12}$ , and the major Poisson's ratio,  $\nu_{12}$ . These constants are typically determined by mechanical



tests but can be approximated given the fiber and matrix properties and the volume percent of fiber in each ply.

The ply principal axes (1-2) are typically not coincident with the laminate reference axes (x-y). A Mohr's circle transformation can be used to rotate the laminate stress and strain through an angle  $\theta$ , i.e.

$$\begin{Bmatrix} \sigma_1 \\ \sigma_2 \\ \tau_{12} \end{Bmatrix} = [T] \begin{Bmatrix} \sigma_x \\ \sigma_y \\ \tau_{xy} \end{Bmatrix} \quad (\text{A-4})$$

and

$$\begin{Bmatrix} \varepsilon_1 \\ \varepsilon_2 \\ \gamma_{12}/2 \end{Bmatrix} = [T] \begin{Bmatrix} \varepsilon_x \\ \varepsilon_y \\ \gamma_{xy}/2 \end{Bmatrix} \quad (\text{A-5})$$

where

$$[T] = \begin{bmatrix} m^2 & n^2 & 2mn \\ n^2 & m^2 & -2mn \\ -mn & mn & m^2 - n^2 \end{bmatrix}; \quad \begin{matrix} m = \cos \theta \\ n = \sin \theta \end{matrix} \quad (\text{A-6})$$

Note that the x-axis corresponds to  $\theta=0$ . The factor of 2 in the shear strain rotation is required to use the T-matrix as shown and is a result of differences in the definitions of engineering strain and tensorial strain.

The total strain  $\{\varepsilon\}$  of the laminate is derived for simple plate theory by assuming displacements  $u$ ,  $v$ , and  $w$ , as follows:

$$\begin{aligned} u &= u_0 - z \cdot \frac{\partial w}{\partial x} \\ v &= v_0 - z \cdot \frac{\partial w}{\partial y} \\ w &= w_0 \end{aligned} \quad (\text{A-7})$$

which gives for the strains

$$\begin{aligned} \varepsilon_x &\equiv \frac{1}{2} \left[ \frac{\partial u}{\partial x} + \frac{\partial u}{\partial x} \right] = \frac{\partial u_0}{\partial x} - z \cdot \frac{\partial^2 w}{\partial x^2} \\ \varepsilon_y &\equiv \frac{1}{2} \left[ \frac{\partial v}{\partial y} + \frac{\partial v}{\partial y} \right] = \frac{\partial v_0}{\partial y} - z \cdot \frac{\partial^2 w}{\partial y^2} \\ \varepsilon_{xy} &\equiv \frac{1}{2} \left[ \frac{\partial u}{\partial y} + \frac{\partial v}{\partial x} \right] = \frac{1}{2} \left[ \frac{\partial u_0}{\partial y} + \frac{\partial v_0}{\partial x} \right] - 2z \cdot \frac{\partial^2 w}{\partial x \partial y} \end{aligned}$$

or, in matrix form,

$$\{\epsilon\} = \begin{Bmatrix} \epsilon_x \\ \epsilon_y \\ \epsilon_{xy} \end{Bmatrix} = \{\epsilon^0\} + z \cdot \{k\} \quad (\text{A-8})$$

where  $\{\epsilon^0\}$  is the in-plane strain,  $\{k\}$  is the laminate curvature, and  $z$  is the distance from the laminate mid-plane. The stresses in the  $n^{\text{th}}$  ply in the laminate coordinate system can be expressed as functions of the laminate strains by rotating the ply stresses and strains of equation (A-1). The result is

$$\{\sigma\}_n = [\bar{Q}] \{\epsilon\} \quad (\text{A-9})$$

(Note that  $[\bar{Q}]$  is not equivalent to  $[T]^{-1}[Q][T]$  because of the factor of 2 difference between the tensorial strain and the engineering strain.)

Stress resultants in a laminate of thickness,  $h$ , can be defined as the load per unit width of laminate such that

$$\{N\} = \begin{Bmatrix} N_x \\ N_y \\ N_{xy} \end{Bmatrix} = \int_{-h/2}^{h/2} \{\sigma\} dz \quad (\text{A-10})$$

Similarly for flexural loading, we can define

$$\{M\} = \begin{Bmatrix} M_x \\ M_y \\ M_{xy} \end{Bmatrix} = \int_{-h/2}^{h/2} \{\sigma\} z dz \quad (\text{A-11})$$

For a laminate consisting of  $n$  distinct plies, each having a different fiber orientation, equation (A-10) takes the form

$$\{N\} = \sum_n \int_{h_{n-1}}^{h_n} \{\sigma\}_n dz \quad (\text{A-12})$$

Substituting for  $\{\sigma\}_n$  using equations (A-8) and (A-9), the stress-strain relations can be expressed in matrix form as

$$\begin{Bmatrix} N \\ M \end{Bmatrix} = \begin{bmatrix} A & B \\ B & D \end{bmatrix} \begin{Bmatrix} \epsilon^0 \\ k \end{Bmatrix} \quad (\text{A-13})$$

where

$$[A] = \sum_n \int_{h_{n-1}}^{h_n} [\bar{Q}]_n dz = \sum_n [\bar{Q}]_n (h_n - h_{n-1}) \quad (A-14)$$

$$[B] = \sum_n \int_{h_{n-1}}^{h_n} [\bar{Q}]_n z dz = \frac{1}{2} \sum_n [\bar{Q}]_n (h_n^2 - h_{n-1}^2) \quad (A-15)$$

$$[D] = \sum_n \int_{h_{n-1}}^{h_n} [\bar{Q}]_n z^2 dz = \frac{1}{3} \sum_n [\bar{Q}]_n (h_n^3 - h_{n-1}^3) \quad (A-16)$$

( $h_n$  is the distance from the top of the  $n^{\text{th}}$  ply to the midplane).

Equations (A-13) through (A-16) are the basis for stress and strain determinations for composite laminates under static loads. Once the constitutive matrices  $[A]$ ,  $[B]$ , and  $[D]$  are known, the applied loads determine  $\{\epsilon^0\}$  and  $\{k\}$ . The total strain  $\{\epsilon\}$  in any laminae can then be determined from Eq. (A-8). The ply strains in the ply coordinate system (1-2) are then determined by equation (A-5). The ply stresses in the 1-2 system can then be determined using equations (A-1) and (A-3). Failure criteria are normally based on allowable stresses or strains in the 1-2 system.

## A.2. Hygrothermal Effects (Residual Stresses)

When a fiber-reinforced plastic is manufactured, the final curing of the material (i.e. the stress-free state) occurs at relatively high temperatures with no moisture present. As the laminate cools to its service temperature, residual stresses appear because of the different thermal expansion coefficients of the fiber and matrix. The natural tendency of the polymer to absorb moisture from the surroundings also leads to residual stresses because of different swelling coefficients. Any analysis of composite laminates must account for these residual stresses, which

can be substantial in typical applications.

The effects of moisture absorption and post-cure cooldown on an individual ply are assumed to be linear for simplicity. In addition, superposition is assumed, i.e.

$$e_i = \alpha_i \cdot \Delta T + \beta_i \cdot c, \quad i=1,2 \quad (\text{A-17})$$

where  $\alpha$  and  $\beta$  are the thermal expansion and swelling coefficients,  $\Delta T$  is the difference in temperature between the service and the cure conditions, and  $c$  is the equilibrium moisture content of the cured ply under service conditions. The total strain under an applied stress would have to account for this hygrothermal expansion,

$$\{\varepsilon_i\} = \{\varepsilon_i\}^{\text{mech}} + \{e_i\} \quad (\text{A-18})$$

so that

$$\{\sigma_i\} = [Q] \{\varepsilon_i - e_i\} \quad (\text{A-19})$$

Replacing equation (A-1) with (A-19) and following the procedure of the previous section leads to the more general laminate constitutive relation

$$\begin{bmatrix} N \\ M \end{bmatrix} = \begin{bmatrix} A & B \\ B & D \end{bmatrix} \begin{bmatrix} \varepsilon^0 \\ k \end{bmatrix} - \begin{bmatrix} N \\ M \end{bmatrix}^e \quad (\text{A-20})$$

where the superscript  $e$  suggests environmental loading. Thus the laminate strains can be broken up into mechanical and environmental parts

$$\begin{bmatrix} \varepsilon^0 \\ k \end{bmatrix} = \begin{bmatrix} \varepsilon^0 \\ k \end{bmatrix}^{\text{mech}} + \begin{bmatrix} e^0 \\ k^e \end{bmatrix}^{\text{env}} \quad (\text{A-21})$$

(The environmental strains can be determined by assuming that the mechanical load  $N$  and  $M$  in equation (A-20) are zero, then inverting to find the resulting strains.)

The mechanical and environmental ply stresses and strains resulting from mechanical and environmental loads can then be determined in a manner similar to the previous section. The ply residual strains are determined by subtracting the

hygrothermal strains (already in the 1-2 system) from the environmental strains (after rotation into the 1-2 system), i.e.

$$\{\epsilon\}_{\text{resid}} = \{\epsilon\}_{\text{env}} - \{e\} \quad (\text{A-22})$$

then using equation (1) to get the residual stresses. The total stresses and strains in each ply are then the sum of the mechanical and residual components.

### A.3. Bending of Symmetric Composite Beams

For symmetric laminates the B-matrix of section A.1 vanishes, and for pure bending equation (A-11) becomes (for unit width)

$$\{M\} = \begin{Bmatrix} M_x \\ M_y \\ M_{xy} \end{Bmatrix} = \int_{-h/2}^{h/2} [Q] z^2 dz \cdot \{k\} = [D]\{k\} \quad (\text{A-23})$$

For simple beam bending we assume  $M_x=M$  and  $M_y=M_{xy}=0$ , giving

$$k = d_{11} \cdot M \quad (\text{A-24})$$

where  $[d] = [D]^{-1}$  (true only when  $[B]=0$ ).

For the isotropic case the elastic constants of the material are independent of  $z$  and the bending compliance  $d_{11}$  reduces to  $1/EI$ . For the case of the symmetric laminate  $d_{11}$  includes the effects of stiffness and geometry in a non-straightforward manner. The bending compliance  $d_{11}$  can be normalized by the apparent moment of inertia, i.e.

$$I^* = h^3/12 \quad (\text{A-25})$$

to get

$$d_{11}^* = d_{11} \cdot I^* \quad (\text{A-26})$$

The beam curvature can then be written as

$$k = \frac{M}{E_x^f \cdot I} \quad (\text{A-27})$$

where  $E_x^f = 1/d_{11}^*$ . Formulas for the deflection and moment in symmetric beams are

the same as for homogeneous beams with the exception of the calculation of the flexural stiffness. It is worth noting that the equations of general laminate theory do not include the effects of shear, and become less accurate for short beams.

#### A.4. Summary

In summary then, general laminated plate theory begins with basic stress and strain relations (i.e. Hooke's law) for a single ply or lamina. These relations are transformed into the laminate coordinate system using 2-dimensional transformation relations. By satisfying equilibrium between the applied loads and the individual stresses in the plies, the laminate strains can be determined. These strains are then rotated back into the ply coordinates to determine the individual lamina strains, from which the individual ply stresses are determined. Residual stresses caused by temperature changes and moisture absorption should also be included in any stress analysis. For symmetric lay-up composite beams the stress and strain relations can be approximated using simple beam theory for isotropic beams with an effective flexural modulus. The equations of general laminate theory described above have been developed in the program LAMCALC for IBM and compatible personal computer systems. LAMCALC is available as a shareware program from the American Society of Mechanical Engineers ASME/CIME (Computers in Mechanical Engineering) Bulletin Board, at (608) 233-3378.

#### A.5. Bibliography

Halpin, J. C., *Primer on Composite Materials: Analysis*, Technomic Publishing Co., Lancaster, Pennsylvania, 1984.

Tsai, S. W. and Hahn, H. T., *Introduction to Composite Materials*, Technomic, 1980.

Tsai, S. W., *Composites Design*, 4th Ed., Think Composites, Dayton, Ohio, 1988.

**PLEASE NOTE**

**Copyrighted materials in this document have  
not been filmed at the request of the author.  
They are available for consultation, however,  
in the author's university library.**

**219-230**

**University Microfilms International**

The preceding paper was written primarily by Forrest Sloan to document a unique experimental method for research into the effects of environment on crack growth in composite materials. The co-author, Dr. Richard Seymour, provided valuable advice regarding verification of the theory presented in the paper. Dr. Seymour also offered several constructive suggestions which helped to complete the final draft.